THE UNIVERSITY OF QUEENSLAND

AUSTRALIA

U-series geochronology and geochemistry of vein and cave carbonate deposits in Turkey: the relationship between late Quaternary tectonic and climatic events

Ezgi Ünal-İmer

M.Sc., Economic Geology, Middle East Technical University, 2010

B.Sc., Geological Engineering, Middle East Technical University, 2007

A thesis submitted for the degree of Doctor of Philosophy at

The University of Queensland in 2015

School of Geography, Planning and Environmental Management

Abstract

This study is based on the use of vein calcites and speleothems to improve our understanding of late Quaternary tectonic activity and climatic variability in SW Turkey, and to investigate their effects on CO_2 degassing events. To facilitate this, multi-generation carbonate veins and breccia within active faulting zones in Marmaris (Kumlubük and Amos; SW Turkey) and three stalagmites from the Dim Cave (SW Turkey) were studied through thorough petrographical, geochronological (U-series dating), and geochemical (O-C-Sr isotope ratio and trace element concentration) analyses. The findings are presented as a series of four papers.

The tectonic study is based on a 150-kyr long precisely-dated (U-series) record of 160 calcite vein/breccia samples from an extensional zone in SW Turkey. The age distribution of the carbonates is commensurate with periods of low to transitional summer insolation. Net moisture balance was positive during the last glacial period, which primarily reflected reduced evapotranspiration rather than increased precipitation. Host limestone sourced-CO_2 accumulation at depth was enhanced by reduced infiltration of meteoric water from shallow depth; facilitating CO_2 build up in the rupture zones and fault failures. This resulted in substantial CO_2 degassing and carbonates (veins and breccias) formation near and at the surface. [Paper 1]

Further investigations of the vein carbonates using $\delta^{13}C$, $\delta^{18}O$ and Sr- isotope, and Rare Earth Element (and Yttrium) (REY) concentration data were undertaken to determine the sources of solutions responsible for the calcite deposition (272.6 to 20.5 kyr) and the genetic processes involved in vein formation. Based on geochemical characteristics of the veins, it is concluded that the water source for the fluids originated dominantly from meteoric sources with various degrees of interactions with the host limestone and siliciclastic basement rocks. CO_2 is sourced mainly from dissolved host limestone. Microstructural/geochronological observations demonstrate that vein formation is controlled by a crack-seal mechanism, commonly accompanied by the brecciation of the host limestone. Stable isotope (O, C) records of the veins reveal a cyclic nature of CO_2-degassing events with meteoric water infiltration through normal faults influencing growth-cycles of the veins. However, the overall control on faulting is the rate of regional tectonic activity. [Paper 2]

The paleoclimatic work was underpinned by high-resolution stable isotope (O, C) profiles derived from three stalagmites (Dim-E2, Dim-E3, and Dim-E4) in Dim Cave (36 ºN, 232 m a.s.l.), SW Turkey. The record is controlled by 44 high-precision U-series dates spanning from ~90 to 9 kyr, and covers the whole of the last glaciation. Changes in $\delta^{18}O$ can be best explained by the track

changes in the trajectory of winter westerlies between a northerly (less depleted) and a more southerly (more depleted) air mass track. This change in track is attributed to the growth of the Fennoscandian Ice Sheet from MIS 4 to MIS 2, which gradually depressed winter westerly tracks southward. Glacial/interglacial swings in $\delta^{13}C$ appear to reflect changes in the vegetation/soil cover and, critically, interactions with the host limestone. A positive moisture water balance throughout the last glaciation is inferred, based on continuous speleothem growth of the Dim-E3 speleothem. In addition, isotopic responses to Heinrich events are recorded in the Dim Cave. They also reflect changes in the intensity of westerly flow and respond to the gradual change in the westerly track through the last glacial cycle. [Paper 3]

Finally multi-proxy records of stable/radiogenic isotope (O, C, Sr), trace element/Ca (Mg/Ca, Sr/Ca, U/Ca, Ba/Ca, Y/Ca, and Zr/Ca), element concentration of speleothems of the Dim Cave (SW Turkey) were examined. Chemical changes in cave drip water and speleothems are attributed to alternating wet and dry periods in Dim Cave, and are consistent with changes in moisture source characteristics in SW Turkey. Trace elements are sourced from the host dolomitic limestone and display significant interactions with soil and groundwater. Higher values in Zr/Ca, U/Ca, and Y/Ca during periods of higher growth rates of Dim-E3 (during 51–40, 71–63, and 89–80 kyr) are associated with wet periods where more non-calcareous material is fed into the drip system. This may reflect either deposition of aeolian dust and/or increased dissolution of silica-rich rock. Covariance and increased values of Mg/Ca, Sr/Ca, and Ba/Ca are interpreted to be controlled by enhanced interactions between host limestone and drip waters during drier conditions (during times of lower growth rates; 40–18, 63–51, and 80–71 kyr), probably in response to the mechanisms of prior calcite precipitation and differential dissolution of dolomite in the host. [Paper 4]

Declaration by author

This thesis is composed of my original work, and contains no material previously published or written by another person except where due reference has been made in the text. I have clearly stated the contribution by others to jointly-authored works that I have included in my thesis.

I have clearly stated the contribution of others to my thesis as a whole, including statistical assistance, survey design, data analysis, significant technical procedures, professional editorial advice, and any other original research work used or reported in my thesis. The content of my thesis is the result of work I have carried out since the commencement of my research higher degree candidature and does not include any work that has been submitted to qualify for the award of any other degree or diploma in any university or other tertiary institution. I have clearly stated which parts of my thesis, if any, have been submitted to qualify for another award.

I acknowledge that an electronic copy of my thesis must be lodged with the University Library and, subject to the policy and procedures of The University of Queensland, the thesis be made available for research and study in accordance with the Copyright Act 1968 unless a period of embargo has been approved by the Dean of the Graduate School.

I acknowledge that copyright of all material contained in my thesis resides with the copyright holder(s) of that material. Where appropriate I have obtained copyright permission from the copyright holder to reproduce material in this thesis.

Publications during candidature

Peer reviewed papers:

Ünal-İmer E., Shulmeister J., Zhao J.X., Uysal I.T., Feng Y.X. (under review). High-resolution trace element and stable/radiogenic isotope profiles of late Pleistocene to Holocene speleothems from Dim Cave, SW Turkey. *Quat. Sci. Rev.*

Ünal-İmer E., Shulmeister J., Zhao J.X., Uysal I.T., Feng Y.X., Nguyen, A. D., Yüce G. (2015). An 80 kyr-long continuous speleothem record from Dim cave, SW Turkey with paleoclimatic implications for the Eastern Mediterranean. *Nature Sci. Rep*. **5**, 13560; doi: 10.1038/srep13560.

Ünal-İmer E., Uysal I.T., Işık V., Zhao J.X., Shulmeister J., İmer A., Feng, Y.X. (under review). CO_2 outburst cycles in relation to seismicity: constraints from micro-scale geochronology and geochemistry of late Quaternary vein carbonates, SW Turkey. *Geochim. Cosmochim. Acta.*

Ünal-İmer E., Uysal I.T., Shulmeister J., Zhao J.X., Feng Y.X., Işık V., Bolhar R., Larsen J. (under review). Linking CO_2 degassing in active fault zones to long-term changes in moisture balance and surface water circulation, an example from SW Turkey. *Nature Geosci.*

Conference abstracts:

Ünal-İmer E, Shulmeister J., Zhao J.X., Uysal I.T., 2015. Late Pleistocene climate variability in the eastern Mediterranean: Multiproxy speleothem records from Dim Cave in SW Turkey. *Goldschmidt2015 Abstracts*, 3209, Prague, Czech Republic

Uysal I.T., Ring U., Ünal-İmer E., 2014. Geochronology and isotope geochemistry of syntectonic sinter deposits in active fault zones, central Australia. *Goldschmidt2014 Abstracts*, 2543, California, US

Ünal-İmer E., Uysal I.T., Işık V., Zhao J.X., Shulmeister, J. 2014. A high-resolution geochronological and geochemical study on Aegean carbonate deposits, SW Turkey. *Geophysical Research Abstracts* **16,** EGU2014-16265-2, 2014, Vienna, Austria

Ünal-İmer E., Uysal I.T., Shulmeister J., Zhao J.X. 2013. Possible link between CO_2 degassing and climate change in SW Turkey. Goldschmidt2013 (Florence, Italy), *Min. Mag.* **77**(5), 2379

Uysal I. T., Zhao J.X., Ünal-İmer E., and Feng Y.X., 2013. CO_2 degassing events in relation to seismicity and past climate changes. *Acta Geologica Sinica* (Eng. Ed.), **87**(supp.), 388–388.

Peer reviewed papers on related topics:

Ring U., Uysal I.T., Ünal-İmer E., İmer A., Yüce G., Francesco I., Zhao, J.X. (submitted). How stable is Australia? Recent $^{3}He/CO_2$ mantle degassing recorded by carbonic spring deposits along the Oodnadatta Fault Zone, south-central Australia. *Geology*

Uysal I.T., St Pierre E., Ünal-İmer E., Zhao J.X., J. Shulmeister (in prep.). Late Glacial climate oscillations and volcano - tectonic events: Evidence from trace element and isotope records in a precisely dated stalagmite from Southwest Sulawesi, Western Pacific. *Quat. Res.*

Publications included in this thesis

Ünal-İmer E., Uysal I.T., Shulmeister J., Zhao J.X., Feng Y.X., Işık V., Bolhar R., Larsen J. (under review). Linking CO_2 degassing in active fault zones to long-term changes in moisture balance and surface water circulation, an example from SW Turkey. *Nature Geosci.* – as Paper 1.

Contributor	Statement of contribution
Ezgi Ünal-İmer (Candidate)	Designed the research, performed all laboratory work and analysis (90%) Wrote the paper (60%) Field work (20%)
I.Tonguç Uysal	Designed the research (5%) Wrote and edited paper (25%) Field work (20%)
James Shulmeister	Wrote and edited paper (10%)
Jian-Xin Zhao	Wrote and edited the paper (5%)
Yue-Xing Feng	Assisted with the lab analyses (5%)
Veysel Isik	Field work (40%)
Robert Bolhar	Field work (20%)
Joshua Larsen	Assisted with the statistical analyses (100%)

Ünal-İmer. E, Uysal I.T., Işık V., Zhao J.X., Shulmeister J., İmer A., Feng, Y.X. (under review). CO_2 outburst cycles in relation to seismicity: constraints from micro-scale geochronology and geochemistry of late Quaternary vein carbonates, SW Turkey. *Geochim. Cosmochim. Acta* – as Paper 2.

Contributor	Statement of contribution
Ezgi Ünal-İmer (Candidate)	Designed the research, performed all laboratory work and analysis (90%) Wrote the paper (80%) Field work (40%)

I.Tonguç Uysal	Designed the research (5%) Wrote and edited paper (10%) Field work (20%)
Veysel Isik	Field work (40%)
Jian-Xin Zhao	Wrote and edited paper (5%)
James Shulmeister	Edited the paper (2.5%)
Ali Imer	Edited the paper (2.5%)
Yue-Xing Feng	Assisted with the lab analyses (5%)

Ünal-İmer. E, Shulmeister J., Zhao J.X., Uysal I.T., Feng Y.X., Nguyen, A. D., Yüce G. (2015). An 80 kyr-long continuous speleothem record from Dim Cave, SW Turkey with paleoclimatic implications for the Eastern Mediterranean. *Nature Sci. Rep.* ***5****, 13560; doi: 10.1038/srep13560.*– as Paper 3.

Contributor	Statement of contribution
Ezgi Ünal-İmer (Candidate)	Designed the research, performed all laboratory work and analysis (90%) Wrote the paper (70%) Field work (40%)
James Shulmeister	Wrote and edited paper (25%)
Jian-Xin Zhao	Wrote and edited paper (5%)
I.Tonguç Uysal	Field work (50%)
Yue-Xing Feng	Assisted with the lab analyses (5%)
Ai Duc Nguyen	Assisted with the lab analyses (5%)
Galip Yuce	Field work (10%)

Ünal-İmer. E, Shulmeister J., Zhao J.X., Uysal I.T. Feng Y.X. (under review) High-resolution trace element and stable/radiogenic isotope profiles of late Pleistocene to Holocene speleothems from Dim Cave, SW Turkey. *Quat. Sci. Rev.* – as Paper 4.

Contributor	Statement of contribution
Ezgi Ünal-İmer (Candidate)	Designed the research, performed all laboratory work and analysis (95%) Wrote the paper (80%) Field work (50%)
James Shulmeister	Wrote and edited paper (15%)
Jian-Xin Zhao	Edited paper (5%)
I. Tonguç Uysal	Field work (50%)
Yue-Xing Feng	Assisted with the lab analyses (5%)

Contributions by others to the thesis

No contributions by others.

Statement of parts of the thesis submitted to qualify for the award of another degree

None.

Acknowledgements

This research was undertaken with the financial assistance of UQ International Postgraduate Research Scholarship (IPRS) and also by the generous support of the Queensland Geothermal Energy Centre of Excellence (QGECE). I would like to particularly acknowledge support and personal encouragement of Hal Gürgenci (QGECE). The School of Geography, Planning and Environmental Management (GPEM) and QGECE Travel Awards are greatly appreciated for allowing me to perform field work, attend international conferences, and travel for collaborative research.

I would like to sincerely thank to my supervisors: I.Tonguc Uysal, James Shulmeister, and Jian-Xin Zhao. I am very grateful to I.Tonguc Uysal for his encouragement, his generosity with his time and knowledge, and for his endless enthusiasm for this research. Huge thanks go to James Shulmeister for his never-ending support, invaluable advice and criticism, and for being a true scientist and a role model for many of his lucky students. I wish to thank Jian-Xin Zhao for his help, constructive comments, and encouragement throughout my doctoral study. It was a pleasure to work with and learn from all of you. Many thanks to Yue-Xing Feng, Ai Duc Nguyen, Wei Zhou, Kim Baublys, Irena Kinaev, and Sue Golding for their professional help during the lab work, for helpful discussions, and for being always kind to me. I also would like to thank Veysel Işık, Robert Bolhar, Joshua Larsen, Tyler Faith, and Kevin Welsh for their valuable input.

Further thanks to administrative staff of QGECE, School of Earth Sci., and GPEM; most notably to Judy Nankiville, Glenda Heyde, Helen Smith, Alan Victor, and Pamela Cooper.

I owe special thanks to my family and friends: Ali İmer, Eray Çağlar Ünal, Sevgi Ünal, Hüseyin Ünal, Guia Morelli, Aslı Oflaz, Evren Etel, Chantinee Boonchai, Lincoln Steinberger, Missaka Hettiarachchi, Kelsey Lowe, Donata Morelli, Andrea Picanza, Nguyễn Thanh Phong, Payal Bal, William Goulding, Alvaro Salazar Perez, Lydia Mckenzie, Selçuk Bengin, Cemre M. Üstünkaya, Nathan Wright, Nathan Siddle, Tom Paris, Parviz Pourmehrab, and Alexandra Bratanova.

Yaşamaya Dair

- I -

Yaşamak şakaya gelmez,
büyük bir ciddiyetle yaşayacaksın
bir sincap gibi mesela,
yani, yaşamanın dışında ve ötesinde hiçbir şey beklemeden,
yani bütün işin gücün yaşamak olacak.
Yaşamayı ciddiye alacaksın,
yani o derecede, öylesine ki,
mesela, kolların bağlı arkadan, sırtın duvarda,
yahut kocaman gözlüklerin,
beyaz gömleğinle bir laboratuvarda
insanlar için ölebileceksin,
hem de yüzünü bile görmediğin insanlar için,
hem de hiç kimse seni buna zorlamamışken,
hem de en güzel en gerçek şeyin
yaşamak olduğunu bildiğin halde.
Yani, öylesine ciddiye alacaksın ki yaşamayı,
yetmişinde bile, mesela, zeytin dikeceksin,
hem de öyle çocuklara falan kalır diye değil,
ölmekten korktuğun halde ölüme inanmadığın için,
yaşamak yanı ağır bastığından.

On Living

- I -

Living is no laughing matter:
you must live with great seriousness
like a squirrel, for example,
I mean without looking for something beyond and above living,
I mean living must be your whole occupation.
Living is no laughing matter:
you must take it seriously,
so much so and to such a degree,
that, for example, your hands tied behind your back,
your back to the wall,
or else in a laboratory
in your white coat and safety glasses,
you can die for people,
even for people whose faces you've never seen,
even though you know living
is the most real, the most beautiful thing.
I mean, you must take living so seriously
that even at seventy, for example, you'll plant olive trees,
and not for your children, either,
but because although you fear death you don't believe it
because living, I mean, weighs heavier.

Nâzım Hikmet Ran, 1948 *(Translated by Randy Blasing & Mutlu Konuk)*

Keywords

Paleotectonics, paleoclimate, vein/breccia calcites, summer insolation, stalagmites, U-series dating, stable isotopes, Sr-isotopes, trace elements, Amos, Kumlubük, Dim Cave, SW Turkey, Eastern Mediterranean, westerlies, last glaciation, Fennoscandian ice sheet

Australian and New Zealand Standard Research Classifications (ANZSRC)

ANZSRC code: 040313, Tectonics, 30%
ANZSRC code: 040605, Palaeoclimatology, 50%
ANZSRC code: 040203, Isotope Geochemistry, 20%

Fields of Research (FoR) Classification

FoR code: 0403, Geology, 45%
FoR code: 0406, Physical Geography and Environmental Geoscience, 40%
FoR code: 0402, Geochemistry, 15%

Table of Contents

List of Figures

INTRODUCTION

PAPER 1

PAPER 2

PAPER 3

PAPER 4

INTRODUCTION

1. Background

Turkey is a tectonic crossroad between the Arabian, African and European plates (Fig.1.1). It also lies on the boundary between mid-latitude temperate and sub-tropical arid climatic zones in the Eastern Mediterranean. The Turkish landscape reflects the interaction of these tectonic and climatic regimes. Because the climate is at least seasonally arid over much of Turkey targets for reconstructing the tectonic and climate histories, so as to better understand the driving processes, are limited. This thesis focuses on the use of carbonate deposits (calcite veins, travertines and speleothems) to decipher and distinguish the role of tectonic and climatic processes in Turkey, focussing in particular on the SW corner of the country, where these deposits are available.

Carbon dioxide (CO_2) discharge along tectonically active zones can be traced using surface manifestations of bedded travertines and calcium carbonate vein/breccia deposits (Hancock et al. 1999). Well-dated (U-series dating) calcium carbonate precipitates can be used to understand the temporal relationship between fault movements and vein/breccia formations (e.g. Uysal et al. 2011; Nuriel et al. 2012; Uysal et al. 2007; Nuriel et al. 2011; Uysal et al. 2009). Further, precisely-dated calcite veins have been successfully used to obtain insights about past climate conditions when the deposition occurred (e.g. Winograd et al. 1992). Likewise, speleothems, which are defined as secondary carbonate deposits in caves are of great value in understanding terrestrial paleoclimate (e.g. Hendy 1971; Baker et al. 1997; Bar-Matthews et al. 2003; Zhao et al. 2003; Vaks et al. 2003; Fleitmann et al. 2009). They are common in the extensive karst terranes of Turkey and provide an unprecedented opportunity to investigate the relationship between climate and environmental processes and human evolution and to help differentiate between tectonic and climatic effects on carbonate deposition (e.g. Zhao et al. 2001; Wang et al. 2001; Kagan et al. 2005; Vaks et al. 2007; Bar-Matthews et al. 2010). Crustal moisture levels as a function of the accumulation and migration of carbonate precipitating CO_2-rich fluids are driven by both geological controls and climatic conditions. SW Turkey is a tectonically active region with widespread calcite precipitation related to both active faulting, and climatically induced speleothem development, in the limestones bordering the Mediterranean Sea. Combined U-series age analyses and microanalysis of multiple geochemical tracers (i.e. O- and C-isotopes and trace elements) from both carbonate veins and speleothems offers new insights into the complex interplay of late Quaternary CO_2 outburst, fault movement, and hydrological processes. This allows for the reconstruction of both tectonic and climate histories in SW Turkey, and for improved understanding of both the tectonic and climatic processes and their interactions, especially in terms of the role of meteoric waters in both processes.

1.1. Carbon dioxide degassing, high-pressure fluids and active tectonism

The long-term physicochemical behaviour of carbon dioxide (CO_2) and the geochemical factors that govern its storage, migration and degassing from natural accumulations within the crust are topical and important subjects. It has been recently recognized that the natural crustal traps of CO_2 and high-fluid CO_2-rich pressures can be one of the causes inducing seismicity in a region (Chiodini 2004; Miller 2013). Local high-pressure CO_2 traps at crustal depth and degassing episodes can modify regional stress regimes in a tectonically active region, and thereby can play an active role in geodynamics by contributing directly to crustal deformation. For instance, pressure diffusion between deep overpressurized CO_2 reservoirs and shallower regions at hydrostatic fluid pressure is regarded as the leading factor for seismic events in the Central Apennines of Italy (e.g. Chiodini 2004). In other words, overpressurized, (mostly) mantle-derived CO_2 chambers are inferred to induce further seismicity or aftershocks by concurrently releasing and propagating high-pressure fluids along the damaged (e.g. faulted) zones created by the main shock (Miller et al. 2004). Scenarios which support CO_2-rich fluid-driven events includes the Mw = 6.3 2009 L'Aquila Earthquake in the Apennines of Italy (Miller 2013). Further, local high pore pressures fed by gas accumulations (e.g. CO_2 and He) in a reservoir, which is bounded by an inactive fault zone, are considered to be one of the causes that might be capable of creating fault slippage and the reactivation of previously inactive normal faults (Wiprut & Zoback 2000). Likewise, mantle-derived fluid overpressures (~12 MPa at 1.5 km depth) observed within the San Andreas Fault (SAF) strike-slip system (California, U.S.) in association with fluid migration between ductile (lower crust) and brittle (upper crust) are considered to have contributed to fault-weakening mechanisms (Kennedy et al. 1997). In addition, meteoric water accumulation within large continental extension systems as long-term fractured zones (i.e. normal faults) may facilitate waters to migrate downward and provide a natural trap for CO_2-rich fluids, sourced from various geological environments and processes (e.g. from mantle or dissolution of limestone or mantle-derived igneous rocks). Current research recognizes that the high-pressure or trapped fluids involved in fault zones including hydrothermal/metamorphic, magmatic or meteoric fluids all have important roles in triggering earthquakes, by reducing the effective normal stress by means of generating excess pore water pressure (Costain et al. 1987; Miller 2013). It is arguable that continuing input of fluids can lead to higher levels of fluid pressures at depth, which can modify fluid pressure build-ups and drops triggering fault movements (e.g. Costain et al. 1987; Branquet et al. 1999; Saar & Manga 2003; Miller 2013). Furthermore, a considerable amount of CO_2 can be produced during large fault movements (i.e. friction induced CO_2-rich melt by seismic slip) and this may cause fluid pressure to rise rapidly so as to trigger additional slips or aftershocks (Famin et al.

2008). Strong CO_2 discharges, similar to hydrothermal eruptions, are known from ancient Roman documents in central Italy (Chiodini & Frondini 2001). Similarly, hydrothermal eruptions in New Zealand or Western Turkey geothermal fields have been commonly generated by high volatile pressures, which were developed in response to declining groundwater level during dry climate conditions (Browne & Lawless 2001; Uysal et al. 2011).

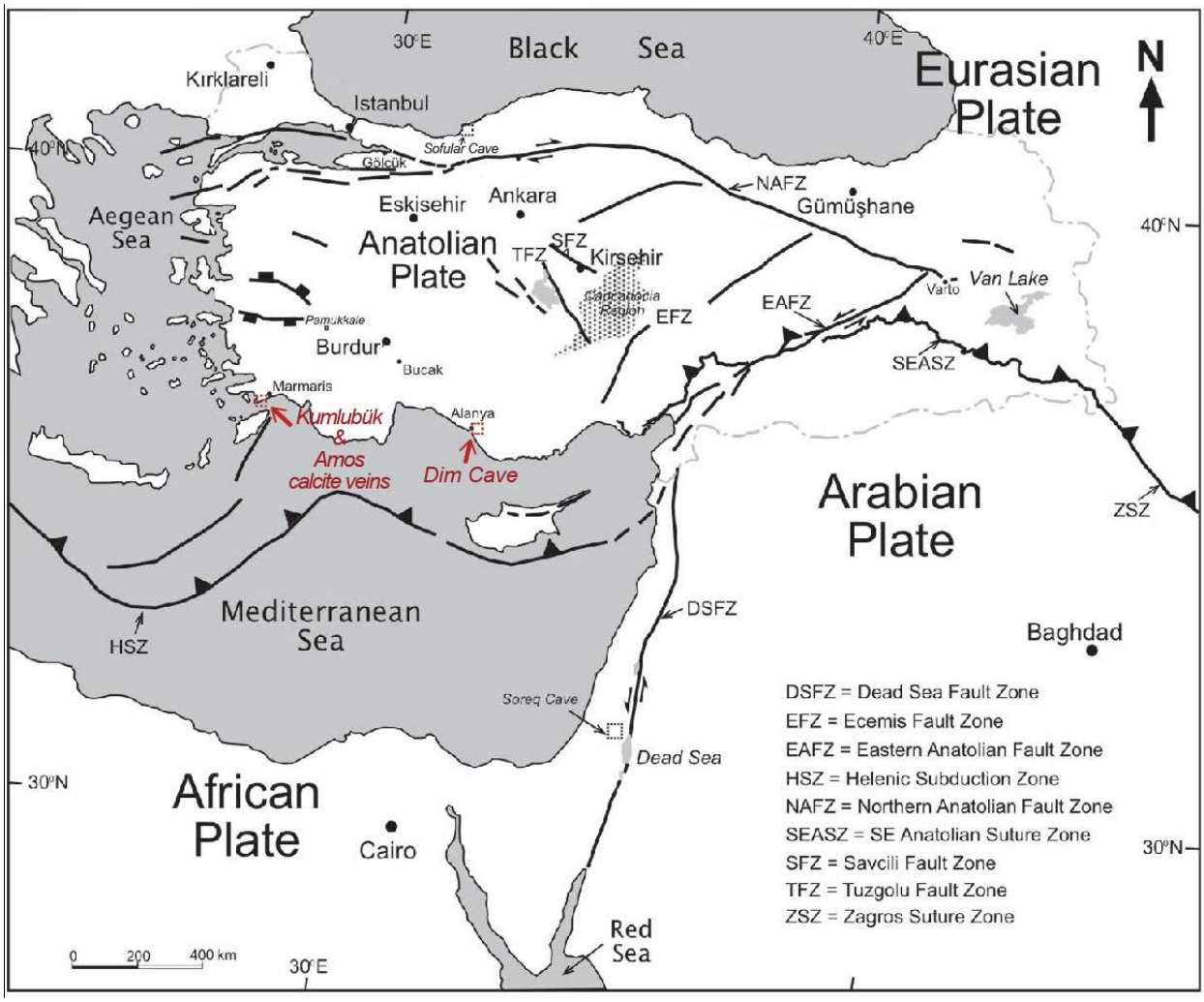

Figure 1.1 Simplified tectonic map of Turkey with sample sites for the present study (red arrows and rectangular areas) (modified from Uysal et al. 2009).

CO_2 discharge is commonly associated with seismically active fault zones (Irwin & Barnes 1980) and manifests commonly as widespread travertine carbonate deposits at the surface (Fig. 1.1) (Rihs et al. 2000; D'Alessandro et al. 2007; Kampman et al. 2012; Hancock et al. 1999; Chiodini 2004; Priewisch et al. 2014; Brogi & Capezzuoli 2008). Travertine deposits are defined as terrestrial carbonate deposits (or form of limestone) deposited by mineral springs fed by CO_2-rich hydrothermal waters (>20 degrees C) and formed as response to rapid precipitation of calcium carbonate minerals (e.g. calcite or aragonite – $CaCO_3$) (Pentecost 2005). Precipitates of carbonate minerals (as travertine; Fig.1.2 or cave deposits; Fig.1.3) are often found at the mouth of a hot

spring fed by deep hydrothermal fluid circulation within faulted/fractured host rock or in a cave, in which acidic (CO_2-rich) water weathers the host rock (limestone or dolomite) forming karst topography. Calcite precipitation processes from aqueous solution are controlled by an equilibrium series, one of the reactions releasing CO_2 gas shown below (Eq. 1.1).

Eq. 1.1 $Ca_{2+} + 2HCO_{3-} = CaCO_3(s) + CO_2(g) + H_2O$; s:solid; g:gas

Figure 1.2 Panoramic view of Hierapolis-Pamukkale (the cotton castle) with recent travertine terraces trending ~NW-SE in Denizli/SW Turkey (Hierapolis-Pamukkale 2013). Most of the travertines are found deposited within co-seismic extensional fissures/faults in western Turkey (e.g. Uysal et al. 2009; De Filippis et al. 2013).

Figure 1.3 Interior view of the Dim Cave, SW Turkey.

Natural CO_2 degassing is commonly associated with calcite vein and breccia deposits occurring in crustal damage zones of active fault systems where dilation took place in order for fractures to provide pathways for fluid flow (Miller 2013 and references therein). Calcite-filled veins suggest that CO_2-rich fluids were once present in fractures (or in large scale faults) and flowed during and/or after deformation and precipitated. Vein-related active tectonism studies offer valuable information on both composition and processes including; (i) deformation kinetics and mechanics (from fabrics of crystal aggregates and microstructures), which provide insights to the seismicity of a region, (ii) pressure, temperature and composition of the fluid (via fluid inclusions, stable isotope ratio, and trace element analyses), which is significant for determining rock strength, pressure/temperature changes during fluid flow, the degree of water/rock interaction, and fluid source (Lee et al. 1996), and (iii) semi-continuous stable isotope (Oxygen and Carbon) time series (based on U-series dating; Zhao et al. 2009) obtained from calcite vein, which can provide important terrestrial record for local and global climate by defining paleotemperatures and thus identifying long-term climatic variations in a region (e.g. >500 kyr continuous calcite vein record from Devil's Hole, Nevada, USA; Winograd et al. 1992; Coplen 2007; Riggs et al. 1994). Specifically in relation to paleotemperature reconstruction, Holocene Devils Hole calcite vein record provided an alternative water-calcite fractionation equation (Coplen's temperature equation; Coplen 2007), differing from previous equilibrium equations (Kim & O'Neil 1997; Friedman & O'Neil 1977). With significantly constant geological conditions over thousands of years, Devils Hole slow-growth calcite precipitation is assumed to represent thermodynamic oxygen isotope equilibrium and provided fairly reliable calcite–water oxygen isotopic fractionation factor (Coplen 2007).

Turkey is one of the most seismically active regions on Earth (Fig. 1.3) located between the Eurasian, Arabian and African plates. It provides an excellent study area for investigating CO_2 degassing and its surface manifestations, as both travertine calcite veins and breccia formation occur widely within faulted zones (e.g. North Anatolian Fault Zone (NAFZ) – strike slip faulting and the West Anatolian Extensional Zone – normal, dip-slip faulting or graben systems). Turkey is affected by both collisional (e.g. along the Bitlis-Zagros Suture Zone in Fig. 1.3) and extensional tectonics, which cause frequent earthquakes (Şengör et al. 2005; Bozkurt 2001). More than 100 moderate to major historical and recent earthquakes (464 BC to 1995 AD; Ambraseys & Jackson 1998) occurred along the NAFZ and the EAFZ as well as in the central and western Anatolia regions. Normal fault systems are considered to be dominant faulting mechanism in western and central Anatolia due to the ongoing N-S oriented extensional regime in the Aegean. The west and southwest Anatolian Province is known as one of the most rapidly extending regions (30–40

mm/year) on Earth with associated seismic and volcanic activities (McClusky et al. 2000). This extensional area is bounded by the Aegean–Cyprian subduction zone in the south-southwest, the dextral North Anatolian Fault System in the north and the dextral Tuzgölu Fault System (TFZ) to the east (Fig., 1.3). Carbonate deposits occur generally parallel or subparallel to active normal fault systems in this area (Hancock et al. 1999). One prominent example for such fault-bound travertine depositions is the Pamukkale geothermal field (e.g. Brogi et al. 2014). In this context, continental large-scale extension and associated spreading and thinning of overthickened crust based on the orogenic collapse model (Seyitoglu & Scott 1991) favours asthenospheric mantle degassing supplying continuous heat and gas (e.g. ^{3}He – mantle-He and -CO_2) to widespread geothermal systems in western Turkey (Güleç et al. 2005; Mutlu et al. 2008). An alternative CO_2 source is the dissolution of widely distributed Mesozoic carbonate rocks (e.g. limestone–$CaCO_3$ and dolostone–$(Mg,Ca)CO_3$) in western Turkey. Carbonate bedrock dissolves under the action of H_2CO_3 carbonic acid rich solution buffered with rainwater and groundwater/soil CO_2 that contains calcium and bicarbonate ions (see Eq. 1.2) from which $CO_2(g)$ is released at near-surface depths when water starts to degas (Eq.1.3). Palaeozoic metamorphic basement rocks can also contribute CO_2 by liberating CO_2 gas when carbonate minerals undergo metamorphism (or fluid-induced hydrothermal metasomatism). For instance, ankerite $(Ca,Fe,Mg)CO_3$ or dolomite (with the generalized formula of $(Ca,Mg)CO_3)_2$; Armenteros 2010) occur in low-grade metamorphic rocks and occasionally act as CO_2 source when they are subject to high grade metamorphism (e.g. Eq. 1.4).

Eq. 1.2 $CO_2(aq) + H_2O(l) + CaCO_3(s) = Ca^{2}+(aq) + 2HCO_3^{-}(aq)$

Eq. 1.3 $Ca_2+(aq) + 2HCO_3-(aq) = H_2O(g) + CO_2(g) + CaCO_3(s)$

Eq. 1.4 $2CaMg(CO_3)_2$ (dolomite)+ $SiO_2(aq) = Mg_2SiO_4$ (forsterite) + $2CaCO_3 + 2CO_2(g)$

1.2. Active tectonics and climate

Accumulation, distribution and emission of CO_2 in spring or geothermal waters is known to be governed by tectonism, magmatism, climate and hydrology (Kerrick 2001; Rihs et al. 2000; Chiodini 2004; D'Alessandro et al. 2007; Priewisch et al. 2014; Minissale et al. 2002; Faccenna et al. 2008). Hydrogeological conditions are dominantly affected by climate and paleo-hydrological history (Priewisch et al. 2014; Hainzl et al. 2006; Costain 2008). A number of studies revealed that surface travertine deposition in geothermal (or hydrothermal) systems occurs preferentially during Northern Hemisphere humid periods in the late Quaternary (e.g. Dilsiz et al. 2004; Rihs et al. 2000; Frank et al. 2000). This results from enhanced availability of meteogene geothermal waters (Sturchio et al. 1993; Minissale et al. 2002; Rihs et al. 2000). It is well recognised that cave deposits

deposit more consistently and faster during warm and wet periods (Baker et al. 1995; Wang et al. 2001), in response to increased meteoric infiltration. On the other hand, current study of Luetscher et al. (2015) revealed that bio-influenced speleothems can grow during cold periods such as the LGM. Speleothem growth in subsurface karst of the temperate areas is controlled principally by the availability of water rather than temperature, regulating the saturation index of the drip water (Tanner 2010). Similarly, the formation of a large number of fracture-filling carbonates in Western Turkey dated by the U-series method correlate well with periods of persistently cold climate intervals across the Northern Hemisphere (De Filippis et al. 2012; Uysal et al. 2011). This has been explained due to a significant reduction in surface CO_2 flux by spring or geothermal waters during dry climate periods, which may have promoted CO_2 oversaturation in deep reservoirs (Uysal et al., 2009, 2011). Therefore it is believed that climate affected the hydrologic conditions and caused CO_2 accumulation, which is released along damage zones of crustal depth up to the surface. In fact, the amount of surface water percolating to the deeper (?) levels by means of (mostly) permeable deformation zones (e.g. fracture networks) is inferred to be regulated by the amount of effective infiltration. This is in turn controlled by regional moisture-carrying atmospheric/oceanic trajectories in the Eastern Mediterranean.

Research on possible links between tectonism and climate variability is poorly developed in Turkey and elsewhere. Subsurface CO_2 discharge along tectonically active zones has been largely studied as a geological occurrence mostly related to fault movements rather than a combination of tectonism, magmatism, climate and hydrology. The understanding of natural degassing of subsurface CO_2 and late Quaternary climate variations needs to be improved. Fissure calcite vein U-series ages have been used to assess the meaning of local and regional climatic changes, with the majority of sample ages being observed to coincide with late Quaternary cold and dry (?) climate events in some pilot studies from Turkey (Uysal et al. 2009 and 2011). In analogy to what observed in Italy, where travertine studies suggest that the times of enhanced pluvial activity (i.e. wet conditions) and climate-driven water table changes are relevant to pervasive travertine formations and their depositional/erosional cycles (Minissale et al. 2002; Faccenna et al. 2008). Further, U-series dated carbonate veins from the Colorado Plateau (US) have been used to address the relationship between CO_2 leakages from faults to local climate over the last 135,000 years (Kampman et al. 2012). It has been argued that each major surface CO_2 degassing pulse occurred after the onset of major local climatic warming, specifically at the transition from glacial to interglacial termination. Therefore, it is crucial to understand whether there is a correlation between fissure calcite U/Th ages and cold/warm climatic episodes and how that relationship may operate if one exists.

Similar to vein carbonates, calcite precipitation in SW Turkish caves is capable of discerning possible climate forcing since speleothems have been interpreted to respond to climate changes as the vein calcites along the faults. In fact, speleothems are formed relatively in protected environments (i.e. cave systems), and are excellent archives of palaeoclimatic information with, normally, little tectonic control at the scale of regional suite of speleothems. They can be interpreted through the same geochemical proxies as calcite veins including stable isotope ratios (Carbon and Oxygen) and trace element/Ca ratios, and can be precisely dated by U-Series dating. Therefore, the use of speleothems in addition to vein calcites helps to improve our understanding of the late Quaternary climatic variability in SW Turkey, and its possible influences on meteoric precipitation and near-surface hydrological circulation.

1.3. Climatology of Turkey and the Eastern Mediterranean region

1.3.1. Global climate patterns during the last glacial-interglacial cycles

Major ice ages have been thought to occur approximately every 100,000 years throughout the last 800,000-years Earth's history, persisting nearly 90,000 years followed by an approximate 10,000-year interglacial period (Berger 1978; Pollard 1978; Schneider & Thompson 1979; Williams et al. 1993). This periodic change throughout the Quaternary period (the past 2.65 million years) has been claimed to occur at every ~40 kyr for the previous 1.85 million years (Ruddiman et al. 1989). The primary controls on ice ages are Milankovitch cycles (driven by orbital eccentricity (~100 kyr), axial obliquity (~40 kyr) and precession (~20 kyr) of the Earth) as an external forcing mechanism (Imbrie et al. 1992; Berger 1988; Schneider & Thompson 1979; Hays et al. 1976). However, the driving mechanisms that transmit the Milankovitch cycles to global climate is either i) through Greenhouse gas forcing of the atmosphere and/or or b) transmission through oceanic circulations notably thermohaline circulation (Broecker 1991; Broecker et al. 1989; Bond et al. 1993). As an internal forcing mechanism, thermohaline circulation has been proposed to play a key role in changing the global climate on longer timescales by redistributing the heat via World's oceans at millennial time scales. The last time the major continental ice sheets (e.g. Laurentide, Cordilleran, and Fennoscandian) in the Northern Hemisphere and their ice shelves formed was during the last glacial period (74–14 kyr) in the Pleistocene Epoch. They modified global climate significantly by among other things, changing global albedo, raising the average elevation of the land surface over extensive areas of the planet and by redirecting zonal circulations into lower latitudes, thereby transmitting cooling from the higher latitudes where the ice sheets existed.

The last glacial period was its peak at the last glaciation maximum (LGM ~18 to 21 thousand years ago) when the ice-sheets covered much of North America and northern Europe (Hughes et al. 2013;

Peltier 1994) above 50°N. The regional impacts of glaciation are still an ongoing issue worldwide. Evidence points to times of colder, drier, and dustier conditions than during interglacial periods. The scale of cooling is variable and the determination of past precipitation is challenging (McDermott 2004), bearing in mind some well-documented estimates (Rozanski et al. 1993; Gat & Carmi 1987). In addition, up to ~20 decadal to millennial scale warm-cold oscillations were recorded in central Greenland ice cores (Johnsen et al. 1992; Rahmstorf et al. 2007), each of which represents rapid climate events in the last glacial period (Dansger-Oescher (D-O) and Heinrich (H) events). The triggering/driving mechanism of the D-O and H events are still under debate and the global signature of these events will help to constrain both the causes and impacts of these fluctuations. While some researchers consider it as the youngest H event, the Younger Dryas (YD) event prevailed from 13,000 to 11,700 years before present (Fairbanks 1990) is recognised widely, though not ubiquitously, around the world. It is reflected in Turkish climate archives (e.g. Fleitmann et al. 2009; Litt et al. 2014). More frequent (sub-millennial to inter-annual) climatic oscillations such as the North Atlantic Oscillation (NAO; Appenzeller et al. 1998) – see description below) are also related to oceanic and atmospheric climate patterns, and changes discerned from records in the EM can help to constrain how these phenomena manifest themselves.

In summary, high quality regional records can strengthen current knowledge of climate change by constraining responses to climatic forcers. Thus, it is important to examine the glacial-interglacial climatic evolution of the EM region as a significant component of the global climate system. This will be attempted as a by-product of constructing high-quality speleothem records from SW Turkey to distinguish between regional tectonic and climatic control of calcite formation. Extended speleothem records are particularly valuable since they have both the continuity and resolution to complement deep-sea and ice-core records.

1.3.2. Paleoclimatology of Turkey

A number of studies have investigated the Late Quaternary climate of the Eastern Mediterranean including Turkey, focussing mainly on paleo-temperature and paleo-precipitation trends (e.g. Türkeş 1996; Jex et al. 2011; Roberts et al. 2008; Hasanean 2001; Ben-Gai et al. 2001; Mariotti et al. 2002; Türkeş & Erlat 2003; Türkeş & Erlat 2005; Karabörk et al. 2005; Kwiecien et al. 2009; Göktürk et al. 2011; Brandimarte et al. 2011; Chronis et al. 2011; Touchan et al. 2007; Kuzucuoglu et al. 2011; Bar-Matthews et al. 2003; Bar-Matthews et al. 1999; Fleitmann et al. 2009). Increasing knowledge on Turkish glacial history focuses mainly on timing and extents of LGM on Turkish glaciers (e.g. Akçar et al. 2014; Sarıkaya et al. 2008; Sarıkaya et al. 2014). However, the paleoclimatology of Eastern Mediterranean, specifically of Turkey, is only partially understood,

mainly due to the paucity of high precision and continuous paleoclimatic records (Nicoll & Küçükuysal 2012). In the case of Turkey, the best information comes from the Black Sea region where Sofular Cave (Fig. 1.1) provides a high-resolution, well-dated, 50 kyr-long continuous speleothem record (Fleitmann et al. 2009). This study provides a better understanding of the responses to Greenland Interstadials (GI) (also known as D-O events) on the EM and offers insights into precipitation regimes during the Holocene in Black Sea region (Fleitmann et al. 2009; Göktürk et al. 2011). High-precision stalagmite oxygen ($\delta^{18}O$) and carbon ($\delta^{13}C$) time series from Sofular Cave suggested rapid climate and ecosystem response in the EM to hemispheric climate changes that resulted in GIs. This is demonstrated by comparing $\delta^{13}C$ time series with marine sediment, terrigenous input, and pollen records from Black and Aegean Seas (Fleitmann et al. 2009; Kwiecien et al. 2009). In addition, by tracking the sea surface isotopic variability, Pleistocene hydrological condition of the Black Sea has been investigated through the $\delta^{18}O$ time series revealing at least seven intervals when isotopically depleted freshwater from Caspian Sea mixed with the Black Sea (Badertscher et al. 2011). In eastern Turkey, the long-term drilling project from Lake Van (Fig.1.1) provides longest continental pollen record continuously for 600 kyr (Litt et al. 2014; Litt et al. 2012). This pollen-based record indicates that Lake Van responded to the glacial-interglacial cycles by marked vegetation swings between dwarf-shrub steppe during glacials and oak steppe-forest during interglacials.

Beyond Turkey, the most significant research is speleothem work from Israel (e.g. Soreq (Fig.1.1), Peqiin, Ma'ale–Deragot, Ma'ale–Efrayim, Tzavoa, Jerusalem West caves). These records provide information about past climatic variability of the southern part of the Mediterranean climate zone over the last 250 kyr (Bar-Matthews et al. 1997; Bar-Matthews et al. 1999; Ayalon et al. 2002; Bar-Matthews et al. 2003; Bar-Matthews et al. 2000; Vaks et al. 2006; Frumkin et al. 1999; Ayalon et al. 1999; Kaufman et al. 1998; Vaks et al. 2003). Changes in speleothem $\delta^{18}O$ is interpreted as primarily reflecting i) moisture source and ii) the amount effect of the paleo-precipitation regime on the Israeli speleothems (McDermott 2004 and references therein). Bar-Matthews et al. (1997, 1999) demonstrated that several cold peaks observed in $\delta^{18}O$ and $\delta^{13}C$ isotopic profiles are coeval with global events such as H1, H2, and H5 Northern Hemispheric and YD events within an interval of 60–17 kyr. In detail, the decrease in $\delta^{18}O$, $\delta^{13}C$, $^{87}Sr/^{86}Sr$, U, and Sr concentrations of the speleothems were interpreted as responses to changes in temperature, annual rainfall, vegetation and weathering, and the effects of the Mediterranean Sea on precipitation trends between the last glaciation and early/mid Holocene (Bar-Matthews et al. 1999). According to isotope ratios (O, C, U and Sr) and trace element concentrations of the speleothems of Soreq cave, climatic conditions during the last glacial period (60 to 17 kyr) were argued to be cold and dry, after 17 kyr (after

LGM) relatively warmer and wetter conditions occurred (Ayalon et al. 1999; Bar-Matthews et al. 1999). In addition, a recent composite study regarding both speleothem and stramatolites of Lake Lisan in Israel (Lisker et al. 2010) reveals a long-term record covering last three glacial cycles from 354 to 12 kyr. The authors infer cold and moist conditions for the last glacial period (MIS 4 to 2) using the positive correlations between high lake levels and speleothem age frequency. Similarly, they also imply that MIS 6 was wetter than following MIS 5. In fact, Frumkin et al. (2011) argue for increased precipitation as well as more moisture availability during glacial periods.

1.3.3. Modern climatology of Turkey

Turkey is located geographically in the Mediterranean and has a Mediterranean climate linked to Near and Middle East and the North Atlantic (Türkeş, 1996). This is characterised by hot, dry summers and mild, wet winters. This is modified by altitude and continentality so that the Anatolian heartland has more continental climate and colder winters. The northern lowlands along the Black Sea are perennially moist with up to 2200 mm of precipitation per year at the eastern end (Şensoy et al. 2008) (Fig. 1.4). The primary control on Turkish climate and consequently on the formation of speleothems and calcite veins dependent on meteoric water is the effectiveness of wet season precipitation. Hot/dry summers are due to the northward shift of the Inter-tropical Convergence Zone (ITCZ) into the Northern Hemisphere during summer which displaces the sub-tropical anticyclonic belt (STAB) to the latitude of Turkey. Northern shift of STAB results in sinking stable, dry air masses in the Turkish region, except the Black Sea region and the continental north-eastern part of the Anatolian Peninsula (Türkeş & Erlat 2005; Türkeş & Erlat 2009). The dominant sub-tropical air masses from North Africa and Middle East-Arabia during summers leads to long-lived warm and dry periods in Turkey (Eken et al. 2005). In winter, as the ITCZ moves south, westerly air masses derived from the Atlantic penetrate the Mediterranean Basin and bring precipitation to Turkey, particularly on the western and southern coastal margins and in the mountains (Northern Anatolian Mountains and the Taurus Mountains; Fig. 1.4). Most of the rainfall in Turkey is winter-focused, except in continental central Anatolia and the Black Sea region where the rainfall still has a winter maximum but is more evenly distributed (Türkeş & Erlat 2005). In this study, mean annual winter precipitation variability over Turkey is given >30%, while it decreases to 24–26% along the Black Sea coast.

Interannual variations in the westerly wind flow control the main moisture supply to Turkey. This inter-annual variation is largely driven by the North Atlantic Oscillation (NAO) and is related to pressure differences between the Icelandic Low and the Azores High. Positive phases of the NAO (Fig. 1.5a) are periods of strong pressure differential between these systems. They enhance westerly

wind flow and force the flow northward so that storm tracks (and consequently precipitation) occur in northern Europe. Negative NAO (Fig. 1.5b) patterns are associated with pressure differentials between the Azores and Iceland. This allows westerlies to push south into the high pressure belt and brings storms and enhanced rainfall to the Mediterranean Basin including Turkey. In short, periods of speleothem formation should be associated with phases of enhanced westerly flow over Turkey (Negative NAO) and periods of non-deposition should relate to periods of weaker westerly flow (Positive NAO).

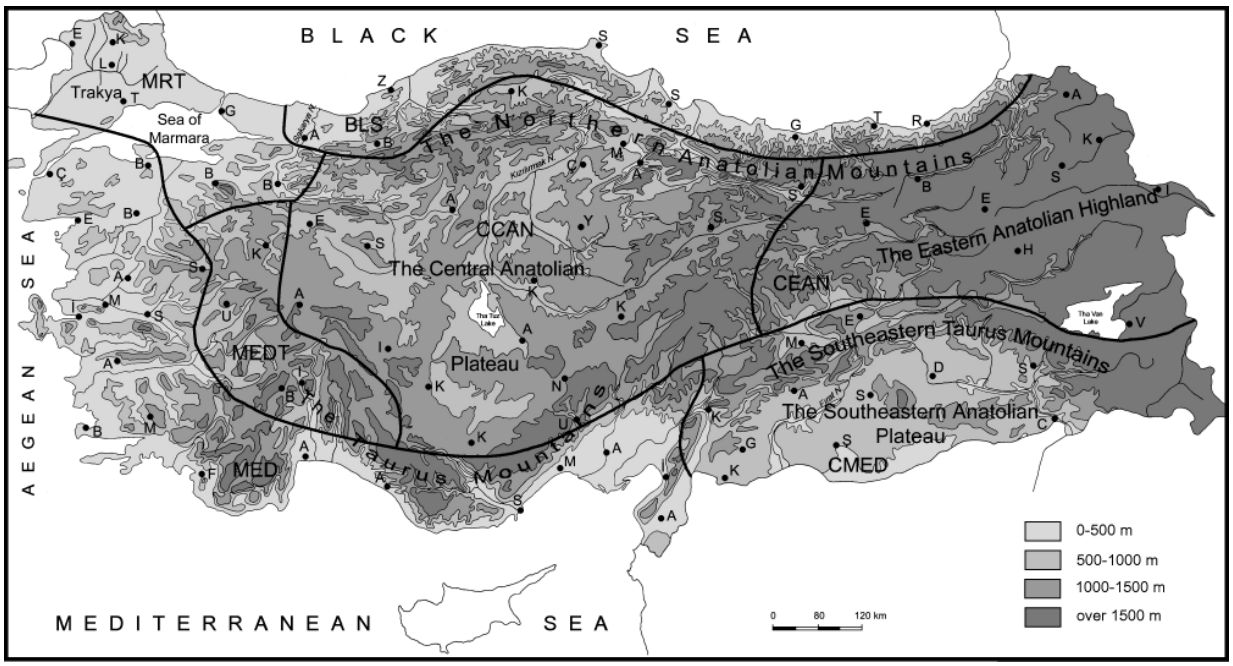

Figure 1.4 Long-term rainfall distribution patterns of Turkey along with geographic elevations, BLS: Black Sea; MRT: Marmara Transition; MED: Mediterranean; MEDT: Mediterranean Transition; CMED: Continental Mediterranean; CCAN: Continental Central Anatolia; CEAN: Continental Eastern Anatolia (letters show the rainfall observation stations, from Türkeş & Erlat 2005).

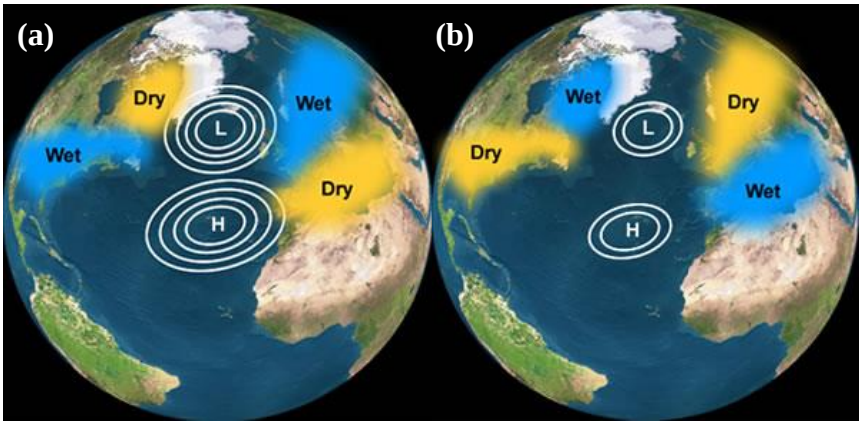

Figure 1.5 Positive – large pressure gradient **(a)** and negative – weak pressure gradient **(b)** phases of the NAO (Ncar.ucar.edu 2015). Negative phases generate stronger winter rains in Turkey.

2. Purpose of the thesis

This study is mainly concerned with the genetic investigation and timing of CO_2 outbursts in tectonically active zones of SW Turkey and understanding the tectonic regime and climate relationships of these events. Micro and macro deformational/structural observations together with stable isotope, Sr-isotope, trace element geochemistry and U-series age data constitute prime material to investigate the geochemical and temporal characteristics of co-seismic calcite veins that occur in highly fractured limestone hosts. Calcite growth histories are examined in order to understand seismic and/or climate-induced geological processes, fluid flow evolutions and possible fluid sources. It is crucial to determine the controlling factors of these processes that can be linked to magmatic, tectonic, climatic or, commonly, combination of any. High-resolution calcite vein growth studies can provide detailed insights for earthquake-related hazard studies in seismically active regions worldwide (e.g. Nuriel et al. 2012). To support the tectonic hypothesis, high-resolution speleothem-based climate records from SW Turkey (Dim Cave) will be investigated to constrain the local/regional climatic conditions during the time of calcite vein/breccia formations. Speleothem growth histories, mineral fabrics, growth rates, oxygen/carbon/strontium isotope ratios, and trace element/Ca ratio profiles along the growth axes will be interpreted to reflect the variations in paleoclimatic/paleohydrological conditions. This study will contributes significantly to understanding the late Quaternary paleoclimatology of Turkey and especially SW Turkey.

While speleothem-based studies have been carried out by a number of researchers in the Eastern Mediterranean, there has been little focus on the relationship between subsurface CO_2 leakage and climate change. The principal goal of this study is to investigate the relationship between CO_2 degassing, late Quaternary faulting, and the nature and effect of climatic variability on CO_2 accumulation and degassing in SW Turkey.

The specific objectives of the study are:

- To establish high-precision U-series age datasets from late Quaternary calcite veins in SW Turkey and to characterize temporal and regional distribution patterns of calcite vein growth through a synthesis of this work with previously published data (i.e. Uysal et al. 2009 and 2011) (Paper 1)

- To reconstruct trace element, stable (O & C) ratios and radiogenic (Sr) isotope time series from co-seismic calcite veins. This will help to constrain the frequency of the seismic recurrence, hydrologic conditions, and geochemical characteristics of the CO_2-rich fluids including fluid origins and changes during fluid migration and precipitation (e.g. via water-rock interaction) (Paper 2)

- To reconstruct speleothem-based high-resolution stable isotope (O & C) ratios and trace element time profiles controlled by a precise age (U-series) dataset. This is aimed at reconstructing regional climate variability in the Late Quaternary for SW Turkey (Papers 3 & 4)

- To compare the calcite vein records to the speleothem records and combine them to discuss possible driving mechanisms that govern CO_2 degassing episodes in association with seismogenesis (or fault movement) and climate in SW Turkey. This synthesis is briefly presented in Conclusion chapter of the thesis, and will be developed as a synthesis paper in the near-future.

3. Outline of the thesis

The structure of the thesis is as follows: The first chapter of the thesis introduces the study by presenting a brief background on CO_2 degassing, high-pressure fluids and active tectonic zones of study areas and by providing an overview of the current research on paleo- and modern climate of Turkey. The rest of the thesis is comprised of four papers that are either under review (papers 1 and 2); published (paper 3) and submitted (paper 4) together with a concluding chapter that synthesises the thesis. The papers are connected by short bridging texts and are as submitted to the journals. Additional details and datasets not included within these papers are included in the Appendices. A combined reference list for all papers is presented at the end of the thesis.

Paper 1 focuses on a large dataset including 160 U-series ages of co-seismic vein calcites deposited in active fault systems in SW Turkey. Over-pressurized fluid-facilitated fault activity is discussed within the concept of local and regional climate in the region. This paper is under review in Nature Geocsiences. Paper 2 covers high-resolution geochemical characteristics of the calcite veins by comparing their isotope and trace element histories along their growth in relation to seismic activity and is subject to revisions in Geochimica Cosmochimica Acta (revised version resubmitted). Paper 3 presents three precisely-dated speleothem stable isotope time series from Dim Cave (SW Turkey) and details the local/regional climatic conditions in the Eastern Mediterranean over 80 kyr (published in Nature Sci. Rep.; Unal-Imer et al. 2015). Paper 4 concentrates mainly on the high-resolution trace element/Ca variations of the Dim speleothems over specific time windows and synthesises multiple climate-sensitive proxies including stable/radiogenic isotope (O, C, Sr) profiles in Dim Cave (SW Turkey) and has been submitted to Quaternary Science Review. In the final chapter, the key findings of the study are summarised. In particular, the significance of improved understanding of the seismicity in SW Turkey is presented along inferences on how the climate does (or does not) affect the tectonic processes. Finally, key questions raised by this study are highlighted for future study.

REFERENCES (INTRODUCTION)

Akçar, N. et al., 2014. Glacier response to the change in atmospheric circulation in the eastern Mediterranean during the Last Glacial Maximum. Quaternary Geochronology, 19, pp.27–41. Available at: http://linkinghub.elsevier.com/retrieve/pii/S1871101413000885 [Accessed December 13, 2013].

Ambraseys, N.N. & Jackson, J.A., 1998. Faulting associated with historical and recent earthquakes in the Eastern Mediterranean region. Geophysical Journal International, 133, pp.390–406.

Appenzeller, C., Stocker, T.F. & Anklin, M., 1998. North Atlantic Oscillation Dynamics Recorded in Greenland Ice Cores. Science, 282(October), pp.446–450.

Armenteros, I., 2010. Diagenesis of Carbonates in Continental Settings. In A. M. Alonso-Zarza & L. H. Tanner, eds. Developments in Sedimentology: Carbonates in Continental Settings: Geochemistry, Diagenesis and Applications. Oxford: Elsevier, pp. 61–151.

Ayalon, A. et al., 2002. Climatic conditions during marine oxygen isotope stage 6 in the eastern Mediterranean region from the isotopic composition of speleothems of Soreq Cave , Israel. Geology, 30, pp.303–306.

Ayalon, A. et al., 1999. Petrography, strontium, barium and uranium concentrations, and strontium and uranium isotope ratios in speleothems as palaeoclimatic proxies : Soreq Cave, Israel. The Holocene, 6, pp.715–722.

Badertscher, S. et al., 2011. Pleistocenewater intrusions from the Mediterranean and Caspian seas into the Black Sea. Nature Geoscience, 4(4), pp.1–4. Available at: http://www.nature.com/doifinder/10.1038/ngeo1106 [Accessed August 21, 2012].

Baker, A. et al., 1997. Elevated and variable values of 13C in speleothems in a British cave system. Chemical Geology, 136(3-4), pp.263–270. Available at: http://linkinghub.elsevier.com/retrieve/pii/S0009254196001295.

Baker, A., Smart, P.L. & Lawrence Edwards, R., 1995. Paleoclimate implications of mass spectrometric dating of a British flowstone. Geology, 23(4), p.309.

Bar-Matthews, M. et al., 2010. A high resolution and continuous isotopic speleothem record of paleoclimate and paleoenvironment from 90 to 53 ka from Pinnacle Point on the south coast of

South Africa. Quaternary Science Reviews, 29(17-18), pp.2131–2145. Available at: http://linkinghub.elsevier.com/retrieve/pii/S0277379110001459 [Accessed December 15, 2014].

Bar-Matthews, M. et al., 2003. Sea–land oxygen isotopic relationships from planktonic foraminifera and speleothems in the Eastern Mediterranean region and their implication for paleorainfall during interglacial intervals. Geochimica et Cosmochimica Acta, 67(17), pp.3181–3199.

Bar-Matthews, M. et al., 1999. The Eastern Mediterranean paleoclimate as a reflection of regional events: Soreq cave, Israel. Earth and Planetary Science Letters, 166(1-2), pp.85–95. Available at: http://linkinghub.elsevier.com/retrieve/pii/S0012821X98002751.

Bar-Matthews, M., Ayalon, A. & Kaufman, A., 1997. Late Quaternary Paleoclimate in the Eastern Mediterranean Region from Stable Isotope Analysis of Speleothems at Soreq Cave, Israel. Quaternary Research, 47(47), pp.155–168.

Bar-Matthews, M., Ayalon, A. & Kaufman, A., 2000. Timing and hydrological conditions of Sapropel events in the Eastern Mediterranean, as evident from speleothems, Soreq cave, Israel. Chemical Geology, 169(1-2), pp.145–156. Available at: http://linkinghub.elsevier.com/retrieve/pii/S0009254199002326.

Ben-Gai, T. et al., 2001. Temperature and surface pressure anomalies in Israel and North Atlantic Oscillation . Theoretical and Applied Climatology, 69, pp.171–177.

Berger, A., 1988. Milankovitch Theory and Climate. Reviews of Geophysics, 26(4), pp.624–657.

Berger, A.L., 1978. Long-Term Variations of Daily Insolation and Quaternary Climatic Changes. Journal of Atmospheric Sciences, 35, pp.2362–2367.

Bond, G. et al., 1993. Correlations between climate records from North Atlantic sediments and Greenland ice. Nature, 365, pp.143–147.

Bozkurt, E., 2001. Neotectonics of Turkey – a synthesis. Geodinamica Acta, 14(1-3), pp.3–30. Available at: http://linkinghub.elsevier.com/retrieve/pii/S098531110101066X.

Brandimarte, L. et al., 2011. Relation Between the North-Atlantic Oscillation and Hydroclimatic Conditions in Mediterranean Areas. Water Resources Management, 25(5), pp.1269–1279.

Available at: http://www.springerlink.com/index/10.1007/s11269-010-9742-5 [Accessed August 21, 2012].

Branquet, Y. et al., 1999. Fluidized hydrothermal breccia in dilatant faults during thrusting: the Colombian emerald deposits. Geological Society, London, Special Publications, 155(1), pp.183–195. Available at: http://sp.lyellcollection.org/cgi/doi/10.1144/GSL.SP.1999.155.01.14 [Accessed January 15, 2014].

Broecker, W.S. et al., 1989. Routing of meltwater from the Laurentide Ice Sheet during the Younger Dryas cold episode. Nature, 341, pp.318–321.

Broecker, W.S., 1991. The Great Ocean Conveyor. Oceanography, 4, pp.79–89.

Brogi, A. et al., 2014. Evolution of a fault-controlled fissure-ridge type travertine deposit in the western Anatolia extensional province: the Cukurba fissure-ridge (Pamukkale, Turkey). Journal of the Geological Society, 171(3), pp.425–441. Available at: http://jgs.lyellcollection.org/cgi/doi/10.1144/jgs2013-034 [Accessed July 18, 2014].

Brogi, A. & Capezzuoli, E., 2008. Travertine deposition and faulting: the fault-related travertine fissure-ridge at Terme S. Giovanni, Rapolano Terme (Italy). International Journal of Earth Sciences, 98(4), pp.931–947.

Browne, P.R.L. & Lawless, J.V., 2001. Characteristics of hydrothermal eruptions, with examples from New Zealand and elsewhere. Earth Science Reviews, 52, pp.299–331.

Chiodini, G., 2004. Carbon dioxide Earth degassing and seismogenesis in central and southern Italy. Geophysical Research Letters, 31(7).

Chiodini, G. & Frondini, F., 2001. Carbon dioxide degassing from the Albani Hills volcanic region, Central Italy. Chemical Geology, 177, pp.67–83.

Chronis, T. et al., 2011. The Summer North Atlantic Oscillation Influence on the Eastern Mediterranean. Journal of Climate, 24, pp.5584–5596.

Coplen, T.B., 2007. Calibration of the calcite–water oxygen-isotope geothermometer at Devils Hole, Nevada, a natural laboratory. Geochimica et Cosmochimica Acta, 71(16), pp.3948–3957. Available at: http://linkinghub.elsevier.com/retrieve/pii/S0016703707003043 [Accessed May 25, 2015].

Costain, J.K., 2008. Intraplate Seismicity, Hydroseismicity, and Predictions in Hindsight. Seismological Research Letters, 79(4), pp.578–589. Available at: http://srl.geoscienceworld.org/cgi/doi/10.1785/gssrl.79.4.578 [Accessed January 15, 2014].

Costain, J.K., Bollinger, G.A. & Speer, J.A., 1987. Hydroseismicity — A hypothesis for the role of water in the generation of intraplate seismicity. Geology, 15, pp.618–621.

D'Alessandro, W. et al., 2007. Geochemistry and mineralogy of travertine deposits of the SW flank of Mt. Etna (Italy): Relationships with past volcanic and degassing activity. Journal of Volcanology and Geothermal Research, 165(1-2), pp.64–70.

Dilsiz, C., Marques, J.M. & Carreira, P.M.M., 2004. The impact of hydrological changes on travertine deposits related to thermal springs in the Pamukkale area (SW Turkey). Environmental Geology, 45(6), pp.808–817. Available at: http://link.springer.com/10.1007/s00254-003-0941-8 [Accessed June 13, 2013].

Eken, M. et al., 2005. Klimatoloji II, Ankara: Turkish State Meteorological Service.

Faccenna, C. et al., 2008. Late Pleistocene depositional cycles of the Lapis Tiburtinus travertine (Tivoli, Central Italy): Possible influence of climate and fault activity. Global and Planetary Change, 63(4), pp.299–308. Available at: http://linkinghub.elsevier.com/retrieve/pii/S0921818108000696 [Accessed February 19, 2014].

Fairbanks, R.G., 1990. The Age and Origin of the "Younger Dryas Climate Event" In Greenland Ice Cores. Palaeogeography, 5(6), pp.937–948.

Famin, V. et al., 2008. Earthquakes produce carbon dioxide in crustal faults. Earth and Planetary Science Letters, 265(3-4), pp.487–497. Available at: http://linkinghub.elsevier.com/retrieve/pii/S0012821X07006838 [Accessed July 18, 2014].

De Filippis, L. et al., 2012. Growth of fissure ridge travertines from geothermal springs of Denizli Basin, western Turkey. Geological Society of America Bulletin, 124(9-10), pp.1629–1645. Available at: http://gsabulletin.gsapubs.org/cgi/doi/10.1130/B30606.1 [Accessed November 28, 2012].

De Filippis, L. et al., 2013. Plateau versus fissure ridge travertines from Quaternary geothermal springs of Italy and Turkey: Interactions and feedbacks between fluid discharge, paleoclimate,

and tectonics. Earth-Science Reviews, 123, pp.35–52. Available at: http://linkinghub.elsevier.com/retrieve/pii/S0012825213000706 [Accessed February 2, 2014].

Fleitmann, D. et al., 2009. Timing and climatic impact of Greenland interstadials recorded in stalagmites from northern Turkey. Geophysical Research Letters, 36(19), pp.1–5. Available at: http://www.agu.org/pubs/crossref/2009/2009GL040050.shtml [Accessed August 10, 2012].

Frank, N. et al., 2000. Warm Period Growth of Travertine during the Last Interglaciation in Southern Germany. Quaternary Research, 54(1), pp.38–48. Available at: http://linkinghub.elsevier.com/retrieve/pii/S0033589400921355 [Accessed January 2, 2015].

Friedman, I. & O'Neil, J.R., 1977. Compilation of Stable Isotope Fractionation Factors of Geochemical Interest 6th ed., Washington D.C.: Geological Survey, United States government printing office.

Frumkin, A., Ford, D.C. & Schwarcz, H.P., 1999. Continental Oxygen Isotopic Record of the Last 170,000 Years in Jerusalem. Quaternary Research, 51, pp.317–327.

Gat, J.R. & Carmi, I., 1987. Effect of climate changes on the precipitation patterns and isotopic composition of water in a climate transition zone: Case of the Eastern Mediterranean Sea area. In The Influence of Climate Chnage and Climatic Variability on the Hydrolic Regime and Water Resources. Vancouver: IAHS Publ. no. 168, pp. 513–524.

Göktürk, O.M.M. et al., 2011. Climate on the southern Black Sea coast during the Holocene: implications from the Sofular Cave record. Quaternary Science Reviews, 30(19-20), pp.2433–2445. Available at: http://linkinghub.elsevier.com/retrieve/pii/S0277379111001430 [Accessed July 28, 2012].

Güleç, N. et al., 2005. Isotope Composition of Geothermal Fluids along the North Anatolian Fault Zone : Spatial and Temporal Variations in Relation to Seismic Activities SETTING AND RECENT. In Proceedings World Geothermal Congress. pp. 24–29.

Hainzl, S. et al., 2006. Evidence for rainfall-triggered earthquake activity. Geophysical Research Letters, 33(19), p.L19303. Available at: http://doi.wiley.com/10.1029/2006GL027642 [Accessed January 22, 2014].

Hancock, P.L. et al., 1999. Travitonics: using travertines in active fault studies. Journal of Structural Geology, 21, pp.903–916.

Hasanean, H.M., 2001. Fluctioations of surface air temperature in the Eastern Meditterranean. Theoretical and Applied Climatology, 68, pp.75–87.

Hays, J.D., Imbrie, J. & Shackleton, N.J., 1976. Variations in the Earth 's Orbit: Pacemaker of the Ice Ages. Science, 194(4270), pp.1121–1132.

Hendy, C.H., 1971. The isotopic geochemistry of speleothems-I. The calculation of the effects of different modes of formation on the isotopic composition of speleothems and their applicability as paleoclimatic indicators. Geochimica et Cosmochimica Acta, 35(8), p.80l–824.

Hierapolis-Pamukkale, 2013. Hierapolis-Pamukkale. Available at: http://whc.unesco.org/en/list/485.

Hughes, P.D., Gibbard, P.L. & Ehlers, J., 2013. Timing of glaciation during the last glacial cycle: evaluating the concept of a global "Last Glacial Maximum" (LGM). Earth-Science Reviews, 125, pp.171–198. Available at: http://linkinghub.elsevier.com/retrieve/pii/S0012825213001190 [Accessed July 18, 2014].

Imbrie, J. et al., 1992. On the Structure and Origin of Major Glaciation Cycles 1. Linear Responses to Milankovitch Forcing. Palaeogeography, 7(6), pp.701–738.

Irwin, W.P. & Barnes, I., 1980. Tectonic Relations of Carbon Dioxide Discharges and Earthquakes. Journal of Geophysical Research, 85, pp.3115–3121.

Jex, C.N. et al., 2011. A 500yr speleothem-derived reconstruction of late autumn–winter precipitation, northeast Turkey. Quaternary Research, 75(3), pp.399–405. Available at: http://linkinghub.elsevier.com/retrieve/pii/S0033589411000160 [Accessed August 21, 2012].

Johnsen, S.J. et al., 1992. Irregular glacial interstadials recorded in a new Greenland ice core. Nature, 359, pp.311–313.

Kagan, E.J. et al., 2005. Dating large infrequent earthquakes by damaged cave deposits. Geology, 33(4), p.261.

Kampman, N. et al., 2012. Pulses of carbon dioxide emissions from intracrustal faults following climatic warming. Nature Geoscience, 5, pp.352–358.

Karabörk, M.Ç. et al., 2005. The influences of the Southern and North Atlantic Oscillations on climatic surface variables in Turkey. Hydrological Processes, 19(6), pp.1185–1211. Available at: http://doi.wiley.com/10.1002/hyp.5560 [Accessed August 21, 2012].

Kaufman, A. et al., 1998. U-Th isotope systematics from the Soreq cave, Israel and climatic correlations. Earth and Planetary Science Letters, 156, pp.141–155.

Kennedy, B.M. et al., 1997. Mantle Fluids in the San Andreas Fault System, California. Science, 278(5341), pp.1278–1281. Available at: http://www.sciencemag.org/cgi/doi/10.1126/science.278.5341.1278 [Accessed January 25, 2013].

Kerrick, D.M., 2001. Present and Past Nonanthropogenic CO_2 Degassing from the Solid Earth. Reviews of Geophysics, 39, pp.565–585.

Kim, S.-T. & O'Neil, J.R., 1997. Equilibrium and nonequilibrium oxygen isotope effects in synthetic carbonates. Geochimica et Cosmochimica Acta, 61(16), pp.3461–3475. Available at: http://linkinghub.elsevier.com/retrieve/pii/S0016703797001695.

Kuzucuoglu, C. et al., 2011. Mid- to late-Holocene climate change in central Turkey: The Tecer Lake record. The Holocene, 21(1), pp.173–188. Available at: http://hol.sagepub.com/cgi/doi/10.1177/0959683610384163 [Accessed August 21, 2012].

Kwiecien, O. et al., 2009. North Atlantic control on precipitation pattern in the eastern Mediterranean/Black Sea region during the last glacial. Quaternary Research, 71(3), pp.375–384. Available at: http://linkinghub.elsevier.com/retrieve/pii/S0033589408001555 [Accessed August 21, 2012].

Lee, Y.-J., Morse, J.W. & Wiltschko, D. V., 1996. An experimentally verified model for calcite precipitation in veins. Chemical Geology, 130(3-4), pp.203–215. Available at: http://linkinghub.elsevier.com/retrieve/pii/0009254196000083.

Lisker, S. et al., 2010. Late Pleistocene palaeoclimatic and palaeoenvironmental reconstruction of the Dead Sea area (Israel), based on speleothems and cave stromatolites. Quaternary Science Reviews, 29(9-10), pp.1201–1211. Available at: http://linkinghub.elsevier.com/retrieve/pii/S0277379110000302 [Accessed July 18, 2014].

Litt, T. et al., 2012. 500,000 Years of Environmental History in Eastern Anatolia: The PALEOVAN Drilling Project. Scientific Drilling, (14, September 2012), pp.18–29. Available at: http://www.sci-dril.net/14/18/2012 [Accessed July 18, 2014].

Litt, T. et al., 2014. A 600,000 year long continental pollen record from Lake Van, eastern Anatolia (Turkey). Quaternary Science Reviews. Available at: http://linkinghub.elsevier.com/retrieve/pii/S027737911400095X [Accessed July 18, 2014].

Luetscher, M. et al., 2015. North Atlantic storm track changes during the Last Glacial Maximum recorded by Alpine speleothems. Nature communications, 6, p.6344. Available at: http://www.pubmedcentral.nih.gov/articlerender.fcgi?artid=4351561&tool=pmcentrez&rendertype=abstract [Accessed May 25, 2015].

Mariotti, A., Zeng, N. & Lau, K.-M., 2002. Euro-Mediterranean rainfall and ENSO—a seasonally varying relationship. Geophysical Research Letters, 29, p.59 (1–4).

McClusky, S. et al., 2000. Global Positioning System constraining on plate kinematics and dynamics in the eastern Mediterranean and Caucasus. Journal of Geophysical Research, 105(B3), pp.5695–5719.

McDermott, F., 2004. Palaeo-climate reconstruction from stable isotope variations in speleothems: a review. Quaternary Science Reviews, 23(7-8), pp.901–918. Available at: http://linkinghub.elsevier.com/retrieve/pii/S0277379104000198 [Accessed July 9, 2014].

Miller, S.A. et al., 2004. Aftershocks driven by a high-pressure CO2 source at depth. Nature, 427, pp.724–727.

Miller, S.A., 2013. The role of fluids on tectonic and earthquake processes. In R. Dmowska, ed. Advances in Geophysics. Cambridge, USA: Elsevier, pp. 1–47.

Minissale, A. et al., 2002. Geochemistry of Quaternary travertines in the region north of Rome (Italy): structural, hydrologic and paleoclimatic implications. Earth and Planetary Science Letters, 203(2), pp.709–728. Available at: http://linkinghub.elsevier.com/retrieve/pii/S0012821X02008750.

Mutlu, H., Gulec, N. & Hilton, D., 2008. Helium–carbon relationships in geothermal fluids of western Anatolia, Turkey. Chemical Geology, 247(1-2), pp.305–321. Available at: http://linkinghub.elsevier.com/retrieve/pii/S0009254107004706 [Accessed August 18, 2012].

Ncar.ucar.edu, 2015. National Center for Atmospheric Research. Available at: https://ncar.ucar.edu [Accessed January 17, 2015].

Nicoll, K. & Küçükuysal, C., 2012. Emerging Multi-Proxy Records of Late Quaternary Palaeoclimate Dynamics in Turkey and the Surrounding Region. Turkish Journal of Earth Sciences, 21, pp.1–19.

Nuriel, P. et al., 2011. Formation of fault-related calcite precipitates and their implications for dating fault activity in the East Anatolian and Dead Sea fault zones. Geological Society, London, Special Publications, 359(1), pp.229–248. Available at: http://sp.lyellcollection.org/cgi/doi/10.1144/SP359.13 [Accessed August 21, 2012].

Nuriel, P. et al., 2012. U-Th dating of striated fault planes. Geology, 40, pp.647–650. Available at: http://geology.gsapubs.org/cgi/doi/10.1130/G32970.1 [Accessed August 1, 2012].

Peltier, W.R., 1994. Ice Age Paleotopography. Science, 265(5169), pp.195–201.

Pentecost, A., 2005. Travertine, Berlin Heidelberg: Springer-Verlag.

Pollard, D., 1978. An investigation of the astronomical theory of the ice ages using a simple climate-ice sheet model. Nature, 272, pp.233–235.

Priewisch, A. et al., 2014. U-series geochronology of large-volume Quaternary travertine deposits of the southeastern Colorado Plateau: Evaluating episodicity and tectonic and paleohydrologic controls. Geosphere, 10(2), pp.401–423. Available at: http://geosphere.gsapubs.org/cgi/doi/10.1130/GES00946.1 [Accessed January 15, 2015].

Rahmstorf, S. et al., 2007. Recent Climate Observations Compared to Projections. Science, 316(May), p.2007.

Riggs, A.C. et al., 1994. Tectonic speleogenesis of Devils Hole, Nevada, and implications for hydrogeology and the development of long, continous paleoenvironmental records. Quaternary Research, 42, pp.241–254.

Rihs, S., Condomines, M. & Poidevin, J.-L., 2000. Long-term behaviour of continental hydrothermal systems: U-series study of hydrothermal carbonates from the French Massif Central (Allier Valley). Geochimica et Cosmochimica Acta, 64(18), pp.3189–3199.

Roberts, N. et al., 2008. Stable isotope records of Late Quaternary climate and hydrology from Mediterranean lakes: the ISOMED synthesis. Quaternary Science Reviews, 27(25-26), pp.2426–2441.

Rozanski, K., Araguas, L.A. & Gonfiantini, R., 1993. Isotopic Patterns in Modern Global Precipitation. In P. K. Swart et al., eds. Climate Change in Continental Isotopic Records. Geophysical Monograph 78. Washington D.C., pp. 1–36.

Ruddiman, W.F. et al., 1989. Pleistocene Evolution: Northern Hemisphere Ice Sheets and North Atlntic Ocean. Paleoceanography, 4(4), pp.353–412.

Saar, M.O. & Manga, M., 2003. Seismicity induced by seasonal groundwater recharge at Mt. Hood, Oregon. Earth and Planetary Science Letters, 214(3-4), pp.605–618. Available at: http://linkinghub.elsevier.com/retrieve/pii/S0012821X03004187 [Accessed January 15, 2014].

Sarıkaya, M.A. et al., 2014. An early advance of glaciers on Mount Akdağ, SW Turkey, before the global Last Glacial Maximum; insights from cosmogenic nuclides and glacier modeling. Quaternary Science Reviews, 88, pp.96–109. Available at: http://linkinghub.elsevier.com/retrieve/pii/S0277379114000298 [Accessed March 18, 2014].

Sarıkaya, M.A. et al., 2008. Cold and wet Last Glacial Maximum on Mount Sandıras, SW Turkey, inferred from cosmogenic dating and glacier modeling. Quaternary Science Reviews, 27(7-8), pp.769–780. Available at: http://linkinghub.elsevier.com/retrieve/pii/S027737910800005X [Accessed December 3, 2012].

Schneider, S.H. & Thompson, S.L., 1979. Ice Ages and Orbital Variations : Some Simple Theory and Modeling. Quaternary Research, 12, pp.188–203.

Şengör, A.M.C. et al., 2005. The North Anatolian Fault: A New Look. Annual Review of Earth and Planetary Sciences, 33(1), pp.37–112.

Şensoy, S. et al., 2008. Climate of Turkey, Turkish State Meteorological Service.

Seyitoglu, G. & Scott, B., 1991. Late Cenozoic crustal extension and basin formation in West Turkey. Geological Magazine, 128(2), pp.155–166. Available at: http://geolmag.geoscienceworld.org/cgi/content/long/128/2/155 [Accessed January 14, 2014].

Sturchio, N.C., Dunkley, P.N. & Smith, M., 1993. Climate-driven variations in geothermal activity in the northern Kenya rift valley. Nature, 362, pp.233–234.

Tanner, L.H., 2010. Continental Carbonatesas Indicators ofPaleoclimate. In A. M. Alonso-Zarza & L. H. Tanner, eds. Developments in Sedimentology: Carbonates in Continental Settings: Geochemistry, Diagenesis and Applications. Oxford: Elsevier, pp. 179–214.

Touchan, R. et al., 2007. May–June precipitation reconstruction of southwestern Anatolia, Turkey during the last 900 years from tree rings. Quaternary Research, 68(2), pp.196–202.

Türkeş, M., 1996. Spatial and Temporal Analysis of Annual Rainfall Variations in Turkey. International Journal of Climatology, 16, pp.1057–1076.

Türkeş, M. & Erlat, E., 2005. Climatological responses of winter precipitation in Turkey to variability of the North Atlantic Oscillation during the period 1930–2001. Theoretical and Applied Climatology, 81(1-2), pp.45–69.

Türkeş, M. & Erlat, E., 2003. Precipitation changes and variability in Turkey linked to the North Atlantic oscillation during the period 1930-2000. International Journal of Climatology, 23(14), pp.1771–1796. Available at: http://doi.wiley.com/10.1002/joc.962 [Accessed July 17, 2012].

Türkeş, M. & Erlat, E., 2009. Winter mean temperature variability in Turkey associated with the North Atlantic Oscillation. Meteorology and Atmospheric Physics, 105(3-4), pp.211–225.

Ünal-İmer. E, Shulmeister J., Zhao J-X., Uysal I.T., Feng Y-X., Nguyen, A. D. and Yuce G. (2015) An 80 kyr-long continuous speleothem record from Dim Cave, SW Turkey with paleoclimatic implications for the Eastern Mediterranean. *Nature Sci. Rep.***5**, 13560.

Uysal, I. et al., 2007. U-series dating and geochemical tracing of late Quaternary travertine in co-seismic fissures. Earth and Planetary Science Letters, 257(3-4), pp.450–462. Available at: http://linkinghub.elsevier.com/retrieve/pii/S0012821X0700163X [Accessed August 21, 2012].

Uysal, I.T. et al., 2009. Hydrothermal CO2 degassing in seismically active zones during the late Quaternary. Chemical Geology, 265(3-4), pp.442–454.

Uysal, I.T. et al., 2011. Seismic cycles recorded in late Quaternary calcite veins: Geochronological, geochemical and microstructural evidence. Earth and Planetary Science Letters, 303(1-2), pp.84–96.

Vaks, A. et al., 2007. Desert speleothems reveal climatic window for African exodus of early modern humans. Geology, 35(9), p.831. Available at: http://geology.gsapubs.org/cgi/doi/10.1130/G23794A.1 [Accessed December 19, 2014].

Vaks, A. et al., 2006. Paleoclimate and location of the border between Mediterranean climate region and the Saharo–Arabian Desert as revealed by speleothems from the northern Negev Desert, Israel. Earth and Planetary Science Letters, 249(3-4), pp.384–399. Available at: http://linkinghub.elsevier.com/retrieve/pii/S0012821X06005000 [Accessed December 19, 2014].

Vaks, A. et al., 2003. Paleoclimate reconstruction based on the timing of speleothem growth and oxygen and carbon isotope composition in a cave located in the rain shadow in Israel. Quaternary Research, 59(2), pp.182–193. Available at: http://linkinghub.elsevier.com/retrieve/pii/S0033589403000139 [Accessed November 12, 2012].

Wang, Y.J. et al., 2001. A high-resolution absolute-dated late Pleistocene Monsoon record from Hulu Cave, China. Science (New York, N.Y.), 294(5550), pp.2345–2348. Available at: http://www.ncbi.nlm.nih.gov/pubmed/11743199 [Accessed October 30, 2012].

Williams, M.A.J. et al., 1993. Quaternary Environments, London: Edward Arnold.

Winograd, I.J. et al., 1992. Continuous 500,000-Year Climate Record from Vein Calcite in Devils Hole, Nevada. Science, 255-258, pp.255–260.

Wiprut, D. & Zoback, M.D., 2000. Fault reactivation and fluid flow along a previously dormant normal fault in the northern North Sea. Geology, 28(7), pp.595–598.

Zhao, J. et al., 2003. Speleothem U-series dating of semi-synchronous climate oscillations during the last deglaciation. Earth and Planetary Science Letters, 216(1-2), pp.155–161.

Zhao, J. et al., 2001. Thermal ionization mass spectrometry U-series dating of a hominid site near Nanjing, China. Geology, 29, pp.27–30.

Zhao, J., Yu, K. & Feng, Y., 2009. High-precision 238U–234U–230Th disequilibrium dating of the recent past: a review. Quaternary Geochronology, 4(5), pp.423–433.

PAPER 1

The following paper presents a large U-series age dataset from fault-related calcite veins and breccia highlighting how CO_2 degassing and fault activity in extensional systems can be correlated to changes in regional climate; notably moisture balance affecting surface hydrological systems within an intensely faulted/fractured host rock.

Linking CO_2 degassing in active fault zones to long-term changes in moisture balance and surface water circulation, an example from SW Turkey

Abstract

Calcite veins and breccias are common in damage zones of active normal fault systems in southwest Turkey. Carbonate precipitation is a result of sudden pressure drops immediately after earthquake-induced ruptures. In this study, , we reconstructed a 150 thousand-year (kyr) long precisely-dated record using U-series dating to investigate the timing of vein formation and to relate it to tectonic and/or climatic processes. Vein formation is focused during glacial periods and in particular during phases of low to intermediate summer insolation. Though net moisture balance was always positive during the last glacial period, this primarily reflected reduced evapotranspiration rather than increased precipitation. We conclude that CO_2 accumulation at depth was enhanced by reduced infiltration of meteoric water from shallow depths. This facilitated CO_2 overpressure build up in the rupture zones. Failure of the faults resulted in the release of substantial volumes of CO_2 rich fluids and the generation of carbonates (veins and breccias) near and at the surface. Initial fault ruptures are represented by breccias, whereas subsequent CO_2 discharges along the same fractures result in laminated veins.

The CO_2 is derived from gradual dissolution of the Mesozoic host limestone in the crust and likely from frictional heating during slip events. When meteoric water circulation reaches deep levels, CO_2 is convected to the surface and discharged as passive degassing. In contrast, during phases when surface water does not penetrate to deeper crustal levels, CO_2 builds up and degassing is associated largely with rupture events. While regional tectonics is the ultimate driver of fault activity, climate-driven near surface hydrological changes have played an important role in modulating CO_2-rich fluid circulation and vein formation.

Keywords: Normal faults, carbonate veins, breccia, U-series dating, CO_2 overpressure, paleohydrology, degassing, SW Turkey

1. Introduction

The role of fluids in triggering earthquakes has been widely recognized (Hickman et al. 1995; Miller 2013). Fault activity occurs due to release of accumulated elastic energy in rheologically strong rocks, which facilitates mechanical failure in response to declining shear stress (Scholz 2002). This failure can in turn be promoted by high pore fluid pressure, which reduces the effective frictional strength (or shear stress) thus inducing fault weakening. A number of previous studies demonstrate this phenomenon through laboratory experiments (Di Toro et al. 2011), numerical models (Costain et al. 1987), geophysical (Roeloffs 2000), and field studies (Ma et al. 2012). It has been proposed that fluid pressure variations might even affect the timing of earthquakes (Miller 1996). Fluid overpressures can also be responsible for aseismic fault creep, which occurs during the time interval between large stress-releasing earthquakes on a fault or as "afterslip" immediately following an earthquake (Çakır et al. 2012).

Widespread carbonate deposits occur in western Turkey as vein networks in fracture zones of active fault systems, precipitated from CO_2-rich, deeply circulating meteoric water (Uysal et al. 2009, 2011; De Filippis et al. 2012). Calcite vein and breccia formations were interpreted as having been initiated as hydro-fractures in basement rocks by CO_2-rich fluid overpressure and subsequently propagated to the surface (Uysal et al. 2009; De Filippis et al. 2012). Carbonate precipitation as fracture and breccia filling is attributed to sudden pressure drops immediately after earthquake-induced rupture (Uysal et al. 2009; Uysal et al. 2011; Kampman et al. 2012).

Apart from being a seismicity recorder, calcite veins can be excellent terrestrial climate proxies by recording long-term climatic variations in a region (Winograd et al. 1992; Rihs et al. 2000; Minissale et al. 2002). A possible link between climate-controlled hydrological processes and seismicity in areas already under stress and near failure has been proposed by Costain et al. 1987 and, subsequently by Saar & Manga 2003. “Hydroseismicity” is hypothesized as precipitation-induced seismicity whereby the continuous input of fluids can lead to higher levels of fluid pressures at depth (<20 km), which can modify fluid pressure within the fault zone, triggering brittle deformation. A possible causal relationship between climate and intraplate seismicity has been proposed for the central Virginia seismic zone (CVSZ) (Costain & Bollinger 1991). A more recent study showed that seismic activity in Bavaria, Germany may be due to seasonal rainfall variations (Hainzl et al. 2006), which has then led to the hypothesis that rain-triggered seismicity would be stronger in karst regions (Miller 2013; Miller 2008) like SW Turkey.

In the present study, we report a 150 thousand years (kyr) long record obtained from precisely dated (uranium (U)-series) 160 calcite veins and breccia that precipitated from CO_2-bearing meteoric waters associated with active normal faulting in southwest Turkey (Uysal et al., 2011; Ünal-İmer et al.,2014). We correlate the dataset with periods of weaker winter precipitation related to reduced summer insolation in the Northern Hemisphere (at 30°N - Berger and Loutre, 1991) and discuss the key findings for their implications for climate-driven hydrological changes, that might be effective in modulating deep CO_2-rich fluid circulation and fault activity.

2. Study location

The study area is located in southwest Turkey, surrounded by a series of tectonically active Quaternary sedimentary basins bounded by normal faults (Figs. 1a and 1b), which are aligned with the general trend of large-scale extensional deformation in southwestern Turkey (Nyst & Thatcher 2004). Broadly EW trending active normal faulting currently controls the regional (southwestern Turkey) tectonics and is associated with frequent seismic activity (ten Veen et al. 2009) (Fig.1). The NE-SW oriented Fethiye-Burdur Fault Zone (FBFZ, Fig. 1a) is an important structural component bordering the Isparta Angle (Barka et al. 1995) and interpreted as a seismically active continental continuation of the Pliny-Strabo Trench (ten Veen & Kleinspehn 2002) (Fig. 1a). Calcite vein and breccia samples investigated in this study were collected from two active extensional systems (Kumlubük Canyon and the Amos vein systems, Figs. 1c, S1a and S1b) located 12 km south of Marmaris in SW Turkey (Figs.1b and 1c). They are hosted within Mesozoic limestone of Lycian Nappes (Fig. S2), which consists of a stack of internally sliced and imbricated south-vergent thrust sheets (Collins & Robertson 1999). The calcite veins (Fig. 3a–k) represent Mode I extension fractures (i.e. opened by a tensile stress normal to the plane of the fracture) that occur in the damage zone of normal faults and are oriented parallel/sub-parallel to the fault planes. Veins strike mostly NW and EW with an average dip of 70°-85° towards SE, which is consistent with the orientation of the regional extensional stress regime (N–S), similar to the majority of the trends of the main EW active faults (Figs. 1a–c). Similarly, bi-directional rose diagrams plotted for calcite veins of the study area (Amos and Kumlubük) reveal two dominant stress orientations of ~N–S and ~E–W for the regions respectively, which is consistent with the regional active normal faults (Fig. 1c). Historical and instrumental records show that during the past century the study area (Fig. 1a) underwent a number of seismic events (>7500 earthquakes of Mw>2.0; Uysal et al. 2011). The most recent seismic events that occurred during the 2013–2015 period in Marmaris included around 106 primary earthquakes (Richter scale, Ml >2.0) with the majority of the focal depths at an average of 13.5 km (KOERI 2015). Magnitudes of the latest (July 2015) earthquakes recorded in/around the Marmaris region are 4 of Ml (KOERI, 2015).

3. Methods summary

Calcite vein hand specimens were micro-sampled by using hand drills equipped with diamond coated grinders and drill bits with a spatial resolution of 1-2 mm in length. Sample preparation was completed at the Rock Laboratory at the School of Earth Sciences (The University of Queensland). Geochemical and geochronological analyses were carried out in the Radiogenic Isotope Facility (RIF) at the School of Earth Sciences (The University of Queensland). U-series isotopic analyses were carried out on a Nu Plasma multi-collector ICP-MS in the RIF laboratory. Detailed sampling and analytical procedures for U-series dating are provided in the *SI App. 1*.

4. Results

The distributions of U-series ages (Tables S1, S2, *SI App. 1*) are summarized using probability density functions (pdf), which incorporate the 2-sigma range of each date (Figs.2 and S4). When plotted against a millennial scale insolation curve for 30ºN latitude in summer (Berger & Loutre 1991), we observe a tendency for peaks on the probability curves to correlate with periods of summer insolation minima (10 events) and transitional values (10 events), but rarely with insolation maxima (1 event). The only high insolation exception is at 12.0 kyr (Fig. S4, *App. 1*), which is during the well-known Younger Dryas climate reversal (Grootes & Stuiver 1997; Fleitmann et al. 2009), a noted cold period.

Analysing the data set, we empirically assign a summer insolation value of 498 Wm^{-2}as a threshold that separates common occurrence of veins (<498 Wm^{-2}) from their rare occurrence (>498 Wm^{-2}). The proportion of the calcite vein formation at insolation values below this threshold (~83%) as compared to that predicted using the natural insolation distribution as a base (~62%) (Figs. S5a and S5b) is statistically significant (Chi-2=22.4; d.f.=5; p<0.001: *see details in App. 1,* Tables S3, S4, and S5). Where calcite vein ages cluster above the insolation level of 498 Wm^{-2}, these tend to be during glacial intervals (74–17 kyr and 150–128 kyr) rather than during interglaciations and are prevalent during well-known cool periods including the Younger Dryas (YD) and some Heinrich (H) events (H1, H2, and H4, Fig. 2). Indeed some 42% of the calcite age data between 62–10 kyr time period fall into Heinrich events, though we have not (yet) discovered veins formed during all Heinrich events. In summary, vein formation occurs preferentially during periods of low to intermediate isolation or low temperature, but requires a positive (but weak) moisture balance.

We compared our results with oxygen isotope profiles of some robust long-term speleothem-records in the region (e.g. Dim Cave; Ünal-İmer et al., 2015, Sofular Cave; Fleitmann et al. 2009 and Soreq Cave; Bar-Matthews et al. 2003). The trend is very similar to Dim and Soreq Cave records but there

is poor correlation with Sofular Cave and to the wider global deep-sea/ice-core records (Svensson et al. 2008; Grootes & Stuiver 1997) records (Fig. 2). We also compiled our results with previously published U-series dates of travertine from Turkey (Uysal et al. 2009; De Filippis et al. 2012; Uysal et al. 2011), which collectively demonstrate similar correlations with the insolation minima as well as with some of the Heinrich events (H1 and H2, Fig.2).

5. Discussion

5.1 Calcite vein/breccia formation and active extensional faulting

The textures of the vein systems in the Kumlubük Canyon record a history of 1) incremental extensional opening of laminated veins through calcite growth with columnar crystals (Figs. S6a and S6c, *App. 1*), and 2) multiple-episode brecciation and carbonate re-cementation with euhedral crystal growth (Figs. S6b, S6d, and S3b). Microstructural evidence under transmitted light reveals that the growth of columnar calcite crystals is terminated at sharp borders with inclusion bands (Figs. S5a and S5c) along the veinlet borders (limestone particles from the host rock, Figs. 2g, S5b, and S5d) and inclusion trails parallel to the vein growth (Fig. S5b), suggesting that the veins were formed through a crack-seal mechanism (cf. Uysal et al., 2009). Specifically the laminated nature of these veins, with the inclusion of wall-rock slivers indicates episodic carbonate precipitation (cf. Uysal et al., 2011). It is interpreted that such repeated fracturing is the role of seismic/tectonic activity, where the stress levels rise and fall episodically and large volumes of fluids are likely to be expelled from fluid-filled fractures during earthquakes (Sibson 1981; Mawer & Williams 1985; Brogi et al. 2014; Faccenna et al. 2008).

Breccia-filled with euhedral calcite could be directly associated with the earthquake rupture (mainshock), while the laminated veins are more likely to be associated with long-term post-seismic processes (aftershocks or swarm activity) assuming that large earthquakes induce large fluid flow events. Alternatively or additionally, the formation of the laminated veins may be linked to aseismic deformations that occur at slow strain rates and could also produce synchronous opening of extensional fractures and cementation (Blenkinsop & Sibson 1992). Aseismic areas can correlate with zones of abnormally high pore fluid pressure (e.g. in central Coast Ranges, California; Melchiorre et al. 1999) and episodic fluid flow (e.g. in the Gulf of Mexico; Losh & Haney 2006). Statistically indistinguishable U-series ages were observed both in some of the breccia samples and laminated veins, suggesting that the main rupture events were followed shortly by post-seismic aftershocks or earthquake swarm activities (e.g. calcite vein KB1b, Fig. 3d, Table S2).

5.2 Climatic implication of U-series age dataset

The primary control on the flux of water available for deep percolation within the Eastern Mediterranean (EM) is the effectiveness of winter precipitation, which is in turn influenced by the intensity and seasonal displacement of westerly wind flow over the region. Turkey has a Mediterranean climate and is under the effect of two climatic regimes and associated atmospheric/oceanic circulation patterns (Eken et al. 2005). These are the sub-tropical anticyclonic belt, which dominates during summer, and the Northern Hemisphere westerlies, which control winter climate. As a result, Turkey is characterized by dry, warm summers (Jun-Aug) and wet, cool winters (Dec-Feb). About 80% of all precipitation falls in winter and the shoulder months of early Spring and late Autumn. Consequently, all significant hydrological change in Turkey is related to changes in the winter westerlies (Türkeş & Erlat 2009). Changes to westerly flows occur on a variety of timescales from different forcings, and range from multi-millennial Milankovitch and ice sheet forcing (e.g. Ünal-İmer et al., 2015) to interannual and decadal changes such as the North Atlantic Oscillation (NAO; Kwiecien et al., 2009).

For the Last Glacial Maximum (LGM, ~19–23,000 cal yr), there is good ancillary evidence that moisture balance was more positive than in the late Holocene in areas experiencing Mediterranean-type climate in the Mediterranean region (Kwiecien et al. 2009; Sarıkaya et al. 2008; Harrison et al. 1996; Frumkin et al. 2000; Sarıkaya et al. 2014; Lisker et al. 2010; Şenkul & Doğan 2013; Frumkin et al. 2011).

Many of the eastern Mediterranean speleothem oxygen isotope records (e.g. Soreq, Bar-Matthews et al., 2003; Sofular, Fleitmann et al., 2009) are interpreted in terms of rainfall histories. Such interpretations are challenging given the wide range of controls on isotope values and more recent records have been interpreted in terms of changes in moisture source and wind track (e.g. Ünal-İmer et al., 2015). Nevertheless, all these records display speleothem growth during the last glaciation, which indicates that overall moisture balances were positive throughout the last glacial period (74–14 kyr). Growth rates were lower during cooler periods such as the LGM, indicating lower but still positive levels of available moisture at these times. The overall strength of zonal westerly circulation in both hemispheres is driven by the pole-equator temperature contrast and this is highest during periods of maximum seasonality (e.g. Shulmeister et al. 2004). Modelling confirms that increased winter precipitation occurs between 30-45°N during periods of enhanced seasonality, particularly during winter insolation minima, which intensify the winter storm tracks (Kutzbach et al. 2014). This means that on first principles winter rainfall should be at a minimum during periods of low seasonality, which is what we observe in the record.

Consequently the positive water balance observed through glacial times will be derived from reduced evapotranspiration associated with reduced temperatures (negative 6–8 C for the LGM; Essallami et al. 2007; Hughes et al. 2013; Sarıkaya et al. 2014) cooler than at present. This would result in increased effective precipitation while total precipitation is either stable or reduced. We propose that under low and intermediate insolation regimes associated with reduced westerly flow, especially during glacial periods when average temperatures were lower, a decrease in total precipitation could have limited the surface water infiltration into the deeper crustal levels. This would have assisted with the build-up of deeply generated CO_2 pressures and would have favoured co-seismic CO_2-degassing and subsequent calcite formation in SW Turkey.

5.3 CO_2 production, water availability, and possible influence of climate on CO_2 degassing in seismically active extensional regime

Regions of extensional tectonics represent typical settings, where steep and deeply-penetrating fracture and fault systems occur, which facilitate downward movement of large amounts of surface water (Taylor 1990). In such settings, meteoric fluids extensively infiltrate not only brittle-deformed shear and fracture zones, but also lower plate rocks of core complexes undergoing plastic deformation (Morrison 1994). The meteoric origin of fluids from which the travertine and carbonate veins precipitated in the study area and other locations in southwest Turkey has been confirmed previously (Uysal et al. 2009; Uysal et al. 2011). If surface water was available, it would penetrate to crustal depths.

We propose that the amount and flux rate of meteoric water supplied into the active normal fault systems in the study area may have controlled the timing and pattern of CO_2-degassing events in association with fault movements (as seismic and/or aseismic creep), and related carbonate vein and breccia formations.

We believe that the CO_2 enrichment in deeper parts of fault and fracture zones is related directly to hydrological conditions. If surface water circulation reaches deeper parts of the fault zone, upward convection of CO_2-laden water occurs along the permeable zones with subsequent degassing at surface. In contrast, when relatively little meteoric surface water reaches the fault zone, carbonate-sourced CO_2 gradually builds up in sealed reservoirs until it is degassed abruptly during earthquake events (Fig. 3a and 3b).

Crustal CO_2 production through metamorphic decarbonation (in addition to mantle degassing) is widespread in extensional systems in Italy, where a number of deep wells encountered CO_2-pressured reservoirs (Giggenbach 1988; Chiodini & Cioni 1989; Rogie et al. 2000). Particularly in

central Italy, where fluid discharge is higher in response to a dominantly wet climate, CO_2 is emitted to the surface by circulating groundwaters, creating widespread CO_2-rich springs and bedded travertine deposits (Chiodini et al. 1995; De Filippis et al. 2013). Indeed, U-series ages of late Quaternary travertine deposition in central Italy correlate with enhanced periods of pluvial activity (warm and humid periods) (Minissale et al. 2002; De Filippis et al. 2013).

In contrast to the expansive CO_2-degassing centers with associated carbonate deposits in Italy, carbonate deposition in SW Turkey occurs in narrow zones largely as injected vein and breccia systems (Uysal et al., 2009; Uysal et al., 2011; De Filippis et al., 2013). As we show in this study, calcite vein/breccia formation events correlate well in timing with periods of cold climate periods, rather than warm periods as appears to be the case in central Italy. Episodes of lower growth rates of stalagmites from Dim Cave (SW Turkey; Ünal-İmer et al., 2015) coincide with vein and breccia formation supporting the argument for less positive moisture balance and low water flux rates penetrating into deep groundwater reservoirs. These somewhat drier periods, which cause depressed groundwater tables and hence decreased deep meteoric water circulation, aided CO_2 build-up at depth. Reduce in groundwater levels (Türkeş, 1999) can lead to decrease in hydrostatic pressure and hence facilitate further CO_2 build up at depth. Further, unloading of hydrostatic pressure due to declined volume of water may induce more frequent seismic activity (e.g. González et al. 2012) and thus more generation of CO_2 (through limestone friction-see below and mantle degassing) to degas at or near the surface.

The release of large amounts of CO_2 in closed systems is also possible, without a regional heat flow and water circulation, through decarbonisation at high slip velocities during earthquake events (Famin et al. 2008; Italiano et al. 2005; Italiano et al. 2008; Di Toro et al. 2011; Paola et al. 2011). The abrupt temperature rise due to frictional heating can also result in rapid thermal pressurization of CO_2-rich fluids trapped within the slip zones. We suggest that such deeply-sourced CO_2 in southwest Turkey has not been significantly dissipated by circulating groundwater with subsequent gradual degassing from surface springs as is commonly the case in Italy. Rather, the CO_2 accumulates in sealed reservoirs until it erupts to the surface after rupture events due to sudden depressurization and high buoyancy of the CO_2. This process was responsible for the creation of the hydro-fractures as calcite injection veins and breccias (cf. Uysal et al., 2009; Uysal et al., 2011; De Filippis et al., 2013). Indeed, internal- (slip-induced) CO_2 production is consistent with carbon and oxygen isotope values of the calcite samples ($\delta^{13}C_{VPDB}$: -10.6 to -4.6, $\delta^{18}O_{VPDB}$: -5.9 to -1.7‰; Ünal-İmer et al. 2014), suggesting high degrees of decarbonisation or dissolving of the host limestone ($\delta^{18}O_{VPDB}$: 2.15, $\delta^{13}C_{VPDB}$: 2.4‰; Uysal et al. 2011) during earthquake events.

Finally, we propose that, even if there is no additional CO_2 supply through mantle degassing, frictional heating events through frequent earthquakes and/or higher levels of water-limestone interactions can promote high pore fluid pressure. Although not proven in this study, it has been argued that high pore fluid pressure, particularly CO_2-rich fluids can reduce the effective normal stress and hence the shear strength for a given friction coefficient (cf. Rice 2006), have an additional effect on triggering of fault slip and aftershocks (Miller et al. 2004).

6. Conclusions

Earthquake-induced calcite formations in SW Turkey are interpreted to have occurred as a result of oversaturation of CO_2 in deep reservoirs during lower insolation phases within the glacial periods; due to lower flux rates limiting the dissipation of deeply sourced CO_2 by downward infiltrating meteoric water. While we believe that the fault movement is primarily driven by the background extensional tectonics in such an actively extending region, we argue that accumulation of CO_2-rich fluid pressure in the hypocentral zones of the faults during periods of lower infiltration, with a likely effect on fault failures. This study highlights the need for further investigations of earthquake behaviour in non-extensional fault systems with different fluid sources.

7. Acknowledgements

This research was funded by the Queensland Geothermal Energy Centre of Excellence (QGECE), with some support by the School of Geography, Planning, and Environmental Management through E. Ü.İ.'s PhD project fund. L. Steinberger and A. Imer are particularly thanked for improving the draft. E.Ü.İ particularly acknowledges strong support and personal encouragement given by Hal Gürgenci (Director of QGECE), as well as the support of a University of Queensland post-graduate award. J.-X.Z. and Y.-X.F. acknowledge the support of an Australian Research Council LIEF grant (LE0989067) for U-series dating. The data for this paper are available at Radiogenic Isotope Facility (RIF; http://earth.uq.edu.au/content/radiogenic-isotope-facility) database at the School of Earth Sciences (The University of Queensland) and can also be requested from co-authors J.-X.Z. and Y.-X.F.

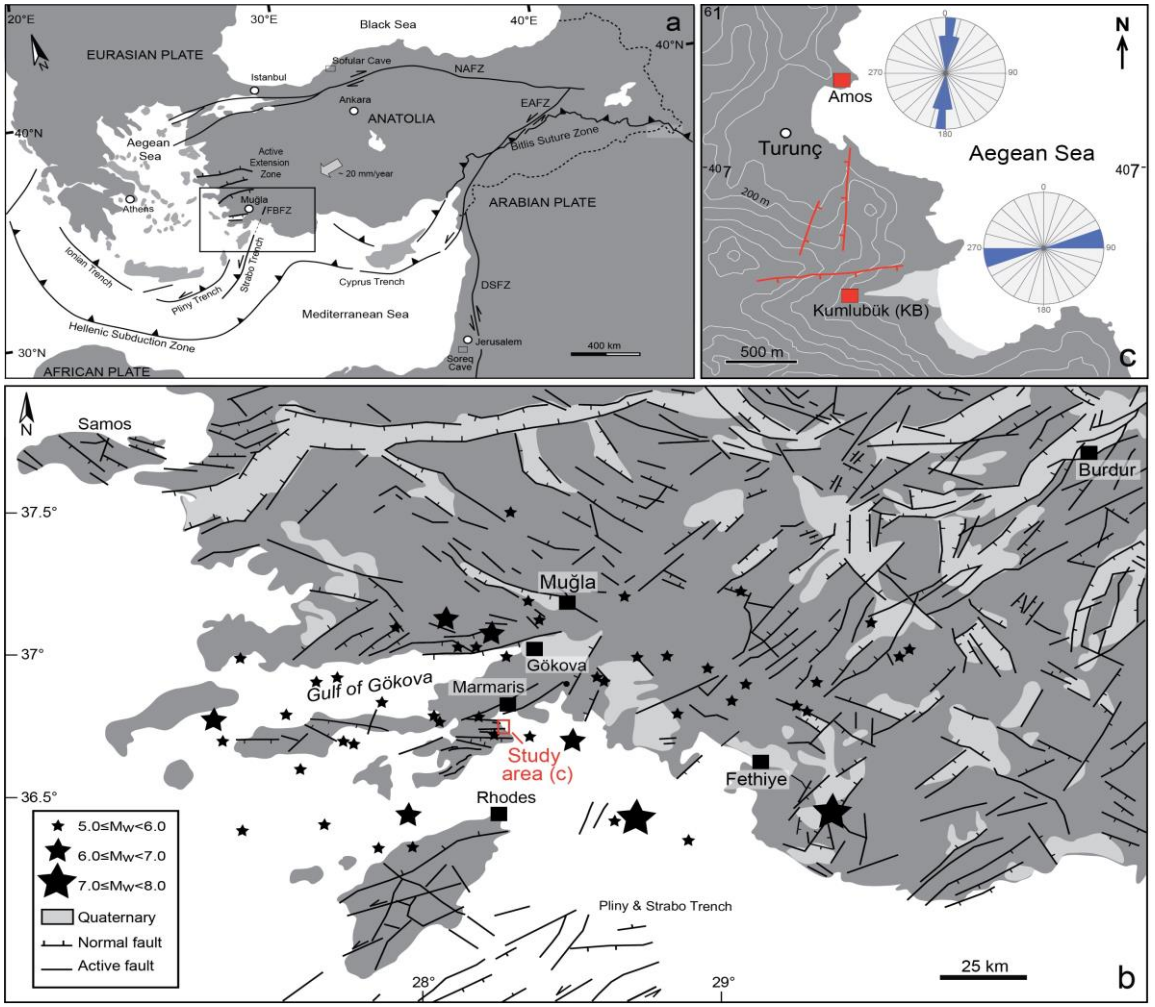

Figure 1 Generalized geodynamic map of Turkey (Uysal et al. 2011) **(a),** Muğla/Marmaris region **(b),** and simplified structural map of the study area (Amos and Kumlubük vein systems) with rose diagrams of the calcite veins (top: Amos; below: Kumlubük) **(c)**. Stars denote large earthquake epicentres (Mw >5) for the past century. Note that Amos and Kumlubük calcite-filled veins represent regional tectonic activity and are conformable with ~N–S and ~E–W trending normal faults. NAFZ: North Anatolian Fault Zone, EAFZ: East Anatolian Fault Zone, DSFZ: Dead Sea Fault Zone, FBFZ: Fethiye-Burdur Fault Zone.

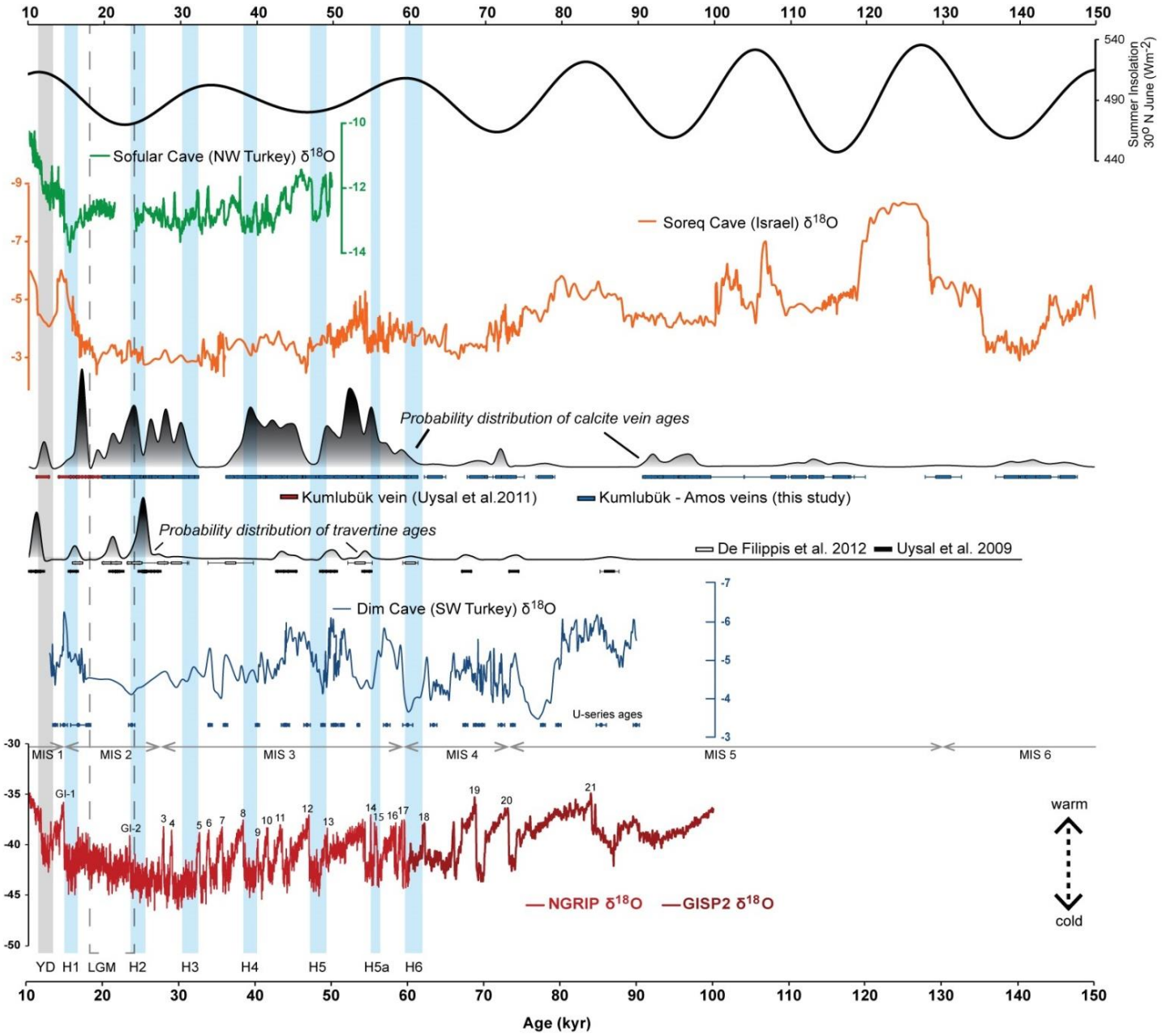
Summer Insolation 30° N June (Wm-2)
Sofular Cave (NW Turkey) δ18O
Soreq Cave (Israel) δ18O
Probability distribution of calcite vein ages
Kumlubük vein (Uysal et al.2011)
Kumlubük - Amos veins (this study)
Probability distribution of travertine ages
De Filippis et al. 2012
Uysal et al. 2009
Dim Cave (SW Turkey) δ18O
U-series ages
MIS 1
MIS 2
MIS 3
MIS 4
MIS 5
MIS 6
NGRIP δ18O
GISP2 δ18O
warm
cold
YD
H1
LGM
H2
H3
H4
H5
H5a
H6
Age (kyr)

Figure 2 (above) Summary of U-series ages for calcite veins (red bars, (Uysal et al. 2011) and blue bars, this study) and travertine deposits (black, (Uysal et al. 2009) and white bars, (De Filippis et al. 2012)) from SW Turkey compared with summer insolation (30°N June; Berger and Loutre 1991) and global and regional high-resolution paleoclimate records. Oxygen isotope profiles for speleothems from Sofular (Fleitmann et al. 2009) (green) and Soreq (Bar-Matthews et al. 2003) (orange), and Dim (Unal-Imer et al. 2015) (blue) Cave are presented. Oxygen isotope records for ice-cores from Greenland NGRIP (Svensson et al. 2008) (red) and GISP2 (Grootes & Stuiver 1997) (dark red) are shown, with numbers indicating Greenland Interstadials (e.g. GI 1) and Marine Isotope Stages (e.g. MIS 1). The durations of the Younger Dryas (YD), LGM, and Heinrich (H) events are highlighted with light grey, dashed grey, and light blue shading, respectively. The distributions of U-series ages are shown by the probability density function curves (shaded grey to black). The records from this study show similarity to those from Soreq and Sofular Caves. Note that the scale on the Sofular record is inverted as per that publication. Greenland data are provided to constrain Heinrich and other climate events.

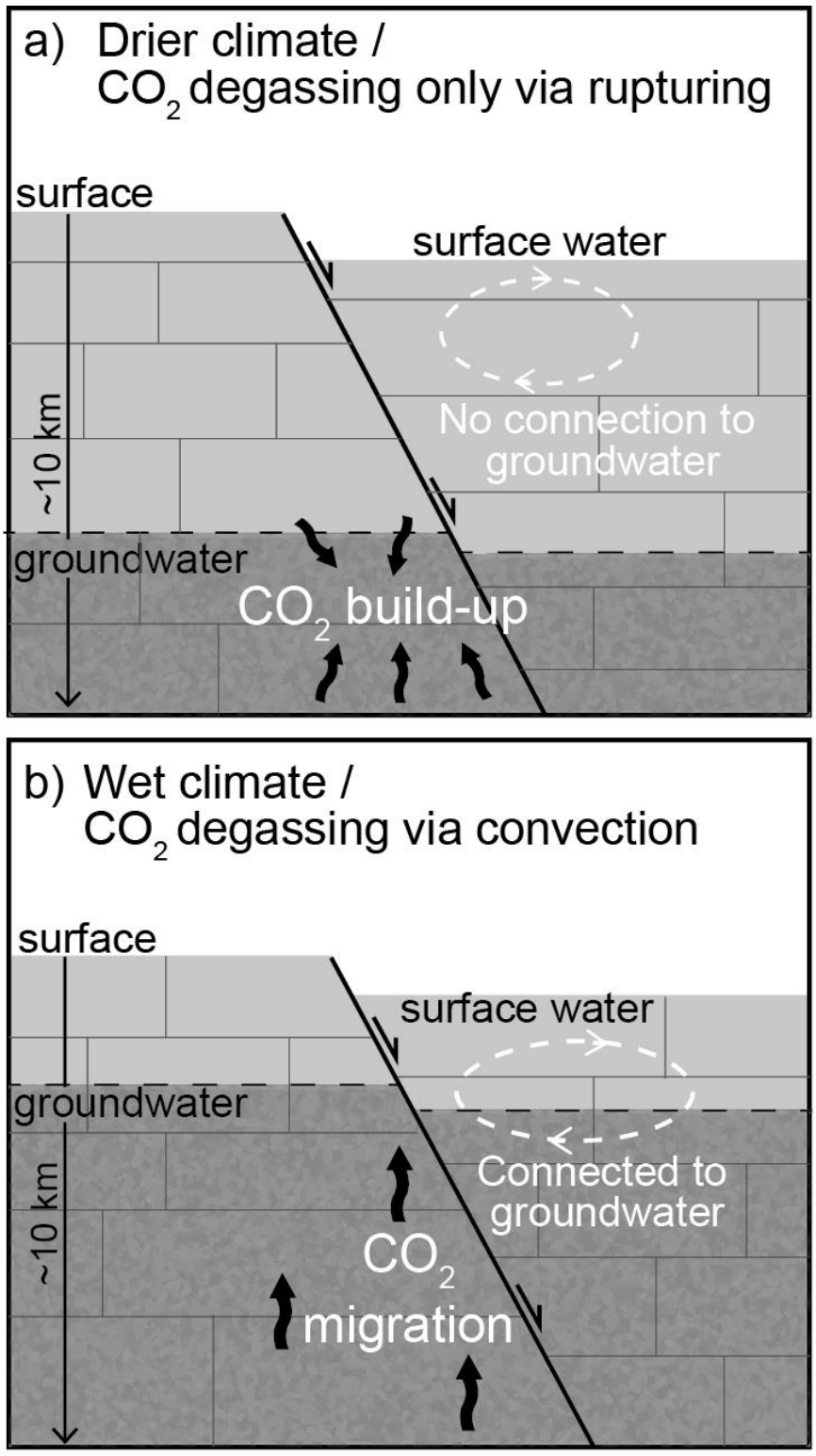

Figure 3 Sketch model demonstrating conceptualized difference between dry **(a)** and wet (b) climate CO_2 degassing events.

APPENDIX 1: Supporting Information (SI) of Paper 1

Linking CO_2 degassing in active fault zones to long-term changes in moisture balance and surface water circulation, an example from SW Turkey

E. Ünal-İmer, I.T. Uysal, J. Shulmeister, J.-X. Zhao, Y. Feng, V. Işık, R. Bolhar, J. Larsen

Detailed Materials and Methods

Collected calcite samples were polished in order to remove any weathered surfaces, and then cleaned ultrasonically. Each calcite vein was microdrilled for initial investigation from bottom and top (wall to vein) veinlets with 1-2 mm drill bits. Based on the initial U/Th age distribution of the first stage microsampling, more calcite sub-samples (either in the form of powder or chip) were separated by grinding and drilling (for powders) or cutting (for chips) from bands of each vein at different distances from the wall to top of the vein, and with different thicknesses (sub-sample names/sample I.D. in Table S1 refer to the location of the band, in mm, from vein wall). In order to avoid contamination with host rock material, samples were taken at least one mm away from the vein walls.

U-series dating was carried out using a Nu Plasma multi-collector inductively-coupled plasma mass spectrometer (MC-ICP-MS) at the Radiogenic Isotope Facility (RIF) in School of Earth Sciences, The University of Queensland following chemical treatment procedures described in Cheng et al., 2000 and Clark et al. 2012 and MC-ICP-MS analytical protocols described in Roff et al. 2013 and Zhao et al. 2001. Powdered or chipped sub-samples weighing 20–200 mg were completely dissolved in concentrated HNO_3 with a mixed ^{229}Th-^{233}U spike. After digestion, each sample was treated with H_2O_2 to decompose trace amounts of organic matters (if any) to facilitate complete sample-spike homogenization. U and Th were separated using conventional anion-exchange column chemistry using Bio-Rad AG 1-X8 resin. After stripping off the matrix from the column using double-distilled 7N HNO as eluent, 3 ml 2% HNO_3 mixed with trace amount of HF was used to elute both U and Th into a 3.5-ml pre-cleaned test tube, ready for MC-ICP-MS analyses, without the need for further drying down and re-mixing. U and Th can be collected together as the samples in this study contain relatively low levels (sub-ppm) of U.

After column chemistry, the U-Th mixed solution was injected into the MC-ICP-MS through a DSN-100 desolvation nebuliser system with an uptake rate of around 0.12 ml per minute. U-Th isotopic ratio measurement was performed on the MC-ICP-MS using a detector configuration described in Zhou et al. 2011 and Roff et al. 2013 to allow simultaneous measurements of both U and Th isotopes. Working sensitivity is about 0.45-0.6 volt per ppb for U and 0.40-0.55 volt per ppb

of Th. The time taken to measure each sample was approximately 20 minutes. Once the analysis of each sample was completed, a vigorous 15-minute cleaning procedure was undertaken and all isotopes were monitored and raw counts measured on their respective detectors to ensure no carry-over memories from previous samples. A 'drift monitoring' solution was repeatedly measured after every six unknown samples, and the results of this 'drift monitor' were used to correct for long-term drift in a number of parameters such as ion counter gain (gain values were interpolated from bracketing the 'drift monitors' if ^{229}Th and/or ^{233}U signals in the samples were too small), and minor bias in the ^{230}Th/^{238}U and ^{234}U/^{238}U ratios during each session (the bias was mainly caused by the imperfect signal peak shapes and alignments). This 'drift monitor' was made by adding ^{229}Th and ^{233}U spikes separately into a dilute solution of a uranium oxide impurity standard New Brunswick Laboratory-6 (NBL-6) from the USA. The working U concentration in the 'drift monitor' is ~6 ppb, with ^{238}U, ^{233}U and ^{229}Th signal sizes typically around ~3 volt (V), ~8 mV and ~2 mV at typical machine sensitivities, respectively. This 'drift monitor' has been precisely calibrated against the secular equilibrium Harwell Uraninite, HU-1, which was also used for calibration of the ^{229}Th/^{233}U ratios our spikes, although the spike concentrations were calibrated against a gravitationally prepared U metal (SRM-960 or called CRM-112A from New Brunswick Laboratory, USA) standard solution (Zhao et al. 2001; Hellstrom 2003)

Measurements of samples, standards, and carryover memories were performed automatically using a Cetac ASX-110FR autosampler. A long-term monitoring of the carryover memories over 20 months shows that ^{230}Th memory is mostly less than 0.1 counts per second (cps), which is negligible for our samples, as ^{230}Th signals in all of our samples are higher than 100 cps. The memories for all other isotopes are also negligible. The total procedural ^{230}Th blank was determined to be $1.18 \pm 0.24 \times 10^{-10}$ nmol or 0.27±0.05 fg (N=10); contributing average 4 yr to the ^{230}Th ages, based on average sample size and U level of the samples in this study. The corresponding procedural blanks for ^{238}U and ^{232}Th were averaged at $1.4 \pm 0.9 \times 10^{-5}$ nmol (or 3.3±2.2 pg) and $3.0 \pm 1.9 \times 10^{-6}$ nmol (or 0.69±0.41 pg), which are both negligible. All procedural blanks were extracted from the samples in the Microsoft Excel spreadsheet used for U/Th age calculation.

The ^{230}Th/^{238}U and ^{234}U/^{238}U activity ratios of the samples were calculated using the decay constants given in Clark et al. (2012). The non-radiogenic ^{230}Th was corrected using an assumed bulk-Earth atomic ^{230}Th/^{232}Th ratio of $4.4 \pm 2.2 \times 10^{-6}$, which has a minimal impact on the corrected ^{230}Th ages of those samples with the ^{230}Th/^{232}Th activity ratios higher than 20 as typical of most samples in this study (Richards et al., 2003). The impact of several other samples with lower ^{230}Th/^{232}Th activity ratios (e.g. KB3-010, -030, and -320) is slightly more significant as seen in the differences between the corrected and uncorrected ages.

U-Th ages were calculated using the Isoplot/Ex 3.0 Program (Ludwig, 2003) and their probability curves were calculated/constructed using cumulative probability macro option of KaleidaGraph version 4.02 (Synergy Software, Reading, PA).

Figure S1 Field view of Kumlubük (KB) canyon **(a)** and Google image of Amos and Kumlubük active extensional systems **(b)**. Further field observations about Kumlubük canyon are provided in Uysal et al. 2011.

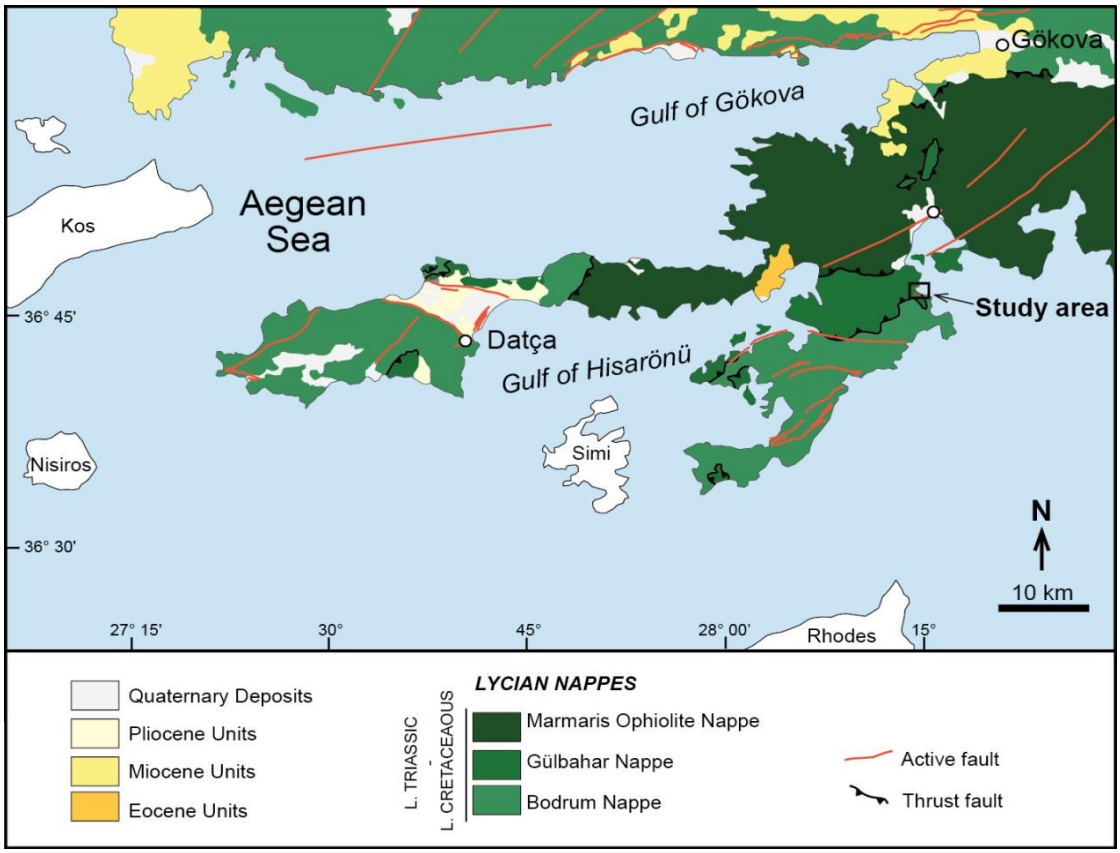

Figure S2 Simplified geological map of the study area with active faults (modified from Duman et al. 2011; Emre et al. 2011; Şenel et al. 2007).

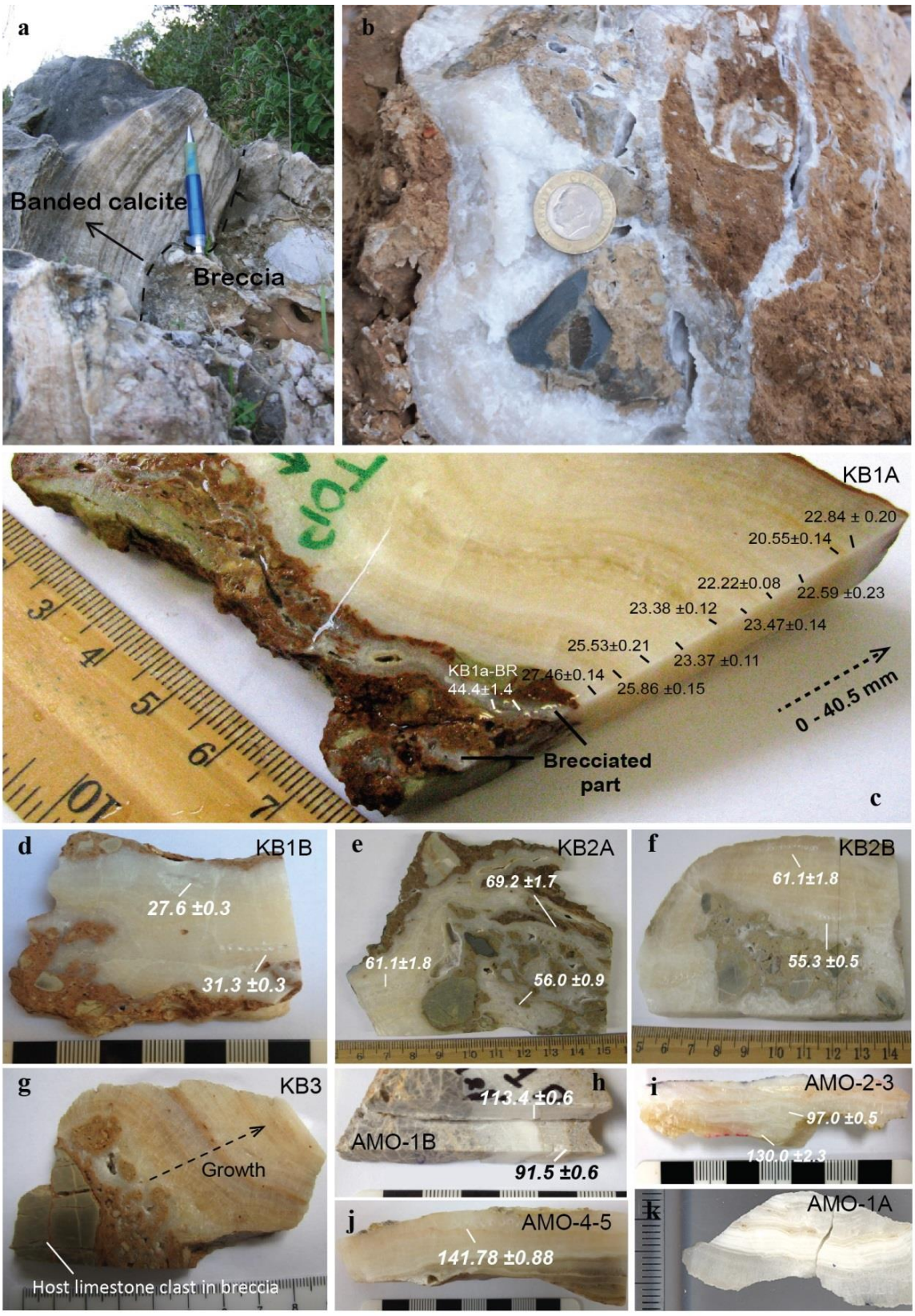

Figure S3 Representative field views of two of the investigated veins (**a ,b**) and photos of micro-sampled and dated calcite vein hand specimens from KB vein system (**c, d, e, f, g)** and from Amos vein system **(h, i, j**). Numbers in italics are the U-series ages (in kyr) summarized in Table S2.

U-series dataset of calcite vein and breccia deposits, SW Turkey

140 new U-series dates were obtained for Mesozoic limestone-hosted calcite veins and breccia from SW Turkey (Kumlubük and Amos calcite vein systems). They are combined with 20 previously published ages in ref S8. Collectively, the age results span from 10 to 150 kyr (Figs. 2 and S4; Tables S1 and S2).

According to the new dataset, Kumlubük calcite vein and breccia samples show relatively younger ages when compared to Amos vein samples. While Kumlubük samples yield an age interval between 141.1 ±4.3 kyr to 20.55 ±0.14 kyr, Amos samples give ages from 146.4 ±1.2 kyr to 68.8 ±1.3kyr. Breccia ages obtained from some of the Kumlubük (KB) samples range from 116.6 ±3.2 to 26.78 ±0.27 kyrs (Table S2). Brecciation and related calcite cementation are observed to have occurred as initial events relative to the subsequent vein formations (layering) in KB1a, KB2a, and KB2b (Figs. S3a–h and S6d). However, the sample KB1b (Fig. S3d) does not show older ages for brecciated parts yielding 26.78 ±0.27 and 29.42 ±0.59 kyr, which fall into the same time period with calcite layering (Table S2). They also display a shorter duration of deposition (i.e. ~3.4 kyr) in KB1b, which differs from other KB samples that reveal longer deposition durations from around 13 to 73 kyrs. A number of individual sub-millimetre scale veinlets with sharp borders were observed between 20 to 27 kyr age interval in KB1a and ~28 to ~30 kyr age interval in KB1b. KB2a and KB2b show mutually complementary age intervals that lasted for about 40 and 69 kyr, respectively. Although the veins show progressively younger ages from the wall, age distributions show that there are sudden young and old vein formations/remainings in contrast to general growth (see Table S1 showing the distances from wall for each sub-sample and the corresponding age results). No breccia age was gathered from KB3, KB4, and Amos calcite vein samples (Table S2) due to contamination (fine limestone particles) in calcite powders microdrilled from brecciated parts of these samples. Layered calcite age data of Amos (146.4 ±1.2–68.8 ±1.3 kyr, Table S2) shows more continuous and consecutive U-series age distributions compared to the fluctuating age trends (i.e. sudden older and younger age reversals along the vein growth) of KB samples. Amos vein depositions appear to have lasted longer time periods (46–21 kyr) than the ones developed in Kumlubük area.

Table S1 MC-ICP-MS Uranium (U)-series age data for calcite veins from Kumlubük and Amos extensional systems (Marmaris, SW Turkey).

Sample ID	Distance from wall (mm)	U (ppm)	±2σ	^{232}Th (ppb)	±2σ	(^{230}Th/^{232}Th)	±2σ	(^{230}Th/^{238}U)	±2σ	(^{234}U/^{238}U)	±2σ	Uncorr. Age (kyr)	±2σ	*Corr. Age (kyr)	±2σ	Corr. Initial (^{234}U/^{238}U)	±2σ
KB1a-BR	NA	0.2614	0.0001	25.62	0.03	11.30	0.05	0.3650	0.0014	1.0376	0.0012	47.20	0.24	44.4	1.4	1.0517	0.0009
KB1a-0050	0.5	0.2287	0.0002	5.26	0.009	31.64	0.18	0.2399	0.0013	1.0440	0.0014	28.46	0.18	27.81	0.37	1.0479	0.0015
KB1a-0375	3.75	0.2449	0.0001	1.710	0.003	101.39	0.33	0.2333	0.0007	1.0410	0.0008	27.66	0.10	27.46	0.14	1.0444	0.0008
KB1a-0475	4.75	0.2297	0.0002	4.37	0.005	37.19	0.40	0.2333	0.0025	1.0421	0.0017	27.63	0.34	27.09	0.43	1.0457	0.0018
KB1a-0575	5.75	0.2898	0.0001	1.30	0.002	138.6	0.76	0.2051	0.0011	1.0432	0.0013	23.87	0.14	23.74	0.16	1.0463	0.0014
KB1a-0750	7.50	0.2929	0.0001	2.370	0.004	82.97	0.28	0.2215	0.0007	1.0407	0.0009	26.09	0.10	25.86	0.15	1.0438	0.0009
KB1a-1025	10.25	0.3169	0.0001	3.740	0.003	56.68	0.23	0.2205	0.0009	1.0437	0.0008	25.87	0.12	25.53	0.21	1.0472	0.0009
KB1a-1100	11.00	0.4072	0.0003	0.72	0.002	341.7	2.8	0.1988	0.0015	1.0417	0.0018	23.10	0.20	23.05	0.21	1.0445	0.0019
KB1a-1275	12.75	0.3092	0.0002	1.03	0.002	188.4	1.3	0.2068	0.0014	1.0440	0.0014	24.07	0.18	23.98	0.19	1.0471	0.0015
KB1a-1400	14.00	0.4327	0.0002	1.36	0.01	195.3	1.2	0.2019	0.0008	1.0432	0.0008	23.45	0.10	23.37	0.11	1.0462	0.0009
KB1a-1825	18.25	0.4126	0.0002	0.970	0.001	261.2	1.2	0.2016	0.0009	1.0420	0.0009	23.44	0.11	23.38	0.12	1.0449	0.0009
KB1a-1900	19.00	0.3217	0.0002	3.60	0.006	55.73	0.29	0.2056	0.0010	1.0432	0.0012	23.93	0.14	23.61	0.21	1.0463	0.0013
KB1a-2025	20.25	0.3420	0.0002	0.58	0.001	335.03	2.4	0.1865	0.0013	1.0489	0.0011	21.34	0.16	21.29	0.16	1.0520	0.0012
KB1a-2150	21.50	0.3954	0.0001	3.010	0.003	81.21	0.26	0.2038	0.0006	1.0441	0.0006	23.682	0.083	23.47	0.14	1.0472	0.0007
KB1a-2525	25.25	0.3484	0.0002	1.560	0.002	131.40	0.33	0.1934	0.0004	1.0438	0.0008	22.348	0.060	22.221	0.087	1.0467	0.0009
KB1a-2720	27.20	0.3621	0.0002	1.81	0.004	114.66	0.74	0.1891	0.0012	1.0494	0.0018	21.67	0.15	21.52	0.17	1.0525	0.0020
KB1a-2800	28.00	0.3405	0.0002	1.47	0.004	136.64	1.47	0.1941	0.0020	1.0481	0.0014	22.33	0.26	22.21	0.27	1.0512	0.0015
KB1a-2850	28.50	0.3926	0.0004	0.37	0.001	814.1	3.6	0.2522	0.0009	1.0395	0.0011	30.28	0.13	30.26	0.14	1.0430	0.0012
KB1a-2925	29.25	0.4021	0.0002	6.15	0.01	39.52	0.13	0.1993	0.0006	1.0466	0.0007	23.025	0.083	22.59	0.23	1.0499	0.0008
KB1a-3225	32.25	0.4470	0.0002	3.260	0.004	75.50	0.32	0.1812	0.0007	1.0458	0.0007	20.754	0.094	20.55	0.14	1.0486	0.0007
KB1a-3400	34.00	0.8809	0.0008	11.22	0.02	47.90	0.17	0.2011	0.0006	1.0490	0.0012	23.200	0.087	22.84	0.20	1.0524	0.0013
KB1b-T	NA	0.2433	0.0001	1.930	0.004	90.1	1.1	0.2348	0.0027	1.0416	0.0018	27.85	0.37	27.62	0.39	1.0451	0.0019
KB1b-B	NA	0.3553	0.0002	5.37	0.06	52.95	0.72	0.2639	0.0021	1.0444	0.0015	31.74	0.29	31.31	0.36	1.0487	0.0016
KB1b-BR1	NA	0.3098	0.0001	6.69	0.01	32.46	0.12	0.2308	0.0008	1.0432	0.0013	27.26	0.12	26.78	0.27	1.0469	0.0014
KB1b-BR2	NA	0.2855	0.0002	14.85	0.02	14.900	0.060	0.2556	0.0010	1.0444	0.0011	30.58	0.14	29.42	0.59	1.0489	0.0012

KB1b-195	19.5	0.3926	0.0004	0.37	0.001	814.1	3.6	0.2522	0.0009	1.0395	0.0011	30.28	0.13	30.26	0.14	1.0430	0.0012
KB1b-190	19.0	0.3467	0.0002	1.050	0.002	255.39	0.93	0.2546	0.0009	1.0415	0.0012	30.55	0.12	30.48	0.13	1.0453	0.0012
KB1b-140	14.0	0.3763	0.0003	1.840	0.003	156.01	0.80	0.2508	0.0012	1.0402	0.0010	30.07	0.17	29.96	0.18	1.0438	0.0011
KB1b-115	11.5	0.3122	0.0002	5.04	0.010	48.51	0.26	0.2582	0.0013	1.0373	0.0014	31.20	0.19	30.73	0.30	1.0409	0.0016
KB1b-100	10.0	0.2922	0.0002	2.580	0.004	85.51	0.44	0.2485	0.0013	1.0400	0.0013	29.76	0.18	29.56	0.20	1.0436	0.0014
KB1b-080	8.0	0.3404	0.0003	0.48	0.001	518.4	3.2	0.2407	0.0014	1.0424	0.0014	28.61	0.19	28.57	0.20	1.0460	0.0015
KB1b-070	7.0	0.3328	0.0002	1.770	0.003	138.69	0.66	0.2431	0.0011	1.0422	0.0011	28.96	0.15	28.84	0.16	1.0459	0.0012
KB1b-040	4.0	0.2191	0.0003	1.27	0.002	123.30	0.66	0.2357	0.0012	1.0382	0.0019	28.07	0.18	27.90	0.20	1.0414	0.0020
KB1b-035	3.5	0.2466	0.0002	1.470	0.002	120.03	0.61	0.2355	0.0012	1.0389	0.0014	28.02	0.17	27.89	0.18	1.0422	0.0015
KB1b-015	1.5	0.2213	0.0001	2.710	0.004	58.20	0.28	0.2348	0.0011	1.0416	0.0012	27.85	0.15	27.57	0.20	1.0452	0.0013
KB2a-T	NA	0.4059	0.0003	9.40	0.01	55.73	0.26	0.4254	0.0019	1.0569	0.0018	55.94	0.35	55.29	0.47	1.0669	0.0021
KB2a-M	NA	0.1887	0.0001	2.94	0.01	83.7	1.1	0.4291	0.0055	1.0584	0.0029	56.45	0.96	56.02	0.99	1.0687	0.0033
KB2a-B	NA	0.3745	0.0001	43.39	0.05	13.440	0.070	0.5133	0.0027	1.0527	0.0018	72.51	0.58	69.2	1.7	1.0662	0.0025
KB2a-BR1	NA	0.4289	0.0001	43.40	0.07	14.410	0.050	0.4805	0.0013	1.0528	0.0006	66.16	0.25	63.3	1.4	1.0649	0.0012
KB2a-BR2	NA	0.4227	0.0002	161.7	0.3	5.330	0.020	0.6719	0.0017	1.0525	0.0008	109.70	0.49	98.5	5.4	1.0775	0.0047
KB2a-BR3	NA	0.4154	0.0002	95.0	0.1	9.410	0.030	0.7091	0.0018	1.0417	0.0011	123.23	0.64	116.6	3.2	1.0618	0.0026
KB2a-250	25.0	0.4439	0.0012	0.77	0.001	702.3	3.7	0.4031	0.0023	1.0492	0.0018	52.71	0.40	52.66	0.40	1.0571	0.0021
KB2a-230	23.0	0.4472	0.0002	1.140	0.001	475.7	1.3	0.3998	0.0011	1.0524	0.0010	51.96	0.19	51.90	0.20	1.0607	0.0011
KB2a-210	21.0	0.4186	0.0002	0.52	0.001	984.2	3.8	0.4046	0.0013	1.0530	0.0012	52.71	0.24	52.68	0.24	1.0615	0.0013
KB2a-175	17.5	0.3815	0.0002	0.790	0.001	594.3	1.6	0.4052	0.0010	1.0511	0.0008	52.93	0.18	52.87	0.18	1.0594	0.0010
KB2a-160	16.0	0.3236	0.0001	6.99	0.007	59.03	0.20	0.4200	0.0013	1.0514	0.0012	55.42	0.25	54.81	0.38	1.0604	0.0015
KB2a-150	15.0	0.3422	0.0001	2.81	0.004	152.08	0.50	0.4115	0.0012	1.0510	0.0008	54.00	0.22	53.77	0.24	1.0595	0.0009
KB2a-140	14.0	0.3680	0.0003	1.10	0.002	414.27	1.82	0.4095	0.0017	1.0548	0.0017	53.40	0.31	53.32	0.31	1.0638	0.0019
KB2a-135	13.5	0.3691	0.0002	2.290	0.003	201.14	0.51	0.4119	0.0009	1.0539	0.0006	53.87	0.16	53.70	0.18	1.0628	0.0006
KB2a-100	10.0	0.2873	0.0001	12.97	0.02	30.13	0.10	0.4483	0.0014	1.0506	0.0011	60.44	0.27	59.16	0.67	1.0606	0.0013
KB2a-085	8.5	0.3116	0.0001	1.84	0.003	216.15	1.09	0.4197	0.0020	1.0553	0.0016	55.08	0.36	54.91	0.37	1.0647	0.0018
KB2a-070	7.0	0.3083	0.0001	2.230	0.002	177.60	0.48	0.4231	0.0011	1.0552	0.0008	55.66	0.19	55.46	0.22	1.0647	0.0009
KB2a-055	5.5	0.31994	0.00010	1.00	0.003	410.3	2.2	0.4224	0.0019	1.0586	0.0021	55.31	0.36	55.22	0.37	1.0685	0.0024
KB2a-045	4.5	0.3141	0.0002	2.570	0.002	157.42	0.44	0.4242	0.0011	1.0550	0.0009	55.87	0.21	55.64	0.23	1.0645	0.0010
KB2a-010	1.0	0.2810	0.0001	3.400	0.003	107.88	0.31	0.4299	0.0012	1.0516	0.0006	57.10	0.21	56.77	0.26	1.0607	0.0007
KB2b-BR1	NA	0.3657	0.0001	1.600	0.002	281.33	0.69	0.4046	0.0009	1.0529	0.0012	52.72	0.17	52.60	0.18	1.0614	0.0013

KB2b-BR2	NA	0.2918	0.0002	15.28	0.02	25.94	0.13	0.4476	0.0021	1.0539	0.0011	60.03	0.38	58.56	0.81	1.0646	0.0014
KB2b-310	31.0	0.2191	0.0002	13.82	0.028	16.12	0.15	0.3351	0.0031	1.0639	0.0014	41.14	0.47	39.38	0.98	1.0726	0.0017
KB2b-295	29.5	0.2020	0.0001	6.52	0.01	34.29	0.13	0.3648	0.0012	1.0533	0.0013	46.25	0.21	45.34	0.49	1.0612	0.0015
KB2b-290	29.0	0.1907	0.0001	1.98	0.003	104.63	0.55	0.3574	0.0018	1.0518	0.0016	45.16	0.29	44.87	0.33	1.0590	0.0018
KB2b-250	25.0	0.2904	0.0002	1.120	0.002	301.1	1.3	0.3826	0.0016	1.0515	0.0011	49.19	0.26	49.08	0.27	1.0593	0.0012
KB2b-230	23.0	0.2970	0.0002	0.32	0.001	1061.1	7.1	0.3811	0.0019	1.0495	0.0015	49.08	0.33	49.05	0.33	1.0568	0.0017
KB2b-210	21.0	0.3122	0.0002	3.90	0.01	98.20	0.39	0.4046	0.0015	1.0497	0.0010	52.93	0.26	52.58	0.31	1.0578	0.0012
KB2b-190	19.0	0.2885	0.0002	4.49	0.008	76.95	0.33	0.3951	0.0016	1.0501	0.0015	51.32	0.28	50.88	0.35	1.0581	0.0017
KB2b-175	17.5	0.2629	0.0002	2.59	0.005	120.18	0.53	0.3908	0.0016	1.0479	0.0010	50.75	0.27	50.48	0.30	1.0553	0.0011
KB2b-160	16.0	0.2871	0.0002	1.850	0.003	183.69	0.71	0.3891	0.0014	1.0505	0.0014	50.31	0.25	50.13	0.26	1.0583	0.0016
KB2b-110	11.0	0.2983	0.0002	4.16	0.01	87.37	0.23	0.4014	0.0010	1.0504	0.0013	52.35	0.19	51.95	0.27	1.0586	0.0015
KB2b-070	7.0	0.2980	0.0002	2.140	0.003	167.59	0.66	0.3964	0.0015	1.0505	0.0008	51.51	0.25	51.31	0.27	1.0585	0.0009
KB2b-050	5.0	0.2474	0.0002	1.42	0.002	212.00	0.95	0.3999	0.0017	1.0492	0.0010	52.18	0.30	52.02	0.31	1.0571	0.0012
KB2b-040	4.0	0.2923	0.0002	2.110	0.003	167.98	0.78	0.4005	0.0018	1.0521	0.0012	52.08	0.31	51.87	0.32	1.0605	0.0014
KB3-005	0.5	0.18	0.0001	5.78	0.01	30.33	0.26	0.3209	0.0027	1.0299	0.0016	40.69	0.42	39.76	0.62	1.0338	0.0018
KB3-010	1.0	0.1364	0.0001	20.8	0.03	7.7	0.06	0.3869	0.0027	1.0319	0.0016	51.17	0.48	46.7	2.3	1.038	0.0021
KB3-015	1.5	0.1691	0.0001	12.47	0.02	17.82	0.13	0.4331	0.0031	1.0286	0.0017	59.51	0.59	57.4	1.2	1.0343	0.0021
KB3-025	2.5	0.1603	0.0001	10.94	0.02	16.03	0.11	0.3605	0.0023	1.0298	0.0018	46.94	0.39	45.0	1.1	1.0345	0.0021
KB3-030	3.0	0.1772	0.0001	23.66	0.04	9.73	0.05	0.4283	0.0023	1.0319	0.0016	58.37	0.43	54.5	2.0	1.0386	0.0021
KB3-045	4.5	0.2086	0.0001	9.94	0.02	21.82	0.19	0.3427	0.0029	1.0297	0.002	44.1	0.48	42.73	0.83	1.0339	0.0023
KB3-050	5.0	0.2228	0.0001	9.7	0.02	22.78	0.3	0.3268	0.0043	1.0333	0.0018	41.43	0.67	40.18	0.91	1.0377	0.002
KB3-065	6.5	0.2455	0.0001	7.74	0.017	31.15	0.22	0.3238	0.0022	1.0268	0.0016	41.29	0.34	40.38	0.57	1.0303	0.0018
KB3-075	7.5	0.2345	0.0001	3.64	0.01	61.11	0.74	0.3122	0.0037	1.0276	0.0016	39.48	0.57	39.03	0.61	1.031	0.0018
KB3-080	8.0	0.2408	0.0002	3.32	0.006	65.59	0.65	0.2982	0.0029	1.0309	0.0013	37.22	0.44	36.83	0.48	1.0344	0.0014
KB3-100	10.0	0.2165	0.0001	8.42	0.01	26.5	0.16	0.3395	0.002	1.0313	0.0008	43.51	0.32	42.39	0.64	1.0357	0.001
KB3-110	11.0	0.237	0.0001	4.25	0.01	53.21	0.34	0.3147	0.0019	1.0299	0.0011	39.75	0.29	39.23	0.4	1.0335	0.0013
KB3-115	11.5	0.2311	0.0001	3.54	0.004	62.15	0.28	0.3139	0.0014	1.0293	0.0014	39.65	0.22	39.21	0.31	1.0329	0.0015
KB3-120	12.0	0.2341	0.0001	4.66	0.01	48.32	0.31	0.3169	0.0019	1.0298	0.0014	40.08	0.29	39.5	0.41	1.0336	0.0015
KB3-125	12.5	0.2498	0.0001	9.08	0.02	28.58	0.17	0.3423	0.0019	1.0308	0.0011	43.96	0.31	42.93	0.61	1.0351	0.0013
KB3-135	13.5	0.2550	0.0001	7.17	0.014	36.11	0.13	0.3348	0.0010	1.0292	0.0016	42.88	0.18	42.07	0.44	1.0331	0.0018
KB3-140	14.0	0.2661	0.0001	2.09	0.01	117.75	0.83	0.3047	0.002	1.0344	0.0017	38.02	0.3	37.79	0.32	1.0384	0.0019

KB3-145	14.5	0.287	0.0001	1.27	0.003	207.95	1.57	0.3029	0.0022	1.0334	0.0014	37.8	0.33	37.67	0.34	1.0372	0.0015
KB3-150	15.0	0.2781	0.0001	6.29	0.01	43.59	0.27	0.3249	0.002	1.0325	0.001	41.17	0.3	40.52	0.44	1.0367	0.0012
KB3-160	16.0	0.2687	0.0001	14.31	0.02	20.09	0.14	0.3525	0.0024	1.0335	0.0016	45.44	0.39	43.9	0.85	1.0384	0.0018
KB3-170	17.0	0.2900	0.0003	6.63	0.013	43.75	0.26	0.3296	0.0018	1.0338	0.0012	41.83	0.29	41.17	0.43	1.0382	0.0014
KB3-175	17.5	0.285	0.0001	5.4	0.01	51.81	0.43	0.3234	0.0026	1.0323	0.0015	40.95	0.41	40.41	0.49	1.0364	0.0017
KB3-185	18.5	0.3242	0.0001	3.25	0.01	95.08	0.62	0.3139	0.002	1.0365	0.0015	39.3	0.32	39.01	0.34	1.0408	0.0017
KB3-190	19.0	0.3445	0.0001	3.63	0.01	90.79	0.43	0.3154	0.0014	1.0321	0.0011	39.75	0.23	39.45	0.27	1.0359	0.0013
KB3-195	19.5	0.3309	0.0001	10.39	0.01	32.22	0.13	0.3334	0.0013	1.0333	0.001	42.44	0.21	41.54	0.49	1.0377	0.0012
KB3-200	20.0	0.3384	0.0002	15.39	0.02	23.39	0.12	0.3506	0.0018	1.0333	0.0008	45.15	0.28	43.84	0.71	1.0381	0.001
KB3-215	21.5	0.41351	0.00037	43.75	0.14	11.96	0.08	0.4171	0.0023	1.0349	0.0014	56.15	0.42	53.1	1.6	1.0417	0.0018
KB3-230	23.0	0.401	0.0002	126	0.2	6.65	0.03	0.6885	0.0027	1.0383	0.0013	117.62	0.87	108.4	4.5	1.0568	0.0033
KB3-235	23.5	0.371	0.0001	37.08	0.07	12.85	0.07	0.4233	0.0021	1.0378	0.0015	57.02	0.38	54.1	1.5	1.0453	0.0019
KB3-240	24.0	0.3696	0.0006	8.89	0.020	42.77	0.32	0.3390	0.0025	1.0388	0.0019	43.01	0.39	42.33	0.52	1.0440	0.0021
KB3-250	25.0	0.3386	0.0001	3.01	0.01	110.43	0.74	0.3239	0.0019	1.0385	0.0014	40.72	0.3	40.47	0.33	1.0433	0.0015
KB3-265	26.5	0.2566	0.0001	4.49	0.01	66.73	0.49	0.385	0.0028	1.0362	0.0014	50.57	0.47	50.07	0.53	1.042	0.0016
KB3-270	27.0	0.19270	0.00022	3.83	0.010	53.29	0.40	0.3494	0.0025	1.0400	0.0027	44.58	0.42	44.02	0.50	1.0455	0.0031
KB3-275	27.5	0.1506	0.0001	12.12	0.02	15.29	0.21	0.4057	0.0054	1.0354	0.0026	54.12	0.95	51.8	1.5	1.042	0.0031
KB3-290	29.0	0.1462	0.0001	3.93	0.01	39.57	0.28	0.3504	0.0024	1.0305	0.0017	45.27	0.4	44.49	0.55	1.0349	0.0019
KB3-320	32.0	0.1927	0.0001	55.5	0.07	8.17	0.04	0.7751	0.0036	1.033	0.0019	149.6	1.6	141.1	4.3	1.0534	0.0038
KB3-330	33.0	0.1671	0.0001	2.52	0.004	67.68	0.51	0.3366	0.0025	1.035	0.0016	42.85	0.4	42.42	0.45	1.0397	0.0019
KB3-335	33.5	0.1524	0.0001	2.87	0.004	56.04	0.45	0.3477	0.0028	1.0369	0.0019	44.48	0.45	43.94	0.52	1.042	0.0021
KB3-340	34.0	0.1843	0.0001	15.22	0.045	16.25	0.13	0.4424	0.0033	1.0348	0.0025	60.68	0.64	58.3	1.3	1.0420	0.0030
KB3-350	35.0	0.178	0.0001	7.59	0.01	29.01	0.14	0.4079	0.0019	1.0364	0.0015	54.43	0.35	53.21	0.69	1.0428	0.0017
KB3-360	36.0	0.1836	0.0001	10.95	0.014	22.83	0.11	0.4489	0.002	1.0359	0.0012	61.78	0.39	60.07	0.92	1.0432	0.0015
KB3-365	36.5	0.2215	0.0001	17.44	0.026	25.70	0.10	0.6668	0.0025	1.0285	0.0014	113.31	0.79	111.0	1.3	1.0398	0.0020
KB3-370	37.0	0.188	0.0001	12.81	0.02	23.87	0.16	0.5363	0.0036	1.0316	0.0012	79.73	0.79	77.8	1.2	1.0401	0.0015
KB3-380	38.0	0.1742	0.0001	8.45	0.01	26.6	0.2	0.425	0.0031	1.0361	0.0016	57.44	0.57	56.05	0.89	1.0428	0.0019
KB3-390	39.0	0.1678	0.0001	5.09	0.01	38.6	0.33	0.3861	0.0033	1.0381	0.0028	50.63	0.58	49.77	0.72	1.0442	0.0033
KB3-395	39.5	0.1811	0.0001	4.66	0.006	44.58	0.24	0.3777	0.0020	1.0357	0.0013	49.39	0.33	48.66	0.49	1.0412	0.0015
KB3-400	40.0	0.2003	0.0001	2.23	0.01	97.4	0.94	0.3576	0.0034	1.0384	0.002	45.96	0.55	45.64	0.57	1.0438	0.0022
KB4/600	60.0	0.1949	0.0001	4.39	0.01	28.95	0.16	0.2147	0.0011	1.0367	0.0012	25.30	0.16	24.80	0.30	1.0396	0.0013

KB4/450	45.0	0.2673	0.0001	2.590	0.004	69.56	0.32	0.2223	0.0010	1.0372	0.0012	26.30	0.13	26.09	0.17	1.0402	0.0013
KB4/250	25.0	0.2256	0.0001	1.450	0.002	106.85	0.63	0.2266	0.0013	1.0516	0.0014	26.44	0.18	26.30	0.19	1.0557	0.0015
KB4/175	17.5	0.1767	0.0002	4.36	0.009	31.36	0.22	0.2552	0.0017	1.0400	0.0012	30.68	0.25	29.98	0.43	1.0438	0.0014
KB4/140	14.0	0.1634	0.0001	40.2	0.1	6.580	0.030	0.5334	0.0021	1.0421	0.0017	77.83	0.50	72.2	2.8	1.0551	0.0030
KB4/070	7.0	0.1754	0.0002	10.07	0.026	18.08	0.11	0.3422	0.0019	1.0320	0.0017	43.89	0.32	42.23	0.88	1.0366	0.0020
KB32-B	NA	0.2614	0.0001	1.170	0.003	284.1	2.0	0.4181	0.0028	1.0503	0.0015	55.17	0.48	55.05	0.49	1.0588	0.0018
KB32-T	NA	0.3900	0.0002	0.570	0.003	834.7	7.0	0.4036	0.0027	1.0519	0.0011	52.62	0.46	52.58	0.46	1.0602	0.0013
KB-GB	NA	0.1982	0.0001	1.360	0.002	271.3	1.3	0.6133	0.0029	1.0401	0.0011	96.50	0.74	96.31	0.75	1.0527	0.0015
AMO-V	NA	3.623	0.002	0.92	0.01	6074	36	0.5101	0.0011	1.0420	0.0007	73.01	0.24	72.10	0.24	1.0517	0.0009
AMO-2-3/020	2.0	0.05780	0.00004	7.67	0.02	20.69	0.17	0.9043	0.0073	1.2433	0.0030	132.1	2.1	130.0	2.4	1.3644	0.0073
AMO-2-3/135	13.5	0.1588	0.0001	3.30	0.01	103.77	0.40	0.7118	0.0024	1.1816	0.0013	97.56	0.56	97.06	0.59	1.2403	0.0017
AMO-2-3/150	15.0	0.0606	0.0001	1.52	0.003	118.98	0.88	0.9838	0.0071	1.2917	0.0032	143.7	2.2	143.2	2.2	1.4402	0.0048
AMO-4-5/300	30.0	0.2088	0.0001	1.790	0.004	284.0	1.9	0.8020	0.0051	1.1905	0.0024	117.1	1.4	116.9	1.4	1.2657	0.0031
AMO-4-5/230	23.0	0.3309	0.0002	0.980	0.002	939.3	3.6	0.9128	0.0032	1.2275	0.0013	139.05	0.98	139.00	0.98	1.3373	0.0018
AMO-4-5/175	17.5	0.1720	0.0001	4.01	0.01	120.58	0.36	0.9254	0.0025	1.2295	0.0017	142.30	0.85	141.78	0.88	1.3448	0.0024
AMO-4-5/100	10.0	0.12800	0.00004	5.43	0.01	67.21	0.27	0.9400	0.0035	1.2274	0.0015	147.3	1.2	146.4	1.2	1.3480	0.0028
AMO-1B/150	15.0	0.07710	0.00004	1.380	0.002	141.18	0.45	0.8315	0.0025	1.2482	0.0015	113.76	0.63	113.36	0.64	1.3437	0.0021
AMO-1B/185	18.5	0.1289	0.0001	0.860	0.002	318.1	1.4	0.7024	0.0025	1.2052	0.0010	92.40	0.52	92.24	0.53	1.2668	0.0013
AMO-1B/215	21.5	0.2001	0.0001	5.00	0.01	82.40	0.36	0.6785	0.0027	1.1699	0.0009	92.13	0.57	91.52	0.62	1.2216	0.0014
AM-1B-L-T	NA	0.1456	0.0001	0.570	0.002	549.1	3.1	0.7113	0.0034	1.1955	0.0015	95.52	0.74	95.43	0.75	1.2563	0.0019
AM-1A	NA	0.1462	0.0001	0.260	0.002	1199.0	12.0	0.7144	0.0052	1.2100	0.0017	94.2	1.1	94.2	1.1	1.2742	0.0023
AM-3A	NA	0.0596	0.0000	3.35	0.01	33.13	0.41	0.6131	0.0076	1.2694	0.0038	70.1	1.2	68.8	1.3	1.3323	0.0051

*The corrected (Corr.) ages (kyr) were calculated using equation given in Cheng et al., 2000, using half-lives specified in Clark et al., 2012.

Note: All errors are given at 2-sigma level.

The letters “T”, “B”, “M”, and “BR” in sample names refer to top (T), bottom (B), middle (M) of the calcite vein, and subsample extracted from brecciated (BR) parts of the sample, respectively. “NA” denote for Not Available. The samples without distance information (i.e. NA) were drilled and dated with an estimate distance from wall (e.g. from top, middle, and bottom) before detailed micro-sampling with high-resolution distances.

Table S2 Summary of U-series ages of Kumlubük and Amos calcite vein and breccia samples.

Sample ID	Breccia ages (kyr)	Layered calcite ages (kyr)
KB1a	44.4 ±1.4	37.9 ±1.2 – 20.55 ±0.14
KB1b	26.8 ±0.27 29.4 ±0.60	31.31 ±0.36 – 27.57 ±0.20
KB2a	63.3 ±1.4 98.5 ±5.4 116.6 ±3.2	69.2 ±1.7 – 51.90 ±0.20
KB2b	52.6 ±0.18 58.56 ±0. 81	52.58 ±0.31 – 39.38 ±0.98
KB3	-	111.0 ±1.3 – 37.67 ±0.34
KB4	-	72.2 ±2.8 – 24.80 ±0.30
AMO-2-3	-	143.2 ±2.2 – 97.06 ±0.59
AMO-4-5	-	146.4 ±1.2 – 116.9 ±1.4
AMO-1B	-	113.36 ±0.64 – 91.52 ±0.62

Additional Statistical Tests

The probability density function (pdf) of calcite vein U-series ages from Kumlubük and Amos (SW Turkey) including both current (140 ages) and previously published (20 ages: Uysal et al. 2011) data were plotted against summer insolation values for 30°N latitude (Berger and Loutre 1991) which is relevant to the study area. The pattern between the probability curves (dark blue and dashed red) and the summer insolation curve in Fig. S4 clearly suggest that the calcite vein formations occur during low to transitional periods of insolation rather than high insolation periods.

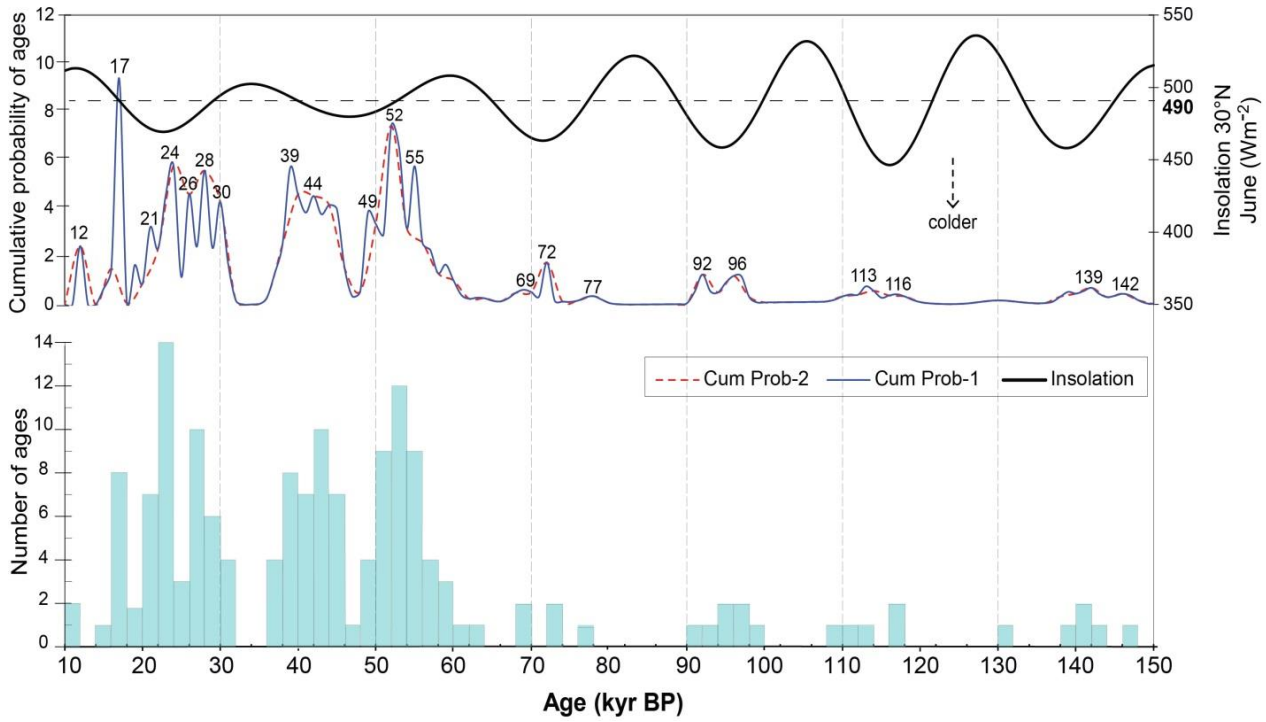

Figure S4 Probability density function (pdf) plot and histogram of U-series ages of calcite veins plotted against summer (June) insolation 30°N (Berger and Loutre 1981). The red dashed curve shows the pdf calculated by using increments of 2 kyr for the age series: 10kyr, 12kyr, 14kyr, n kyr, whereas the dark blue solid curve denotes calculation of pdf by using increments of 1 kyr for the age series. Numbers show peak age in kyr. 490 Wm^{-2} (black dashed line) is the insolation median for 10-150 kyr period.

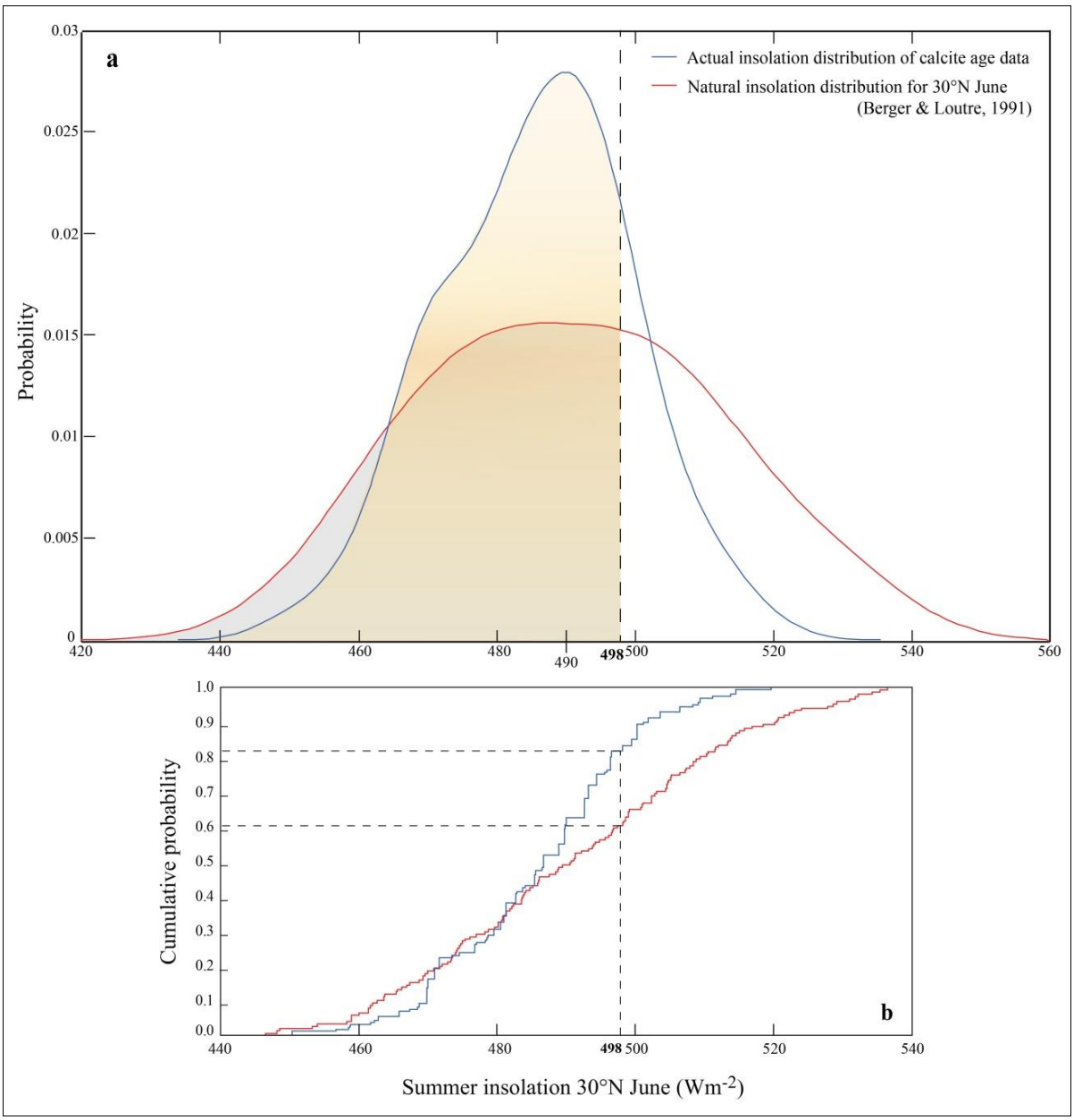

Figure S5 (a) Cumulative probability distribution curves for insolation values corresponding to the calcite vein ages (blue), and the natural insolation distribution (red) for the time period 0-150 kyr. This red graph shows the expected (or natural) distribution of age probabilities around the calculated median insolation value of of 490 Wm^{-2} while the blue graph shows the observed (or actual) distribution of ages with respect to insolation. **(b)** Cumulative probability function of the graph where 498 Wm^{-2} is the threshold insolation value. There is a clear bias (21% overrepresentation) towards lower insolation at times of calcite vein formation.

The area under the probability distributions (i.e. pdf in blue and red curves, Fig. S5a) are the cumulative distribution functions (i.e. cdfs) in Fig. S5b. For the insolation values estimated from U-series calcite ages (Table S1), 498 Wm^{-2} corresponds to the ~83rd percentile, whereas for the natural insolation values, 498 Wm^{-2} is only the ~62nd percentile.

We divided the age data into the 6 insolation cycles (i.e. 32–11 kyr, 62–33 kyr, 82–63 kyr, 106–83 kyr, 125–107 kyr, and 150–126 kyr, Tables S3 and S4) that the results cover. In order to examine the data using the Chi-squared test, we assume that the average values of the cumulative probability values of the calcite vein U-series for ages that fall at insolation points below the cut-off insolation value of 498 Wm^{-2} should be the same as ages that fall above 498 Wm^{-2}. In all six insolation cycles the cumulative probability of ages falling at insolation levels below 498 Wm^{-2} are higher than ages above (ranging from 2.75 to 9.34 times more likely, Table S4). When calculated as Chi-square values the result is significant at $p<0.001$ indicating that calcite vein ages are much more likely to occur during lower insolation phases. The choice of 498 Wm^{-2} as the cut-off was somewhat arbitrary so we also tested cut-offs at 495 Wm^{-2} and 492 Wm^{-2} (Table S5), the results remain significant, but not as significant as for 498 Wm^{-2}.

Table S3 Chi-squared test for insolation cycle 1: 32–11 kyr

1000-year bin	Observed values*	30°N June (Wm^{-2})**
1	0.0000	513.16
2	2.4197	512.98
3	0.0000	511.06
4	0.0044	507.55
5	0.6524	502.75
6	1.4754	497.05
7	9.3817	490.94
8	0.0589	484.89
9	1.6324	479.38
10	0.8616	474.82
11	3.2015	471.52
12	2.3055	469.69
13	4.5384	469.41
14	5.7595	470.63
15	1.1436	473.17
16	4.5794	476.77
17	2.4048	481.09
18	5.5505	485.73
19	2.3517	490.31
20	4.2652	494.47
21	1.7262	497.92
22	0.1766	500.45

Average value for insolation values <498 Wm^{-2} = **3.2023**

Average value for insolation values >498 Wm^{-2} = **0.5422**

Ratio: 3.2023 / 0.5422 = 5.91

Observed value = **3.2023**

Expected value = **0.5422**

$(X^2)_1$ = $(\text{observed-expected})^2$ /expected **= 13.0517**

*Observed values refer to cumulative probabilities of calcite vein U-series ages obtained from Kaleida Graph 4.02

**Dark grey shaded values are the insolation values <498 Wm^{-2} cut-off

Light grey shaded values are the insolation values >498 Wm^{-2} cut-off

Table S4 Results of Chi-squared tests for insolation cycles 2–6: 62–33 kyr, 82–63 kyr, 106–83 kyr, 125–107 kyr, and 150–126 kyr

	Insolation Cycles (kyr BP)				
	62–33	82–63	106–83	125–107	150–126
Average value for insolation values <498 Wm^{-2}	3.6679	0.3787	0.5126	0.3272	0.3112
Average value for insolation values >498 Wm^{-2}	1.2862	0.1139	0.0549	0.1189	0.1594
Ratio between values (<498 Wm^{-2}) /(>498 Wm^{-2})	3.6679/1.2862 = 2.85	0.3787/0.1139 = 3.32	0.5126/0.0549 = 9.34	0.3272/0.1189 = 2.75	0.3112/0.1594 = 1.95
Observed value	3.6679	0.3787	0.5126	0.3272	0.3112
Expected value	1.2862	0.1139	0.0549	0.1189	0.1594
$\mathbf{(X^2)_{2–6}}$ **=**	4.4105	0.6155	4.4105	0.3649	0.1447

Table S5 Results of Chi-squared test for all time periods

$\mathbf{\Sigma(X^2)} = \Sigma[(X^2)_1 + (X^2)_2 + (X^2)_3 + (X^2)_4 + (X^2)_5 + (X^2)_6]$ (cut-off insolation = 498 Wm^{-2})	**22.4069 < 0.001 probability level** (based on X^2 contingency table = significant)
Degrees of freedom	**(#Rows - 1)*(#Columns -1) = (6-1)*(2-1) = 5**
If insolation cut-off is 495 Wm^{-2} , X^2	**18.0070, 0.01<probability<0.001 = significant**
If insolation cut-off is 492 Wm^{-2}, X^2	**13.1652, 0.05<probability<0.01 = significant**

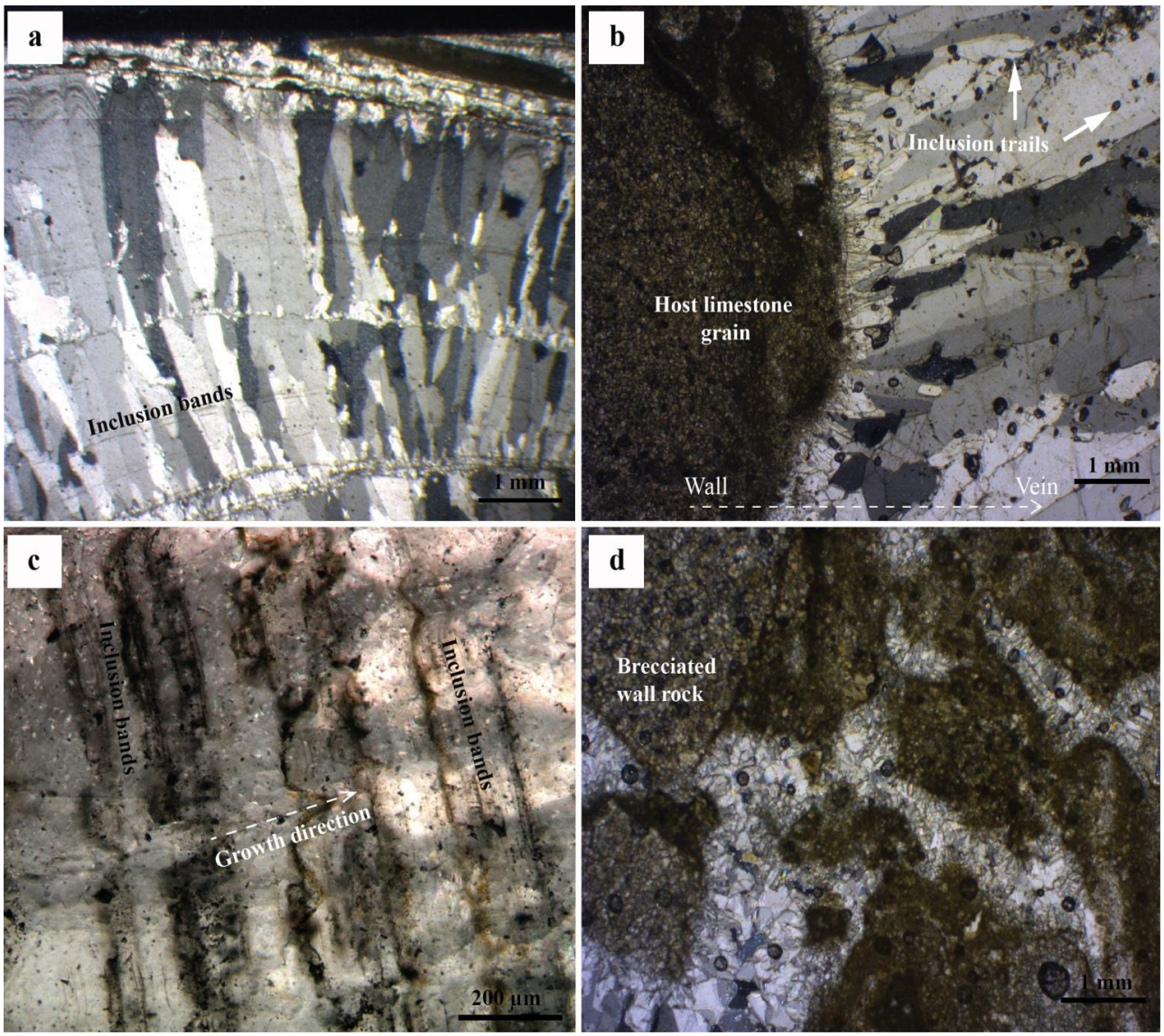

Figure S6 Representative photomicrographs showing the vein characteristics. **(a)** shows columnar forms of calcite crystals with inclusion bands parallel to layering and lateral overgrowths (Frisia 2015), XPL; **(b)** demonstrates inclusion trails and small grain fragments; note that the inclusion trails occur parallel to displacement direction, XPL; **(c)** displays inclusion bands and open columnar calcite with sharp contacts that are arranged perpendicular to growth direction, PPL; and **(d)** highlights fracturing in host rock showing brecciated texture, XPL. Note that fracture vugs are filled with fine-grained blocky calcites. PPL=Plane-polarised light, XPL=Cross-polarised light.

REFERENCES (PAPER 1)

Barka, A. et al., 1995. The Isparta Angle: its importance in the neotectonics of the Eastern Mediterranean Region. Proceedings of the International Earth Sciences Colloquium on the Aegean Region. In *Proceedings of the International Earth Sciences Colloquium on the Aegean Region*. pp. 3–18.

Bar-Matthews, M. et al., 2003. Sea–land oxygen isotopic relationships from planktonic foraminifera and speleothems in the Eastern Mediterranean region and their implication for paleorainfall during interglacial intervals. *Geochimica et Cosmochimica Acta*, 67(17), pp.3181–3199.

Berger, A. & Loutre, M.F., 1991. Insolation values for the climate of the last 10 million years. *Quaternary Science Reviews*, 10(1988), pp.297–317.

Blenkinsop, T.G. & Sibson, R.H., 1992. Aseismic fracturing and cataclasis involving reaction softening within core material from the Cajon Pass Drill Hole. *Journal of Geophysical Research: Solid Earth*, 97(B4), pp.5135–5144. Available at: http://dx.doi.org/10.1029/90JB02285.

Brogi, A. et al., 2014. Evolution of a fault-controlled fissure-ridge type travertine deposit in the western Anatolia extensional province: the Cukurba fissure-ridge (Pamukkale, Turkey). *Journal of the Geological Society*, 171(3), pp.425–441. Available at: http://jgs.lyellcollection.org/cgi/doi/10.1144/jgs2013-034 [Accessed July 18, 2014].

Çakır, Z. et al., 2012. Onset of aseismic creep on major strike-slip faults. *Geology*, 40(12), pp.1115–1118. Available at: http://geology.gsapubs.org/cgi/doi/10.1130/G33522.1 [Accessed January 22, 2014].

Cheng, H. *et al.* The half-lives of uranium-234 and thorium-230. *Chem Geology* **169**, 17–33 (2000).

Chiodini, G. & Cioni, R., 1989. Gas geobarometry for hydrothermal systems and its application to some Italian geothermal areas. *Applied Geochemistry*, 4, pp.465–472.

Chiodini, G., Frondini, F. & Ponziani, F., 1995. Deep Structures and Carbon Dioxide Degassing in Central Italy. *Geothermics*, 24(1), pp.81–94.

Clark, T. R. *et al.* Spatial variability of initial 230Th/232Th in modern Porites from the inshore region of the Great Barrier Reef. *Geochimica et Cosmochimica Acta* **78**, 99–118 (2012).

Collins, A.S. & Robertson, A.H.F., 1999. Evolution of the Lycian Allochthon, western Turkey, as a north-facing Late Palaeozoic to Mesozoic rift and passive continental margin. *Geological Journal*, 34(1-2), pp.107–138. Available at: http://doi.wiley.com/10.1002/%28SICI%291099-1034%28199901/06%2934%3A1/2%3C107%3A%3AAID-GJ817%3E3.0.CO%3B2-L.

Costain, J.K. & Bollinger, G. a., 1991. Correlations between streamflow and intraplate seismicity in the central Virginia, U.S.A., seismic zone: evidence for possible climatic controls. *Tectonophysics*, 186(1-2), pp.193–214. Available at: http://linkinghub.elsevier.com/retrieve/pii/0040195191903937.

Costain, J.K., Bollinger, G.A. & Speer, J.A., 1987. Hydroseismicity — A hypothesis for the role of water in the generation of intraplate seismicity. *Geology*, 15, pp.618–621.

Duman, Y. T., O. Emre, S. Özalp, and H. Elmacı (2011), *1:250,000 Scale Active Fault Map Series of Turkey, Aydın (NJ36-11) Quadrangle. Serial Number 7*, Ankara, Turkey.

Emre, O., Y. T. Duman, and S. Özalp (2011), *1:250,000 Scale Active Fault Map Series of Turkey, Marmaris (NJ36-16) Quadrangle. Serial Number 8*, Ankara, Turkey.

Eken, M. et al., 2005. *Klimatoloji II*, Ankara: Turkish State Meteorological Service.

Essallami, L. et al., 2007. Hydrological changes in the Mediterranean Sea over the last 30,000 years. *Geochemistry, Geophysics, Geosystems*, 8(7), pp.1–11. Available at: http://doi.wiley.com/10.1029/2007GC001587 [Accessed October 2, 2014].

Faccenna, C. et al., 2008. Late Pleistocene depositional cycles of the Lapis Tiburtinus travertine (Tivoli, Central Italy): Possible influence of climate and fault activity. *Global and Planetary Change*, 63(4), pp.299–308. Available at: http://linkinghub.elsevier.com/retrieve/pii/S0921818108000696 [Accessed February 19, 2014].

Famin, V. et al., 2008. Earthquakes produce carbon dioxide in crustal faults. *Earth and Planetary Science Letters*, 265(3-4), pp.487–497. Available at: http://linkinghub.elsevier.com/retrieve/pii/S0012821X07006838 [Accessed July 18, 2014].

De Filippis, L. et al., 2012. Growth of fissure ridge travertines from geothermal springs of Denizli Basin, western Turkey. *Geological Society of America Bulletin*, 124(9-10), pp.1629–1645. Available at: http://gsabulletin.gsapubs.org/cgi/doi/10.1130/B30606.1 [Accessed November 28, 2012].

De Filippis, L. et al., 2013. Plateau versus fissure ridge travertines from Quaternary geothermal springs of Italy and Turkey: Interactions and feedbacks between fluid discharge, paleoclimate, and tectonics. *Earth-Science Reviews*, 123, pp.35–52. Available at: http://linkinghub.elsevier.com/retrieve/pii/S0012825213000706 [Accessed February 2, 2014].

Fleitmann, D. et al., 2009. Timing and climatic impact of Greenland interstadials recorded in stalagmites from northern Turkey. *Geophysical Research Letters*, 36(19), pp.1–5. Available at: http://www.agu.org/pubs/crossref/2009/2009GL040050.shtml [Accessed August 10, 2012].

Frisia, S.A., 2015. Microstratigraphic logging of calcite fabrics in speleothems as tool for palaeoclimate studies. *International Journal of Speleology*, 44(January), pp.1–16.

Frumkin, A., Bar-Yosef, O. & Schwarcz, H.P., 2011. Possible paleohydrologic and paleoclimatic effects on hominin migration and occupation of the Levantine Middle Paleolithic. *Journal of human evolution*, 60(4), pp.437–51. Available at: http://www.ncbi.nlm.nih.gov/pubmed/20541789 [Accessed January 12, 2015].

Frumkin, A., Ford, D.C. & Schwarcz, H.P., 2000. Palcoclimate and vegetation of the last glacial cysles in Jerusalem from a speleothem record. *Global Biogeochemical Cycles*, 14(3), pp.863–870.

Giggenbach, W.F., 1988. Geothermal solute equilibria. Derivation of Na-K-Mg-Ca geoindicators. *Geochimica et Cosmochimica Acta*, 52, pp.2749–2765.

González et al. 2012. The 2011 Lorca earthquake slip distribution controlled by groundwater crustal unloading *Nature Geoscience*, 5, pp. 821–825.

Grootes, P.M. & Stuiver, M., 1997. Oxygen 18/16 variability in Greenland snow and ice with 10 -3- to 105-year time resolution. *Journal of Geophysical Research*, 102(C12), pp.26,455–26,470.

Hainzl, S. et al., 2006. Evidence for rainfall-triggered earthquake activity. *Geophysical Research Letters*, 33(19), p.L19303. Available at: http://doi.wiley.com/10.1029/2006GL027642 [Accessed January 22, 2014].

Harrison, S.P., Yu, G. & Tarasov, P.E., 1996. Late Quaternary Lake-Level Record from Northern Eurasia. *Quaternary Research*, 159(45), pp.138–159.

Hellstrom, J. Rapid and accurate U / Th dating using parallel ion-counting multi- collector ICP-MS. *The Royal Society of Chemistry* **18**, 1346–1351 (2003).

Hickman, S., Sibson, R. & Bruhn, R., 1995. Introduction to special section: Mechanical involvement of fluids in faulting involvement of fluids in faulting. *Journal of Geophysical Research*, 100(B7), pp.12,831–12,840.

Hughes, P.D., Gibbard, P.L. & Ehlers, J., 2013. Timing of glaciation during the last glacial cycle: evaluating the concept of a global "Last Glacial Maximum" (LGM). *Earth-Science Reviews*, 125, pp.171–198. Available at: http://linkinghub.elsevier.com/retrieve/pii/S0012825213001190 [Accessed July 18, 2014].

Italiano, F., Martinelli, G. & Plescia, P., 2008. CO2 degassing over seismic areas: The role of mechanochemical production at the study case of central Apennines. *Pure and Applied Geophysics*, 165, pp.75–94.

Italiano, F., Martinelli, G. & Plescia, P., 2005. Mechanochemical Carbon Dioxide and Methane generation by laboratory simu lated fault friction conditions. In *8th International Conference on Gas Geochemistry*. Pale rmo & Milazzo, p. 34.

Kampman, N. et al., 2012. Pulses of carbon dioxide emissions from intracrustal faults following climatic warming. *Nature Geoscience*, 5, pp.352–358.

KOERI, 2015. Kandilli Observatory and Earthquake Research Institute of Turkey. Available at: http://www.koeri.boun.edu.tr/jeofizik/ [Accessed July, 2015]

Kutzbach, J.E. et al., 2014. Potential role of winter rainfall in explaining increased moisture in the Mediterranean and Middle East during periods of maximum orbitally-forced insolation seasonality. *Climate Dynamics*, 42(3-4), pp.1079–1095. Available at: http://link.springer.com/10.1007/s00382-013-1692-1 [Accessed June 1, 2015].

Kwiecien, O. et al., 2009. North Atlantic control on precipitation pattern in the eastern Mediterranean/Black Sea region during the last glacial. *Quaternary Research*, 71(3), pp.375–384. Available at: http://linkinghub.elsevier.com/retrieve/pii/S0033589408001555 [Accessed August 21, 2012].

Lisker, S. et al., 2010. Late Pleistocene palaeoclimatic and palaeoenvironmental reconstruction of the Dead Sea area (Israel), based on speleothems and cave stromatolites. *Quaternary Science*

Reviews, 29(9-10), pp.1201–1211. Available at: http://linkinghub.elsevier.com/retrieve/pii/S0277379110000302 [Accessed July 18, 2014].

Losh, S. & Haney, M., 2006. Episodic Fluid Flow in an Aseismic Overpressured Growth Fault , Northern Gulf of Mexico. In *Earthquakes: Radiated Energy and the Physics of Faulting*. American Geophysical Union, pp. 199–205.

Ma, K.-F. et al., 2012. Isotropic events observed with a borehole array in the Chelungpu fault zone, Taiwan. *Science*, 337(6093), pp.459–463. Available at: http://www.ncbi.nlm.nih.gov/pubmed/22837526 [Accessed November 18, 2012].

Mawer, C.K. & Williams, P.F., 1985. Crystalline rocks as possible paleoseismicity indicators. *Geology*, 13, pp.100–102.

Melchiorre, E.B., Criss, R.E. & Davisson, M.L., 1999. Relationship between seismicity and subsurface fluids, central Coast Ranges, California. *Journal of Geophysical Research*, 104(B1), p.921. Available at: http://doi.wiley.com/10.1029/1998JB900038.

Miller, S.A. et al., 2004. Aftershocks driven by a high-pressure CO2 source at depth. *Nature*, 427, pp.724–727.

Miller, S.A., 1996. Fluid-mediated influence of adjacent thrusting on the seismic cycle at Parkfield. *Nature*, 382, pp.799–802.

Miller, S.A., 2008. Note on rain-triggered earthquakes and their dependence on karst geology. *Geophysical Journal International*, 173(1), pp.334–338. Available at: http://gji.oxfordjournals.org/cgi/doi/10.1111/j.1365-246X.2008.03735.x [Accessed January 22, 2014].

Miller, S.A., 2013. The role of fluids on tectonic and earthquake processes. In R. Dmowska, ed. *Advances in Geophysics*. Cambridge, USA: Elsevier, pp. 1–47.

Minissale, A. et al., 2002. Geochemistry of Quaternary travertines in the region north of Rome (Italy): structural, hydrologic and paleoclimatic implications. *Earth and Planetary Science Letters*, 203(2), pp.709–728. Available at: http://linkinghub.elsevier.com/retrieve/pii/S0012821X02008750.

Morrison, J., 1994. Meteoric water-rock interaction in the lower plate of the Whipple Mountain metamorphic core complex , California. *Journal of Metamorphic Geology*, 12, pp.827–840.

Nyst, M. & Thatcher, W., 2004. New constraints on the active tectonic deformation of the Aegean. *Journal of Geophysical Research*, 109(B11), p.B11406.

Paola, N. De et al., 2011. Fault lubrication and earthquake propagation in thermally unstable rocks Fault lubrication and earthquake propagation in thermally unstable rocks. *Geology*, 39, pp.35–38.

Rice, J.R., 2006. Heating and weakening of faults during earthquake slip. *Journal of Geophysical Research*, 111, pp.1–29.

Richards, D. . & Dorale, J. a Uranium-series chronology and environmental applications of speleothems. Reviews in mineralogy and geochemistry. *Reviews in Mineralogy and Geochemistry* **52**, 407–460 (2003).

Rihs, S., Condomines, M. & Poidevin, J.-L., 2000. Long-term behaviour of continental hydrothermal systems: U-series study of hydrothermal carbonates from the French Massif Central (Allier Valley). *Geochimica et Cosmochimica Acta*, 64(18), pp.3189–3199.

Roeloffs, E., 2000. The Parkfield , California earthquake experiment : An update in 2000. *Current Science*, 79(9), pp.1226–1236.

Roff, G. *et al.* Palaeoecological evidence of a historical collapse of corals at Pelorus Island, inshore Great Barrier Reef , following European settlement. *Proceedings of The Royal Society - B Biological Sciencces* 280 (2013).

Rogie, D. et al., 2000. Flux measurements of nonvolcanic CO2 emission from some vents in central Italy. *Journal of Geophysical Research*, 105, pp.8435–8445.

Saar, M.O. & Manga, M., 2003. Seismicity induced by seasonal groundwater recharge at Mt. Hood, Oregon. *Earth and Planetary Science Letters*, 214(3-4), pp.605–618. Available at: http://linkinghub.elsevier.com/retrieve/pii/S0012821X03004187 [Accessed January 15, 2014].

Sarıkaya, M.A. et al., 2014. An early advance of glaciers on Mount Akdağ, SW Turkey, before the global Last Glacial Maximum; insights from cosmogenic nuclides and glacier modeling.

Quaternary Science Reviews, 88, pp.96–109. Available at: http://linkinghub.elsevier.com/retrieve/pii/S0277379114000298 [Accessed March 18, 2014].

Sarıkaya, M.A. et al., 2008. Cold and wet Last Glacial Maximum on Mount Sandıras, SW Turkey, inferred from cosmogenic dating and glacier modeling. *Quaternary Science Reviews*, 27(7-8), pp.769–780. Available at: http://linkinghub.elsevier.com/retrieve/pii/S027737910800005X [Accessed December 3, 2012].

Scholz, C.H., 2002. *The Mechanics of Earthquakes and Faulting* 2nd ed., Cambridge University Press.

Şenel, M. (2007), *Geology Map of Turkey, Marmaris Quadrangle. Serial Number 1*, Ankara, Turkey.

Şenkul, Ç. & Doğan, U., 2013. Vegetation and climate of Anatolia and adjacent regions during the Last Glacial period. *Quaternary International*, 302, pp.110–122. Available at: http://linkinghub.elsevier.com/retrieve/pii/S1040618212002649 [Accessed October 2, 2014].

Shulmeister, J. et al., 2004. The Southern Hemisphere westerlies in the Australasian sector over the last glacial cycle: a synthesis. *Quaternary International*, 118-119, pp.23–53. Available at: http://linkinghub.elsevier.com/retrieve/pii/S1040618203001290 [Accessed February 12, 2015].

Sibson, R.H., 1981. Fluid flow accompanying faulting: field evidence and models. In D. W. Simpson & P. G. Richards, eds. *Earthquake Prediction:An International Review*. Am. Geophys. Un. Maurice Ewing Series, pp. 593–603.

Svensson, A. et al., 2008. A 60,000 year Greenland stratigraphic ice core chronology. *Climate of the Past*, 4, pp.47–57.

Taylor, H.P., 1990. Oxygen and hydrogen isotope constraints on the deep circulation of surface waters into zones of hydrothermal metamorphism and melting. In *Geophysics Study Committee, The role of fluids in crustal processes*. Washington, D.C.: National Academy Press, pp. 72–95.

Di Toro, G. et al., 2011. Fault lubrication during earthquakes. *Nature*, 471(7339), pp.494–8. Available at: http://www.ncbi.nlm.nih.gov/pubmed/21430777 [Accessed November 11, 2012].

Türkeş, M. 1999. vulnerability of Turkey to desertification with respect to precipitation and aridity conditions. *Tr. J. of Engineering and Environmental Science*, 23, 363–380.

Türkeş, M. & Erlat, E., 2009. Winter mean temperature variability in Turkey associated with the North Atlantic Oscillation. *Meteorology and Atmospheric Physics*, 105(3-4), pp.211–225.

Ünal-İmer, E. et al., 2015. An 80 kyr-long continuous speleothem record from Dim Cave, SW Turkey with paleoclimatic implications for the Eastern Mediterranean. *Nature Scientific Reports* **5**, 13560; doi: 10.1038/srep13560.

Ünal-İmer, E. et al., 2014. A high-resolution geochronological and geochemical study on Aegean carbonate deposits, SW Turkey. In *Geophysical Research Abstracts*. Vienna, pp. 16 EGU2014–16265–2.

Uysal, I.T. et al., 2009. Hydrothermal CO2 degassing in seismically active zones during the late Quaternary. *Chemical Geology*, 265(3-4), pp.442–454.

Uysal, I.T. et al., 2011. Seismic cycles recorded in late Quaternary calcite veins: Geochronological, geochemical and microstructural evidence. *Earth and Planetary Science Letters*, 303(1-2), pp.84–96.

Ten Veen, J.H., Boulton, S.J. & Alçiçek, M.C., 2009. From palaeotectonics to neotectonics in the Neotethys realm: The importance of kinematic decoupling and inherited structural grain in SW Anatolia (Turkey). *Tectonophysics*, 473(1-2), pp.261–281. Ten Veen, J.H. & Kleinspehn, K.L., 2002. Geodynamics along an increasingly curved convergent plate margin: Late Miocene-Pleistocene Rhodes, Greece. *Tectonics*, 21(3), pp.8–1–8–21. Available at: http://doi.wiley.com/10.1029/2001TC001287.

Winograd, I.J. et al., 1992. Continuous 500,000-Year Climate Record from Vein Calcite in Devils Hole, Nevada. *Science*, 255-258, pp.255–260.

Zhao, J., Hu, K., Collerson, K. D. & Xu, H. Thermal ionization mass spectrometry U-series dating of a hominid site near Nanjing, China. *Geology* **29**, 27–30 (2001).

Zhou, H., Zhao, J., Qing, W., Feng, Y. & Tang, J. Speleothem-derived Asian summer monsoon variations in Central China, 54-46 ka. *Journal of Quaternary Science* **26**, 781–790 (2011).

PAPER 2

Having demonstrated that water availability is critical for vein formation, Paper 2 focuses mainly on how fluid chemistry of the vein calcites is affected through multi-cyclic deformation phases in shallower parts of active fault systems. Microscale U-series geochronology, microstructural and geochemical (C-O-Sr isotope and rare-earth element and yttrium (REY) analyses are used to determine the geochemical characteristics of the calcite veins.

CO_2 outburst cycles in relation to seismicity: constraints from microscale geochronology and geochemistry of late Quaternary vein carbonates, SW Turkey

Abstract

Vein and breccia carbonates precipitated in a highly fractured/faulted carbonate bedrock in SW Turkey were investigated through high-resolution U-series geochronology, microstructural and geochemical studies including C-O-Sr isotope and rare-earth element and yttrium (REY) analyses. Microscopic observations are interpreted as evidence that the calcite veins formed through crack-seal mechanism, mostly accompanied/initiated by intensive hydraulic fracturing of host limestone in response to high-pressure fluids, which is manifested by multi-stage breccia deposits. Microscale U-series dates (272.6–20.5 kyr) and geochemical compositions of the vein/breccia samples provide information on the timing and mechanism of the vein formation and identify the source of CO_2-bearing fluids responsible for the carbonate precipitation. $\delta^{18}O$ and $\delta^{13}C$ VPDB values of the calcite veins range between -5.9 and -1.7‰, and -10.6 and -4.6‰, respectively. The isotopic compositions of the veins show highly fluctuating values as calcite grew successively perpendicular to vein walls, which, in combination with microstructural and geochronological constraints, are interpreted to reflect episodic CO_2 degassing events. Oxygen and Sr isotope compositions ($\delta^{18}O$ VPDB: -5.9 to -1.7‰; $^{87}Sr/^{86}Sr$: 0.7082 to 0.7085) together with REY concentrations indicate deep infiltration of meteoric waters with various degrees of interactions with the host limestone and siliciclastic basement rocks. Carbon isotope compositions suggest CO_2 degassing through intensive limestone dissolution. While majority of the veins display similar Post-Archaean Australian Shale (PAAS)-normalized REY variations, some of the veins show positive Eu anomalies, which could be indicative of contribution from a deeply derived, heated, and reduced fluid component, giving rise to multiple fluid inventory for the calcite veins. Vein calcite formed in fault-induced fractures provide useful information on structural features, genetic characterization of the parental fluids, and late Quaternary degassing cycles of subsurface CO_2 accumulations.

Keywords: Calcite vein/breccia deposits, U-series dating, stable (O, C) isotopes, radiogenic Sr-isotope ratio, REY compositions, SW Turkey

1. Introduction

Continental extensional systems provide significant fluid pathways for large amounts of meteoric water and carbon dioxide (CO_2) to infiltrate through normal faults and fracture systems within the brittle upper crust (Taylor 1988). Investigating the long-term physicochemical behaviour of subsurface CO_2, together with factors that facilitate CO_2 accumulation and transport at crustal depths, are of great importance as CO_2, when degassed in large amounts, can trigger seismicity or intensive hydrothermal eruptions (Zoback & Gorelick 2012; Irwin & Barnes 1980; Wiprut & Zoback 2000; Uysal et al. 2009). In addition, enhancing our knowledge on subsurface CO_2 helps to assess the fate of geo-sequestered CO_2, since natural CO_2 accumulations provide a unique opportunity to examine crustal evolution of CO_2 and to investigate the geological factors controlling CO_2-leakage (e.g. Pearce 2006). Under favourable pressure and temperature conditions, CO_2 may exist as a supercritical fluid that has lower density and viscosity than groundwater and may allow plumes of CO_2 to migrate upwards toward the caprock and outwards away from the structural discontinuity. This buoyancy effect coupled with injection pressure may lead to the creation of new fractures or the opening of existing fractures, thus reducing the sealing capacity of the caprock (Tsang 2009).

Natural release of CO_2 commonly takes place in or around crustal damage zones and is commonly manifested as widespread travertine deposits, occurring either in fissure-filling and/or in breccia forms, as described elsewhere (Altunel & Hancock 1996; Hancock et al. 1999; Chiodini 2004; D'Alessandro et al. 2007; Kampman et al. 2012; Rihs et al. 2000; De Filippis et al. 2013; De Filippis et al. 2012). Carbonate deposition within hydrothermal environments occurs from ascending CO_2-rich groundwater that migrate through open channels under several geological and climatic conditions (Pentecost 2005). The location, water supply and influencing factors of travertine and vein calcite formations as well as their depositional cycles are usually controlled by active fault-related deformation nearby (e.g. Temiz et al. 2013; Ceron et al. 1998; Faccenna et al. 2008; De Filippis et al. 2013; Brogi et al. 2014). Accordingly, studies on the origin of CO_2 provides significant means for understanding vein growth mechanisms under various chemical conditions (e.g. pressure and temperature), have increased recently (e.g. Nuriel et al. 2011; Nuriel et al. 2012; Uysal et al. 2011; De Filippis et al. 2013), but need to be strengthened further by more precise and detailed datasets.

Turkey, along with some Mediterranean countries (e.g. Italy), is one of the most active tectonic regions on Earth due to its location between the actively-deforming Eurasian, Arabian, and African plates, and has experienced compressional and extensional tectonic regimes (Fig. 1) (Le Pichon &

Angelier 1979; Şengör & Yılmaz 1981). Western Turkey, in particular, is characterised by widespread horst/graben systems and associated large-scale fracture systems (Fig. 1a), which are regarded as major path ways for deeply-circulating hydrothermal fluids (Çakir 1999; Van Noten et al. 2013; Uysal et al. 2009). For instance, Hetzel et al. (2013) reported that the infiltration of meteoric waters through the low-angle detachment faults reached the upper levels of mylonitic rocks (at a depth of about 4–8 km) of the Menderes Massif in western Turkey. Previous studies of thermogene travertine deposits from the central Anatolian strike-slip and south western Anatolian extensional tectonic zones of Turkey have demonstrated the seismic nature of CO_2 degassing caused by over-pressurized fluids having long-trapped CO_2 volatile contents (Uysal et al., 2009, 2011).

The current research elaborates on earlier pilot studies and includes a large number of precisely dated (by U-series) calcite micro-samples at high resolution (0.5 to 1 mm). Age data are combined with trace element, Sr-isotope, and stable isotopes (O, C) analyses. These dataset allow us to constrain the periods of CO_2 degassing recurrences, possibly in association with local seismic activity, and to characterise the origin of CO_2-rich fluids.

2. Tectonic framework of the region

The Anatolian Plate, covering a large part of the mainland Turkey, is a rigid continental microplate bounded by the Eurasian Plate in the north and the Arabian Plate in the south (Fig.1a). At the present, large sections of this continental fragment are characterized by high levels of seismic activity as it is actively being translated towards the west along two transform structures, namely the North Anatolian and East Anatolian Fault Zones (Fig. 1a; McKenzie 1970; Şengör & Yılmaz 1981). The westward escape of the Anatolian Plate initiated in response to 1) the indentation of the Arabian plate into the Eurasian plate in the east and, 2) the slab roll-back and subsequent back-arc opening in the west to the north of the Aegean Subduction Zone since middle to late Miocene (Fig. 1a; McKenzie 1978).

The area encompassing the study location lies on the western margin of the Anatolian Plate (Figs. 1a and 1b), in a region commonly referred to as the Western Anatolian Extensional Province. Active lithospheric thinning and N–S-directed extension (at a rate of 30–40 mm/yr; McClusky et al. 2000) in this part of Turkey is commonly ascribed to the roll-back of the northward subducting Aegean slab since the late Miocene times (Royden 1993; van Hinsbergen 2010; Le Pichon & Angelier 1979).

The structural architecture of the Western Anatolian Extensional Province (i.e. Active Extension Zone in Fig.1a) is dominated by a series of roughly E–W- or WNW-trending graben systems (e.g. Büyük Menderes and Alaşehir (Gediz) Grabens; Fig. 1a). Extension is associated with normal faulting commonly accompanied by widespread sedimentary basin formation and young volcanic activity (Aldanmaz et al. 2000; Yilmaz et al. 2000; Purvis & Robertson 2004; Seyitoglu & Scott 1991).

SW Turkey has experienced a substantial translation and counterclockwise rotation within an active deformation regime in the Western Anatolian Extensional Province (McClusky et al. 2000). The NE–SW oriented Fethiye-Burdur Fault Zone comprises an important structural component bordering the so-called Isparta Angle (Barka et al. 1995) in the region (e.g. Verhaert et al. 2009). The Fethiye-Burdur Fault is interpreted as the seismically active continental continuation of the Pliny–Strabo Trench (ten Veen & Kleinspehn 2002) (Fig. 1a). Based on the fault plane solutions, earthquakes occurring in SW Turkey are associated with normal faulting (Eyidoğan et al. 1996; Barka et al. 1995). The sampling site for this study is located along the Aegean coastline, on the western flank of an east-facing embayment about 12 km south of the town of Marmaris (Fig. 1b). The basement geology of the region includes a stack of internally sliced and imbricated south-vergent thrust sheets collectively referred to as the Lycian Nappes, which were derived from the rifted passive margin of the northern NeoTethys Ocean (Collins & Robertson 1999). The overall tectonostratigraphy of the Lycian Nappes (Middle Triassic–Late Cretaceous) is complex but detailed studies conducted over the years has enabled coherent subdivision of different thrust slices (e.g. Bodrum nappe, Gülbahar nappe, and Marmaris ophiolith nappe of (Şenel 2007).

Cliffs that lie within and to the north of the sampling locations expose a succession of pillow lavas overlain and partly intercalated with pelagic limestones and radiolarian chert. This unit, which spans an interval of Late Triassic to Maastrichtian age, is regionally known as the Gülbahar Nappe (Fig. 1b; Poisson 1977); equivalent of the Köyceğiz Thrust Sheet of Collins & Robertson (1999) and the Turunç Nappe of Ersoy (1997). It has been partly overlain by Eocene to Recent terrigenous sedimentary rocks that postdate emplacement of the nappe. The investigated carbonate vein samples formed within the Bodrum and Gülbahar Nappes and are hosted by dolomite, recrystallized limestone, micritic limestone, and siliceous to sandy limestone.

Both the basement units and the younger sedimentary cover have been cut and disrupted by active normal faults (Figs. 1b–e and Fig. 2) many of which follow the regional E–W fabric. These include the bounding faults of the graben system that lie to the north of the Gulf of Gökova (Figs. 1b and c) near the study area (Fig. 1b; Görür et al. 1995) as well as the active structures of the Selimiye and

Taşlıca Fault Zones (Figs. 1d and e). Based on GPS velocity measurements; Barka & Reilinger (1997) reported a N–S-directed extension rate of 5 ± 5 mm/yr across the Gökova Graben. Overall N–S stretching rates across the Marmaris Peninsula, however, reach up to 14 ± 5 mm/yr as indicated by GPS velocity measurements (Reilinger et al. 1997). Latest (2013–2015) seismic events in Marmaris included around 106 primary earthquakes (Richter scale, Ml >2.0) with a majority of focal depths ~13.5 km (KOERI 2015). Most recently (July 2015), an earthquake storm started at 6.2 km depth with a magnitude of ~4 followed by 15 aftershocks with magnitude 3 and less (KOERI 2015).

3. Field and microstructural observations

Calcite vein/breccia samples were collected from the south of Marmaris in SW Turkey (Fig. 1b and Fig. 2). The sampling site covers two small-scaled extensional vein systems located close to the settlement of Turunç: Amos (in the North) and Kumlubük (~1.5 km south of Amos) (Fig. 2). Calcite veins in both systems fill extensional structures with dips averaging 70°-85° towards SE. Bi-directional rose diagrams plotted for joints and calcite-filled veins of the study area (Amos and Kumlubük-KB) reveal that there are two dominant orientations of ~N–S and ~E–W for the regions, respectively (Figs. 2a–d). This is in line with the regional active normal faults trending NW and EW (Figs.1a–e).

Calcite-filled veins within limestone outcrops display changes in colour from milky white, light grey, and yellow to brown (Fig. 3a and 3b). Based on the field observations, vein formations can be roughly classified into three groups; 1) wide 2) thin, and 3) non-systematically-filled (or brecciated) forms. While wide veins are generally 5–50 cm thick and a few tens of meters long, thin veins are a few- to 10-mm-thick and up to 1 meter long. The former group display distinct banding (crustiform) of several individual and parallel calcite veinlets with changing color tones (Fig .3a), which is indicative of a periodic alternation of organic content within the water supply due to meteoric diagenesis (Frisia et al. 2000). In contrast, thin veins show relatively weak banding structures with more massive fabrics. Such veins display white and greyish colours. Both type of vein formations trend in conformity with the regional fracture systems (Fig. 2). Vein formations also occur as a breccia matrix material within the host rock. This reveals that the mineral fillings are not only developed progressively (or systematically) in the region; but also formed as irregular products of hydraulic brecciation. Calcite veins that formed in brecciated carbonate host rock are found as separate individual fillings or as connected anastomosing forms (Fig. 3b).

The characteristics of vein textures depend on the nucleation of the filling material, the growth kinetics, the kinematics of vein opening (or dilation), and the host rock geometry (Blenkinsop

2000). Vein textures are defined mostly by elongated and open columnar calcite crystals (Frisia 2015), and occasionally by blocky calcite (Fig. 4a). Optical continuity can be seen for elongated columnar calcite formations along the entire vein (e.g. Fig. 4b). When the optical continuity terminates, another crystal elongation is found to be initiated. There is a thin iron staining occurring as secondary mineralisation between the boundaries of separate calcite bands as traces of terminated calcite formation (Fig. 3a; Fig. 4c). Specifically, elongated/open columnar calcites contain pervasive fluid inclusions. Most of the inclusions are aligned parallel to the wall-rock contact resulting in layering within calcite caused by bands of inclusions. The thicknesses of these inclusion bands range from 15 to 300 μm (Figs. 4b and 4c). Some of the inclusion bands trend parallel to calcite elongations and perpendicular to the boundary of wall rock, whereas some others develop oblique by smaller degrees (Figs. 4c and 4d). These are represented as inclusion trails giving information about the vein dilation vector and also vein growth direction during successive layering (Fig. 4d). Relative placements of the veins change occasionally within intensively jointed and/or fractured host limestone (Figs. 4a). Deposits of blocky or blocky-columnar calcite cements formed around angular pieces of host rock are interpreted to represent precipitation from fluids injected during or immediately following the initial brecciation event (Cox & Etheridge 1983).

4. Analytical methods

Samples of calcite veins were cut and polished in order to remove any weathered surfaces, and then cleaned ultrasonically. The polished slabs were then microdrilled from the bottom and top for preliminary investigation using 1-2 mm drill bits. Based on the initial U-series ages, a second set of calcite sub-samples was obtained by grinding and drilling (for powders) or by cutting (for chips) the veins at measured distances perpendicular to growth layering from the wall rock (sub-sample names/sample I.D. in Table 1 refer to the distance of the sub-sampled calcite band, in mm, from vein wall). In order to avoid contamination with host rock material, samples were taken at least 1 mm away from the vein walls. Resulting sub-samples were then used for trace element and C-O-Sr isotope analyses, as well as U-series dating.

U-series dating was carried out using a Nu Plasma multi-collector inductively-coupled plasma mass spectrometer (MC-ICP-MS) in the Radiogenic Isotope Facility (RIF) at School of Earth Sciences, The University of Queensland (UQ) following chemical treatment procedures and MC-ICP-MS analytical protocols described elsewhere (Zhao, Hu, et al. 2001; Clark et al. 2012; Roff et al. 2013; Clark et al. 2014). Powdered or chipped sub-samples weighing 20–200 mg were spiked with a mixed ^{229}Th-^{233}U tracer and then completely dissolved in concentrated HNO_3. After digestion, each sample was treated with H_2O_2 to decompose trace amounts of organic matters (if any) and to

facilitate complete sample-tracer homogenisation. U and Th were separated using conventional anion-exchange column chemistry using Bio-Rad AG 1-X8 resin. After stripping off the matrix from the column using double-distilled 7N HNO as eluent, 3 ml of a 2% HNO_3 solution mixed with trace amount of HF was used to elute both U and Th into a 3.5-ml pre-cleaned test tube, ready for MC-ICP-MS analyses, without the need for further drying down and re-mixing. U and Th can be collected together as the samples in this study contain relatively low levels (sub-ppm) of U. After column chemistry, the U-Th mixed solution was injected into the MC-ICP-MS through a DSN-100 desolvation nebuliser system with an uptake rate of around 0.12 ml per minute. U-Th isotopic ratio measurement was performed on the MC-ICP-MS using a detector configuration to allow simultaneous measurements of both U and Th isotopes (Zhou et al. 2011; Roff et al. 2013; Clark et al. 2014). The $^{230}Th/^{238}U$ and $^{234}U/^{238}U$ activity ratios of the samples were calculated using the decay constants given in (Cheng et al. 2000). The non-authigenic ^{230}Th was corrected using an assumed bulk-Earth atomic $^{230}Th/^{232}Th$ ratio of 4.4±2.2×10-6 which requires minimal $^{230}Th/U$-age-corrections to account for initial ^{230}Th in samples with $^{230}Th/^{232}Th$ activity ratios higher than 20 as typical of most samples in this study (Richards & Dorale 2003). U-series ages were calculated using the Isoplot/Ex 3.0 Program (Ludwig 2003).

Sr isotopic ratios were measured on a VG sector-54 thermal ionization mass spectrometer (TIMS) also in the RIF Laboratory at the School of Earth Sciences, University of Queensland (UQ). They were corrected for mass discrimination using $^{86}Sr/^{88}Sr$ ratio=0.1194. National Institute of Standards and Testing (NIST) SRM-987 Sr-isotope standard was used to monitor instrument drift and bias. Repeated analyses (no data outlier exclusion) of SRM-987 during January–May 2012 yielded an average $^{87}Sr/^{86}Sr$ value of 0.710222 ± 20 (2σ), which was used to calibrate against the laboratory's previous long-term mean, 0.710249 ± 28 (2σ) for all samples.

For trace element analysis, small aliquots (~2 mg) of carbonate samples were dissolved in a 2% nitric acid solution doped with a multi-element internal standard solution consisting of 12 ppb ^{6}Li, and 6 ppb ^{61}Ni, Rh, In, Re, Bi, and ^{235}U. The final diluted solutions (with typical dilutions by 2000–4000 times) were analysed on a Thermo X-series II ICP-MS equipped with an ESI FC4 autosampler, using the protocol modified after Eggins et al. (1997) and Kamber et al. (2003). The ICP-MS was run with conditions of 13 L/min cooling gas, 0.8 L/min auxiliary gas, 0.82–0.88 L/min neb gas, forward power of 1400W, peristaltic pump at 12 RPM, and a Nebulizer flow rate of 0.4ml/min. The USGS W-2 diabase rock standard and a known concentration profile (by laboratory) were used for calibration (Li et al. 2005). Other reference materials such as BIR-1 and BHVO-2 were also used for cross reference. The raw data were corrected for the low, but detectable blank, internal and external drifts, and for interference of oxides, doubly charged species, and

isobars. The results are reported in ppb with analytical errors of 10% at the1-sigma uncertainty level.

Carbonate C and O isotope analyses of carbonates were conducted in the Stable Isotope Geochemistry Laboratory at UQ. Pure calcite samples (3–4 mg, powdered) were analysed online using an Isoprime Dual Inlet Isotope Ratio Mass Spectrometer (DI-IRMS) with a multiprep device attached. Samples were reacted with orthophosphoric acid at 90°C for 1000 s. Stable isotope analytical results are reported in per mil (‰) values relative to VSMOW and VPDB for oxygen and VPDB for carbon with analytical uncertainties better than ± 0.2‰ (2σ) for both $\delta^{13}C$ and $\delta^{18}O$. The results were calibrated against NBS-19 and NBS-18, analysed as unknowns in addition to an internal standard.

5. Results

5.1. U-series geochronology

A total 86 powdered sub-samples obtained from 8 calcite veins (samples IDs: KB1a, KB1b, KB2a, KB2b and AMO1B, AMO-4-5, AMO-B, AMO-2-3) from the Kumlubük and Amos extensional vein systems (Fig. 2) were dated using the high-precision MC-ICP-MS U-series dating method. The U-series age data are shown in Table 1 (partly reported in Ünal-İmer et al. 2013; Ünal-İmer et al. 2014). The ages of the samples from Kumlubük range from 116.6 ± 3.2 to 20.55 ± 0.14 kyr, whereas those from Amos yielded an older age range between 273 ± 12 and 92.24 ± 0.53 kyr.

Two closely-spaced veins from Kumlubük (KB); KB1a (Fig.5a–e) and KB1b reveal deposition from 38 to ~21 kyr. This period extends to 44.4 ± 1.4 kyr (KB1a-BR) with the brecciated calcite ages including 26.78 ± 0.27 kyr (KB1b-BR1), and 29.42 ± 0.59 kyr (KB1b-BR2). From the wall contact to the other end of the vein within the unsealed fracture, vein KB1a (~35 mm; Figs. 5a and 5b) grew in 17 kyr and occasionally contains younger intrusions in agreement with thin section observations that demonstrate sharp boundaries and truncated textures between calcite bands (Fig.5b). Conversely, vein KB1b (~21 mm) shows relatively continuous growth during a shorter time period from ~30 to 27.6 kyr, which represents a single episode of growth (or a crack-seal event) as spatially continuation of vein KB1a. The other two vein samples investigated (KB2a and KB2b) represent earlier (older) stages of vein formations in Kumlubuk between 116.6 ± 3.2 kyr and 39.38 ± 0.98 kyr (Table S1). Excluding the breccia ages, vein KB2a deposited over a period of ~4.9 kyr (from 56.8 to 51.9 kyr) with an average growth rate of 4.9 mm/kyr, whereas closely-spaced vein KB2b formed within a shorter time frame of 19 kyr (58.56 ± 0.81 to 39.38 ± 0.98 kyr) and shows two distinct growth periods with different growth rates (4 to 25 mm and 25 to 31 mm). KB2b sub-

samples with distances of 4 to 31 mm from the wall (27 mm total) that grew over a 12.6 kyr period (52–39 kyr) yield a growth rate of 2.1 mm/kyr. Parallel veinlets formed during later-stage cracking and sealing represent fluid injections after the original vein growth. An older outlier age of 59.16 ± 0.67 kyr (at 10 mm distance to wall, S1) in KB2a suggests the presence of remnant older material mixed with younger calcite. We note that individual episodic rates for veins could be much faster with intervening depositional hiatuses.

Amos calcite vein samples (i.e. AMO-1B, AMO-4-5, AMO-B, and AMO-2-3) yielded U-series age distributions that were relatively consistent with their microstratigraphic sequence (e.g. AMO-1B in Fig. 6a–e), in contrast to Kumlubük veins that commonly showed age reversals. The only exception is sub-sample AMO-2-3/150, which exhibits a dramatic older age (143.2 kyr; Table S1) than the neighbouring sub-samples closest to the wall (Table S1). The average growth rates of Amos samples are relatively lower than those observed in Kumlubük samples. For instance, vein AMO-1B (Fig. 6a and 6b) has a growth rate of 0.16 mm/kyr, while AMO-B grew at a rate of 0.08 mm/kyr, estimated by the oldest and youngest ages for a given thickness of veins (Table S1). In addition, calcite veins at Amos are relatively narrow with the thicknesses varying from 30 mm (AMO-4-5) to 8.5 mm (AMO-B).

5.2. Stable/radiogenic isotope and trace element geochemistry

5.2.1. Stable isotope (Oxygen and Carbon) compositions

Nearly 240 sub-samples from eight calcite veins/breccia obtained by micro-drilling at spatial resolutions of 1–2 mm were analysed for their stable (O and C) isotope compositions. The results are shown in Table S2 and Figs. 5c and 6c (also in Figs. S1–S4). Stable isotope compositions of host-rock marine limestone (Mesozoic Lycian Nappe) has distinctly higher isotope ratios ($\delta^{18}O_{VPDB}$ = 2.15‰, $\delta^{13}C$ = 2.4‰, and $\delta^{18}O_{VSMOW}$ = 32.8‰; data from Uysal et al. 2011) compared to results from vein calcites (Table S2 and Fig. 7a–c). The $\delta^{18}O$ value of the host-rock is significantly altered relative to the primary isotopic compositions of middle Triassic-aged limestone and Lycian Nappes (Frisia-Bruni et al. 1989; Rosales et al. 2001; Muchez et al. 2008) (Fig. 7c). A distal (undeformed) limestone (Uysal et al. 2011) with $\delta^{18}O$: ~ -1.15 and $\delta^{13}C$: ~ 2.3‰ shows primary isotopic signatures, falling into the range of source rock (Lycian Nappe) areas (Fig. 7c). $\delta^{18}O$ and $\delta^{13}C$ values of calcite veins from Kumlubük and Amos demonstrate simple positive relationships (Figs. 7c). The average $\delta^{18}O_{VPDB}$ value for Kumlubük and Amos veins are -3.79±1.14‰ (n = 174), and -4.05±1.42‰ (n = 66), respectively. KB veins have slightly less depleted average of $\delta^{13}C$: -8.30‰, whereas AMO samples have lower average of $\delta^{13}C$: -9.66‰. Breccia samples of Kumlubük are generally isotopically heavier than the subsequent vein samples. While overall U-series ages

decrease as the vein growth continued, stable isotope values vary largely as separate rise and fall episodes (Figs. 5 and 6). For example, in sample KB1a, roughly 4 episodic growths can be observed based on the fluctuations in $\delta^{18}O$ and $\delta^{13}C$ (Fig. 5c). Likewise, sample AMO-1B shows around 3 cycles of growth with the fluctuations in $\delta^{18}O$ and $\delta^{13}C$ trends (Fig. 6c), where U-series ages decrease from 183 to 91.5 kyr towards open end of the vein.

5.2.2. Strontium (Sr) isotope compositions

Strontium isotope ratios ($^{87}Sr/^{86}Sr$) were measured for 55 calcite vein and breccia sub-samples from Kumlubük and Amos, and the analytical results are presented in Fig. 7d and Table S2 (with $\pm 2\sigma$ analytical error values). $^{87}Sr/^{86}Sr$ ratios of calcite vein/breccia show a range varying from 0.708245 ± 0.000013 to 0.708499 ± 0.000009. This range is significantly higher than the $^{87}Sr/^{86}Sr$ ratio of the Permian host limestone (0.708003 ± 0.000008; Uysal et al. 2011, Fig. 7d, Table S2) and lower than the modern seawater value of 0.7092 although it plots within the range of Cenozoic seawater between 0.7080 and 0.7090 roughly (Capo et al. 1998).

Although the analyses are not at the highest resolution, $^{87}Sr/^{86}Sr$ ratios of the vein KB1a and KB2a show overall declines from around 0.70844 (at 7.5 mm from wall) to 0.70831 (30 mm) in KB1a and from 0.7084 (7 mm) to 0.7083 (135 mm) in KB2a. In contrast, reverse and randomly distributed relationships are observed in samples KB2b and KB1b, with an increasing trend ($^{87}Sr/^{86}Sr$: 0.70823 to 0.70836; Table S2) in the former, and no correlation in the latter. Veins KB1a and KB1b define negative relationships between $\delta^{18}O$ and $^{87}Sr/^{86}Sr$ values with a R^2 value of 0.59 (Fig. 8a). Two breccia samples (KB1b-BR1 and -BR2; red plus signs in Fig. 8a) at the tail of the pattern show lower $^{87}Sr/^{86}Sr$ and higher $\delta^{18}O$ values, which are consistent with the host rock compositions. Analysed calcite vein samples from Amos yielded a relatively lower average $^{87}Sr/^{86}Sr$ value of 0.708322 compared to the average value 0.708366 from Kumlubük (Fig. 7c). $^{87}Sr/^{86}Sr$ of Amos samples range between 0.708245 ± 0.000013 (sample AMO-1B) and 0.708404 ± 0.000007 (sample AMO-B), with no relation to the distances across the veins. A weak correlation (R^2= 0.35) between $^{87}Sr/^{86}Sr$ and $\delta^{18}O$ for the vein AMO-1B (Fig. 8b) suggests host rock signatures towards the initial stages of precipitation with older ages (159. 8 and 165.3 kyr). Likewise, a significant reverse relationship (R^2=0.91, Fig. 8b) between $^{87}Sr/^{86}Sr$ and $\delta^{18}O$ ratios of vein AMO-4-5 indicates increasing $\delta^{18}O$ and decreasing $^{87}Sr/^{86}Sr$ towards older bands (165.9 kyr at 4 mm distance from the wall; Table S1).

5.2.3. Rare-earth element and Yttrium (REY) data

Rare-earth element (including Yttrium) contents of the 56 calcite veins/breccia samples are listed in Table S3. When plotted on a Post-Archaean Australian Shale (PAAS)-normalised (Taylor & McLennnan 1985) REY diagrams, all calcite samples exhibit negative Ce and positive Y anomalies (Figs. 9a–9i), similar to near-surface (and low temperature) carbonate and/or chemical sedimentary rocks derived from seawater (Bau et al. 1997; Bolhar et al. 2004). Analysed samples also display REY characteristics that are closely-linked with the host-rock limestone (Fig. 9e), suggesting significant genetic association. One breccia sample (KB1a-BR) shows almost the same REY pattern as the host rock (Fig. 9e). The host limestone is characterised by higher concentrations of normalised-REY compositions compared to other breccia samples (i.e. KB2a-BR1, -BR2, and -BR3; KB2b-BR1, and -BR2). The sub-samples of KB1a, -1b, KB2a, -2b, and AMO-4-5 have enrichments in heavy rare earth elements (HREE) (Figs. 9a–d and i). AMO-B and some of the sub-samples of KB1a and -1b show distinct positive Eu anomalies accompanied by relatively lower total REY values and Y/Ho ratios (e.g. Fig. 5d and 5e). Specifically, Eu_{PAAS} in samples AMO-B consistently have the highest concentrations relative to other REE elements (Figs. 9h). Similarly, veins KB1a and AMO-1B have enriched Eu values relative to neighbouring REE (Eu/Eu* >1.0; Figs. 5e-6e). Eu is relatively more enriched in the darker more organic section (~18 mm from wall; 23-24 kyr) of the KB1a Fig. 5a and 5e) and extremely high (>3.0) in the oldest (~183 kyr) section of AMO-1B, close (~7 mm) to the vein wall (Fig. 6e).

When $^{87}Sr/^{86}Sr$ ratios of samples KB1a and -1b are plotted together against their total REY (ppb) concentrations (Fig. 8c), a negative (exponential) relationship is observed (R^2 = 0.48). In contrast, they display a positive relationship between $\delta^{18}O$ and total REY values also with an R^2 value of 0.48 (Fig. 8d). When plotted against Sr-isotope and $\delta^{18}O$ ratios, Y/Ho element pair ratios of vein Kb1b exhibit significant negative relations (R^2= 0.59 and R^2= 0.93 in Figs. 8e and 8f, respectively). In contrast to samples KB1a and -1b, vein KB2b shows a positive relationship (R^2= 0.55) between Sr-isotope and total REY (Fig. 8g). The statistical correspondence between these two geochemical indicators becomes more significant (i.e. the correlation coefficients rise to 0.86 and 0.99) when the relationship is examined individually within two sub-groups (Figs. 8h and 8i). Sample KB2b also displays an opposite trend between Sr-isotope and Y/Ho ratio (Fig. 8j), where the breccia samples have no characteristic trend among other vein samples. Total REY data of sample AMO-1B exhibits a negative relationship with Y/Ho ratio (Figs. 6e and 8k, Table S3) and that of the sample AMO-4-5 reveals a negative relationship with Sr-isotope ratios (R^2:0.95, Fig. 8l). Similar to KB1a (Fig. 5) and KB1b, vein AMO-4-5 has a positive relation between $\delta^{18}O$ and total REY (Fig. 8m).

6. Discussion

6.1. CO_2 degassing cycles along the vein growths

Based on field and microscopic studies, progressive vein growth within distinctive episodes can be traced along the successively banded calcites, which are dominantly initiated by breccia formation (Figs. 3 and 4). Individual laminae/layer formations are interpreted to have formed by sealing of dilatant fractures immediately after a rupture event. Crystal fabrics of the veins and the presence of the inclusion trails (Fig. 4) suggest a crack-seal mechanism for the formation of successive veins (Ramsay 1980; Cox 1987). Corresponding episodic fluid injection and sealing pattern is also supported by clear individual bands with sharp contacts/crystal boundaries detected in several veins investigated (e.g. Fig. 4b). Widespread multi-stage breccia formations re-cemented with euhedral, blocky calcite (e.g. Fig. 4a and 4e) can be interpreted as being formed during the initial CO_2 degassing and associated fluid flow event. This may be due to the hydraulic and/or mechanical fracturing of the host rock, whereas later laminated veins may be due to continuing re-opening of the existing veins. Alternatively or additionally, the formation of the laminated veins may also be linked to aseismic steady-state deformation that occurs at slow strain rates and could also produce synchronous opening of extensional fractures and cementation (Blenkinsop & Sibson 1992). In other words, crack-seal textures of calcite (specifically in vein AMO-1B; Fig. 6) and formation of breccia could also reflect subcritical crack growth, a slow deformation process that does not require seismic ruptures (e.g. Violay et al. 2013). However, episodic and sometimes concurrent change in stable isotope ratio, and other geochemical traces such as REY and Eu* ratios over millennial timescales (e.g. KB1a; Fig. 5a–e) are thought to be an indication of episodic seismic activity controlling the opening of fractures and repeated fluid injections. Each pulse of these CO_2-bearing fluid injections is represented by micro-scale differences in geochemistry and microstructure (Figs. 5 & 6 and Figs. S1–S4), indicating possible physico-chemical modifications promoted by fluid-involved seismic activity in carbonates (Violay et al. 2013; Sulem and Famin 2009). As upwelling of deeply derived CO_2-bearing fluids continues and loses its intensity over time, mineral sealing processes within the fractured zones decline. Subsequently, another cycle of CO_2 accumulation will take place in reservoirs until the rupture of the seal rocks. The latter process occurs as a result of tectonic strain leading the brittle fracturing and/or fluid overpressures causing hydraulic fracturing. This cyclic behaviour of fluid migration (passively or forcefully) is commonly associated with syn-tectonic vein formation within or near fault zones as is the case in the current study area (c.f. Famin et al. 2005; Sibson et al. 1988; Boullier & Robert 1992; Cox 1995; Robert et al. 1995).

While the isotopic signatures could also be climatic, the patterns of isotopic change do not resemble the behaviour of known climatic events. The best candidate for our isotope signal is the roughly 1500 year climate cycle known as the Dansgaard-Oescher (D-O) cycle. The cause of this cycle is still uncertain with ideas focussing on either change in the northern ice sheets and/or in ocean circulation. They are represented by very rapid warming in Greenland to near interglacial conditions, over a matter of decades, followed by a gradual decline towards full glacial conditions and they are frequently followed by an extended period of stability. Our records differ in that we have three events between 16 and 22 kyr, whereas only a single D-O is recorded in ice cores (e.g. Grootes et al 1993). In addition, the abrupt phase in the D-O cycles is a warming, whereas if our oxygen isotopic signature is simplistically interpreted as a temperature change, the abrupt component would be a cooling. Furthermore, while the D-O cycles display an initial gradual cooling there is normally an abrupt transition back to glacial conditions. Our calcite isotope records display abrupt changes in only one direction. Possible driving forces for D-O cycles are a solar cycle at 1470 years and/or a lunar cycle at ~1800 years and more recent work has dismissed the likely solar forcing (Ramsdorf, 2003). A purely orbital signature without an oceanic, atmospheric or glacial feedback is not compatible with the abrupt changes seen in our record. In short, there is neither evidence for a significant climate forcing operating at the recurrence interval observed during the best defined period in our records, nor can we envision how likely drivers could yield the patterns observed. We conclude that a climatic control on the isotope signal is highly unlikely. However, the variations in $\delta^{18}O$ and $\delta^{13}C$ observed in vein profiles may also be related to different mechanisms such as changes in input from different fluid sources, temperature, CO2 sources as competing limestone dissolution and surface plant material. Nevertheless, the study area is one of the most seismically active regions on Earth, which is supported by multiple brecciation and fluid injection (younger vein fluid injections in older vein materials; Fig. 5c) events. Thus seismicity is preferable mechanism controlling the CO_2-degassing and hence vein generation, facilitating episodic fluid movements (see below).

Phase separation (via volatile - CO_2 loss) of the fluid consisting of a H_2O-CO_2 mixture is interpreted as governed by rapid fluid pressure fluctuations. Accordingly, isotopic exchange via near-surface isotopic equilibrium between CO_2 and H_2O is affected by CO_2 degassing events (Bergfeld et al. 2012; Cartwright et al. 2002; Pauwels et al. 1997; Vuataz and Goff, 1986). Miscibility gap and related isotopic fractionation within an open H_2O-CO_2 system at ambient temperatures are subject to changes in response to varying fluid pressure, pH, and temperature (Bowers 1991). When upwelling CO_2 gas is absorbed into the shallow cold groundwater, isotopic equilibrium is reached via subsequent loss of CO_2, which concurrently enriches CO_2 gas and depletes water in ^{18}O

(Bergfeld et al. 2012; Cartwright et al. 2002). This is supported by an increased degree of $\delta^{18}O$-$\delta^{13}C$ kinetic fractionation as temperature decreases (Friedman and O'Neil, 1977), and is represented by the younger bands of vein KB1 showing almost the same variations in $\delta^{18}O$ and $\delta^{13}C$ (Fig. 5c). Successive build-up and drop of the fluid pressure and precipitation of calcite veins is demonstrated by high-resolution $\delta^{18}O$ and $\delta^{13}C$ shifts through the veins (Figs. 5c–6c). The C-O isotopic variations suggest that fluid becomes episodically enriched and depleted in CO_2 (i.e. CO_2-rich and -poor phases; Fig. 5c and 6c), revealing an episodic fluid movement that may be attributed to the active tectonism of the region (e.g. Pili et al. 2002). Consequently, low temperature deviations in $^{18}O/^{16}O$ ratio or $\delta^{18}O$ values of the veins are interpreted to have been controlled by fluid immiscibility as a function of (CO_2 gas) pressure drop (Bergfeld et al. 2012). Hence, each pressure step associated with seismicity recurrences could affect preferential ^{18}O partition into water and vapour CO_2, whereby ^{18}O is preferentially incorporated into vapour CO_2 (Bottinga 1968).

The initiation time for the vein formation dates back to 117 kyr when multi-stage brecciation in KB2a (117–63 kyr) occurred. The vein growth continued from 59–39 kyr in KB2a-b and 38–20 kyr in KB1a-b. We argue that the vein growth represents an accumulation of episodic single events as we observe sharp contact between veinlets (Fig. 4) and the injection of younger veinlets into the older ones (Fig. 5c and Fig. 3 cf. Uysal et al. 2011). While initial veinlets in KB1a and KB1b precipitated from CO_2-rich fluids, samples KB2a and KB2b are interpreted to have been deposited from waters with relatively low CO_2 following significant CO_2 degassing at the initial stages of the vein growths (Figs. 5d and S1 and S3). Similarly, the Amos system (272–92 kyr) represents vein growth from water with both higher and lower dissolved CO_2. For example, sample AMO-2-3 demonstrates precipitation from initial fluid with higher CO_2, whereas the opposite relation is observed for other Amos samples (Figs. S2 and S4). Fluid with elevated initial CO_2 values such as AMO-2-3 may indicate seismically induced de-pressurisation of fluids immediately after and/or during the major rupture events (Figs. S2 and S4). Later calcite bands likely represent the water with lower CO_2 gas and/or volatile content after brecciation events (Figs. 8a, b).

6.2. Source and evolution of CO_2-bearing fluids

The extension veins hosted by Lycian Nappe limestones in the study area are previously interpreted to have originated from meteoric water (cf. Uysal et al. 2011). Oxygen and carbon isotope compositions of the carbonates vary widely between the Kumlubük and Amos systems. Large variations indicate major isotopic fractionation and heterogeneity within these two systems. Long-term (1960–2014) average, maximum, and minimum annual temperatures of Muğla region are 15, 21, and 10ºC, respectively (TSMS, 2015) and they would be ~6 degrees colder for whole last glacial

period as 9, 15, 4 ºC, respectively (Hughes et al. 2013; Sarikaya et al., 2014). Based on calcite-water fractionation equation of Coplen et al. (2007) and assumed temperatures during the last glacial period, calcite veins/breccia of Kumlubük are calculated to precipitate from waters having average $\delta^{18}O$ value of -6.3‰, within the range of -5.0 to -7.4‰ SMOW. Additionally, calcite veins of Amos are found to have precipitated from waters with an average $\delta^{18}O$ value of -6.5‰, within the range of -5.2 to -7.7‰ SMOW, when minimum and maximum temperature values are considered. These $\delta^{18}O$-water ranges fall in the corrected $\delta^{18}O$-water range (-8.5 to -4.5‰ SMOW) from Dim Cave in SW Turkey (Ünal-İmer et al., 2015). The temperature range: 15–4 ºC of the calcite deposition reflects typical near-surface meteoric conditions for the carbonate depositions given the glaciation conditions (Sarikaya et al. 2014; Pentecost 2005). Shallow meteoric water conditions can be supported by significant depletion in ^{13}C compared to the host and distal limestones (Fig. 7c), reflecting intensive interaction with soil-derived CO_2 and/or H_2O-CO_2 mixed fluids such as meteoric water percolating between fault-related fractures dissolving the host limestone (Nuriel et al. 2012). In addition, active faulting in the region could result in significant production (release) of CO_2 from limestones (Famin et al. 2008), which in turn causes further isotopic exchange between H_2O and CO_2 at elevated temperatures. Also a microthermometric study (Verhaert et al. 2004) from Burdur (a close region to the study area) suggests that the Quaternary meteoric water-sourced calcite veins of a normal fault setting (SW Turkey) precipitated at 187°–42°C, which is significantly higher than the temperature range estimated in current study (~15–4°C).

Based on the average carbon isotopic compositions of the veins ($\delta^{13}C$: -8.3 and -9.7‰ VPDB), carbon isotopes can be interpreted to have originated from multiple sources: dominantly dissolving host-rock limestone with possible contributions from atmospheric and C_3-type Mediterranean soil-derived CO_2 near-surface (Rollinson 1993; Baker et al. 1997; Bar-Matthews et al. 2003). In fact, without the values of mostly rock-buffered breccia calcite, vein-filling calcite is deduced to have an important contribution from an organic source (e.g. methanogens; Mattey et al. 2013) owing to the low $\delta^{13}C$ values (-10.6 to -6.1‰ VPDB) (Salomons et al. 1978), which is very similar to the $\delta^{13}C$ values of extension veins in a nearby area (-10.4 to -3.0‰; Burdur, SW Turkey; Verhaert et a. 2004), and to the $\delta^{13}C$ values of a previous study from the same location (-10.2 to -6.9‰; Uysal et al. 2011). Changing contamination of organic source (via local variations in hydrological changes) could also be reflected by the vein $\delta^{13}C$.

PAAS-normalised REY diagrams (Fig. 9) of all vein and breccia samples reveal a seawater (marine) signature characterised by distinct negative (oxidising) Ce and positive Y anomalies together with elevated (HREE) concentrations (Bau et al. 1997), similar to the host-rock limestone

(Uysal et al. 2011). REY patterns indicate no significant fractionation (or deviations) among individual calcite veins inferred from generally well-preserved Ce- and Y-anomalies along the growth axis. Significant fluid-rock interaction between host-rock limestone and precipitating CO_2-bearing meteoric waters is evidenced by host-rock-like REY behaviours of the veins. This is also consistent with Y/Ho values of the veins ranging around 30–45 at the initial growth stages (Figs. 5e, 6e, 8e, 8f, and 8k;Table S3) reflecting host limestone signatures (Bau & Dulski 1996).

Sr isotope ratios ($^{87}Sr/^{86}Sr$) averaging around 0.70835 of all vein/breccia samples are higher than the Mesozoic host limestone (0.70800, Fig. 7c, Table S2). This indicates the involvement of radiogenic external components in the CO_2-bearing fluids, possibly derived from Rb-rich siliciclastic (or non-carbonate) rocks in the basement, which is represented by carbonaceous meta-pelitic rocks in the study area (i.e. the Menderes Massif; Okay 1989). The interaction of deeply infiltrated meteoric water with metamorphic basement rocks is likely to have occurred at temperatures >200 °C under reducing conditions as inferred from positive Eu anomalies (distinct Eu^{+2} segregation relative to neighbouring elements; i.e. Sm^{+3} and Gd^{+3}) in Fig. 9 (Bau et al. 2010). Increasing input from heated meteoric fluids can dissolve more limestone giving rise to the elevated production and accumulation of CO_2, and hence fluid over-pressurisation, which leads to multi-stage brecciation, possibly immediately after seismically-induced pressure release. This is particularly demonstrated by sample KB1a-b and the Amos samples (positive Eu anomalies in Fig. 9). With progressive vein growth, Y/Ho moves towards higher values than those of the breccia (e.g. Fig. 8e-f), which may indicate the transition from a largely host rock-buffered fluid system to a fluid-rich zone where Y and Ho are fractionated due to some external fluid contributions (cf. Bau and Dulski 1996). This is similar to the fractionation between Y and Ho within fluid-rich systems that involve large degrees of aqueous components (Loges et al. 2013).

7. Summary and Conclusions

Fault-related extension vein and breccia carbonates from two different fracture systems (Kumlubük and Amos) in SW Turkey were investigated through a detailed study combining high-resolution geochemistry (rare-earth and yttrium concentrations as well as C, O, and Sr-isotope compositions) and geochronology (U-series dating). Geochronological data indicate that vein formation in the study area occurred between ~273 and 20.5 kyr. Based mainly on petrographic observations and U-series ages, vein formation is interpreted to be controlled by a crack-seal mechanism, commonly initiated by intense multi-stage fracturing of the host-rock limestone (brecciation – main rupture), and associated with the fault activity in the region. Local normal faulting trending NNW-SSE and E-W in Kumlubük and Amos respectively appears to govern the main stress distributions of the

extension veins, in agreement with the regional deformation regime. It is interpreted that calcite precipitating CO_2-bearing fluids were dominated by near-surface meteoric water within zones of structural weaknesses, while CO_2 is sourced mainly from the dissolution of the host limestone. Stable isotope records (O, C) of the veins reveal the episodic nature of CO_2-degassing events and meteoric water infiltrations through normal faults affecting multiple growth-cycles of the veins, all of which are ultimately controlled by regional seismic activity (including inter-seismic periods). Increasing accumulation of CO_2 within brittle upper crust can result in significant fluid overpressures, which in turn is thought to have led to initial fracturing (or crack opening) and multi-episodic brecciation in the region. While the interaction of meteoric waters with the host limestone mainly controlled the trace element and isotope geochemistry of the veins at initial growth stages; elevated Sr-isotope and noticeably positive Eu anomalies imply minor contributions of fluid that interacted with basement rocks at higher temperatures. We propose that calcite veins precipitated initially from deep CO_2-rich fluids during a mainshock, with a subsequent deposition from less CO_2-bearing fluid following the main-shock events. Overall, calcite precipitations have the potential to provide strong insights into the geochemical and isotopic characteristics (e.g. pressure and temperature variations) and genesis of the parental fluids.

8. Acknowledgements

This research was funded by the Queensland Geothermal Energy Centre of Excellence (QGECE), with some support by the School of Geography, Planning, and Environmental Management through E. Ü.İ.'s PhD project fund. We thank A.D. Nguyen, Wei Zhou, and Kim Baublys for the laboratory assistance. E.Ü.İ particularly acknowledges strong support and personal encouragement given by Hal Gürgenci (Director of QGECE), as well as the support of a University of Queensland post-graduate award. J.-X.Z. and Y.-X.F. acknowledge the support of an Australian Research Council LIEF grant (LE0989067) for U-series dating.

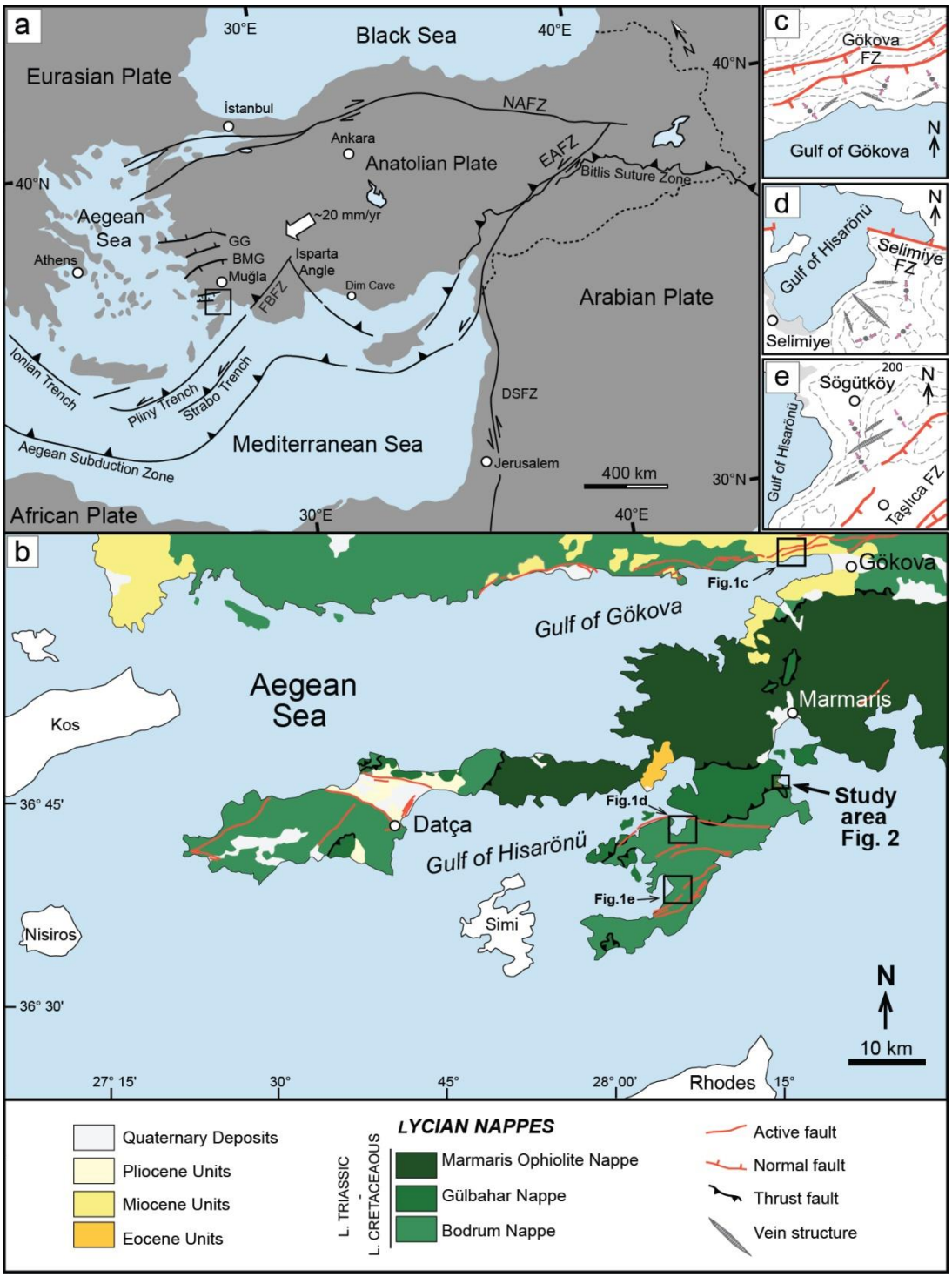

Figure 1 (a) Simplified regional structural map of the Eastern Mediterranean region (modified from Uysal et al. 2011 and references therein). **(b)** Simplified geological map of the study area with active faults (modified from Şenel 2007; Duman et al. 2011; Emre et al. 2011). **(c, d, and e)** Maps showing active normal faults (bar and ball on downthrown side) and structural positions of veins (lens-shaped symbols). Short (pink) arrows show minimum (σ_3) principal stresses for the vein opening. Dark grey dashed lines are the elevations in meters. NAFZ: North Anatolian Fault Zone, EAFZ: East Anatolian Fault Zone, DSFZ: Dead Sea Fault Zone, GG: Gediz (Alaşehir) Graben, and BMG: Büyük Menderes Graben. FBFZ: Fethiye Burdur Fault Zone.

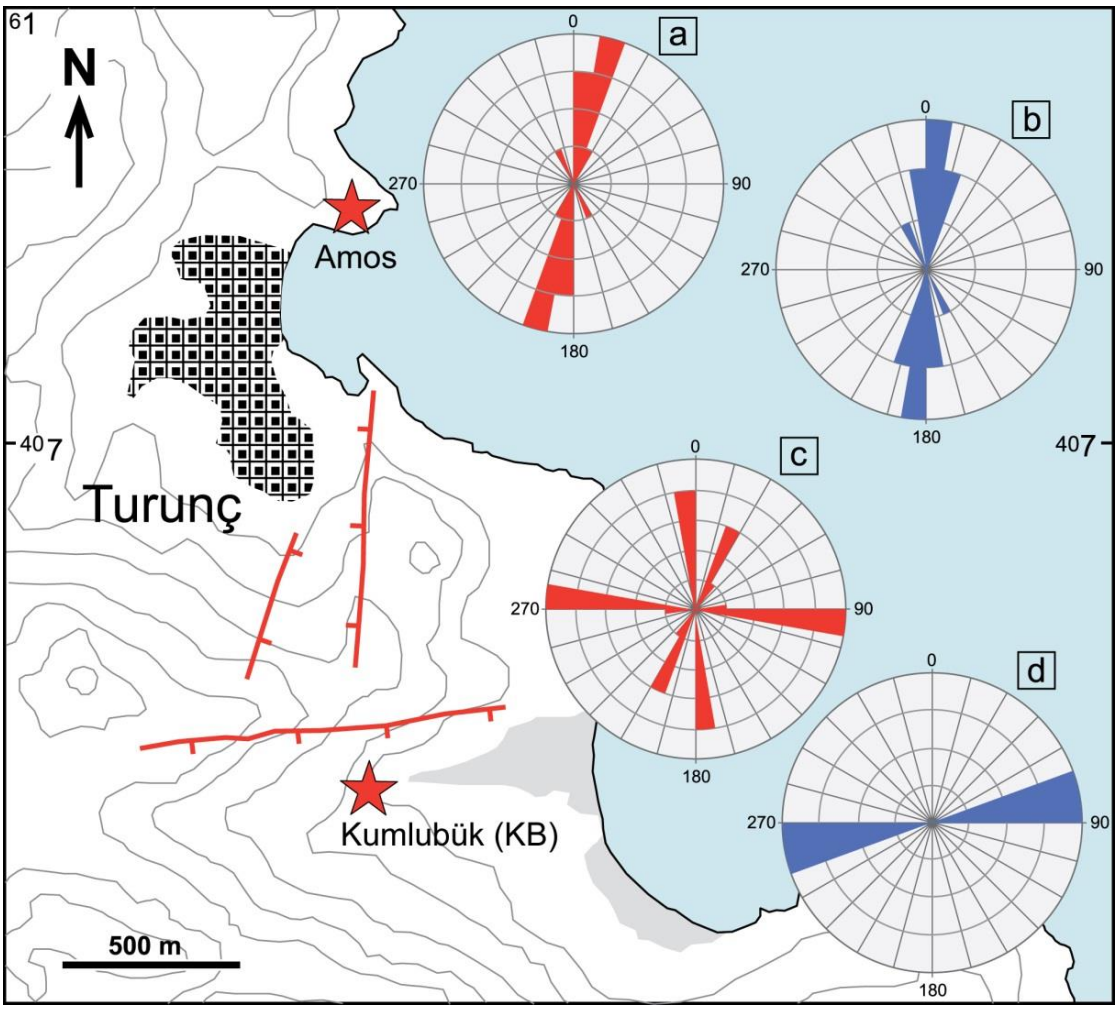

Figure 2 Close-up structural map of the study area (Amos and Kumlubük vein systems). **(a)** and **(b)** show the rose diagrams of joints (red) and calcite veins (blue) in Amos; **(c)** and **(d)** are the rose diagrams representing joints (red) and calcite veins (blue) of the Kumlubük system. Active normal faults are represented by red lines as on the main map in Figure 1. Note that both joints and calcite-filled veins are conformable with regional tectonic activity including ~N–S and ~E–W trending normal faults in the region.

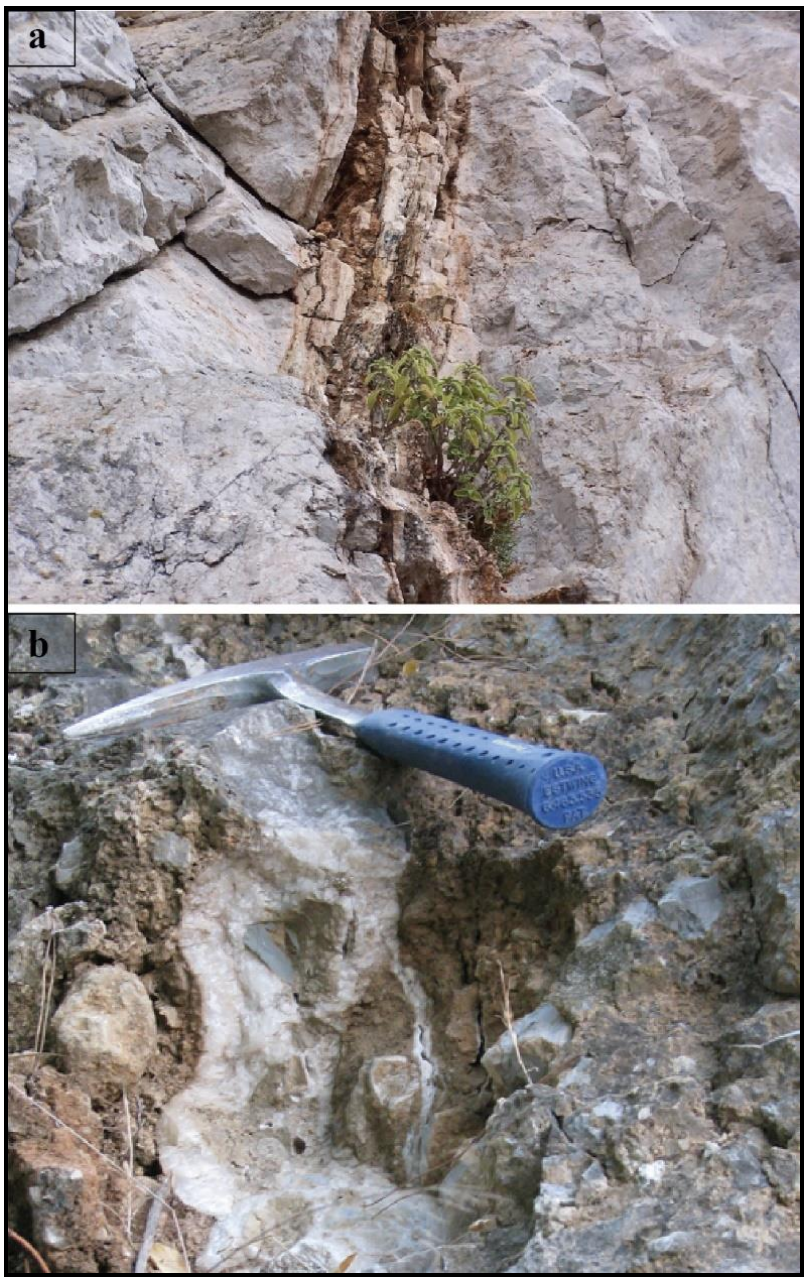

Figure 3 Outcrop photographs of extensional veins associated with active normal faults in the study area. **(a)** Close-up view of wide, coloured and banded calcite veins cutting the limestone. **(b)** Close-up view of a cemented breccia and calcite vein showing anastomosing structure.

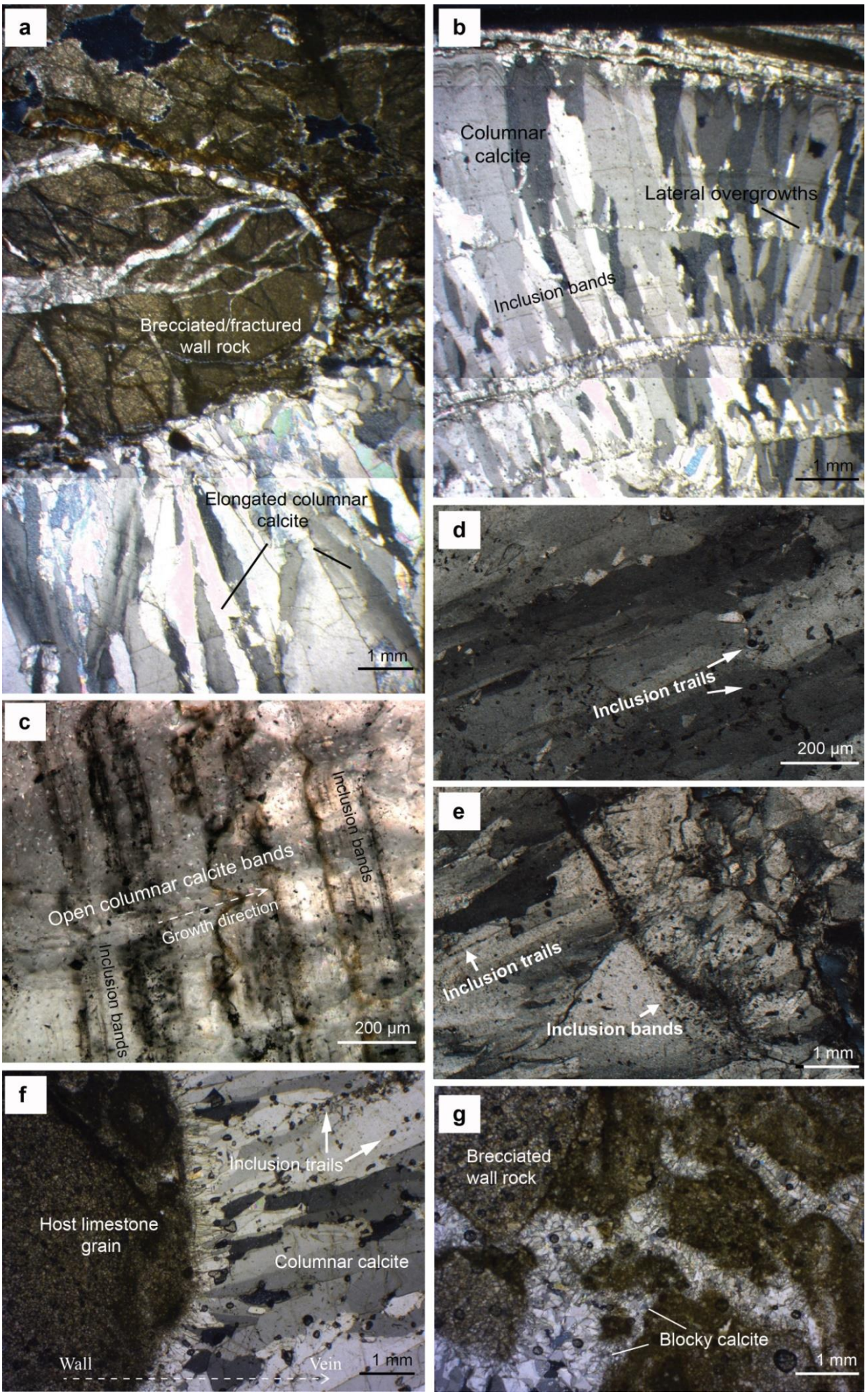
a
Brecciated/fractured
wall rock
Elongated columnar
calcite
1 mm
b
Columnar
calcite
Lateral overgrowths
Inclusion bands
1 mm
c
Open columnar calcite bands
Growth direction
Inclusion bands
Inclusion bands
200 µm
d
Inclusion trails
200 µm
e
Inclusion trails
Inclusion bands
1 mm
f
Inclusion trails
Host limestone
grain
Columnar calcite
Wall
Vein
1 mm
g
Brecciated
wall rock
Blocky calcite
1 mm

Figure 4 (above) Photomicrographs showing banded calcite vein and breccia samples under plane- and cross-polarised light. **(a)** View of calcites with elongated columnar and blocky forms. Note that some blocky calcites are adjacent to brecciated host rock at top of left of photo, CPL, **(b)** inclusion bands are arranged perpendicular to displacement direction and continue along calcite bands, CPL. Note that spacing of inclusion bands is 15-200 µm. **(c)** Calcite bands show sharp, truncated contacts between sealing hiatuses and small assemblages of inclusion bands and trails, PPL, **(d)** close-up view of sample KB1b showing inclusion trails formed perpendicular and oblique to the growth direction during sealing hiatus, indicated by truncated, zig-zag shaped contacts, CPL, **(e)** Inclusion trails and bands formed in the sample AMO-1B, **(f)** Lateral overgrowths along the host limestone grain and typical columnar calcite (sample AMO-1B), and **(g)** brecciated wall rock, impregnated by blocky calcite (PPL=Plane-polarized light; CPL=Cross-polarized light).

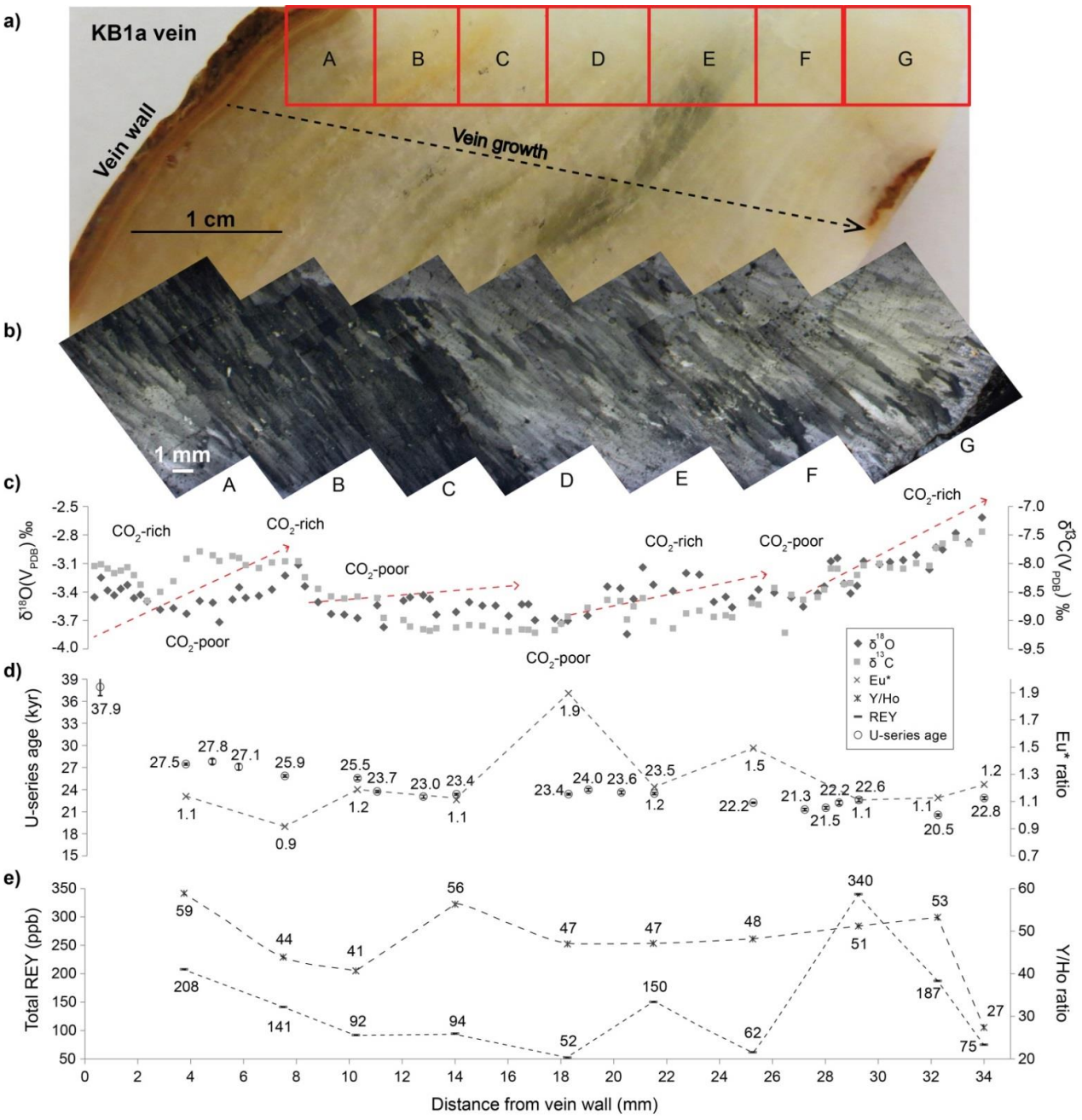

Figure 5 Polished slice of vein KB1a (a) against its microstratigraphy (CPL) (b). $\delta^{18}O$ and $\delta^{13}C$ isotope ratio values of the veins against their growth/depth are shown in (c). (d) corresponds to the composite plot of U-series ages (in numbers; kyr) and Eu* ratios against depth, while (e) shows the change in total REY values and Y/Ho ratios against depth of the veins. Note that red dashed arrows are indicative of growth periods. Capital letters in panel (b) represent the red areas in (a). CPL=Cross-polarized light.

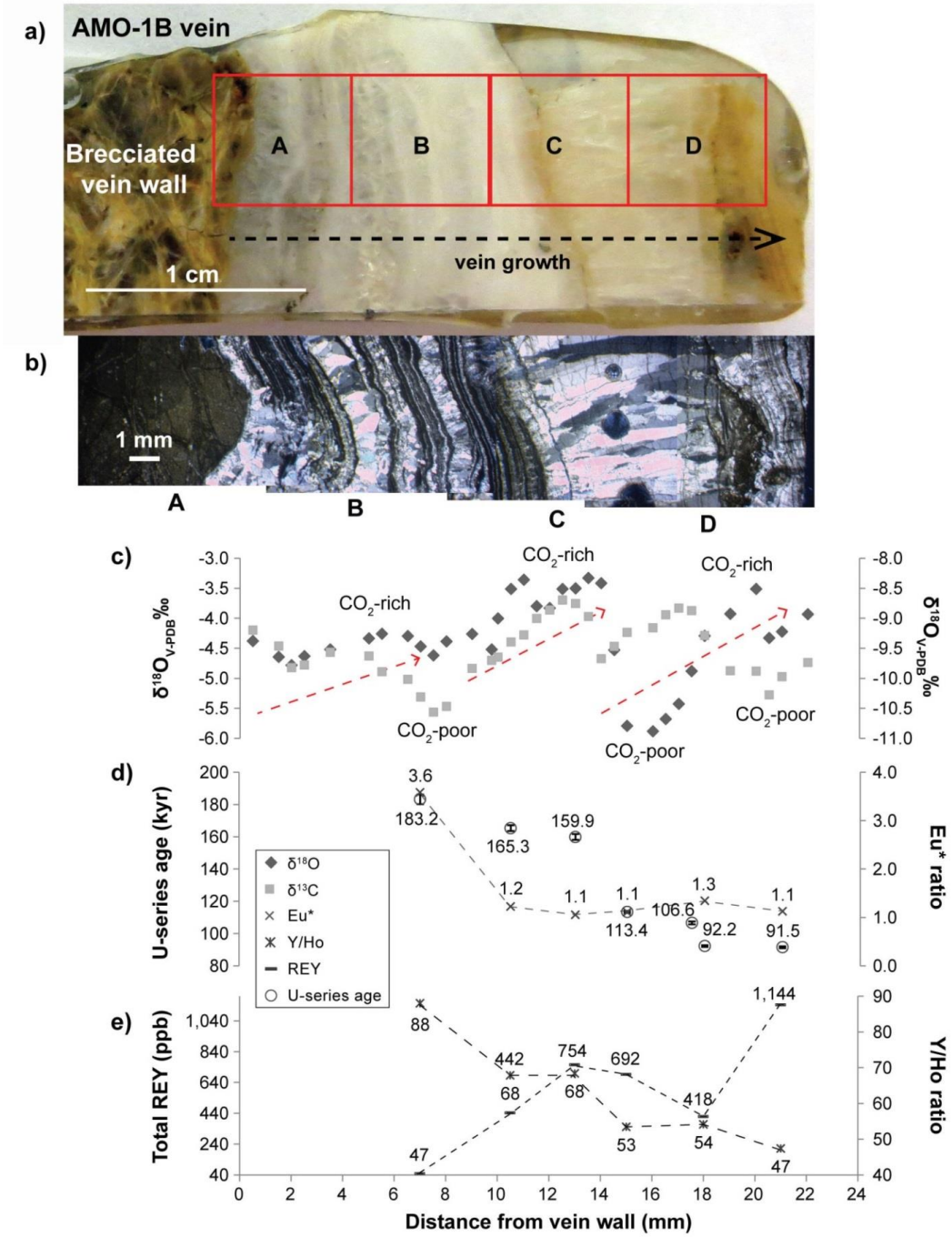

Figure 6 Polished slice of vein AMO-1B **(a)** against its microstratigraphy (CPL) **(b)**. **(c)** show $\delta^{18}O$ and $\delta^{13}C$ values against vein growth/depth (mm). **(d)** corresponds to the composite plot of U-series ages (in numbers; kyr) and Eu* ratios against depth, while **(e)** shows change in total REY values and Y/Ho ratios agains depth. Note that red dashed arrows are indicative of rough growth periods. Capital letters in panel **(b)** represent the red areas in **(a)**. CPL=Cross-polarized light.

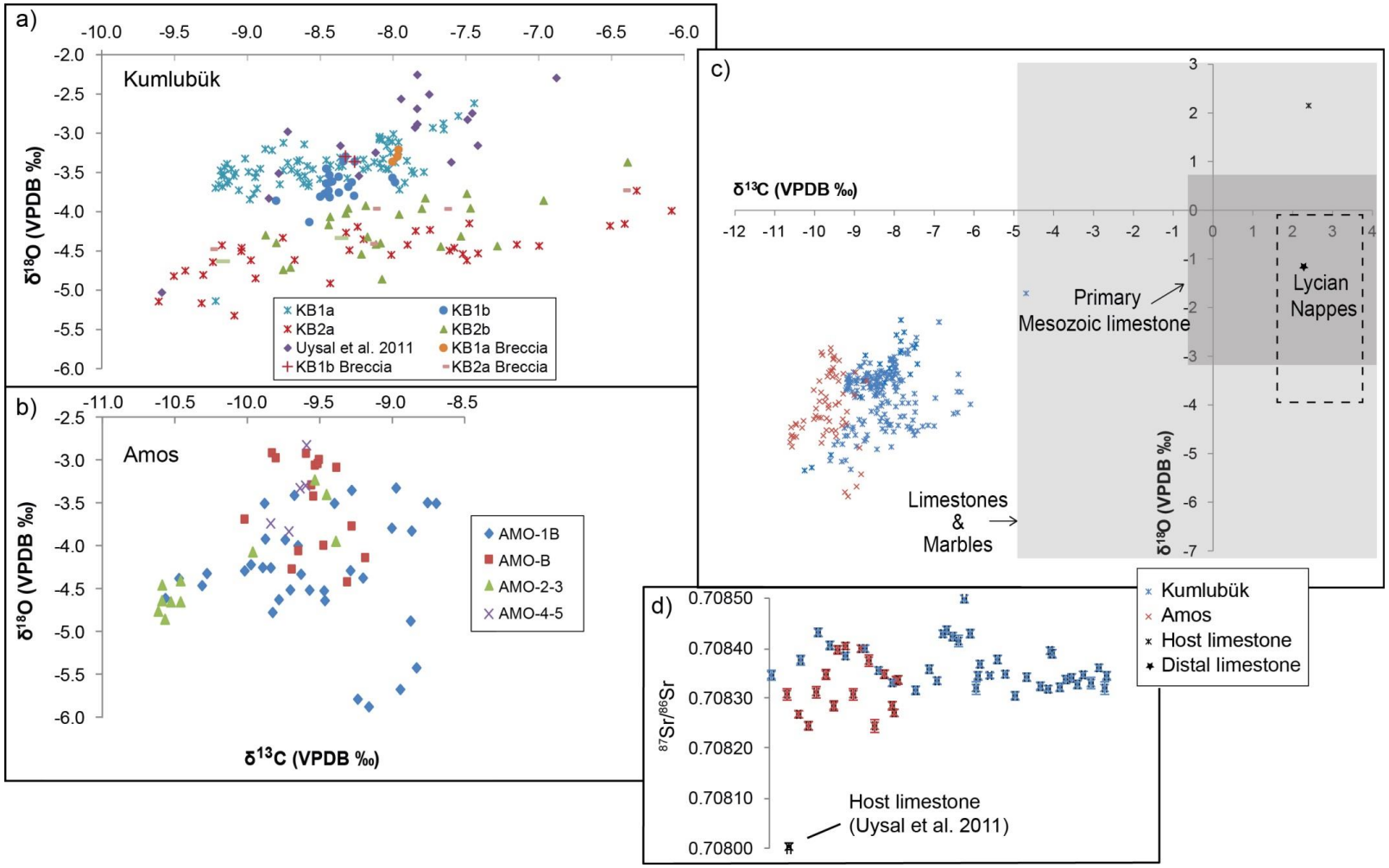

Figure 7 Stable isotope ($\delta^{18}O$ and $\delta^{13}C$ ‰, VPDB) plots of calcite vein/breccia samples from **(a)** Kumlubük and **(b)** Amos areas. $\delta^{18}O$ and $\delta^{13}C$ values of the calcite veins are compared with host and distal limestone (Uysal et al. 2011), Lycian Nappe (Muchez et al. 2008), primary Mesozoic limestone (Frisia-Bruni et al. 1989; Rosales et al. 2001), and limestone and marble areas (Rollinson 1993) **(c)**. $^{87}Sr/^{86}Sr$ isotope ratios of the calcite veins/breccia and the host limestone are shown in **(d)**. Note that there is a positive relationship between $\delta^{18}O$ and $\delta^{13}C$ values for most Kumlubük and Amos samples.

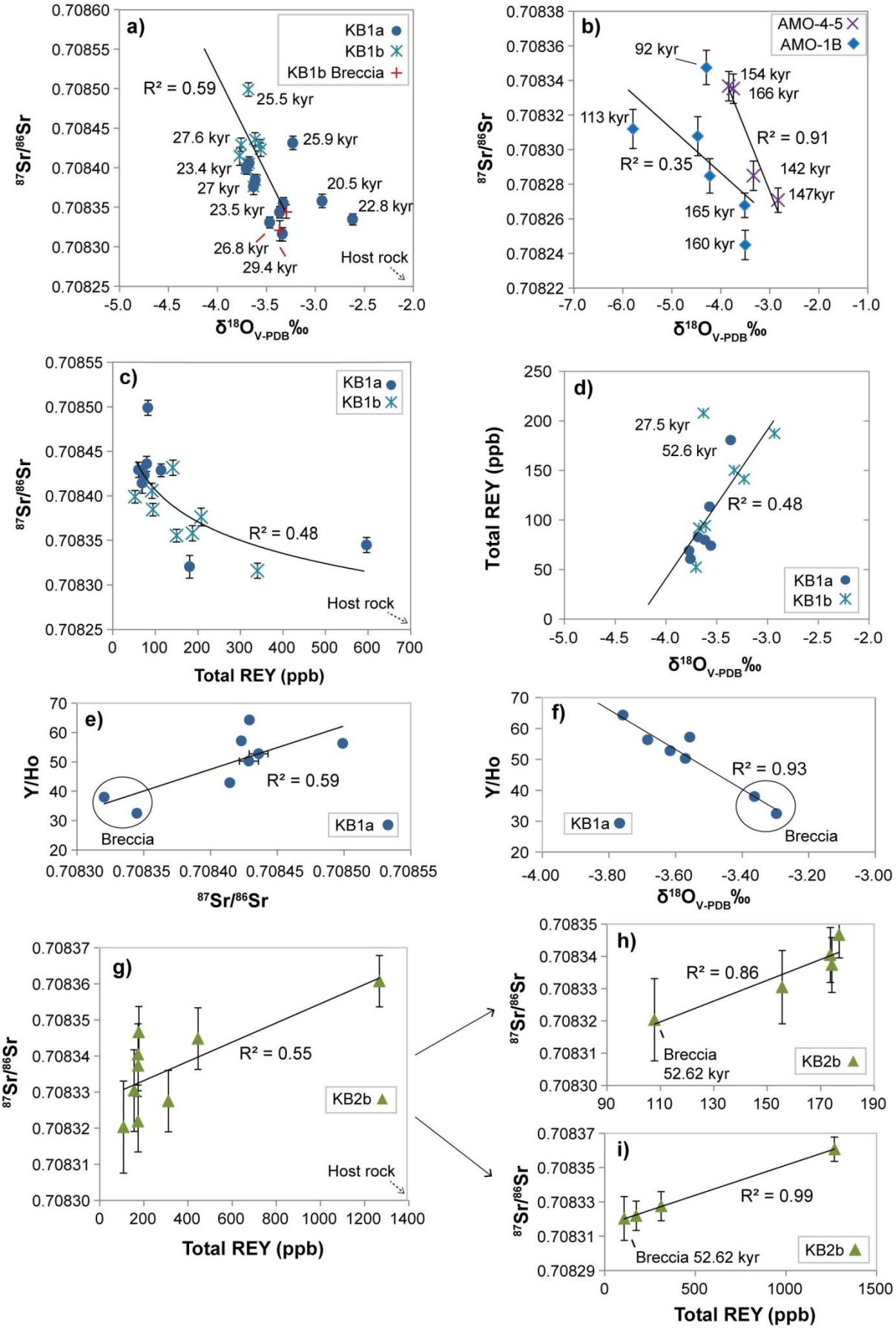
a)
KB1a
KB1b
KB1b Breccia
R² = 0.59
25.5 kyr
27.6 kyr
25.9 kyr
23.4 kyr
27 kyr
20.5 kyr
23.5 kyr
22.8 kyr
26.8 kyr
29.4 kyr
Host rock
87Sr/86Sr
δ18OV-PDB‰
b)
AMO-4-5
AMO-1B
92 kyr
154 kyr
166 kyr
113 kyr
R² = 0.91
R² = 0.35
142 kyr
147kyr
165 kyr
160 kyr
87Sr/86Sr
δ18OV-PDB‰
c)
KB1a
KB1b
R² = 0.48
Host rock
87Sr/86Sr
Total REY (ppb)
d)
27.5 kyr
52.6 kyr
R² = 0.48
KB1a
KB1b
Total REY (ppb)
δ18OV-PDB‰
e)
R² = 0.59
KB1a
Breccia
Y/Ho
87Sr/86Sr
f)
R² = 0.93
KB1a
Breccia
Y/Ho
δ18OV-PDB‰
g)
R² = 0.55
KB2b
Host rock
87Sr/86Sr
Total REY (ppb)
h)
R² = 0.86
Breccia
52.62 kyr
KB2b
87Sr/86Sr
i)
R² = 0.99
Breccia 52.62 kyr
KB2b
87Sr/86Sr
Total REY (ppb)

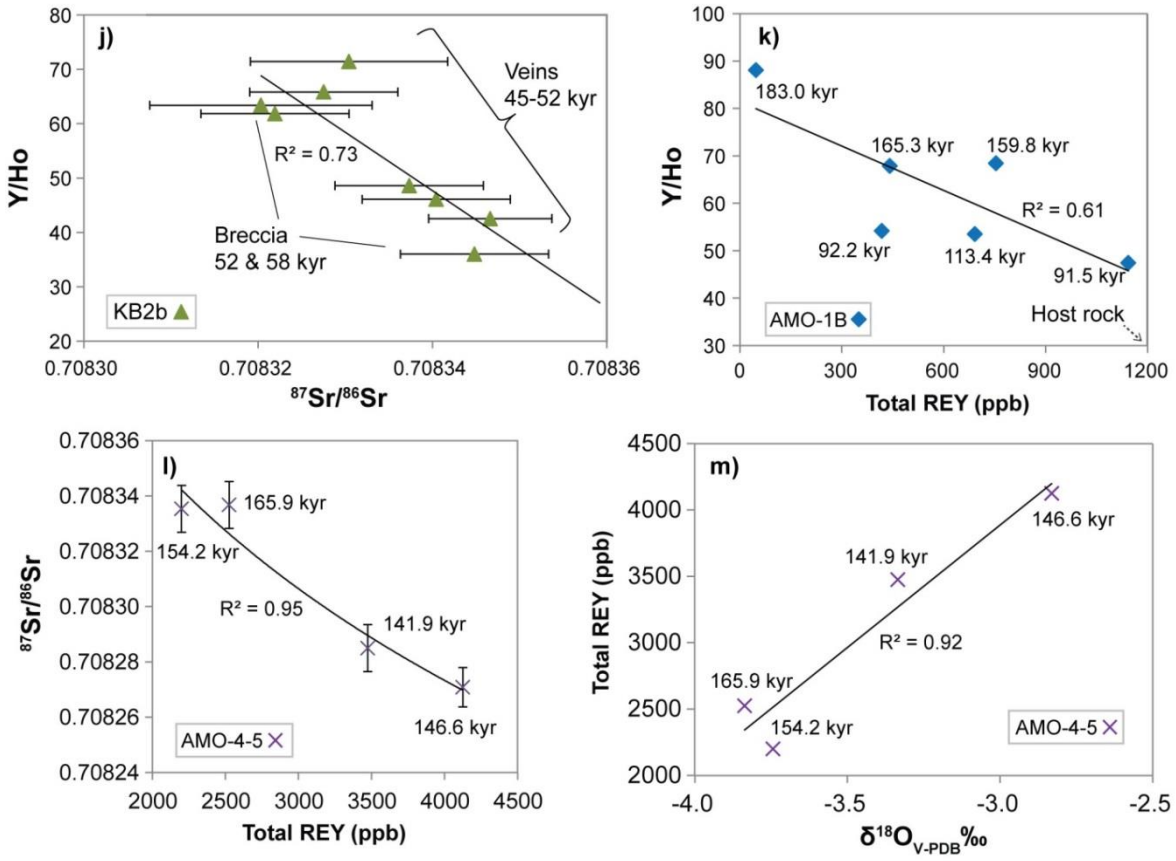

Figure 8 Geochemical plots for selected calcite veins from Kumlubük and Amos systems. **(a)** and **(b)** $^{87}Sr/^{86}Sr$ versus $\delta^{18}O$ plots of KB1a, KB1b, AMO-4-5 and AMO-1B; **(c)** $^{87}Sr/^{86}Sr$ versus plots for KB1a and KB1b; **(d)** total REY versus $\delta^{18}O$ plots of KB1a and KB1b; **(e)** Y/Ho versus $^{87}Sr/^{86}Sr$, and **(f)** $\delta^{18}O$ plots of KB1a; **(g), (h)**, and **(l)** $^{87}Sr/^{86}Sr$ versus total REY values for the sample KB2b; **(j)** Y/Ho versus $^{87}Sr/^{86}Sr$ plot of KB2b; **(k)** Y/Ho versus total REY plot for AMO-1B; **(l)** $^{87}Sr/^{86}Sr$ versus total REY plot of AMO-4-5; **(m)** total REY values versus $\delta^{18}O$ plot of the sample AMO-4-5. Host limestone values are reported in Uysal et al. (2011).

Figure 9 Rare Earths and Yttrium (REY) patterns of calcite vein, breccia, and host rock limestone **(a–i)** samples normalised to Post-Archaean Australian shale (PAAS) (Taylor and McLennan 1985), which are reported in Table S2. Note that the sub-sample names are indicated in the legends of each REY plot. Host limestone REY values are from Uysal et al. (2011).

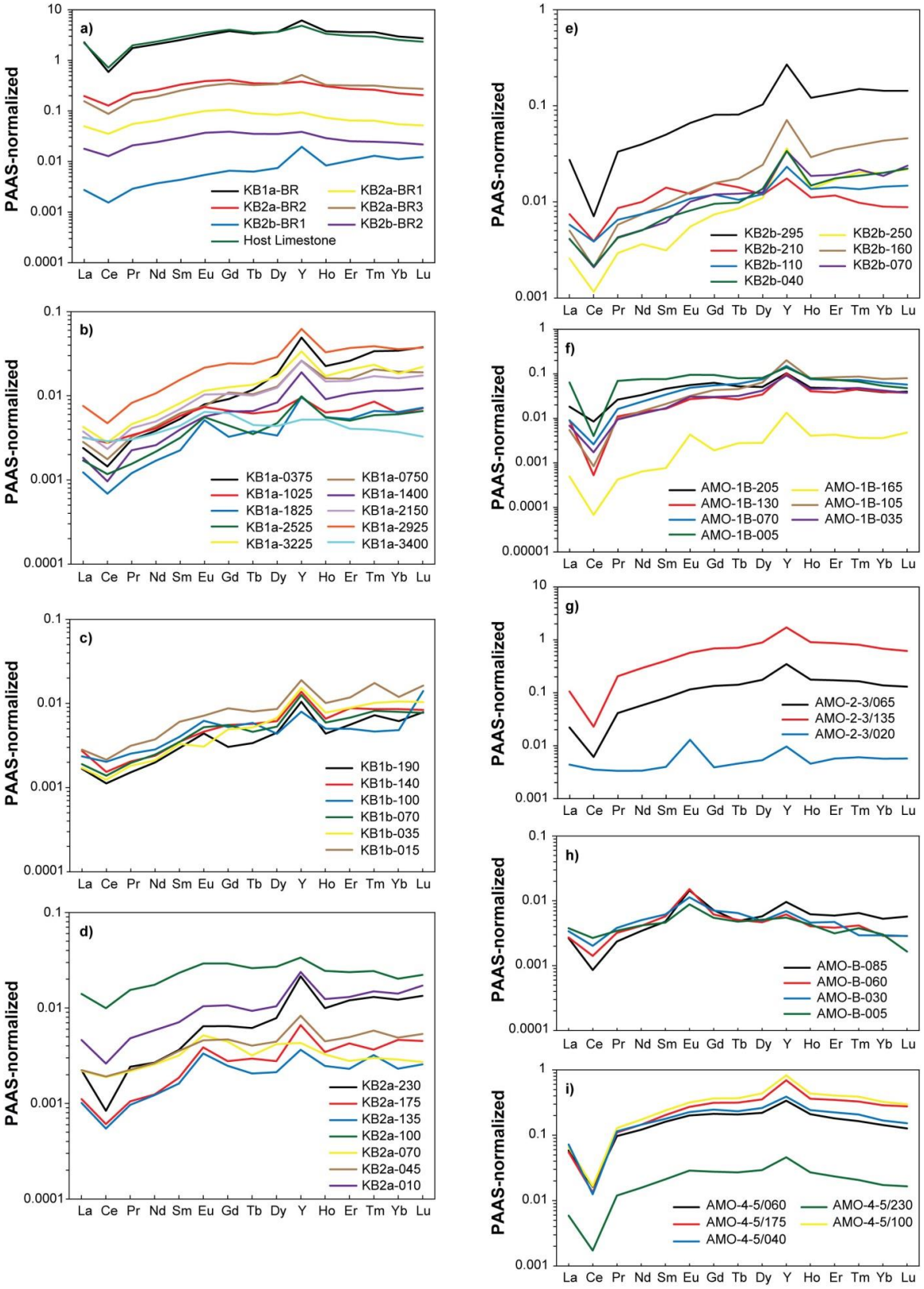
a)
PAAS-normalized
KB1a-BR
KB2a-BR1
KB2a-BR2
KB2a-BR3
KB2b-BR1
KB2b-BR2
Host Limestone
b)
KB1a-0375
KB1a-0750
KB1a-1025
KB1a-1400
KB1a-1825
KB1a-2150
KB1a-2525
KB1a-2925
KB1a-3225
KB1a-3400
c)
KB1b-190
KB1b-140
KB1b-100
KB1b-070
KB1b-035
KB1b-015
d)
KB2a-230
KB2a-175
KB2a-135
KB2a-100
KB2a-070
KB2a-045
KB2a-010
e)
KB2b-295
KB2b-250
KB2b-210
KB2b-160
KB2b-110
KB2b-070
KB2b-040
f)
AMO-1B-205
AMO-1B-165
AMO-1B-130
AMO-1B-105
AMO-1B-070
AMO-1B-035
AMO-1B-005
g)
AMO-2-3/065
AMO-2-3/135
AMO-2-3/020
h)
AMO-B-085
AMO-B-060
AMO-B-030
AMO-B-005
i)
AMO-4-5/060
AMO-4-5/230
AMO-4-5/175
AMO-4-5/100
AMO-4-5/040
La Ce Pr Nd Sm Eu Gd Tb Dy Y Ho Er Tm Yb Lu

APPENDIX 2: Supplementary Data for Paper 2

CO_2 outburst cycles in relation to seismicity: constraints from microscale geochronology and geochemistry of late Quaternary vein carbonates, SW Turkey

Ezgi Ünal-İmer, I. Tonguç Uysal, Jian-Xin Zhao, Veysel Işık, James Shulmeister, Ali İmer, Yue-Xing Feng

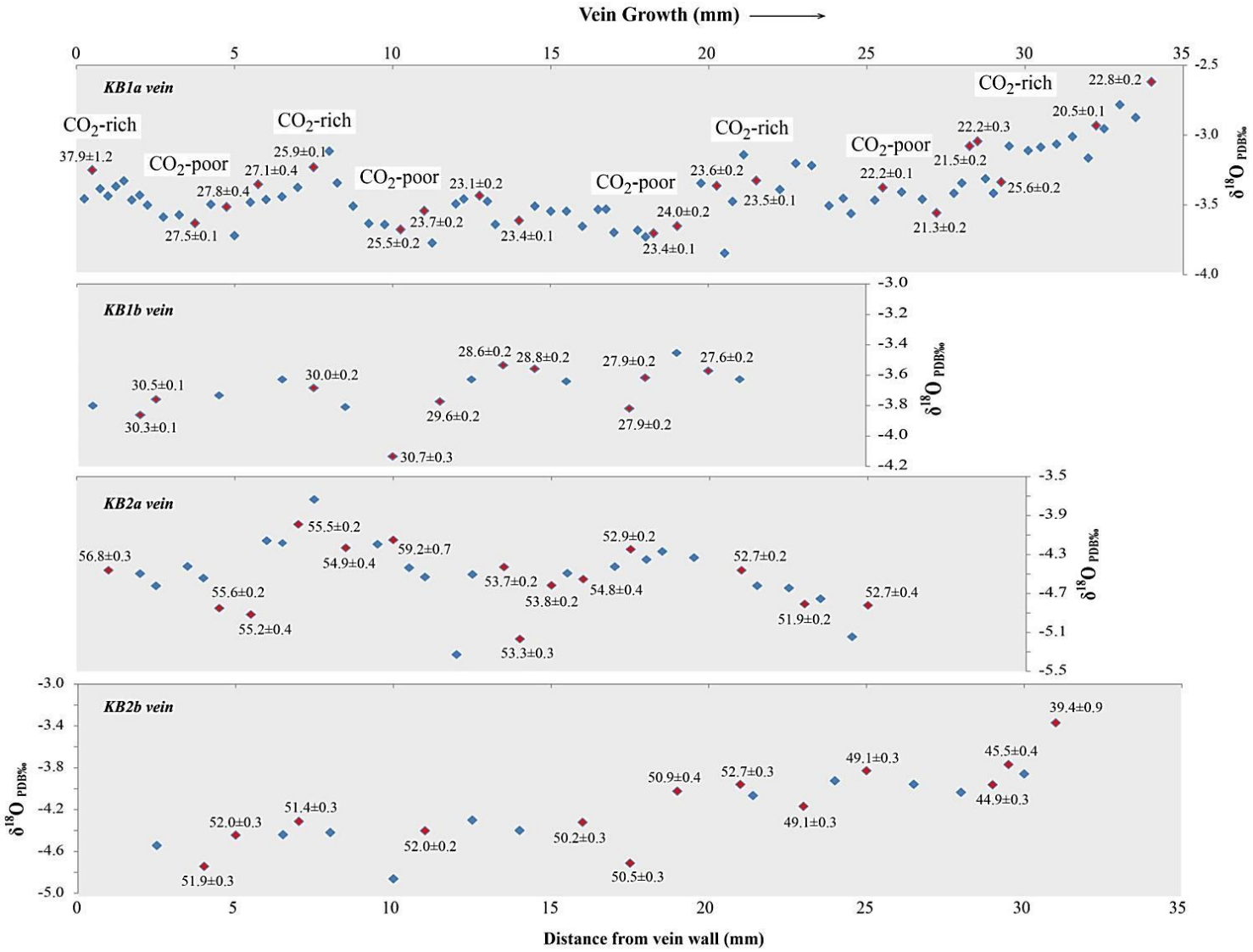

Figure S1 Plots of oxygen isotope ratios ($\delta^{18}O$ ‰VPDB) against vein depths (mm) of Kumlubük samples: KB1a, KB1b, KB2a, and KB2b.

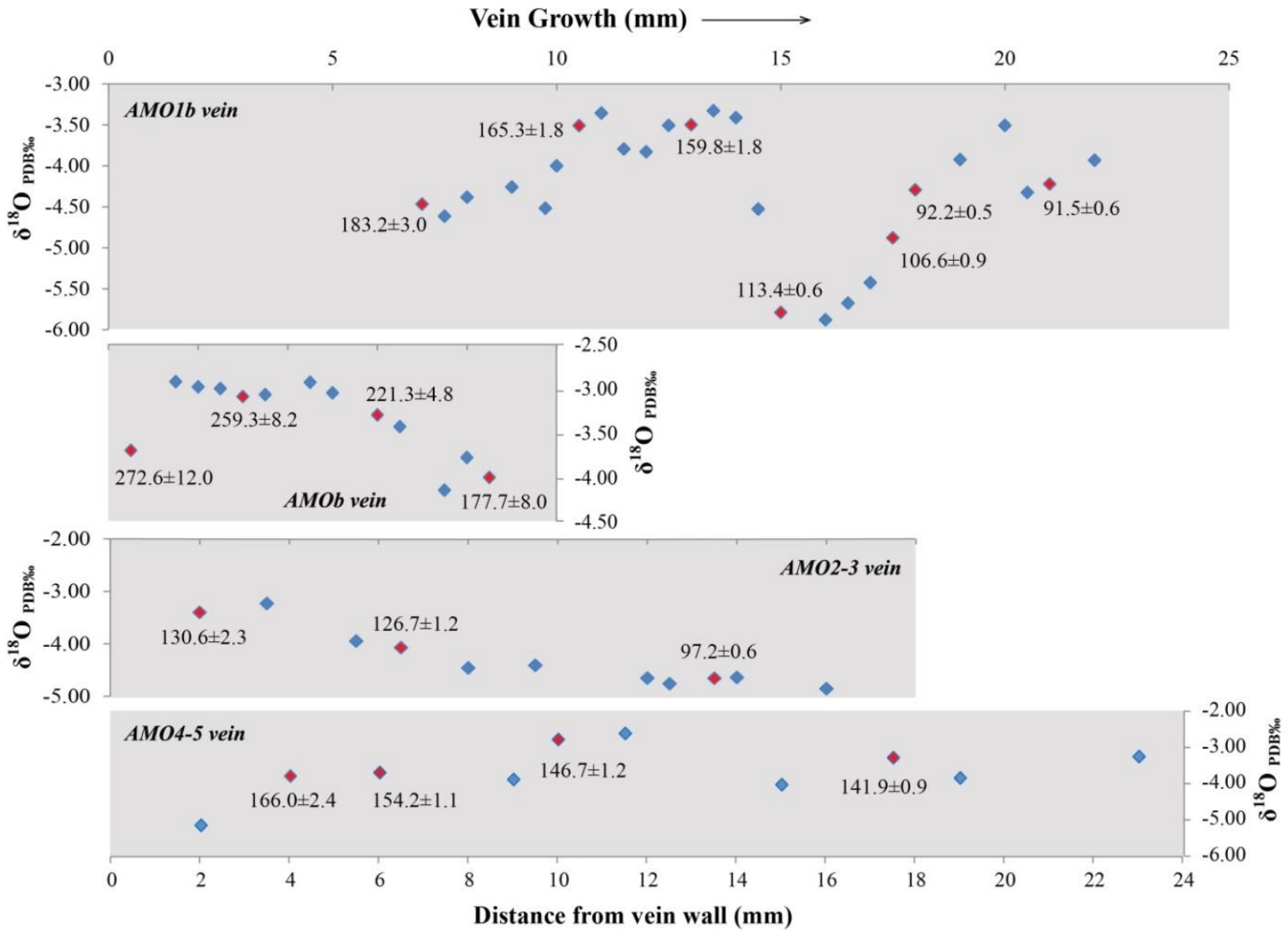

Figure S2 $\delta^{18}O$ (VPDB ‰) values versus vein depth (mm) plots for (a) AMO-1B, (b) AMO-B, (c) AMO-2-3, and (d) AMO4-5 calcite veins.

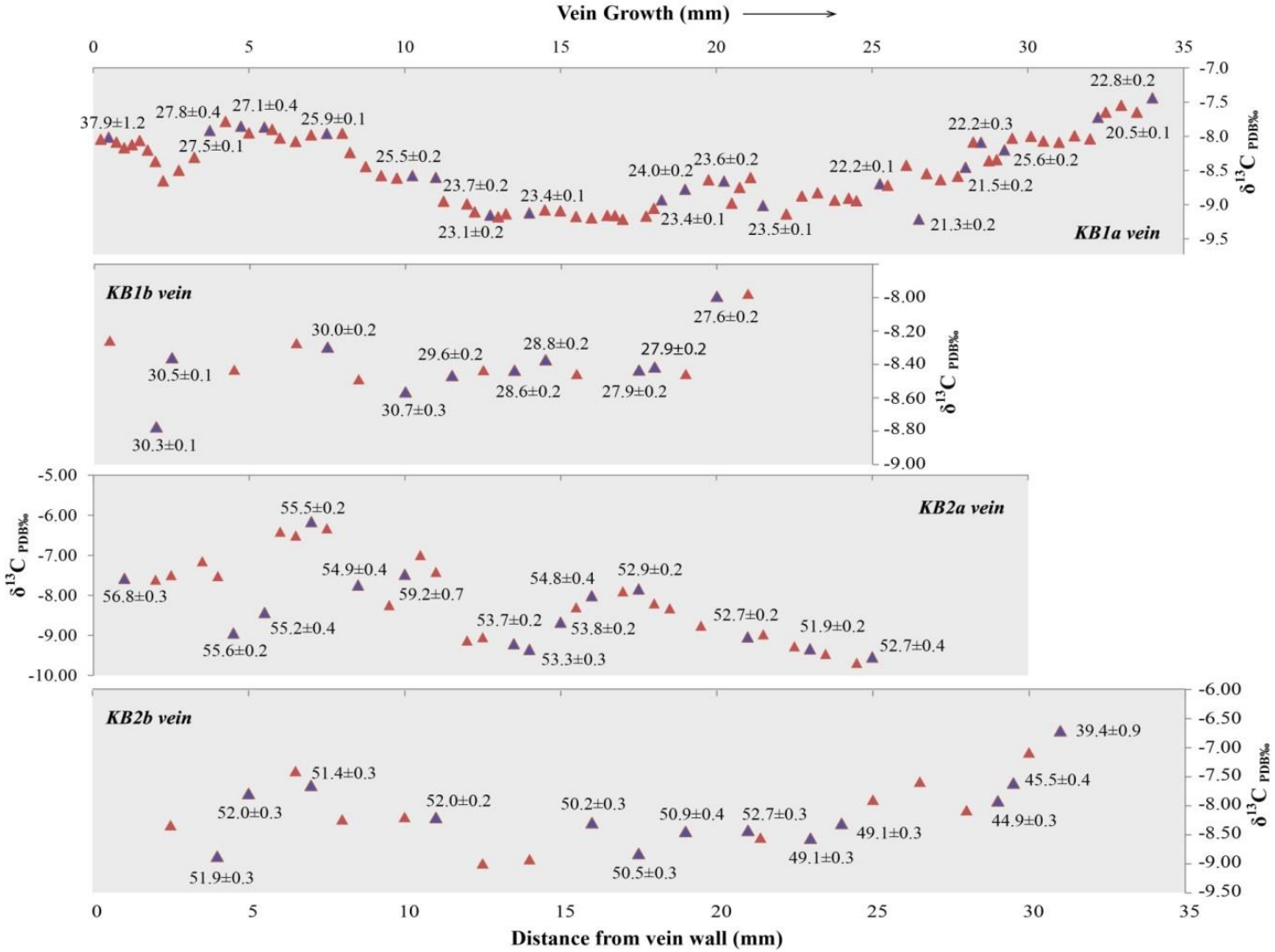

Figure S3 Plots of carbon isotope ratios (δ^{13}C VPDB ‰) against vein depths (mm) of Kumlubük veins: KB1a, KB1b, KB2a, and KB2b.

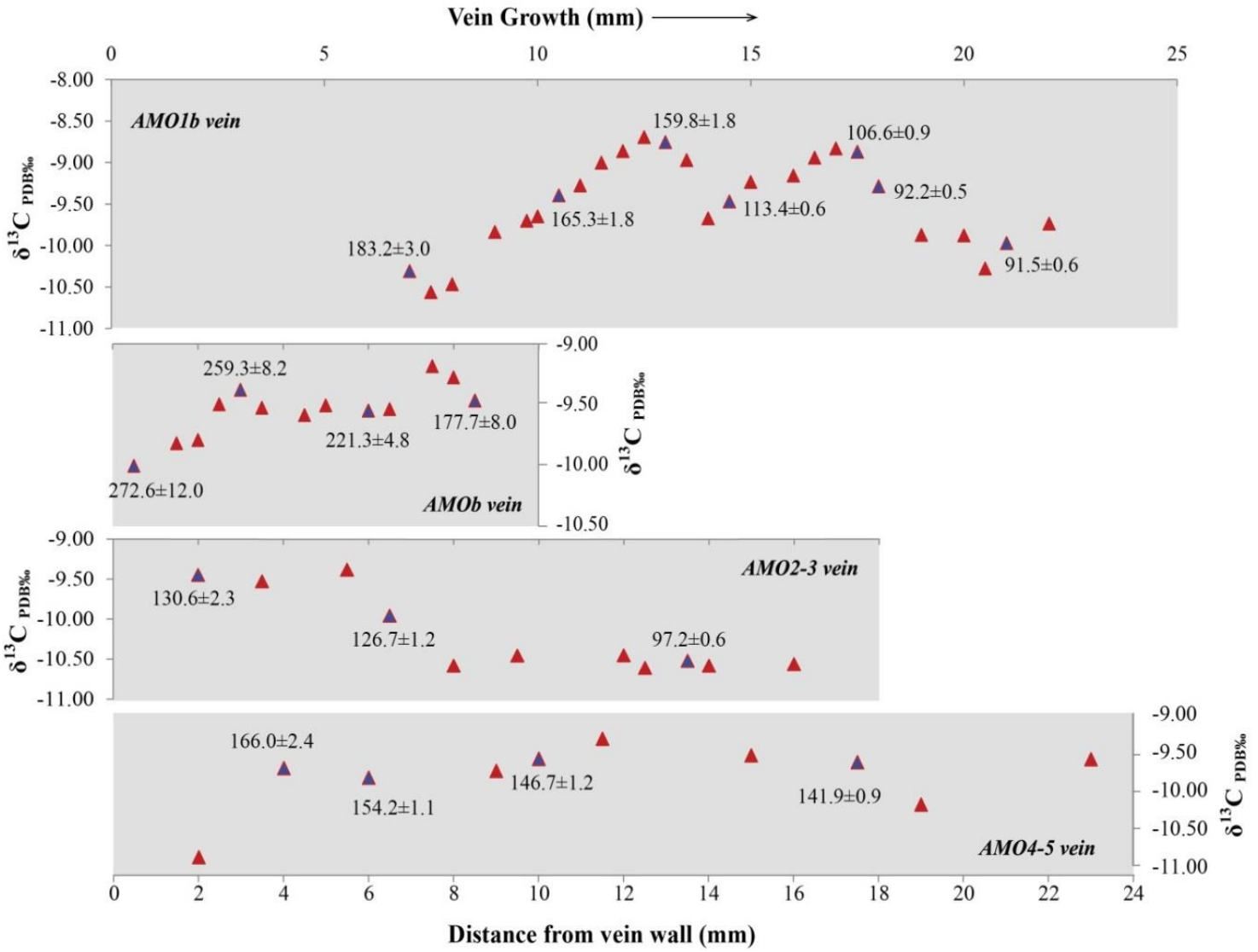

Figure S4 $\delta^{13}C$ (VPDB ‰) values versus vein depth (mm) plots for (a) AMO-1B, (b) AMO-B, (c) AMO-2-3, and (d) AMO4-5 calcite veins.

Table S1 Summary of MC-ICP-MS Uranium (U)-series age data of extension calcite vein/breccia from Kumlubük and Amos (Marmaris, SW Turkey)

Sample	Distance from wall (mm)	U (ppm)	±2σ	^{232}Th (ppb)	±2σ	(^{230}Th/ ^{232}Th)	±2σ	(^{230}Th/^{238}U)	±2σ	(^{234}U/^{238}U)	±2σ	Uncorr. Age (kyr)	±2σ	*,#Corr. Age (kyr)	±2σ	Corr. Initial (^{234}U/ ^{238}U)	±2σ
KB1a-BR	NA	0.2614	0.0001	25.62	0.03	11.3	0.05	0.365	0.0014	1.0376	0.0012	47.2	0.24	44.4	1.4	1.0517	0.0009
KB1a-0050	0.5	0.22600	0.00010	18.50	0.024	11.95	0.06	0.3226	0.0016	1.0432	0.0012	40.29	0.25	37.9	1.2	1.0492	0.0015
KB1a-0375	3.75	0.2449	0.0001	1.71	0.003	101.39	0.33	0.2333	0.0007	1.041	0.0008	27.66	0.1	27.46	0.14	1.0444	0.0008
KB1a-0475	4.75	0.22865	0.00017	5.26	0.009	31.64	0.18	0.2399	0.0013	1.0440	0.0014	28.46	0.18	27.81	0.37	1.0479	0.0015
KB1a-0575	5.75	0.22970	0.00015	4.37	0.005	37.19	0.40	0.2333	0.0025	1.0421	0.0017	27.63	0.34	27.09	0.43	1.0457	0.0018
KB1a-0750	7.5	0.2929	0.0001	2.37	0.004	82.97	0.28	0.2215	0.0007	1.0407	0.0009	26.09	0.1	25.86	0.15	1.0438	0.0009
KB1a-1025	10.25	0.3169	0.0001	3.74	0.003	56.68	0.23	0.2205	0.0009	1.0437	0.0008	25.87	0.12	25.53	0.21	1.0472	0.0009
KB1a-1100	11	0.2898	0.0001	1.30	0.002	138.56	0.76	0.2051	0.0011	1.0432	0.0013	23.87	0.14	23.74	0.16	1.0463	0.0014
KB1a-1275	12.75	0.4072	0.0003	0.72	0.002	341.7	2.8	0.1988	0.0015	1.0417	0.0018	23.10	0.20	23.05	0.21	1.0445	0.0019
KB1a-1400	14	0.4327	0.0002	1.36	0.01	195.3	1.2	0.2019	0.0008	1.0432	0.0008	23.45	0.1	23.37	0.11	1.0462	0.0009
KB1a-1825	18.25	0.4126	0.0002	0.97	0.001	261.2	1.2	0.2016	0.0009	1.042	0.0009	23.44	0.11	23.38	0.12	1.0449	0.0009
KB1a-1900	19	0.3092	0.0002	1.03	0.002	188.4	1.3	0.2068	0.0014	1.0440	0.0014	24.07	0.18	23.98	0.19	1.0471	0.0015
KB1a-2025	20.25	0.3217	0.0002	3.60	0.006	55.73	0.29	0.2056	0.0010	1.0432	0.0012	23.93	0.14	23.61	0.21	1.0463	0.0013
KB1a-2150	21.5	0.3954	0.0001	3.01	0.003	81.21	0.26	0.2038	0.0006	1.0441	0.0006	23.682	0.083	23.47	0.14	1.0472	0.0007
KB1a-2525	25.25	0.3484	0.0002	1.56	0.002	131.4	0.33	0.1934	0.0004	1.0438	0.0008	22.348	0.06	22.22	0.09	1.0467	0.0009
KB1a-2720	27.2	0.3419	0.0002	0.58	0.001	335.03	2.42	0.1865	0.0013	1.0489	0.0011	21.34	0.16	21.29	0.16	1.0520	0.0012
KB1a-2800	28	0.3621	0.0002	1.81	0.004	114.66	0.74	0.1891	0.0012	1.0494	0.0018	21.67	0.15	21.52	0.17	1.0525	0.0020
KB1a-2850	28.5	0.3404	0.0002	1.47	0.004	136.64	1.47	0.1941	0.0020	1.0481	0.0014	22.33	0.26	22.21	0.27	1.0512	0.0015
KB1a-2925	29.25	0.4021	0.0002	6.15	0.01	39.52	0.13	0.1993	0.0006	1.0466	0.0007	23.025	0.083	22.59	0.23	1.0499	0.0008
KB1a-3225	32.25	0.4470	0.0002	3.26	0.004	75.5	0.32	0.1812	0.0007	1.0458	0.0007	20.754	0.094	20.55	0.14	1.0486	0.0007
KB1a-3400	34	0.8809	0.0008	11.22	0.02	47.9	0.17	0.2011	0.0006	1.049	0.0012	23.2	0.087	22.84	0.2	1.0524	0.0013
KB1b-BR1	NA	0.3098	0.0001	6.69	0.01	32.46	0.12	0.2308	0.0008	1.0432	0.0013	27.26	0.12	26.78	0.27	1.0469	0.0014
KB1b-BR2	NA	0.2855	0.0002	14.85	0.02	14.9	0.06	0.2556	0.001	1.0444	0.0011	30.58	0.14	29.42	0.59	1.0489	0.0012
KB1b-002	2	0.3926	0.0004	0.37	0.001	814.1	3.6	0.2522	0.0009	1.0395	0.0011	30.28	0.13	30.26	0.14	1.043	0.0012
KB1b-025	2.5	0.3467	0.0002	1.05	0.002	255.39	0.93	0.2546	0.0009	1.0415	0.0012	30.55	0.12	30.48	0.13	1.0453	0.0012
KB1b-075	7.5	0.3763	0.0003	1.84	0.003	156.01	0.8	0.2508	0.0012	1.0402	0.001	30.07	0.17	29.96	0.18	1.0438	0.0011

KB1b-100	10	0.3122	0.0002	5.04	0.01	48.51	0.26	0.2582	0.0013	1.0373	0.0014	31.2	0.19	30.73	0.30	1.0409	0.0016
KB1b-115	11.5	0.2922	0.0002	2.58	0.004	85.51	0.44	0.2485	0.0013	1.04	0.0013	29.76	0.18	29.56	0.20	1.0436	0.0014
KB1b-135	13.5	0.3404	0.0003	0.48	0.001	518.4	3.2	0.2407	0.0014	1.0424	0.0014	28.61	0.19	28.57	0.20	1.046	0.0015
KB1b-145	14.5	0.3328	0.0002	1.77	0.003	138.69	0.66	0.2431	0.0011	1.0422	0.0011	28.96	0.15	28.84	0.16	1.0459	0.0012
KB1b-175	17.5	0.2191	0.0003	1.27	0.002	123.3	0.66	0.2357	0.0012	1.0382	0.0019	28.07	0.18	27.90	0.20	1.0414	0.002
KB1b-180	18	0.2466	0.0002	1.47	0.002	120.03	0.61	0.2355	0.0012	1.0389	0.0014	28.02	0.17	27.89	0.18	1.0422	0.0015
KB1b-200	20	0.2213	0.0001	2.71	0.004	58.2	0.28	0.2348	0.0011	1.0416	0.0012	27.85	0.15	27.57	0.2	1.0452	0.0013
KB2a-BR1	NA	0.4289	0.0001	43.4	0.07	14.41	0.05	0.4805	0.0013	1.0528	0.0006	66.16	0.25	63.3	1.4	1.0649	0.0012
KB2a-BR2	NA	0.4227	0.0002	161.7	0.3	5.33	0.02	0.6719	0.0017	1.0525	0.0008	109.7	0.49	98.5	5.4	1.0775	0.0047
KB2a-BR3	NA	0.4154	0.0002	95	0.1	9.41	0.03	0.7091	0.0018	1.0417	0.0011	123.23	0.64	116.6	3.2	1.0618	0.0026
KB2a-250	25	0.4439	0.0012	0.77	0.001	702.3	3.7	0.4031	0.0023	1.0492	0.0018	52.71	0.4	52.66	0.40	1.0571	0.0021
KB2a-230	23	0.4472	0.0002	1.14	0.001	475.7	1.3	0.3998	0.0011	1.0524	0.001	51.96	0.19	51.90	0.20	1.0607	0.0011
KB2a-210	21	0.4186	0.0002	0.52	0.001	984.2	3.8	0.4046	0.0013	1.053	0.0012	52.71	0.24	52.68	0.24	1.0615	0.0013
KB2a-175	17.5	0.3815	0.0002	0.79	0.001	594.3	1.6	0.4052	0.001	1.0511	0.0008	52.93	0.18	52.87	0.18	1.0594	0.001
KB2a-160	16	0.3236	0.0001	6.99	0.007	59.03	0.2	0.4200	0.0013	1.0514	0.0012	55.42	0.25	54.81	0.38	1.0604	0.0015
KB2a-150	15	0.3422	0.0001	2.81	0.004	152.08	0.5	0.4115	0.0012	1.051	0.0008	54	0.22	53.77	0.24	1.0595	0.0009
KB2a-140	14	0.3680	0.0003	1.1	0.002	414.27	1.82	0.4095	0.0017	1.0548	0.0017	53.4	0.31	53.32	0.31	1.0638	0.0019
KB2a-135	13.5	0.3691	0.0002	2.29	0.003	201.14	0.51	0.4119	0.0009	1.0539	0.0006	53.87	0.16	53.70	0.18	1.0628	0.0006
KB2a-100	10	0.2873	0.0001	12.97	0.02	30.13	0.1	0.4483	0.0014	1.0506	0.0011	60.44	0.27	59.16	0.67	1.0606	0.0013
KB2a-085	8.5	0.3116	0.0001	1.84	0.003	216.15	1.09	0.4197	0.002	1.0553	0.0016	55.08	0.36	54.91	0.37	1.0647	0.0018
KB2a-070	7	0.3083	0.0001	2.23	0.002	177.6	0.48	0.4231	0.0011	1.0552	0.0008	55.66	0.19	55.46	0.22	1.0647	0.0009
KB2a-055	5.5	0.3199	0.0001	1	0.003	410.3	2.2	0.4224	0.0019	1.0586	0.0021	55.31	0.36	55.22	0.37	1.0685	0.0024
KB2a-045	4.5	0.3141	0.0002	2.57	0.002	157.42	0.44	0.4242	0.0011	1.055	0.0009	55.87	0.21	55.64	0.23	1.0645	0.001
KB2a-010	1	0.2810	0.0001	3.4	0.003	107.88	0.31	0.4299	0.0012	1.0516	0.0006	57.1	0.21	56.77	0.26	1.0607	0.0007
KB2b-BR1	NA	0.3657	0.0001	1.6	0.002	281.33	0.69	0.4046	0.0009	1.0529	0.0012	52.72	0.17	52.6	0.18	1.0614	0.0013
KB2b-BR2	NA	0.2918	0.0002	15.28	0.02	25.94	0.13	0.4476	0.0021	1.0539	0.0011	60.03	0.38	58.56	0.81	1.0646	0.0014
KB2b-310	31	0.2191	0.0002	13.82	0.028	16.12	0.15	0.3351	0.0031	1.0639	0.0014	41.14	0.47	39.38	0.98	1.0726	0.0017
KB2b-295	29.5	0.2020	0.0001	6.52	0.01	34.29	0.13	0.3648	0.0012	1.0533	0.0013	46.25	0.21	45.34	0.49	1.0612	0.0015
KB2b-290	29	0.1907	0.0001	1.98	0.003	104.63	0.55	0.3574	0.0018	1.0518	0.0016	45.16	0.29	44.87	0.33	1.059	0.0018
KB2b-250	25	0.2904	0.0002	1.12	0.002	301.1	1.3	0.3826	0.0016	1.0515	0.0011	49.19	0.26	49.08	0.27	1.0593	0.0012
KB2b-230	23	0.2970	0.0002	0.32	0.001	1061.1	7.1	0.3811	0.0019	1.0495	0.0015	49.08	0.33	49.05	0.33	1.0568	0.0017

KB2b-210	21	0.3122	0.0002	3.9	0.01	98.2	0.39	0.4046	0.0015	1.0497	0.001	52.93	0.26	52.58	0.31	1.0578	0.0012
KB2b-190	19	0.2885	0.0002	4.49	0.008	76.95	0.33	0.3951	0.0016	1.0501	0.0015	51.32	0.28	50.88	0.35	1.0581	0.0017
KB2b-175	17.5	0.2629	0.0002	2.59	0.005	120.18	0.53	0.3908	0.0016	1.0479	0.001	50.75	0.27	50.48	0.3	1.0553	0.0011
KB2b-160	16	0.2871	0.0002	1.85	0.003	183.69	0.71	0.3891	0.0014	1.0505	0.0014	50.31	0.25	50.13	0.26	1.0583	0.0016
KB2b-110	11	0.2983	0.0002	4.16	0.01	87.37	0.23	0.4014	0.001	1.0504	0.0013	52.35	0.19	51.95	0.27	1.0586	0.0015
KB2b-070	7	0.2980	0.0002	2.14	0.003	167.59	0.66	0.3964	0.0015	1.0505	0.0008	51.51	0.25	51.31	0.27	1.0585	0.0009
KB2b-050	5	0.2474	0.0002	1.42	0.002	212	0.95	0.3999	0.0017	1.0492	0.001	52.18	0.3	52.02	0.31	1.0571	0.0012
KB2b-040	4	0.2923	0.0002	2.11	0.003	167.98	0.78	0.4005	0.0018	1.0521	0.0012	52.08	0.31	51.87	0.32	1.0605	0.0014
AMO-1B/215	21.5	0.2001	0.0001	5	0.01	82.4	0.36	0.6785	0.0027	1.1699	0.0009	92.13	0.57	91.52	0.62	1.2216	0.0014
AMO-1B/180	18	0.1289	0.0001	0.86	0.002	318.1	1.4	0.7024	0.0025	1.2052	0.001	92.4	0.52	92.24	0.53	1.2668	0.0013
AMO-1B/175	17.5	0.1444	0.0001	4.03	0.008	82.22	0.43	0.7569	0.0036	1.1842	0.0013	107.27	0.87	106.61	0.90	1.2508	0.0020
AMO-1B/150	15	0.0771	0.0000	1.38	0.002	141.18	0.45	0.8315	0.0025	1.2482	0.0015	113.76	0.63	113.36	0.64	1.3437	0.0021
AMO-1B/130	13	0.0669	0.0000	0.42	0.001	503.75	2.78	1.0394	0.0052	1.2936	0.0020	159.98	1.766	159.85	1.77	1.4621	0.0032
AMO-1B/105	10.5	0.0327	0.0000	0.77	0.002	141.24	0.73	1.0934	0.0050	1.3324	0.0020	165.79	1.754	165.34	1.79	1.5339	0.0036
AMO-1B/070	7	0.0170	0.0000	0.09	0.001	623.31	7.25	1.0736	0.0067	1.2620	0.0032	183.29	3.008	183.19	3.01	1.4403	0.0051
AMO-4-5/300	30	0.2088	0.0001	1.79	0.004	284	1.9	0.802	0.0051	1.1905	0.0024	117.1	1.4	116.9	1.4	1.2657	0.0031
AMO-4-5/230	23	0.3309	0.0002	0.98	0.002	939.3	3.6	0.9128	0.0032	1.2275	0.0013	139.05	0.98	139	0.98	1.3373	0.0018
AMO-4-5/175	17.5	0.1720	0.0001	4.01	0.01	120.58	0.36	0.9254	0.0025	1.2295	0.0017	142.3	0.85	141.78	0.88	1.3448	0.0024
AMO-4-5/100	10	0.1280	0.0000	5.43	0.01	67.21	0.27	0.94	0.0035	1.2274	0.0015	147.3	1.2	146.4	1.2	1.348	0.0028
AMO-4-5/060	6	0.2112	0.0002	13.56	0.02	44.96	0.13	0.95	0.0025	1.21	0.0017	155.33	0.99	154.2	1.1	1.3336	0.0033
AMO-4-5/040	4	0.0561	0.0000	8.12	0.01	21.02	0.11	1.00	0.0051	1.23	0.0023	168.40	2.08	165.89	2.4	1.3801	0.0070
AMO-2-3/020	2	0.0578	0.0000	7.67	0.02	20.69	0.17	0.9043	0.0073	1.2433	0.003	132.1	2.1	130.0	2.4	1.3644	0.0073
AMO-2-3-065	6.5	0.0805	0.0000	1.663	0.003	125.14	0.66	0.8518	0.0043	1.2051	0.0019	127.118	1.240	126.74	1.2	1.2951	0.0027
AMO-2-3/135	13.5	0.1588	0.0001	3.3	0.01	103.77	0.4	0.7118	0.0024	1.1816	0.0013	97.56	0.56	97.06	0.59	1.2403	0.0017
AMO-2-3/150	15	0.0606	0.0001	1.52	0.003	118.98	0.88	0.9838	0.0071	1.2917	0.0032	143.7	2.2	143.2	2.2	1.4402	0.0048
AMO-B-005	0.5	0.0307	0.0000	4.22	0.006	37.55	0.15	1.6992	0.0067	1.6547	0.0029	274.346	4.193	272.65	12.1	2.4697	0.0357
AMO-B-030	3	0.0255	0.0000	2.33	0.004	52.92	0.32	1.5917	0.0094	1.5851	0.0031	260.569	5.395	259.34	8.2	2.2487	0.0228
AMO-B-060	6	0.0255	0.0000	2.06	0.003	56.09	0.28	1.4963	0.0074	1.5734	0.0027	222.493	3.224	221.33	4.9	2.0960	0.0123
AMO-B-085	8.5	0.0467	0.0002	1.17	0.066	159.43	9.51	1.3218	0.0261	1.5291	0.0069	178.100	8.021	177.70	8.0	1.8804	0.0205

*The corrected (Corr.) ages (kyr) were calculated using equation given Cheng et al., 2000 and using half-lives specified in Clark et al., 2012.
The U-series ages <150 kyr are used in Ünal-İmer et al. 2013.
All errors are given at 2-sigma level. NA is Not Available; BR refers to the sample gathered from breccia.

Table S2 $\delta^{18}O$, $\delta^{13}C$ and $^{87}Sr/^{86}Sr$ isotopic values of the calcite vein/breccia samples from Kumlubük and Amos (Marmaris, SW Turkey) (stable isotope values are in ppm: ‰)

Location	Sample	$\delta^{13}C_{VPDB*}$	$\delta^{18}O_{VPDB}$	$\delta^{18}O_{VSMOW**}$	$^{87}Sr/^{86}Sr$	$\pm 2\sigma$
Kumlubük vein system	KB1a-BR	-4.69	-1.71	29.16	0.708346	0.00001
	KB1a-BR2	-8.00	-3.37	27.45		
	KB1a-BR3	-7.97	-3.30	27.52		
	KB1a-BR4	-7.96	-3.21	27.61		
	KB1a-0025	-8.05	-3.46	27.36		
	KB1a-0050	-8.02	-3.25	27.57		
	KB1a-0075	-8.09	-3.38	27.43		
	KB1a-0100	-8.17	-3.44	27.38		
	KB1a-0125	-8.13	-3.37	27.45		
	KB1a-0150	-8.07	-3.33	27.49		
	KB1a-0175	-8.21	-3.47	27.35		
	KB1a-0200	-8.37	-3.43	27.39		
	KB1a-0225	-8.66	-3.50	27.31		
	KB1a-0275	-8.50	-3.59	27.23		
	KB1a-0325	-8.31	-3.57	27.24		
	KB1a-0375	-7.92	-3.63	27.18	0.708376	0.00001
	KB1a-0425	-7.79	-3.50	27.32		
	KB1a-0475	-7.86	-3.51	27.30		
	KB1a-0500	-7.96	-3.72	27.09		
	KB1a-0550	-7.87	-3.48	27.33		
	KB1a-0575	-7.90	-3.35	27.47		
	KB1a-0600	-8.03	-3.46	27.35		
	KB1a-0650	-8.08	-3.44	27.38		
	KB1a-0700	-7.98	-3.37	27.44		
	KB1a-0750	-7.96	-3.23	27.59	0.708432	0.000009
	KB1a-0800	-7.96	-3.12	27.71		
	KB1a-0825	-8.24	-3.34	27.48		
	KB1a-0875	-8.45	-3.51	27.31		
	KB1a-0925	-8.58	-3.63	27.18		
	KB1a-0975	-8.62	-3.64	27.17		
	KB1a-1025	-8.58	-3.68	27.13	0.708406	0.000009
	KB1a-1100	-8.60	-3.54	27.27		
	KB1a-1125	-8.95	-3.77	27.03		
	KB1a-1200	-8.99	-3.49	27.32		
	KB1a-1225	-9.11	-3.46	27.36		
	KB1a-1275	-9.16	-3.43	27.38		
	KB1a-1300	-9.18	-3.47	27.34		
	KB1a-1325	-9.14	-3.64	27.17		
	KB1a-1400	-9.12	-3.61	27.20	0.708385	0.000007

KB1a-1450	-9.08	-3.51	27.31		
KB1a-1500	-9.09	-3.54	27.27		
KB1a-1550	-9.18	-3.54	27.27		
KB1a-1600	-9.20	-3.65	27.16		
KB1a-1650	-9.16	-3.53	27.28		
KB1a-1675	-9.16	-3.53	27.28		
KB1a-1700	-9.22	-3.70	27.11		
KB1a-1775	-9.17	-3.68	27.13		
KB1a-1800	-9.06	-3.73	27.08		
KB1a-1825	-8.93	-3.70	27.11	0.708399	0.000007
KB1a-1900	-8.78	-3.65	27.16		
KB1a-1975	-8.64	-3.34	27.48		
KB1a-2025	-8.66	-3.36	27.46		
KB1a-2050	-8.98	-3.85	26.96		
KB1a-2075	-8.75	-3.48	27.34		
KB1a-2110	-8.61	-3.14	27.68		
KB1a-2150	-9.02	-3.33	27.49	0.708355	0.000007
KB1a-2225	-9.14	-3.39	27.43		
KB1a-2275	-8.88	-3.20	27.62		
KB1a-2325	-8.83	-3.22	27.61		
KB1a-2380	-8.94	-3.51	27.31		
KB1a-2425	-8.91	-3.45	27.36		
KB1a-2450	-8.95	-3.56	27.25		
KB1a-2525	-8.70	-3.47	27.35	0.708331	0.000007
KB1a-2550	-8.72	-3.38	27.44		
KB1a-2610	-8.43	-3.41	27.41		
KB1a-2650	-9.22	-5.14	25.62		
KB1a-2675	-8.55	-3.46	27.36		
KB1a-2720	-8.64	-3.56	27.36		
KB1a-2775	-8.59	-3.42	27.5		
KB1a-2800	-8.46	-3.34	27.48		
KB1a-2825	-8.09	-3.08	27.75		
KB1a-2850	-8.09	-3.04	27.78		
KB1a-2875	-8.36	-3.31	27.51		
KB1a-2900	-8.35	-3.42	27.4		
KB1a-2925	-8.20	-3.34	27.48	0.708316	0.000008
KB1a-2950	-8.03	-3.08	27.75		
KB1a-3010	-8.00	-3.11	27.72		
KB1a-3050	-8.07	-3.09	27.74		
KB1a-3100	-8.09	-3.06	27.76		
KB1a-3150	-8.00	-3.01	27.82		
KB1a-3200	-8.04	-3.16	27.66		
KB1a-3225	-7.73	-2.93	27.90	0.708358	0.000009

KB1a-3250	-7.65	-2.95	27.88		
KB1a-3300	-7.55	-2.78	28.05		
KB1a-3350	-7.65	-2.87	27.96		
KB1a-3400	-7.44	-2.62	28.22	0.708335	0.000007
KB1a-4925	-8.75	-3.12	27.70		
KB1b-005	-7.99	-3.63	27.18		
KB1b-015	-8.00	-3.57	27.24	0.708429	0.000007
KB1b-025	-8.46	-3.45	27.36		
KB1b-035	-8.42	-3.62	27.19	0.708436	0.000009
KB1b-040	-8.43	-3.82	26.99		
KB1b-060	-8.46	-3.64	27.17		
KB1b-070	-8.37	-3.56	27.26	0.708423	0.000009
KB1b-080	-8.44	-3.53	27.28		
KB1b-090	-8.43	-3.63	27.18		
KB1b-100	-8.47	-3.77	27.03	0.708414	0.000011
KB1b-115	-8.57	-4.13	26.66		
KB1b-130	-8.50	-3.81	27.00		
KB1b-140	-8.31	-3.68	27.13	0.708499	0.000009
KB1b-150	-8.28	-3.63	27.18		
KB1b-170	-8.44	-3.73	27.08		
KB1b-190	-8.37	-3.76	27.05	0.708429	0.000009
KB1b-195	-8.80	-3.86	26.94		
KB1b-210	-8.27	-3.80	27.01		
KB1b-BR1	-8.26	-3.36	27.46	0.70832	0.000013
KB1b-BR2	-8.33	-3.30	27.52	0.708345	0.000009
KB2a-0100	-7.58	-4.46	26.32	0.708368	0.000007
KB2a-0200	-7.61	-4.50	26.29		
KB2a-0250	-7.49	-4.62	26.16		
KB2a-0350	-7.15	-4.42	26.37		
KB2a-0400	-7.52	-4.54	26.24		
KB2a-0450	-8.94	-4.85	25.92	0.708345	0.000006
KB2a-0550	-8.43	-4.92	25.86		
KB2a-0600	-6.41	-4.16	26.64		
KB2a-0650	-6.51	-4.18	26.61		
KB2a-0700	-6.09	-3.99	26.81	0.708377	0.000009
KB2a-0750	-6.33	-3.73	27.07		
KB2a-0850	-7.75	-4.23	26.56		
KB2a-0950	-8.24	-4.19	26.6		
KB2a-1000	-7.48	-4.15	26.65	0.708348	0.000007
KB2a-1050	-7.00	-4.44	26.35		
KB2a-1100	-7.42	-4.53	26.25		
KB2a-1200	-9.09	-5.33	25.43		
KB2a-1250	-9.04	-4.51	26.28		

KB2a-1350	-9.17	-4.43	26.36	0.708305	0.000008
KB2a-1400	-9.31	-5.17	25.6		
KB2a-1500	-8.68	-4.62	26.16		
KB2a-1550	-8.30	-4.49	26.29		
KB2a-1600	-8.01	-4.55	26.23		
KB2a-1700	-7.90	-4.42	26.36		
KB2a-1750	-7.84	-4.25	26.55	0.708342	0.000009
KB2a-1800	-8.20	-4.35	26.44		
KB2a-1850	-8.32	-4.27	26.52		
KB2a-1950	-8.76	-4.33	26.46		
KB2a-2100	-9.04	-4.46	26.32		
KB2a-2150	-8.98	-4.62	26.16		
KB2a-2250	-9.24	-4.64	26.14		
KB2a-2300	-9.30	-4.81	25.97	0.708324	0.000008
KB2a-2350	-9.43	-4.75	26.02		
KB2a-2450	-9.61	-5.15	25.62		
KB2a-2500	-9.50	-4.82	25.95		
KB2a-BR1	-9.25	-4.48	26.31	0.708318	0.000007
KB2a-BR2	-8.13	-3.96	26.84	0.708395	0.000007
KB2a-BR3	-8.15	-4.41	26.38	0.708389	0.000009
KB2a-BR4	-7.64	-3.96	26.84		
KB2a-BR5	-6.41	-3.73	27.08		
KB2b-025	-8.22	-4.54	26.24		
KB2b-040	-8.75	-4.74	26.03	0.708322	0.000008
KB2b-050	-7.67	-4.44	26.34		
KB2b-065	-7.28	-4.44	26.35		
KB2b-070	-7.53	-4.31	26.48	0.708337	0.000009
KB2b-080	-8.12	-4.42	26.37		
KB2b-100	-8.07	-4.86	25.91		
KB2b-110	-8.08	-4.40	26.38	0.70834	0.000009
KB2b-125	-8.87	-4.30	26.49		
KB2b-140	-8.80	-4.40	26.39		
KB2b-160	-8.18	-4.32	26.47	0.708328	0.000008
KB2b-175	-8.70	-4.71	26.07		
KB2b-190	-8.32	-4.02	26.77		
KB2b-210	-8.31	-3.96	26.84	0.708347	0.000007
KB2b-214	-8.43	-4.07	26.73		
KB2b-230	-8.44	-4.17	26.63		
KB2b-240	-8.19	-3.92	26.88		
KB2b-250	-7.78	-3.83	26.98	0.70833	0.000011
KB2b-265	-7.47	-3.96	26.84		
KB2b-280	-7.96	-4.04	26.76		
KB2b-290	-7.80	-3.96	26.84		

	KB2b-295	-7.49	-3.77	27.04	0.708361	0.000007
	KB2b-300	-6.97	-3.86	26.94		
	KB2b-310	-6.39	-3.37	27.45		
	KB2b-BR1	-9.17	-4.63	26.15	0.70832	0.000013
	KB2b-BR2	-8.35	-4.34	26.45	0.708345	0.000009
Amos vein system	AMO-1B-005	-9.20	-4.38	26.41		
	AMO-1B-015	-9.46	-4.64	26.14		
	AMO-1B-020	-9.82	-4.78	25.99		
	AMO-1B-025	-9.78	-4.63	26.15		
	AMO-1B-035	-9.57	-4.52	26.26		
	AMO-1B-050	-9.63	-4.34	26.45		
	AMO-1B-055	-9.89	-4.26	26.53		
	AMO-1B-065	-10.02	-4.30	26.49		
	AMO-1B-070	-10.31	-4.47	26.31	0.708308	0.000011
	AMO-1B-075	-10.56	-4.62	26.16		
	AMO-1B-080	-10.47	-4.39	26.40		
	AMO-1B-090	-9.84	-4.26	26.53		
	AMO-1B-0975	-9.70	-4.52	26.26		
	AMO-1B-100	-9.65	-4.00	26.8		
	AMO-1B-105	-9.40	-3.51	27.30	0.708268	0.000007
	AMO-1B-110	-9.28	-3.36	27.46		
	AMO-1B-115	-9.00	-3.80	27.01		
	AMO-1B-120	-8.86	-3.83	26.97		
	AMO-1B-125	-8.70	-3.51	27.30		
	AMO-1B-130	-8.76	-3.50	27.31	0.708245	0.000008
	AMO-1B-135	-8.97	-3.33	27.49		
	AMO-1B-140	-9.67	-3.42	27.40		
	AMO-1B-145	-9.47	-4.53	26.25		
	AMO-1B-150	-9.24	-5.79	24.95	0.708312	0.000011
	AMO-1B-160	-9.16	-5.88	24.86		
	AMO-1B-165	-8.94	-5.68	25.07		
	AMO-1B-170	-8.83	-5.43	25.33		
	AMO-1B-175	-8.87	-4.88	25.89		
	AMO-1B-180	-9.29	-4.30	26.49	0.708348	0.00001
	AMO-1B-190	-9.87	-3.93	26.87		
	AMO-1B-200	-9.88	-3.51	27.30		
	AMO-1B-205	-10.28	-4.33	26.46		
	AMO-1B-210	-9.97	-4.23	26.57	0.708285	0.00001
	AMO-1B-220	-9.74	-3.93	26.87		
	AMO-B-005	-10.02	-3.69	27.11	0.708397	0.000009
	AMO-B-015	-9.83	-2.92	27.91		
	AMO-B-020	-9.80	-2.98	27.85		
	AMO-B-025	-9.51	-3.00	27.83		

	AMO-B-030	-9.38	-3.09	27.74	0.708404	0.000007
	AMO-B-035	-9.53	-3.07	27.76		
	AMO-B-045	-9.59	-2.93	27.91		
	AMO-B-050	-9.51	-3.05	27.78		
	AMO-B-060	-9.56	-3.29	27.53	0.708308	0.000011
	AMO-B-065	-9.54	-3.43	27.39		
	AMO-B-075	-9.19	-4.14	26.65		
	AMO-B-080	-9.28	-3.77	27.03		
	AMO-B-085	-9.47	-4.00	26.8	0.708399	0.000007
	AMO-B-0925	-9.65	-4.06	26.73		
	AMO-B-100	-9.69	-4.27	26.52		
	AMO-B-105	-9.31	-4.42	26.36		
	AMO-2-3-020	-9.45	-3.40	27.41	0.708375	0.000011
	AMO-2-3-035	-9.53	-3.24	27.59		
	AMO-2-3-055	-9.39	-3.95	26.85		
	AMO-2-3-065	-9.96	-4.08	26.72	0.708245	0.000013
	AMO-2-3-080	-10.59	-4.46	26.32		
	AMO-2-3-095	-10.46	-4.41	26.37		
	AMO-2-3-120	-10.46	-4.66	26.12		
	AMO-2-3-125	-10.61	-4.77	26.01		
	AMO-2-3-135	-10.53	-4.66	26.12	0.708348	0.000009
	AMO-2-3-140	-10.59	-4.64	26.13		
	AMO-2-3-160	-10.57	-4.86	25.91		
	AMO-4-5-230	-9.60	-3.30	27.06		
	AMO-4-5-175	-9.64	-3.33	27.52	0.708285	0.000008
	AMO-4-5-100	-9.59	-2.83	27.49	0.708271	0.000007
	AMO-4-5-060	-9.84	-3.74	28.00	0.708335	0.000009
	AMO-4-5-040	-9.71	-3.84	26.97	0.708337	0.000009
Host limestone		2.40	2.15	32.80		
Distal limestone		2.30	-1.15	29.40		

* VPDB: Vienna Peedee Belemnite

**VSMOW: Vienna Standard Mean Ocean Water

Note: Host and distal limestone stable (O and C) and Sr isotope ratios are gathered from Uysal et al. (2011).

Table S3 Summary of Rare Earth Element (including Yttrium: REY) data of calcite vein/breccia from Kumlubük and Amos (Marmaris, SW Turkey). Concentrations ar

Sample ID	La	Ce	Pr	Nd	Sm	Eu	Gd	Tb	Dy	Y	Ho	Er	Tm	Yb	L
KB1a-BR	8575.51	4731.66	1559.20	6703.66	1419.02	345.82	1781.10	257.62	1612.38	16546.21	375.57	1047.68	143.84	832.05	117
KB1a-0375	9.0902	11.5423	2.6698	12.2849	2.9765	0.871	4.29	0.9067	8.081	132.6741	2.2542	7.533	1.3517	9.6141	1.62
KB1a-0750	10.7162	14.0784	2.893	13.8981	3.4567	0.8268	5.1324	0.8012	5.6608	70.6831	1.6104	4.6199	0.8232	5.4113	0.81
KB1a-1025	12.5234	22.1121	3.0137	13.1227	3.2251	0.8076	3.1224	0.4739	2.9114	25.6645	0.6313	1.9745	0.3403	1.7311	0.30
KB1a-1400	6.9501	7.6872	1.9968	8.276	2.227	0.6223	3.054	0.507	3.663	51.244	0.9102	3.0567	0.456	3.2332	0.52
KB1a-1825	4.6691	5.4887	1.0693	5.4029	1.2606	0.5633	1.5244	0.2918	1.4821	26.1158	0.556	1.5338	0.2638	1.7925	0.30
KB1a-2150	14.2561	18.591	3.6603	15.8255	3.9038	1.1343	4.9279	0.7749	5.4926	69.8016	1.4816	4.3415	0.6824	4.5129	0.74
KB1a-2525	6.4411	9.3735	1.3777	6.9508	1.7714	0.6134	2.0742	0.2695	2.0796	26.5451	0.5512	1.4675	0.2352	1.6871	0.28
KB1a-2925	28.7255	37.6449	7.3123	34.2002	8.707	2.369	11.3772	1.8418	12.7127	168.0384	3.2839	10.7156	1.5491	9.9848	1.59
KB1a-3225	16.1975	22.294	4.0886	18.6936	4.5904	1.2616	5.937	1.0365	7.5045	91.072	1.7107	5.9297	0.9338	5.134	0.94
KB1a-3400	12.2968	22.9901	2.7031	11.5887	2.4672	0.7055	2.9248	0.3449	1.9213	14.0236	0.5126	1.1845	0.1583	1.0365	0.14
KB1b-BR1	26.2132	51.02	6.8682	27.3576	6.0438	1.3688	7.0718	0.9794	6.015	39.9726	1.0538	3.2582	0.4103	2.6397	0.40
KB1b-BR2	148.7817	191.8222	24.6839	89.9664	13.7589	3.2018	14.6543	2.2192	12.2073	78.9543	2.4342	6.6147	0.8475	5.4155	0.92
KB1b-025	6.2929	8.9083	1.3386	6.3073	1.6375	0.4769	1.4164	0.2571	1.9482	27.8004	0.4324	1.6025	0.2855	1.7021	0.33
KB1b-075	10.2571	12.2147	1.8019	7.5817	1.9342	0.5017	2.5723	0.4343	2.6735	36.4334	0.6468	2.5078	0.3372	2.3594	0.35
KB1b-115	8.8603	16.0645	2.2283	8.9946	2.2151	0.6736	2.4236	0.4454	1.8956	21.2198	0.4953	1.4291	0.183	1.3315	0.5
KB1b-145	7.1574	11.0073	1.7372	7.8341	1.9303	0.5652	2.5726	0.3495	2.2992	33.3697	0.5839	1.9363	0.3207	2.1838	0.32
KB1b-180	6.4766	9.8488	1.6035	6.6786	1.8325	0.3341	2.2802	0.3924	2.9075	40.4012	0.7656	2.5293	0.3982	2.9049	0.43
KB1b-200	10.6141	16.9684	2.7645	11.8069	3.3422	0.7741	4.0436	0.6068	3.7178	49.9376	0.9939	3.3523	0.6842	3.2856	0.68
KB2a-2300	8.4256	6.7029	2.1558	8.543	2.0278	0.7051	3.0256	0.4739	3.4292	57.6441	0.9913	3.4772	0.5192	3.4073	0.57
KB2a-1750	4.2239	4.8739	0.934	3.9701	1.0375	0.4245	1.3	0.2265	1.2181	17.7877	0.345	1.2303	0.1462	1.2951	0.19
KB2a-1350	3.8381	4.3709	0.8584	3.9124	0.9049	0.3665	1.1616	0.1582	0.9318	9.841	0.2462	0.6671	0.1282	0.6469	0.11
KB2a-1000	53.0183	79.3525	13.7188	55.6981	12.9768	3.1955	13.6357	1.9981	11.8236	90.6614	2.4372	6.837	0.9696	5.6528	0.95
KB2a-0700	8.3122	15.0585	1.9294	8.1989	1.7735	0.5653	2.0826	0.2452	1.8288	11.6049	0.3248	0.8066	0.1194	0.805	0.11
KB2a-0450	8.4657	15.2792	1.9973	8.4615	1.9845	0.5017	2.2012	0.3098	1.9499	22.3243	0.4462	1.4332	0.2308	1.3651	0.22
KB2a-0100	17.5243	20.8834	4.2728	18.6592	3.9597	1.1438	4.9989	0.714	4.5626	64.0491	1.2352	3.7726	0.5952	3.9438	0.73
KB2a-BR1	188.8812	282.8419	49.1449	206.9812	46.2954	10.9205	49.5035	6.8566	36.9891	251.6732	7.3005	18.6673	2.5563	15.1755	2.22
KB2a-BR2	744.5261	1019.0235	196.9678	829.9469	185.858	42.8162	193.1469	27.1826	152.3889	1024.0484	30.5044	78.8578	10.4684	62.1506	8.80
KB2a-BR3	588.7217	700.9057	144.8325	617.4326	142.2093	34.2459	163.3913	24.9639	148.4607	1379.9633	32.5131	92.2301	12.6594	80.0781	11.6
KB2b-BR1	10.3942	12.3294	2.5858	11.8053	2.4462	0.5986	3.0787	0.4837	3.256	52.7872	0.8328	3.0144	0.5204	3.1132	0.52
KB2b-BR2	68.026	101.6803	18.5032	77.315	16.6056	4.0742	18.2239	2.7057	15.3812	104.3123	2.8979	7.2897	0.9818	6.5757	0.9
KB2b-295	103.6454	56.5571	29.5632	127.0535	28.0396	7.2757	37.8552	6.207	45.2188	722.8355	12.0857	38.8804	5.9756	39.9691	6.15
KB2b-250	9.7688	9.2793	2.6072	11.6284	1.7521	0.6083	3.4837	0.6578	4.8424	97.2788	1.3617	4.9365	0.8085	5.6069	0.93
KB2b-210	28.2434	31.1058	7.6563	32.0135	7.8889	1.3317	7.3972	1.0915	5.2187	47.2063	1.1102	3.3745	0.3914	2.4965	0.37
KB2b-160	19.0462	16.8206	5.1515	23.7329	5.3775	1.3857	7.3799	1.3415	10.6843	191.7608	2.9131	10.1654	1.5593	12.1257	1.96
KB2b-110	21.9598	30.9758	5.8028	23.9009	4.8615	1.1878	5.5902	0.8088	5.28	62.5564	1.3574	4.1112	0.5417	4.0327	0.63
KB2b-070	15.6679	16.683	3.8127	16.3227	3.4463	1.1021	5.6362	0.935	5.506	90.5788	1.8641	5.5407	0.8678	5.206	1.0

KB2b-040	15.5526	17.178	3.7635	16.1628	3.8164	0.8943	4.4869	0.7547	6.0171	91.275	1.4762	5.0856	0.7467	5.6125	0.95
AMO-1B/070	1.8842	0.544	0.3757	2.0442	0.4298	0.4771	0.8957	0.2131	1.2407	36.1337	0.4103	1.2488	0.1458	1.0099	0.20
AMO-1B/105	34.3037	4.2539	9.8455	44.9186	9.2316	2.9768	13.8749	2.0474	15.1671	275.342	4.0565	11.084	1.8083	11.0082	1.61
AMO-1B/130	20.7477	6.7648	8.7875	46.5425	11.7769	3.5048	20.3087	3.4963	28.1252	543.2944	7.9374	24.4174	3.4801	21.3912	3.43
AMO-1B/150	34.085	20.8722	14.4397	75.9135	19.2619	5.3458	25.9723	4.6142	33.3162	406.3006	7.596	20.9231	2.9123	17.6539	2.45
AMO-1B/180	26.0421	13.8747	8.3906	40.7589	9.5462	3.3702	14.3044	2.4461	18.4846	247.516	4.5698	13.5132	1.9357	11.8774	1.61
AMO-1B/215	242.3969	32.2638	61.6195	242.6227	42.6217	10.5024	44.208	6.1214	35.8803	376.4021	7.9364	21.3542	2.6664	15.0526	2.0
AMO-2-3/020	16.7288	28.3436	2.9849	10.8196	2.2416	1.4288	1.8353	0.3561	2.3564	26.1153	0.4606	1.6642	0.2431	1.5999	0.24
AMO-2-3/065	84.3927	49.1913	36.967	185.3048	45.0633	12.7473	63.5842	10.9233	77.6832	945.9588	17.8266	50.218	6.6112	38.6082	5.63
AMO-2-3/135	402.3046	184.0801	182.9453	937.7127	226.4565	62.8805	324.8197	54.8953	394.1831	4663.3407	90.6034	252.0385	32.5506	191.0921	26.5
AMO-4-5/060	223.1759	130.3208	86.9363	389.905	90.5627	22.2071	100.5036	16.0374	97.3282	917.1854	21.0442	52.6535	6.6181	40.1816	5.49
AMO-4-5/230	22.4543	13.8733	10.6534	50.4142	11.9082	3.1723	13.0639	2.0944	12.908	124.6739	2.7087	6.8356	0.8322	4.8588	0.71
AMO-4-5/175	211.2006	106.6417	98.3846	464.6423	114.3234	30.0768	147.7435	24.3713	156.4047	1877.3615	36.2956	100.9921	13.1438	80.6833	11.9
AMO-4-5/100	247.9343	133.8956	114.7026	557.3803	133.6497	35.0892	172.9679	28.4371	193.1404	2226.721	43.4859	118.1444	15.6125	90.9662	12.8
AMO-4-5/040	275.6558	100.5498	102.7056	465.2327	100.112	24.9361	116.052	18.0492	115.4066	1055.3783	24.361	64.9945	8.3566	47.2689	6.58
AMO-B-085	10.0859	6.8551	2.1031	10.9431	2.6721	1.5883	3.3829	0.3755	2.5344	25.8961	0.6203	1.7149	0.2605	1.4854	0.24
AMO-B-060	10.3419	11.326	2.8526	13.0867	3.2206	1.662	2.907	0.3914	2.0565	16.632	0.4043	1.1158	0.1663	0.8076	0.12
AMO-B-030	12.9239	16.2141	3.4118	16.0843	3.4616	1.2499	3.3237	0.5004	2.1608	18.7227	0.4622	1.3735	0.118	0.8233	0.1
AMO-B-005	14.4137	21.4429	3.0672	13.3441	2.5848	0.9695	2.5719	0.3685	2.2564	14.9053	0.431	0.9169	0.1517	0.85	0.07
Host limestone	8285.73	5760.93	1766.56	7515.29	1615.6	387.45	1898.35	271.68	1599.62	13092.85	335.16	887.49	118.6	711.19	100

Note: Host limestone REY values are gathered from Uysal et al., 2011.

REFERENCES (PAPER 2)

Aldanmaz, E. et al., 2000. Petrogenetic evolution of late Cenozoic, post-collision volcanism in western Anatolia, Turkey. *Journal of Volcanology and Geothermal Research*, 102(1-2), pp.67–95. Available at: http://linkinghub.elsevier.com/retrieve/pii/S0377027300001827.

Altunel, E. & Hancock, P.L., 1996. Structural Attributes of Travertine-Filled Extensional Fissures in the Pamukkale Plateau, Western Turkey. *International Geology Review*, 38(8), pp.768–777.

Baker, A. et al., 1997. Elevated and variable values of 13C in speleothems in a British cave system. *Chemical Geology*, 136(3-4), pp.263–270. Available at: http://linkinghub.elsevier.com/retrieve/pii/S0009254196001295.

Barka, A. et al., 1995. The Isparta Angle: its importance in the neotectonics of the Eastern Mediterranean Region. Proceedings of the International Earth Sciences Colloquium on the Aegean Region. In *Proceedings of the International Earth Sciences Colloquium on the Aegean Region*. pp. 3–18.

Barka, A. & Reilinger, R., 1997. Active tectonics of the Eastern Mediterranean region: deduced from GPS, neotectonic and seismicity data. *Annali Di Geofisica*, XL, pp.587–610.

Bar-Matthews, M. et al., 2003. Sea–land oxygen isotopic relationships from planktonic foraminifera and speleothems in the Eastern Mediterranean region and their implication for paleorainfall during interglacial intervals. *Geochimica et Cosmochimica Acta*, 67(17), pp.3181–3199.

Bau, M. et al., 2010. Rare earth elements in mussel shells of the Mytilidae family as tracers for hidden and fossil high-temperature hydrothermal systems. *Earth and Planetary Science Letters*, 299(3-4), pp.310–316. Available at: http://linkinghub.elsevier.com/retrieve/pii/S0012821X10005868 [Accessed October 5, 2012].

Bau, M. & Dulski, P., 1996. Distribution of yttrium and rare-earth elements in the Penge and Kuruman iron-formations, Transvaal Supergroup, South Africa. *Precambrian Research*, 79, pp.37–55.

Bau, M., Möller, P. & Dulski, P., 1997. Yttrium and lanthanides in eastern Mediterranean seawater and their fractionation during redox-cycling. *Marıie Chemistry*, 56(96).

Bergfeld D., Evans, W. C., Lowenstern, J. B., Hurwitz, S. (2012) Carbon dioxide and hydrogen sulfide degassing and cryptic thermal input to Brimstone Basin, Yellowstone National Park, Wyoming. *Chem Geol* **330-331**, 233–243.

Blenkinsop, T.G., 2000. *Recognition of Deformation, Microstructures and Mechanisms in Rocks*, Chapman & Hall.

Blenkinsop T. G. and Sibson R.H. (1992) Aseismic fracturing and cataclasis involving reaction softening within core material from the Cajon Pass Drill Hole. *J Geophysical Res.* **97,** 5135–5144.

Bolhar, R. et al., 2004. Characterisation of early Archaean chemical sediments by trace element signatures. *Earth and Planetary Science Letters*, 222(1), pp.43–60. Available at: http://linkinghub.elsevier.com/retrieve/pii/S0012821X04001347 [Accessed May 28, 2013].

Bottinga, Y., 1968. Calculation of Fractionation Factors for Carbon and Oxygen Isotopic Exchange in the System Calcite-Carbon Dioxide-Water. *The Journal of Physical Chemistry*, 72(1), pp.801–808.

Boullier, A. & Robert, F., 1992. Palaeoseismic events recorded in Archaean gold-quartz vein networks, Val d'Or, Abitibi, Quebec, Canada. *Journal of Structural Geology*, 14(2), pp.161–179.

Bowers, T.S., 1991. The deposition of gold and other metals: Pressure-induced fluid immiscibility and associated stable isotope signatures. *Geochimica et Cosmochimica Acta*, 55(9), pp.2417–2434. Available at: http://linkinghub.elsevier.com/retrieve/pii/001670379190363A.

Brogi, A. et al., 2014. Evolution of a fault-controlled fissure-ridge type travertine deposit in the western Anatolia extensional province: the Cukurba fissure-ridge (Pamukkale, Turkey). *Journal of the Geological Society*, 171(3), pp.425–441. Available at: http://jgs.lyellcollection.org/cgi/doi/10.1144/jgs2013-034 [Accessed July 18, 2014].

Cartwright I., Weaver T., Tweed S., Ahearne D., Cooper M., Czapnik K. and Tranter J. (2002) Stable isotope geochemistry of cold CO_2-bearing mineral spring waters, Daylesford, Victoria, Australia: sources of gas and water and links with waning volcanism. *Chem Geol* **185**, 71– 91.

Çakir, Z., 1999. Along-Strike Discontinuity of Active Normal Faults and Its Influence on Quaternary Travertine Deposition; Examples From Western Turkey. *Turkish Journal of Earth Sciences*, 8, pp.67–80.

Capo R. C., Stewart B. W. and Chadwick O. A. (1998) Strontium isotopes as tracers of ecosystem processes: theory and methods. *Geoderma* **82**, 197–225.

Ceron, J.C., Pulido-bosch, A. & Galdeano, C.S. De, 1998. Isotopic identification of CO2 from a deep origin in thermomineral waters of southeastern Spain. *Chemical Geology*, 149, pp.251–258.

Cheng, H. et al., 2000. The half-lives of uranium-234 and thorium-230. *Chemical Geology*, 169(1-2), pp.17–33. Available at: http://linkinghub.elsevier.com/retrieve/pii/S0009254199001576.

Chiodini, G., 2004. Carbon dioxide Earth degassing and seismogenesis in central and southern Italy. *Geophysical Research Letters*, 31(7).

Clark, T.R. et al., 2014. Discerning the timing and cause of historical mortality events in modern Porites from the Great Barrier Reef. *Geochimica et Cosmochimica Acta*, 138, pp.57–80. Available at: http://linkinghub.elsevier.com/retrieve/pii/S0016703714002804 [Accessed August 23, 2014].

Clark, T.R. et al., 2012. Spatial variability of initial 230Th/232Th in modern Porites from the inshore region of the Great Barrier Reef. *Geochimica et Cosmochimica Acta*, 78, pp.99–118. Available at: http://linkinghub.elsevier.com/retrieve/pii/S0016703711007071 [Accessed March 18, 2013].

Collins, A.S. & Robertson, A.H.F., 1999. Evolution of the Lycian Allochthon, western Turkey, as a north-facing Late Palaeozoic to Mesozoic rift and passive continental margin. *Geological Journal*, 34(1-2), pp.107–138. Available at: http://doi.wiley.com/10.1002/%28SICI%291099-1034%28199901/06%2934%3A1/2%3C107%3A%3AAID-GJ817%3E3.0.CO%3B2-L.

Coplen T.B. (2007) Calibration of the calcite–water oxygen-isotope geothermometer at Devils Hole, Nevada, a natural laboratory. *Geochim. Cosmochim. Acta* **71**, 3948–3957.

Cox, S.F., 1987. Antitaxial crack-seal vein microstructures and their relationship to displacement paths. *Journal of Structural Geology*, 9(7), pp.779–787. Available at: http://linkinghub.elsevier.com/retrieve/pii/0191814187900794.

Cox, S.F., 1995. Faulting processes at high fluid pressures: An example of fault valve behavior from the Wattle Gully Fault, Victoria, Australia. *Journal of Geophysical Research: Solid Earth*, 100(B7), pp.12841–12859. Available at: http://dx.doi.org/10.1029/95JB00915.

Cox, S.F. & Etheridge, M.A., 1983. Crack-Seal Fibre Growth Mechanisms and Their Significance in the Development of Oriented Layer Silicate Microstructures. *Tectonophysics*, 92, pp.147–170.

D'Alessandro, W. et al., 2007. Geochemistry and mineralogy of travertine deposits of the SW flank of Mt. Etna (Italy): Relationships with past volcanic and degassing activity. *Journal of Volcanology and Geothermal Research*, 165(1-2), pp.64–70.

Duman, Y.T. et al., 2011. *1:250,000 Scale Active Fault Map Series of Turkey, Aydın (NJ36-11) Quadrangle. Serial Number 7*, Ankara, Turkey.

Eggins, S.M. et al., 1997. A simplemethod for the precise determination of N40 trace elements in geological samples by ICPMS using enriched isotope internal standardisation. *Chemical Geology*, 134, pp.311–326.

Emre, O., Duman, Y.T. & Özalp, S., 2011. *1:250,000 Scale Active Fault Map Series of Turkey, Marmaris (NJ36-16) Quadrangle. Serial Number 8*, Ankara, Turkey.

Ersoy, S., 1997. The syn-collisional deep-water sediments of the Marmaris Complex as a part of the Lycian Nappes, SW Turkey. In *International Earth Sciences Colloquium of the Aegean Region*. Izmir–Güllük, Turkey, pp. 95–111.

Eyidogan, H. et al., 1996. The 1 October 1995 Dinar earthquake, SW Turkey. *Terra Nova*, 8(October 1995), pp.479–485.

Faccenna, C. et al., 2008. Late Pleistocene depositional cycles of the Lapis Tiburtinus travertine (Tivoli, Central Italy): Possible influence of climate and fault activity. *Global and Planetary Change*, 63(4), pp.299–308. Available at: http://linkinghub.elsevier.com/retrieve/pii/S0921818108000696 [Accessed February 19, 2014].

Famin, V. et al., 2008. Earthquakes produce carbon dioxide in crustal faults. *Earth and Planetary Science Letters*, 265(3-4), pp.487–497. Available at: http://linkinghub.elsevier.com/retrieve/pii/S0012821X07006838 [Accessed July 18, 2014].

Famin, V. et al., 2005. Ion probe and fluid inclusion evidence for co-seismic fluid infiltration in a crustal detachment. *Contributions to Mineralogy and Petrology*, 150(3), pp.354–367. Available at: http://link.springer.com/10.1007/s00410-005-0031-x [Accessed July 18, 2014].

De Filippis, L. et al., 2012. Growth of fissure ridge travertines from geothermal springs of Denizli Basin, western Turkey. *Geological Society of America Bulletin*, 124(9-10), pp.1629–1645. Available at: http://gsabulletin.gsapubs.org/cgi/doi/10.1130/B30606.1 [Accessed November 28, 2012].

De Filippis, L. et al., 2013. Plateau versus fissure ridge travertines from Quaternary geothermal springs of Italy and Turkey: Interactions and feedbacks between fluid discharge, paleoclimate, and tectonics. *Earth-Science Reviews*, 123, pp.35–52. Available at: http://linkinghub.elsevier.com/retrieve/pii/S0012825213000706 [Accessed February 2, 2014].

Ersoy S. (1997) The syn-collisional deep-water sediments of the Marmaris Complex as a part of the Lycian Nappes, SW Turkey. *International Earth Sciences Colliquim of the Aegean region*, 9–14 Oct 1995, Izmir, Turkey, **1**, 95–111.

Friedman, I. & O'Neil, J.R., 1977. *Compilation of Stable Isotope Fractionation Factors of Geochemical Interest* 6th ed., Washington D.C.: Geological Survey, United States government printing office.

Frisia, S. (2015) Microstratigraphic logging of calcite fabrics in speleothems as tool for palaeoclimate studies. *Int. J. Spel.* **44**, 1–16.

Frisia, S. et al., 2000. Calcite Fabrics, Growth Mechanisms, and Environments of Formation in Speleothems from the Italian Alps and Southwestern Ireland. *Society for Sedimentary Geology*, 70(5), pp.1183–1196.

Frisia-Bruni, S., Jadoul, F. & Weissert, H., 1989. Evinosponges in the Triassic Esino Limestone (Southern Alps): documentation of early lithification and late diagenetic overprint. *Sedimentology*, 36(4), pp.685–699. Available at: http://doi.wiley.com/10.1111/j.1365-3091.1989.tb02093.x.

Görür, N. et al., 1995. Rift formation in the Gokova region , southwest Anatolia : implications for the opening of the Aegean Sea. *Geological Magazine*, 132(6), pp.637–650.

Grootes P. M., Stuiver M., White J. W. C., Johnsen S. J. and Jouzel J. (1993) Comparison of oxygen isotope records from the GISP2 and GRIP Greenland ice cores. *Nature* **366**, 552-554.

Hancock, P.L. et al., 1999. Travitonics: using travertines in active fault studies. *Journal of Structural Geology*, 21, pp.903–916.

Hetzel, R. et al., 2013. Spatiotemporal evolution of brittle normal faulting and fluid infiltration in detachment fault systems: A case study from the Menderes Massif, western Turkey. *Tectonics*, 32, pp.1–13. Available at: http://doi.wiley.com/10.1002/tect.20031 [Accessed June 13, 2013].

Hughes P.D., Gibbard P.L., Ehlers J. (2013)Timing of glaciation during the last glacial cycle: evaluating the concept of a global 'Last Glacial Maximum' (LGM). *Earth Science Rev.***125,** 171–198.

Van Hinsbergen, D.J.J., 2010. A key extensional metamorphic complex reviewed and restored: The Menderes Massif of western Turkey. *Earth-Science Reviews*, 102(1-2), pp.60–76. Available at: http://linkinghub.elsevier.com/retrieve/pii/S0012825210000620 [Accessed November 8, 2012].

Irwin, W.P. & Barnes, I., 1980. Tectonic Relations of Carbon Dioxide Discharges and Earthquakes. *Journal of Geophysical Research*, 85, pp.3115–3121.

Kamber, B.S. et al., 2003. A refined solution to Earth's hidden niobium: implications for evolution of continental crust and mode of core formation. *Precambrian Research*, 126(3-4), pp.289–308. Available at: http://linkinghub.elsevier.com/retrieve/pii/S0301926803001001 [Accessed March 5, 2014].

Kampman, N. et al., 2012. Pulses of carbon dioxide emissions from intracrustal faults following climatic warming. *Nature Geoscience*, 5, pp.352–358.

KOERI, 2015. Kandilli Observatory and Earthquake Research Institute of Turkey. Available at: http://www.koeri.boun.edu.tr/jeofizik/ [Accessed July, 2015]

Li, H.-C. et al., 2005. 87Sr/86Sr and Sr/Ca in speleothems for paleoclimate reconstruction in Central China between 70 and 280 kyr ago. *Geochimica et Cosmochimica Acta*, 69(16), pp.3933–3947. Available at: http://linkinghub.elsevier.com/retrieve/pii/S001670370500058X [Accessed December 5, 2014].

Loges, A. et al., 2013. An experimental study of the aqueous solubility and speciation of Y(III) fluoride at temperatures up to 250°C. *Geochimica et Cosmochimica Acta*, 123, pp.403–415. Available at: http://linkinghub.elsevier.com/retrieve/pii/S0016703713004195 [Accessed July 18, 2014].

Ludwig, K.R., 2003. Users Manual for Isoplot/Ex version 3.0: a Geochronological Toolkit for Microsoft Excel. , p.70.

Mattey, D. P., Fisher, R., Atkinson, T. C., Latin, J.-P., Durrel, R., Ainsworth, M., Lowry, D., Fairchild, I. J. (2013) Methane in underground air in Gibraltar karst. *Earth Planet. Sci. Lett.* **374**, 71–80.

McClusky, S. et al., 2000. Global Positioning System constraining on plate kinematics and dynamics in the eastern Mediterranean and Caucasus. *Journal of Geophysical Research*, 105(B3), pp.5695–5719.

McKenzie D. (1978) Active tectonics of the Alpine-Himalayan belt: the Aegean Sea and surrounding regions. *Geophys. J. R. Astron. Sot.* **55**, 217–254.

McKenzie D. (1972) Active tectonics of the Mediterranean region. *Geophys. J. Int.* **30**, 109–185.

McKenzie, D., 1970. Plate Tectonics of the Red Sea and East Africa. *Nature*, 228, pp.547–548.

Muchez, P. et al., 2008. Petrography, mineralogy and geochemistry of the rocks in the area of the archaeological site of Sagalassos. In P. J. Waelkens M, ed. *Sagalassos 6. Acta Archaeologica Lovaniensia Monographiae*. Leuven: University Press Leuven, pp. 25–52.

Van Noten, K. et al., 2013. Fracture networks and strike–slip deformation along reactivated normal faults in Quaternary travertine deposits, Denizli Basin, western Turkey. *Tectonophysics*, 588, pp.154–170. Available at: http://linkinghub.elsevier.com/retrieve/pii/S0040195112008074 [Accessed July 18, 2014].

Nuriel, P. et al., 2011. Formation of fault-related calcite precipitates and their implications for dating fault activity in the East Anatolian and Dead Sea fault zones. *Geological Society, London, Special Publications*, 359(1), pp.229–248. Available at: http://sp.lyellcollection.org/cgi/doi/10.1144/SP359.13 [Accessed August 21, 2012].

Nuriel, P. et al., 2012. U-Th dating of striated fault planes. *Geology*, 40, pp.647–650. Available at: http://geology.gsapubs.org/cgi/doi/10.1130/G32970.1 [Accessed August 1, 2012].

Okay, A., 1989. Geology of the Menderes Massif and the Lycian Nappes south of Denizli, western Taurides. *Mineral Research Exploration Bulletin (Ankara)*, 109, pp.37–51.

Pauwels H., Fouillac C., Goff F., Vuataz F. D. (1997) The isotopic and chemical composition of CO_2-rich thermal waters in the Mont-Dore region (Massif-Central, France). *Appl Geochem*. **12**, 411–427.

Rahmstorf S. (2003) Timing of abrupt climate change: A precise clock. *Geophys. Res. Lett.* **30**, 1510, doi:10.1029/2003GL017115.

Pearce, J.M., 2006. What can we learn from natural analogues? An overview of how analogues can benefit the geological storage of CO2. In S. L. et Al., ed. *Advances in the Geological Storage of Carbon Dioxide*. Netherlands: Springer, pp. 129–139.

Pentecost, A., 2005. *Travertine*, Berlin Heidelberg: Springer-Verlag.

Le Pichon, X. & Angelier, J., 1979. The Hellenic Arc and Trench System: A Key To The Neotectonic Evolution of The Eastern Mediterranean Area. *Tectonophysics*, 60, pp.1–42.

Pili, É., Poitrasson, F. & Gratier, J.-P., 2002. Carbon–oxygen isotope and trace element constraints on how fluids percolate faulted limestones from the San Andreas Fault system: partitioning of fluid sources and pathways. *Chemical Geology*, 190(1-4), pp.231–250. Available at: http://linkinghub.elsevier.com/retrieve/pii/S0009254102001183.

Poisson, A., 1977. *Recherches geologiques dans les Taurides occidentales (Turquie)*. Th6se d'Etat Univ. Paris-Sud (Orsay).

Purvis, M. & Robertson, A., 2004. A pulsed extension model for the Neogene–Recent E–W-trending Alaşehir Graben and the NE–SW-trending Selendi and Gördes Basins, western

Turkey. *Tectonophysics*, 391(1-4), pp.171–201. Available at: http://linkinghub.elsevier.com/retrieve/pii/S0040195104002318 [Accessed January 14, 2014].

Ramsay, J.G., 1980. The crack-seal mechanism of rock deformation. *Nature*, 284, pp.135–139.

Reilinger, R.E. et al., 1997. Global Positioning System measurements of present-day crustal movements in the Arabia-Africa-Eurasia plate collision zone. *Journal of Geophysical Research*, 102(B5), p.9983. Available at: http://doi.wiley.com/10.1029/96JB03736.

Richards, D. & Dorale, J. a, 2003. Uranium-series chronology and environmental applications of speleothems. Reviews in mineralogy and geochemistry. *Reviews in Mineralogy and Geochemistry*, 52, pp.407–460.

Rihs, S., Condomines, M. & Poidevin, J.-L., 2000. Long-term behaviour of continental hydrothermal systems: U-series study of hydrothermal carbonates from the French Massif Central (Allier Valley). *Geochimica et Cosmochimica Acta*, 64(18), pp.3189–3199.

Robert, F., Boullier, A. & Firdaous, K., 1995. Gold-quartz veins in metamorphic terranes and their bearing on the role of luids in faulting. *Journal of Geophysical Research*, 100, pp.12,861–12,879.

Roff, G. et al., 2013. Palaeoecological evidence of a historical collapse of corals at Pelorus Island , inshore Great Barrier Reef , following European settlement. In *Proceedings of The Royal Society - B Biological Sciencces*. p. 280.

Rollinson, H.R., 1993. *Using Geochemical Data Evalution, Presentation, Interpretation*, Taylor & Francis.

Rosales, I., Quesada, S. & Robles, S., 2001. Primary and diagenetic isotopic signals in fossils and hemipelagic carbonates: the Lower Jurassic of northern Spain. *Sedimentology*, 48, pp.1149–1169.

Royden, L.H., 1993. Evolution of retreating subduction boundaries formed during continental collision. *Tectonics*, 12(3), pp.629–638. Available at: http://doi.wiley.com/10.1029/92TC02641.

Salomons, W., Goudie, A. & Mook, W.G., 1978. Isotopic Composition of Calcrete Deposits from Europe, Africa and India. *Earth surface Processes*, 3, pp.43–57.

Sarıkaya, M.A. et al. (2014) An early advance of glaciers on Mount Akdağ, SW Turkey, before the global Last Glacial Maximum; insights from cosmogenic nuclides and glacier modeling. *Quat. Sci. Rev.* **88**, 96–109.

Şenel, M., 2007. *Geology Map of Turkey, Marmaris Quadrangle. Serial Number 1*, Ankara, Turkey.

Şengör, A.M.C. & Yılmaz, Y., 1981. Tethyan Evolution Approach of Turkey: A Plate Tectonic Approach. *Tectonophysics*, 75, pp.181–241.

Seyitoglu, G. & Scott, B., 1991. Late Cenozoic crustal extension and basin formation in West Turkey. *Geological Magazine*, 128(2), pp.155–166. Available at: http://geolmag.geoscienceworld.org/cgi/content/long/128/2/155 [Accessed January 14, 2014].

Sibson R. H. (1989) Earthquake faulting as a structural process. *J. Struct. Geol.* **11**, 1–14.

Sibson R. H. (1996) Structural permeability of fluid-driven fault-fracture meshes. *J. Struct. Geol.* **18**, 1031–1042.

Sibson, R.H., Robert, F. & Poulsen, K.H., 1988. High-angle reverse faults , fluid-pressure cycling , and mesothermal gold-quartz deposits. *Geology*, 16, pp.551–555.

Sulem J. and Famin V. (2009) Thermal decomposition of carbonates in fault zones: Slip-weakening and temperature-limiting effects. *J Geophys. Res.* **114**, B03309, doi:10.1029/2008JB006004.

Taylor, H.P., 1988. Oxygen, hydrogen, and strontium isotope constraints on the origin of granites. *Transactions of the Royal Society of Edinburgh: Earth Sciences*, 79(September 1987), pp.317–338.

Taylor, S.R. & McLennnan, S.M., 1985. *The Continental Crust: Its Composition and Evolution: An Examination of the Geochemical Record Preserved in Sedimentary Rocks*, Blackwell, Oxford.

Temiz, U., Gökten, Y.E. & Eikenberg, J., 2013. Strike-slip deformation and U/Th dating of travertine deposition: Examples from North Anatolian Fault Zone, Bolu and Yeniçağ Basins, Turkey. *Quaternary International*, 312, pp.132–140.

Tsang, C., 2009. A Comparative Review of Hydrologic Issues Involved in Geologic Storage of CO2 and Injection Disposal of Liquid Waste. *Lawrence Berkeley National Laboratory*.

TSMS (2015) The Turkish State Meteorological Service. Available at: http://www.mgm.gov.tr/en-US/forecast-5days.aspx (last accessed July 2015).

Ünal-İmer. E, Shulmeister J., Zhao J-X., Uysal I. T., Feng Y-X., Nguyen, A. D. and Yuce G. (2015) An 80 kyr-long continuous speleothem record from Dim Cave, SW Turkey with paleoclimatic implications for the Eastern Mediterranean. *Nature Sci. Rep.* **5**, 13560, doi: 10.1038/srep13560

Ünal-İmer, E. et al., 2014. A high-resolution geochronological and geochemical study on Aegean carbonate deposits, SW Turkey. In *Geophysical Research Abstracts*. Vienna, pp. 16 EGU2014–16265–2.

Ünal-İmer, E. et al., 2013. Possible link between CO_2 degassing and climate change in SW Turkey. *Mineralogical Magazine*, 70(Goldschmidt2013 Abstracts), p.2379.

Uysal, I.T. et al., 2009. Hydrothermal CO2 degassing in seismically active zones during the late Quaternary. *Chemical Geology*, 265(3-4), pp.442–454.

Uysal, I.T. et al., 2011. Seismic cycles recorded in late Quaternary calcite veins: Geochronological, geochemical and microstructural evidence. *Earth and Planetary Science Letters*, 303(1-2), pp.84–96.

Ten Veen, J.H. & Kleinspehn, K.L., 2002. Geodynamics along an increasingly curved convergent plate margin: Late Miocene-Pleistocene Rhodes, Greece. *Tectonics*, 21(3), pp.8–1–8–21. Available at: http://doi.wiley.com/10.1029/2001TC001287.

Verhaert, G. et al., 2009. Fluid impact and spatial and temporal evolution of normal faulting in limestones . A case study in the Burdur- Isparta region (SW Turkey). *Geologica Belgica*, 12, pp.59–73.

Verhaert, G. et al., 2004. Origin of palaeofluids in a normal fault setting in the Aegean region. *Geofluids*, 4(4), pp.300–314. Available at: http://doi.wiley.com/10.1111/j.1468-8123.2004.00094.x.

Violay M., Nielsen S., Spagnuolo E., Cinti D., Di Toro G. and Di Stefano G. (2013) Pore fluid in experimental calcite-bearing faults: Abrupt weakening and geochemical signature of co-seismic processes. *Earth Planet. Sci. Lett.* **361**, 74–84.

Vuataz F. D. and Goff F. (1986) Isotope geochemistry of thermal and nonthermal waters in the Valles Caldera, Jemez Mountains, Northern New Mexico. *J. Geophys. Res*. **91(B2)**, 1835–1853.

Wiprut, D. & Zoback, M.D., 2000. Fault reactivation and fluid flow along a previously dormant normal fault in the northern North Sea. *Geology*, 28(7), pp.595–598.

Yılmaz, Y. et al., 2000. When Did the Western Anatolian Grabens Begin to Develop? *Geological Society, London, Special Publications*, 173(1), pp.353–384. Available at: http://sp.lyellcollection.org/cgi/doi/10.1144/GSL.SP.2000.173.01.17 [Accessed January 14, 2014].

Zhao, J-X. et al., 2001. Thermal ionization mass spectrometry U-series dating of a hominid site near Nanjing, China. *Geology*, 29, pp.27–30.

Zhou, H-Y. et al., 2011. Speleothem-derived Asian summer monsoon variations in Central China, 54-46 ka. *Journal of Quaternary Science*, 26(8), pp.781–790.

Zoback, M.D. & Gorelick, S.M., 2012. Earthquake triggering and large-scale geologic storage of carbon dioxide. *Proceedings of the National Academy of Sciences of the United States of America*, 109(26), pp.10164–8. Available at: http://www.pubmedcentral.nih.gov/articlerender.fcgi?artid=3387039&tool=pmcentrez&rendertype=abstract [Accessed February 19, 2014].

PAPER 3

The following paper presents high-resolution speleothem-based stable isotope (C, O) profiles from Dim Cave (SW Turkey) supported by a high precision U-series chronology. This study provides a significant paleoclimatic reconstruction for the northern part of the Eastern Mediterranean over the period from ~90 to 10 kyr, covering the whole of the last glaciation as well as the transition to the Holocene.

An 80 kyr-long continuous speleothem record from Dim Cave, SW Turkey with paleoclimatic implications for the Eastern Mediterranean

Summary

Speleothem-based stable isotope records are valuable in sub-humid and semi-arid settings where many other terrestrial climate proxies are fragmentary. The Eastern Mediterranean is one such region. Here we present an 80-kyr-long precisely-dated (by U-series) and high-resolution oxygen ($\delta^{18}O$) and carbon ($\delta^{13}C$) records from Dim Cave (~36°N) in SW Turkey. The glacial-interglacial $\delta^{18}O$ variations in the Dim Cave speleothem are best explained in terms of changes in the trajectories of winter westerly air masses. These are along a northerly (European) track (isotopically less depleted) during the early last glaciation but are gradually depressed southward closer to the modern westerly track along the North African coast (more depleted) after c.50 kyr and remain in the southern track through the last glacial maximum. The southward displacement of the westerly track reflects growth of the Fennoscandian ice sheet and its impact on westerly wind fields. Changes in $\delta^{13}C$ are interpreted as reflecting soil organic matter composition and/or thickness. $\delta^{13}C$ values are significantly more negative in interglacials reflecting active carbonic acid production in the soil and less negative in glacial times reflecting carbonate rock values. Several Heinrich events are recorded in the Dim record indicating intensification of westerly flow across this part of the EM.

Keywords: Palaeoclimate, stalagmites, U-series dating, stable isotopes, westerlies, Fennoscandian ice sheet, Eastern Mediterranean

1. Introduction

Understanding the climate history of the Eastern Mediterranean (EM) region is of global significance because it lies on the boundary between two major climate regimes, the northern hemisphere westerlies and the sub-tropical anticyclonic belt, and the region has the potential to unlock long term changes in the track and strength of the westerlies and the intensity of the summer anti-cyclone. To date, high resolution (up to 250 kyr; Ayalon et al. 2002; Bar-Matthews et al. 1997; Bar-Matthews et al. 1999; Bar-Matthews et al. 2003 long) speleothem records have come from Soreq (~31°N) and Peqiin (~33°N) caves in Israel. These records are derived from the semi-arid southernmost part of the EM. They may be subject to more tropical influences and have, in the main, being exploited for the interglacial portion of their records. There is a paucity of records from further north. The longest (50-kyr-long) and best dated terrestrial climate record from the northern EM comes from Sofular cave (41°N) situated in the northwest Black Sea region of Turkey (Fig. 1a). This region has a climate that is modified by the Black Sea and northerly air flows (Fleitmann et al. 2009; Göktürk et al. 2011) unlike the rest of the EM. In contrast, coastal western Turkey has a true Mediterranean climate and is an ideal location to investigate long-term changes in the behaviour of the NH winter westerlies and the summer anti-cyclone. Here we present new $\delta^{18}O$ and $\delta^{13}C$ profiles for three U-series-dated stalagmites (Dim-E2, Dim-E3, and Dim-E4) from Dim Cave in south-western Turkey (Fig. 1a, b). The main focus of the paper is on stalagmite Dim-E3 (~13–89 kyr) but Dim-E2 and Dim-E4 are being reported also so as to provide additional detail during the last deglaciation between 10–15 kyr (Table S1 online).

2. Regional setting and climate of the Dim Cave

The Dim (or locally known as Gavurini) Cave (36°32'N, 32°06'E, 232 m a.s.l.) is located on the western flank of Cebel Reis Mountain (1691 m a.s.l.; Figs. 1b and S1a online) of the Central Taurus Mountains and is situated ~6 km from the Mediterranean coast of SW Turkey (Fig. 1a, b). The cave is 360 m long, 10–15 m wide and high and is formed in late Paleozoic crystalline limestone along a NW-SE trending fault (Fig. S1b; Gündalı et al. 1989). The annual mean temperature inside the cave ranges between 18–19 ºC with a humidity level of about 90% throughout the year. The modern climate above the cave is typical Mediterranean characterized by dry/hot summers (June-August) and wet/mild winters (December-February), with mean summer (winter) air temperature values of 27°C; n=135 (10°C; n=140) (IAEA/WMO 2015). Mean precipitation for the Antalya Station (36°52' N, 30°42' E, 49 m a.s.l. part of the Global Network of Isotopes in Precipitation (GNIP)) is given as 1075 mm for the period 1963–2009 (IAEA/WMO 2015), with 82% (882 mm yr^{-1}) and only

1% (12 mm yr^{-1}) occurring in the core winter months (when shoulder months are included, this rises to 99%) and summer, respectively. Isotopic data on a monthly basis reveals average winter and summer rainfall $\delta^{18}O$ values of -6.12‰ and -3.83‰ (SMOW), respectively (Table S2a online). Most recent data from 2009 shows average $\delta^{18}O$ value of ~ -7‰ (VSMOW) for rainfall from November to March and no precipitation for the summer months (IAEA/WMO 2015) (Table S2b). Hot/dry summers are due to the northward shift of ITCZ into the NH during summer which displaces the sub-tropical anticyclonic (STA) belt to the latitudes of Turkey. In winter, as the ITCZ moves south, westerly air masses derived from the Atlantic penetrate the Mediterranean Basin and bring precipitation to the western and southern coastal margins and mountains of Turkey. Thus, the moisture source for coastal SW Turkey is mostly associated with the intensity and seasonality of NH westerly wind flows and more specifically with Mediterranean Sea storm tracks (Türkeş & Erlat 2009; Wigley et al. 1982).The vegetation cover in the site is characterized by typical Mediterranean maquis scrublands and pine forests towards the higher altitudes (Akman et al. 1986), dominated by C_3-type vegetation (Still et al. 2003), with very thin soil cover (<20cm) above the cave.

3. Methodology

Three stalagmites from narrow passageways and two water samples from pools of Dim Cave were collected in 2009 and 2012 (Fig. S1 online). Due to mainly financial and logistic constraints, we were unable to establish cave monitoring but cave pool waters were sampled. The stalagmites were halved using a circular saw and micro-sampled along their growth axes by using hand drills equipped with diamond coated drill bits (0.5 to 2 mm in length) for U-series dating (sampling locations reported Figs. S2–S4 online), as well as for stable isotope analyses. Sampling interval for the stable isotope analyses was 0.5–1.0 mm depending on the growth rate of the stalagmite. This sampling interval corresponds to a growth period of 100–200 years for Dim-E3, and an average of ~100 years for Dim-E2 and Dim-E4, respectively. An additional 30 sub-samples (5–6 mg each; 5 samples per layer) were microdrilled from each of the growth phases of Dim-E3 and from one of the growth phases of Dim-E2 and Dim-E4 for Hendy tests (Hendy 1971). Powder samples (50–100 mg) were analysed for U-series dates in the Radiogenic Isotope Facility (RIF) at the School of Earth Sciences, The University of Queensland using a Nu Plasma multi-collector ICP-MS, following the analytical procedure first described in Zhou et al. (2011). Stable isotope analyses for sample powders (3–4 mg) and waters (10 ml) were conducted at the Stable Isotope Geochemistry Laboratory (SIGL) of School of Earth Sciences (The University of Queensland) on an Isoprime Dual Inlet Mass Spectrometer with Multiprep (DI-IRMS). CO_2 was liberated from carbonate

samples by reaction under vacuum with H_3PO_4 acid at 90°C for 1000s and calibrated against NBS-18 and NBS-19 international standards. The replicate analyses of internal carbonate standards indicate that the analytical standard deviation of $\delta^{18}O$ and $\delta^{13}C$ averages at ±0.1‰ (n=124, 1σ) and ±0.04‰ (n=124, 1σ) respectively.

4. Results

The stalagmite chronologies of the Dim Cave are constructed based on a total of 44 U-series dates (Table S1). 28 ages of stalagmite Dim-E3 (32cm long) reveal long-term step changes in growth patterns between ~13 and ~90 kyr (Figs. S2a and 2). Similarly, fast-growth stalagmites Dim-E2 (~29cm long) and Dim-E4 (~38cm long) show visually recognizable changes in growth patterns in the period from ~10 to ~15 kyr (Figs. S3 and S4 online). Age corrections for non-radiogenic ^{230}Th contributions are generally very small (Table S1). Micromorphological characteristics of Dim-E2 and -E3 reveal generally similar compact/open columnar calcite fabrics (Fig. S4 and Fig. S5a–e), whereas Dim-E4 is characterized by diagenetically-modified mosaic, dendritic, and open columnar calcite forms (Frisia 2015) (Figs. S4 and S5f online).

A high-resolution stable isotope profile of stalagmite Dim-E3 is based on 442 $\delta^{18}O$ and $\delta^{13}C$ measurements (Table S2), which provides a centennial-scale continuous record for the period from ~13–89 kyr. 138 additional high-resolution (Table S2) stable isotope analyses of Dim-E2 and Dim-E4 extend the time series to ~10 kyr for the stalagmite deposition in Dim Cave. Overall $\delta^{18}O$ values of the stalagmites range between -3.46 and -6.81‰ VPDB, with the lowest value from Dim-E2 at around 9.9 kyr and highest value from Dim-E3 at around 76.7 kyr (Fig. 2). These are comparable with the results reported from Soreq Cave in Israel for ~10–100 kyr (-6.02 to -2.36‰ VPDB; Bar-Matthews et al. 2003). Overturn rates for the Mediterranean Sea are in the order of 100 years(Pinardi & Masetti 2000), consequently glacial-interglacial changes in global sea-levels are important. Adjustment of the Dim $\delta^{18}O$ record for the effect of ice-volume related changes in seawater $\delta^{18}O$ demonstrate that $\delta^{18}O$ was reduced by ~1 per mil during the LGM, while at Marine Isotope Stage (MIS) 4 the change averages closer to 0.5 per mil between uncorrected and ice-volume corrected records(Bintanja & van de Wal 2008) (Fig. S6). In addition, a temperature-dependent stalagmite calcite and drip water fractionation correction (Kim & O'Neil 1997) on Dim-E3 (~90–13 kyr) (Fig. S7) shows that $\delta^{18}O_{water}$ record has a ~31 per mil (in VSMOW) negative shift, assuming that average temperature was 8°C degrees lower than today (Gundali et al. 1989; Hughes et al. 2013; Sarıkaya et al. 2014) (i.e. MAT 10.5 °C) in the cave, during glacial times. Corrected $\delta^{18}O$ speleothem values are consistent with the modern precipitation oxygen isotope range (~ -7.5 to -3.5‰; Gat & Carmi 1987; Gat & Rindsberger 1985). Corresponding $\delta^{13}C$ values of

Dim speleothems vary broadly from -12.55‰ (Dim-E2) to -0.21‰ (Dim-E3) VPDB, pointing to a varying degrees of contributions buffered with vegetation/soil-CO_2 (associated with C_3-type plants) and dolomitic host limestone (Dim-HR $\delta^{13}C$: 5.43, $\delta^{18}O$: -0.71‰ VPDB; Table S3) for the seepage waters(Rollinson 1993; Baker et al. 1997; Bar-Matthews et al. 2003) (Fig. 2; Table S3; Fig. S2–S4). Hendy tests (Hendy 1971) demonstrate that the $\delta^{18}O$ values (-6.4 to -4.4‰ VPDB) have not varied by more than 0.5‰ (Fig. S8) and do not correlate (R^2= 0.2) with $\delta^{13}C$ values (-11.3 to -5.08‰ VPDB) along the tested growth layers (Table S4 online), which means that the deposition of stalagmites was essentially in or close to quasi-isotopic equilibrium, allowing interpretation of the isotopic variations mainly as a climatic indicator in the cave environment.

Modern cave pool waters yield isotopically light $\delta^{18}O$ and δD ratios (-6.3,-6.2 ±0.1‰ and -29.0 ±2.0‰ VSMOW at 1σ respectively; Fig.S1b), which fall within the range of mean winter rainfall $\delta^{18}O$ and δD reported from GNIP Antalya station ($\delta^{18}O$: -5.9 – -6.2‰ and δD: -22.1 – -32.8‰ VSMOW; Table S2a; IAEA/WMO 2015) and are almost identical to the values of $\delta^{18}O$ and δD of precipitation for the year 2009 (-5.59 and -29.48‰ respectively; Table S2b). When $\delta^{18}O$ and δD relationships of mean annual and recent 2009 rainfall GNIP data and modern Dim Cave waters are plotted with respect to Mediterranean Meteoric Water (MMWL; Gat & Carmi 1987) and Meteoric Water Line (MWL), the majority of isotopic data are observed to fall within the meteoric lines (Fig. S9). While water composition of 2009, mean winter rain (indicated with the numbers 1, 2, 11, and 12) and Dim pool waters lie along the MMWL, summer/spring rain mainly show global isotopic signatures, plotting close to the MWL (Fig. S9).

5. Discussion

It is widely recognised that cave environments are complex and a wide range of factors modify isotopic signals of stalagmites. Possible limitations and alternative interpretations have been discussed in the supplementary material (pages: 24–26). Here we summarise the main findings.

Based on the calcite growth rates in Dim-E3 (Fig., S2-a), we argue that the moisture balance was net positive above Dim Cave throughout the last glaciation. Growth rates in Dim-E3 are highest during the interglacial segments and between 72–63 kyr (11.9 mm/kyr). Rates varied between 2.0 mm/kyr at 79–72 kyr through 1.3 mm/kyr at 63–51 kyr to a low of 0.8 mm/kyr between 40 and 18kyr (Fig., S2a) but deposition continued, which is also inferred from dominant compact/open columnar calcite fabrics (Frisia 2015) (Fig. S5a–d). In contrast, after ~8 kyr, speleothem deposition has almost stopped and aragonite has replaced calcite in the speleothems (Wickens et al. 2011), which is interpreted to reflect a trend toward negative modern water balance (Vaks et al. 2003).

The heavy winter rain along the Mediterranean coast of Turkey is connected to westerly flow derived from the North Atlantic Ocean but the moisture for the rainfall is mostly sourced from the EM. The close match of the present-day isotopic composition between monitored winter rainfall in Antalya (average $\delta^{18}O$ and δD values of the months Dec-Feb: -6.12 and -31.3‰ VSMOW respectively; Table S2) and cave pool waters in the Dim Cave (-6.3, -6.2 and -29.0‰ VSMOW; Fig. S1) confirms that the Dim Cave receives mostly winter rain.

Currently the EM region is influenced by four distinct air mass tracks in winter, each characterized by varying moisture content and temperature, depending on the source of the air mass and the extent of interaction with the Mediterranean Sea that modifies the isotopic composition ($\delta^{18}O$ and δD) of the rain water (Gat & Rindsberger 1985; Rindsberger et al. 1990). These four air mass trajectories are 1) a N-S trajectory coming from Russia and modified in the Turkey region by transit over the Black Sea (d: deuterium excess >22 ‰); 2) A NW-SE trajectory across the Balkans (10‰<d<22‰; Fig. 3); 3) a W-E Mediterranean trajectory where the air mass passes over the sea for much of its journey (d<10‰ and 10‰<d<22‰; Fig. 3); and 4) an African trajectory travelling SW-NE (d<10‰) (Rindsberger et al. 1990; Gat & Rindsberger 1985). Of these coastal trajectories, Antalya is affected only by 2) and 3) ($\delta^{18}O$: -5 to -9‰; δD: ~ -25 to -50‰ SMOW (Rindsberger et al. 1983; Rindsberger et al. 1990), as it is protected by major mountain ranges (i.e. Central Taurus Mountains; Fig. 1b) from northerly sourced precipitation and the African trajectory mainly affects areas of the EM far to the south. Based on isotope values of both the rain and pool waters, the Dim Cave is currently primarily affected by W-E precipitation from track 3 (Fig. 3).

Glacial-interglacial $\delta^{18}O$ changes in Dim Cave fluctuate from -3.5 to -7‰ VPDB (or equivalently from 27 to 23‰ VSMOW; Table S3) which are typical of other speleothem records from the Mediterranean region (e.g. Soreq and Peqiin Caves; Bar-Matthews et al. 2003). The successful Hendy tests (Fig. S8) allow us to assume that the isotopic fractionation during speleothem carbonate deposition is negligible (McDermott 2004) despite the fact that some kinetic fractionation via degassing is almost inevitable (Dietzel et al. 2009), and the scale of $\delta^{18}O$ change in the speleothems is consistent with the scale of $\delta^{18}O$ changes in air masses (Fig. S7). The variation can be explained as a response to changes in the track of the air mass from a northerly (Fig. 3) track across the Balkans that yields less depleted $\delta^{18}O$ values during MIS 4 to a southerly Mediterranean track that is dominant in interglacials and yields depleted values in good agreement with track 3 (Figs. 2 and S2–S4). The later part of the last glacial cycle (MIS3/2) appears to demonstrate a progressive but gradual shift from the Balkans track towards the Mediterranean track.

We note that the gradual shift towards isotopically lighter water during the last glaciation would largely disappear if we had not provided an ice volume correction to the $\delta^{18}O$ results. We argue that this relationship is causal. The intensity of westerly circulation is primarily controlled by pressure (temperature) differences between the northern pole and the tropics. With polar amplification of cooling in glacial times, westerly circulation will intensify during glacial times and especially at times of maximal cooling. In the early part of the glaciation (MIS 4) ice sheet development of both the Laurentide and Fennoscandian sheets is restricted and the polar jet may lie at a northerly position pre-conditioning air mass trajectories largely through the Balkans (Fig. S4). As the glaciation continues, both the Laurentide and Fennoscandian ice-sheets gradually extended southwards (and westward in the case of the Fennoscandian). This increase in surface elevation and pressure forces the polar jet southwards and consequently westerly winds and surface fronts will gradually track further south (Prentice et al. 1992; Kwiecien et al. 2009) until they adopt a Mediterranean (W-E) like trajectory 3 (Fig. 3). During the Holocene, overall westerly circulation is likely to be weaker and in the absence of steep temperature gradients at higher latitudes EM moisture is dominated by Mediterranean trajectories.

The longer-term records appear to reflect multi-millennial scale changes in ice volume, but we also note that those Heinrich events present in the record are also marked by phases of isotopic enrichment. This may reflect either the influx of fresh water into the North Atlantic, changing the isotopic composition of the air mass at the source region and/or enhanced westerly flow during Heinrich events. The enhanced flow would occur because of increased temperature contrast to areas further south and would amplify the effect of the northerly (Balkans) track. This process would be most effective when the continental ice sheets are at their smallest extent (i.e. the YD and MIS 4 events show up most strongly) as there is a northerly track available for the westerlies. During MIS 2, the westerlies may be enhanced but there is little chance for NW-SE flow to dominate because the track of the westerlies is depressed far to the south.

The range of $\delta^{13}C$ values (-12.45 to -0.12‰) in the Dim speleothems (Fig. 2) can be explained through a combination of the isotopic signature of the C_3 vegetation type/soil thickness above the cave, atmospheric CO_2, and the signature of the dolomitic limestone (McDermott 2004; Bar-Matthews et al. 1996). $\delta^{13}C$ depletion during the interglacial part of the record reflects mixing of soil organic carbon (~ -25‰; Cerling et al. 1991; Minissale et al. 2002) with rain water. In glacial times interaction with soil organic matter was reduced and the $\delta^{13}C$ was consequently less depleted due to proportionately stronger interactions with the host limestone ($\delta^{13}C$ ~ 5.4 ‰; Table S3). This reflects thinner density of forest/shrubland cover in the area as a consequence of depressed

temperatures and reduced global availability of CO_2 (Pearson & Palmer 2000; Petit et al. 1999) during glacial times. Reduced vegetation results in thinner soils and less evapotranspiration at the site. This gives rise to reduced residence time for the waters flowing through epikarst into the cave, and accordingly we observe a combination of more inherited atmospheric CO_2 ($\delta^{13}C$: ~ -7‰; Abrantes et al. 2012; Rollinson 1993; Hendy 1971) and influences from the dolomitic limestone recorded in speleothems (Fig. 2 and Figs. S2–S4). However, it is still important to note that $\delta^{13}C$ record shows large positive extensions and strong relationships with $\delta^{18}O$ during slower growth stages (i.e. marked as slow (S) periods of Dim-E3 in Fig. S2a). Accordingly we think that degassing (kinetic fractionation) might have played an important role during short and drier periods, but overall we believe that bedrock contribution has an equally important role in the longer term variation of the $\delta^{13}C$ record.

The Dim isotope record is largely in-phase with regional speleothem records from Soreq and Peqiin cave (Bar-Matthews et al. 2003) in Israel but is largely out of phase with the Sofular cave record from NW Turkey (Fleitmann et al. 2009). This appears to reflect the strong Mediterranean influence on moisture sources for the Israeli caves and at Dim, whereas the Sofular record is modified by northerly moisture sourced from the Black Sea. Concurrent $\delta^{18}O$ depletions during interglacial episodes are obvious in both the Israeli and Dim records (Fig. 2c, d). From around 74 to ~41 kyr between Soreq and Dim the records are apparently out of phase. This is can most likely be explained by relative influences of Westerlies at these sites in the early part of the glaciation. Soreq and Peqiin display gradual transitions to glacial conditions whereas the transition is abrupt and significant at Dim Cave. As Dim lies many hundreds of kilometres north of the Israeli sites, it is likely to be much more strongly affected by enhancement of westerly flow as temperatures dropped at the start of the last glaciation and also more likely to reflect enhanced NW-SE flow across the Balkans. The gradual extension of the ice sheets in North America and Europe from MIS4 to MIS2, slowly shifted the westerlies south and by MIS 3 both Dim and the Israeli sites were dominantly controlled by the same air masses (Figs. 2 and 3).

Previous studies have inferred a role of temperature for lighter oxygen isotopes in speleothems during glacial times and have argued for increased summer rainfall during the late Pleistocene in this region (Frumkin et al. 1999; Horowitz & Gat 1984). This would require the northward migration of the ITCZ beyond Holocene limits at a time when the evidence suggests that major zonal circulations in the northern hemisphere are displaced equatorward. As has already been observed (Tzedakis 2007; Kutzbach et al. 2014), this is not climatologically sensible. Part of the reason for the inferences of northward migration of a summer monsoon was that at the Israeli sites,

the $\delta^{13}C$ changes could be explained in part, by inferring more (isotopically less depleted) C_4 vegetation at glacial times (Bar-Matthews et al. 1999; Vaks et al. 2003). At Dim Cave, there is no C_4-type vegetation now and no reason for C_4 vegetation (tropical grasses) during glacial times. The isotopically heavier $\delta^{13}C$ signal is consequently a function of reduced vegetation cover and enhanced bedrock interactions, rather than summer rainfall. Recent research from the Levant region(Frumkin et al. 2011; Lisker et al. 2010) has challenged the previous interpretations and proposed that the glacial periods were wetter in response to higher moisture balance, supporting positive moisture balance throughout the last glaciation in the EM. Subsequently, we are the first to deconvolve the glacial pattern in a climatologically sensible manner and highlight that the records presented here show changes in the westerly trajectories across NW Europe and the Mediterranean.

6. Conclusions

In this study, we reconstruct the paleoclimate of the EM region for the past ~80 kyr using a well-dated continuous speleothem record from S-SW Turkey. Our findings demonstrate that the Dim Cave has had a positive moisture balance from ~9–90 kyr. The changes in composite Dim oxygen isotope time series are interpreted as changes in $\delta^{18}O$ of the oceanic moisture source which is governed by latitudinal shifts in Westerly wind track. Swings in carbon isotope profiles are deduced mostly to reflect relative thicknesses in the vegetation cover and subsequent interactions with the host dolomitic limestone over glacial-interglacial timescales. Although interrupted by short-term fluctuations, long-term patterns of Dim record show synchronous responses to global climatic variations driven by the evolution of the northern hemisphere ice sheets.

7. Acknowledgements

This research was funded by the Queensland Geothermal Energy Centre of Excellence (QGECE), with some support by the School of Geography, Planning, and Environmental Management through E. Ü.İ.'s PhD project fund. We thank Sue Golding, Kim Baublys and Wei Zhou for their help during the stable isotope analyses.

8. Author contributions

E.Ü.İ. performed the laboratory work for U-series dating and stable isotope analyses and drafted the manuscript. J.S. contributed writing the manuscript and edited the draft. J.-X.Z. and I.T.U. edited and revised the manuscript. A.D.N. and Y.-X. F. helped with U-series dating analyses and assisted throughout the study. G.Y. provided help during field works and revisions of the manuscript.

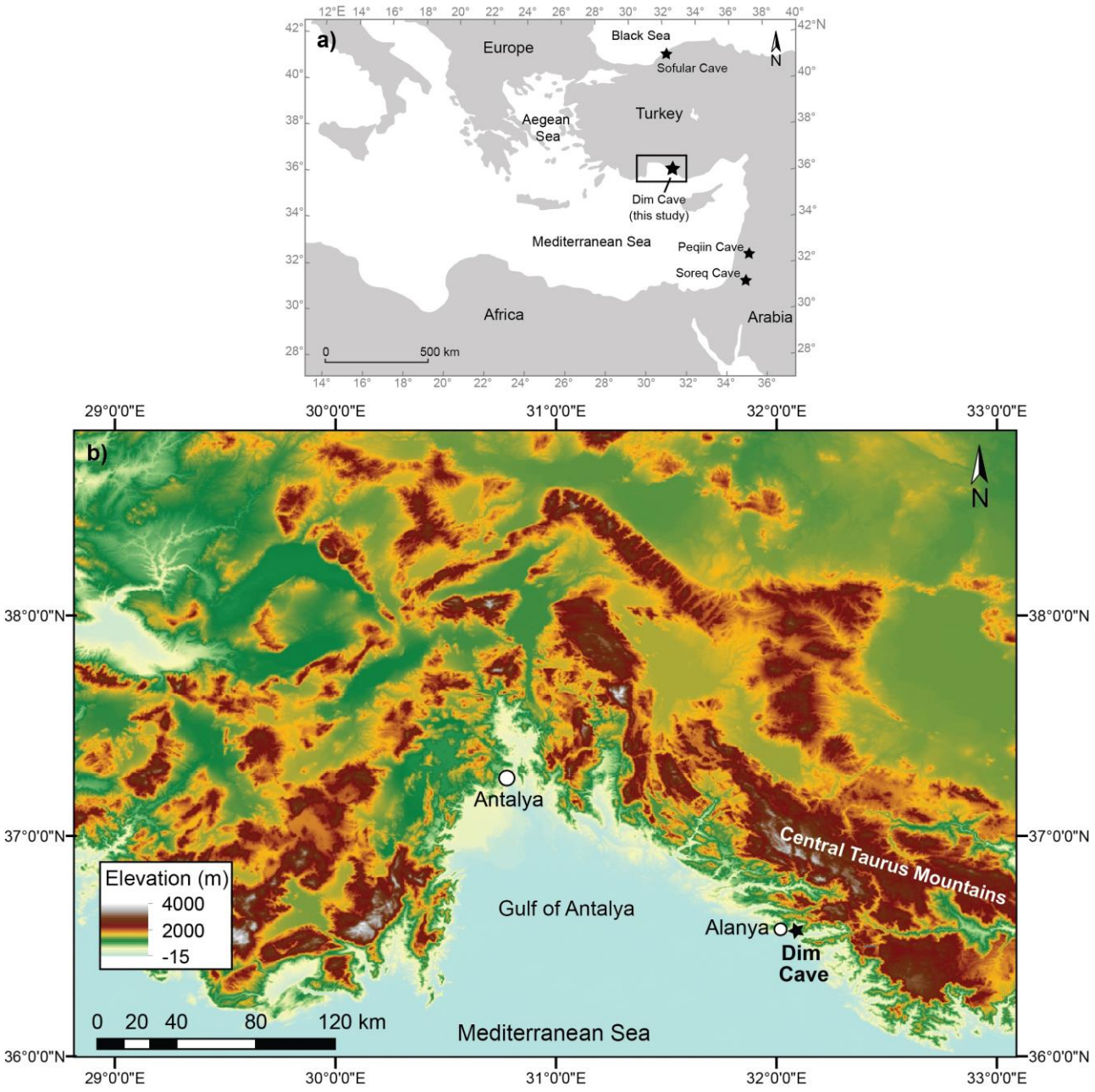

Figure 1 Location map of the Dim Cave, SW Turkey. **a)** Simplified map of Eastern Mediterranean region, showing the study location: Dim Cave. **b)** Elevation map of the SW Turkey. Note that the Dim Cave is situated at 232 m above sea level. Maps are generated using UQ-licensed software Adobe Illustrator CS5, version 15.0.2 (http://www.adobe.com/au/products/illustrator.html).

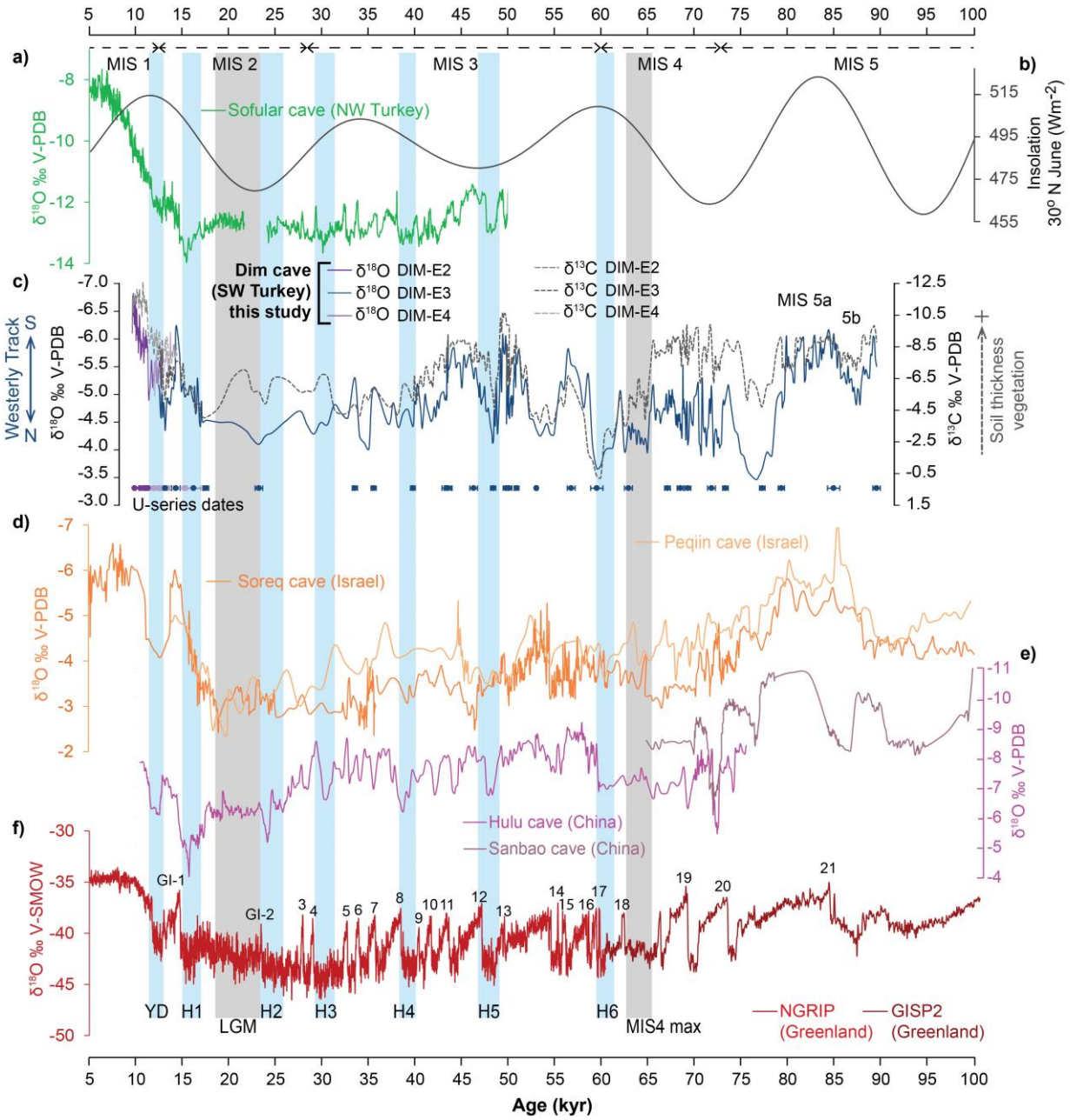

Figure 2 Comparison of the speleothem-based paleoclimatic records over the last 100 kyr. **(a)** $\delta^{18}O$ time series of stalagmites from Sofular Cave, NW Turkey(Fleitmann et al. 2009) (inverted as per that publication); **(b)** summer insolation (30°N June(Berger & Loutre 1991)); **(c)** $\delta^{18}O$ and $\delta^{13}C$ composite time series of stalagmites Dim-E2, Dim-E3, and Dim-E4 from Dim Cave (SW Turkey), colour-coded points denote for the U-series dates. **(d)** Soreq and Peqiin Cave (Israel) $\delta^{18}O$ records(Bar-Matthews et al. 2003); **(e)** composite stalagmite $\delta^{18}O$ records from Hulu and Sanbao Caves (China)(Wang et al. 2001; Wang et al. 2008); **(f)** $\delta^{18}O$ ice-core time series from Greenland NGRIP(Svensson et al. 2008) and GISP2(Grootes & Stuiver 1997), with numbers indicating Greenland Interstadials (e.g., GI-1) and Marine Isotope Stages (e.g. MIS-1). The durations of Younger Dryas (YD), LGM, and Heinrich (H) events are highlighted with light grey, dashed grey, and light blue areas, respectively.

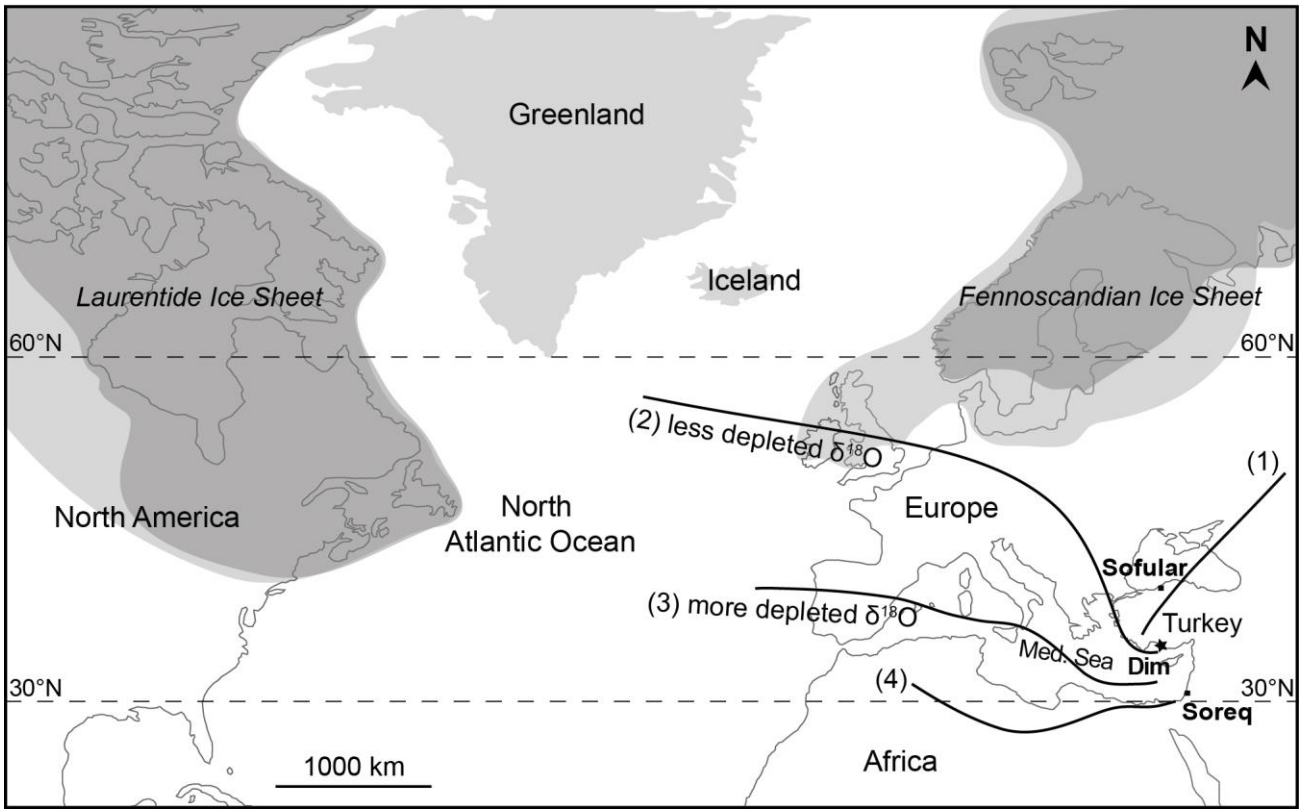

Figure 3 Sketch map of the North Atlantic region showing trajectories of modern precipitating air masses (marked as 1, 2, 3, and 4) over the Eastern Mediterranean (Gat & Rindsberger 1985; Rindsberger et al. 1990) and changes in ice-sheet volumes during MIS4 (dark grey) and MIS2 (light grey shaded areas) (Kleman et al. 2013; Hughes et al. 2013). Dim Cave (black star) receives rain through trajectories 2 and 3. Ice limits are indicative only. Map is generated using UQ-licensed software Adobe Illustrator CS5, version 15.0.2 (http://www.adobe.com/au/products/illustrator.html).

APPENDIX 3: Supporting Information (SI) of Paper 3

An 80 kyr-long continuous speleothem record from Dim Cave, SW Turkey with paleoclimatic implications for the Eastern Mediterranean

by Ezgi Ünal-İmer, James Shulmeister, Jian-Xin Zhao, I. Tonguç Uysal, Yue-Xing Feng, Ai Duc Nguyen, Galip Yüce

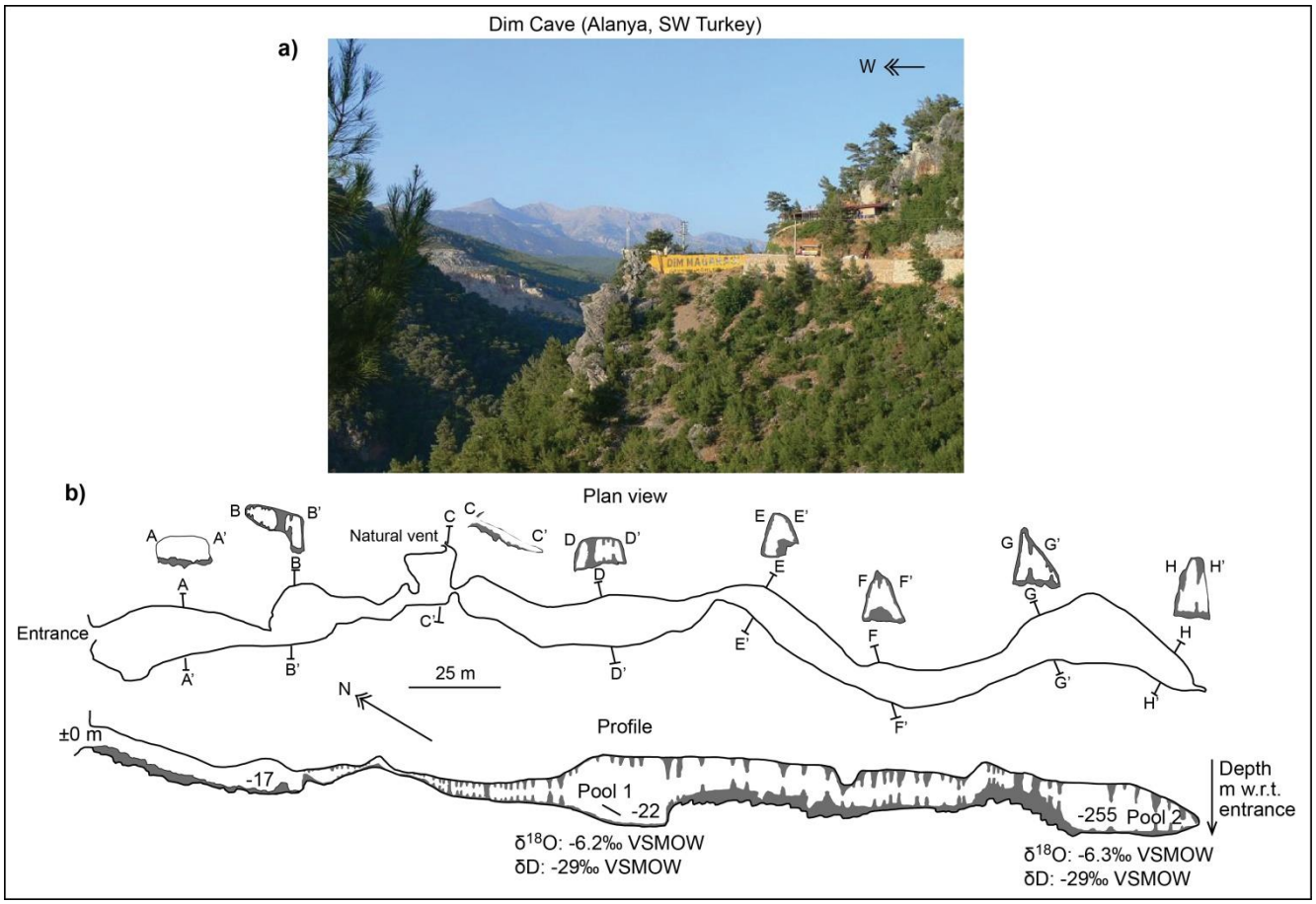

Figure S1 (a) View of the Dim Cave looking north, **(b)** plan view and projected profile of the Dim Cave with $\delta^{18}O$ and δD data of the pool waters. Photograph in **(a)** is taken by E.U.I. Plan and profile views of the cave in **(b)** are re-drawn and simplified from an archived report of the General Directorate of Mineral Research and Exploration (Turkey) (Gündalı et al. 1989), using UQ-licensed software Adobe Illustrator CS5, version 15.0.2 (http://www.adobe.com/support/downloads/product.jsp?platform=Windows&product=27).

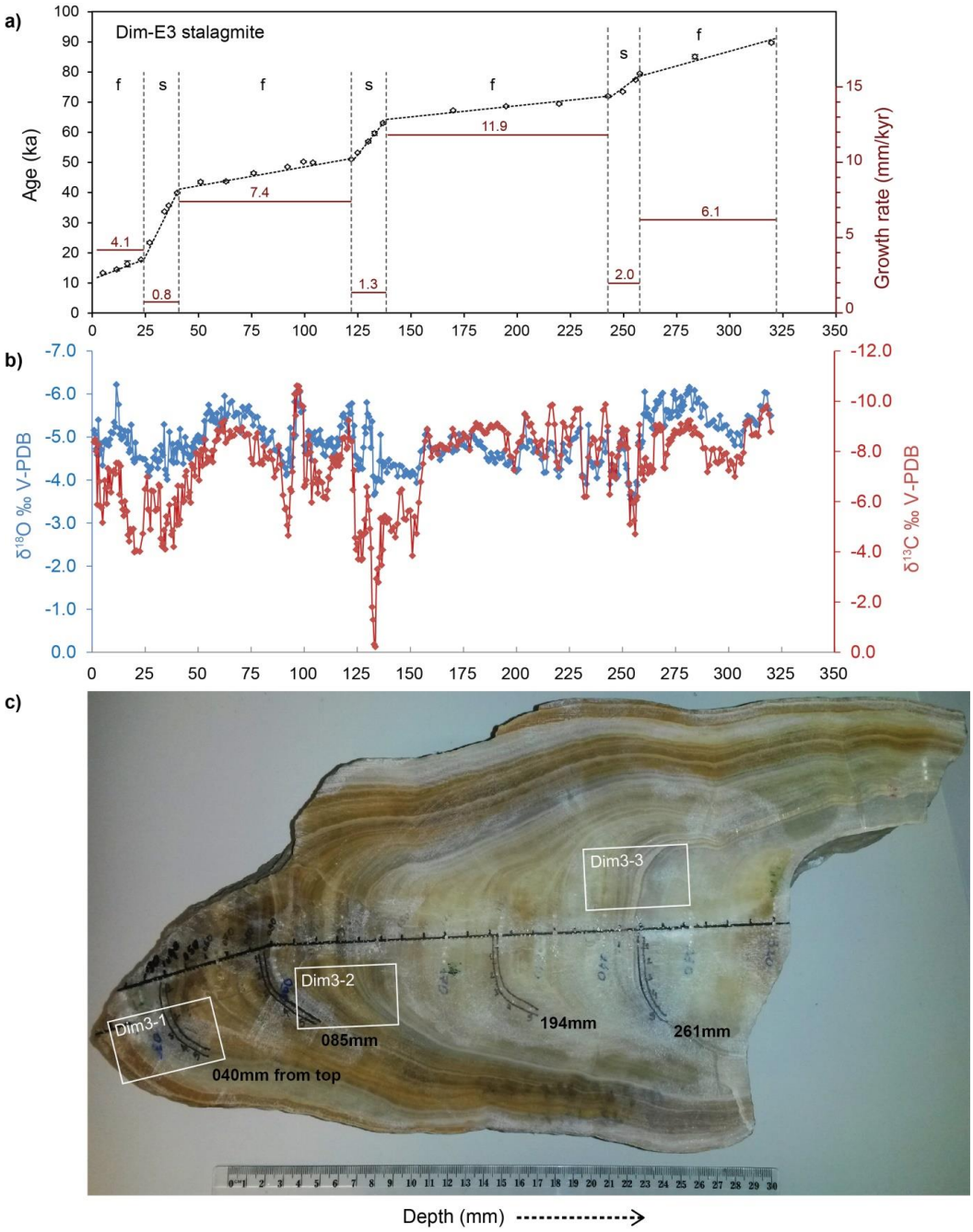

Figure S2 (a) Growth patterns observed in stalagmite Dim-E3 and **(b)** δ18O and δ13C isotopic values measured along the axis (mm) of Dim-E3. **(c)** Photo of Dim-E3 showing the Hendy test locations (covering four distinct growth periods: at 040, 085, 194, and 261mm from the tip). White rectangular areas in (**c**) show locations for the thin sections labelled as Dim3-1, -2, and -3. Sudden enrichment in δ13C (from -9 to -5‰) at ~74 kyr could indicate mixed waters buffered with host dolomitic limestone, forming aragonite layers (Figs. S5c and d) in the speleothem. Possible short hiatuses in Dim-E3 may be associated with lateral offsets and/or sudden colour changes at ~77, 60, 48.5, and between 33 and 23 kyr coinciding with the lowest growth rate (0.8mm/kyr; Fig. S2a) during LGM. None of these putative hiatuses are discernible at the resolution of the dating. Abbreviations: s = slow, f = fast in (**a**).

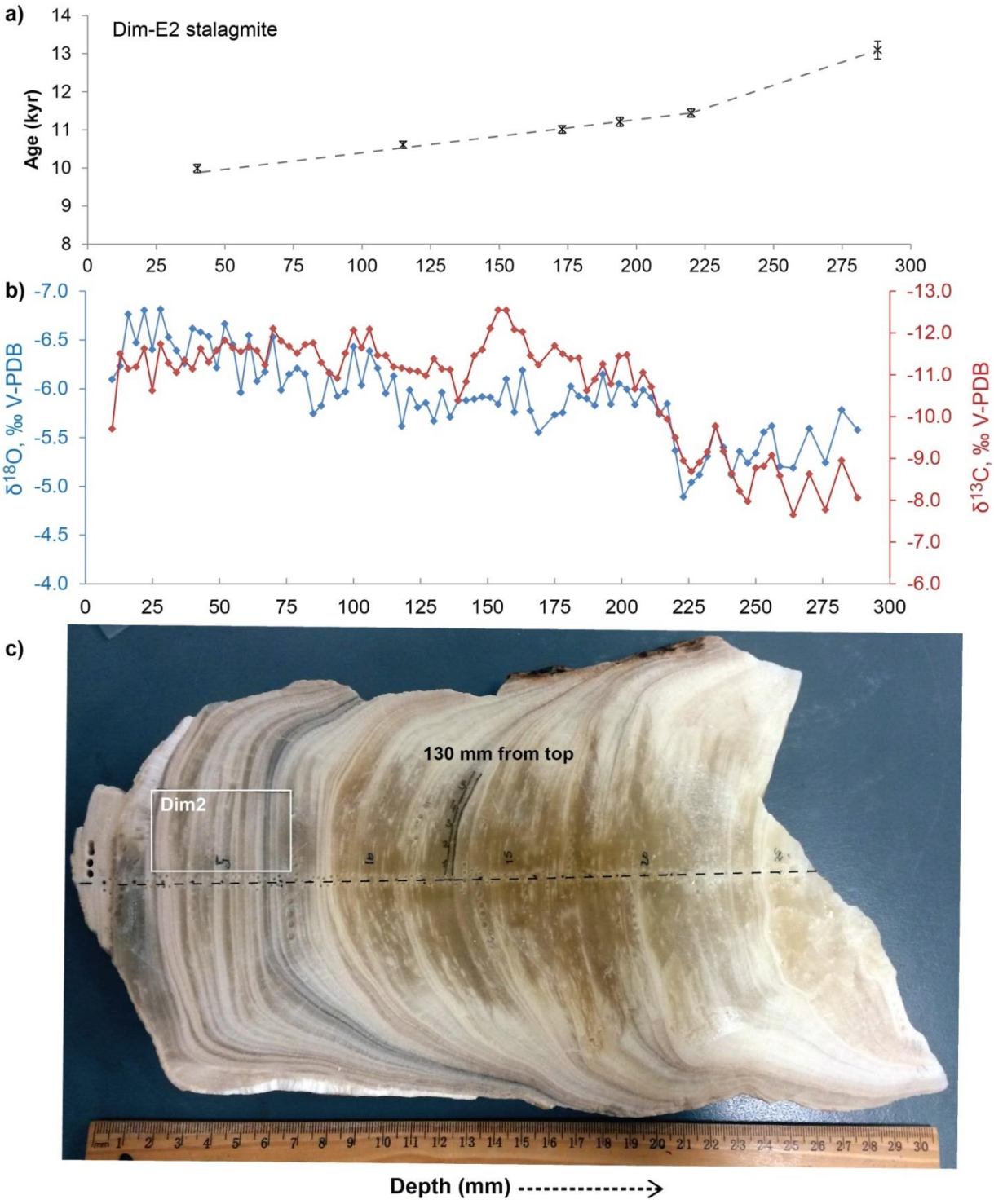

Figure S3 (a) Growth axes of stalagmite Dim-E2 and **(b)** $\delta^{18}O$ and $\delta^{13}C$ isotopic values measured along the axis (mm) of Dim-E2**. (c)** Photo of Dim-E2 showing the Hendy test location at 130 mm from the tip. White rectangular area in (**c**) shows location for the thin section Dim2. Microstratigraphic study indicates open/compact columnar calcite with visible banding. Depending on the age-depth model, Dim-E2 suggests fairly continuous growth at relatively constant drip rate except for a possible hiatus at around 11.4 kyr at about 255 mm from the tip.

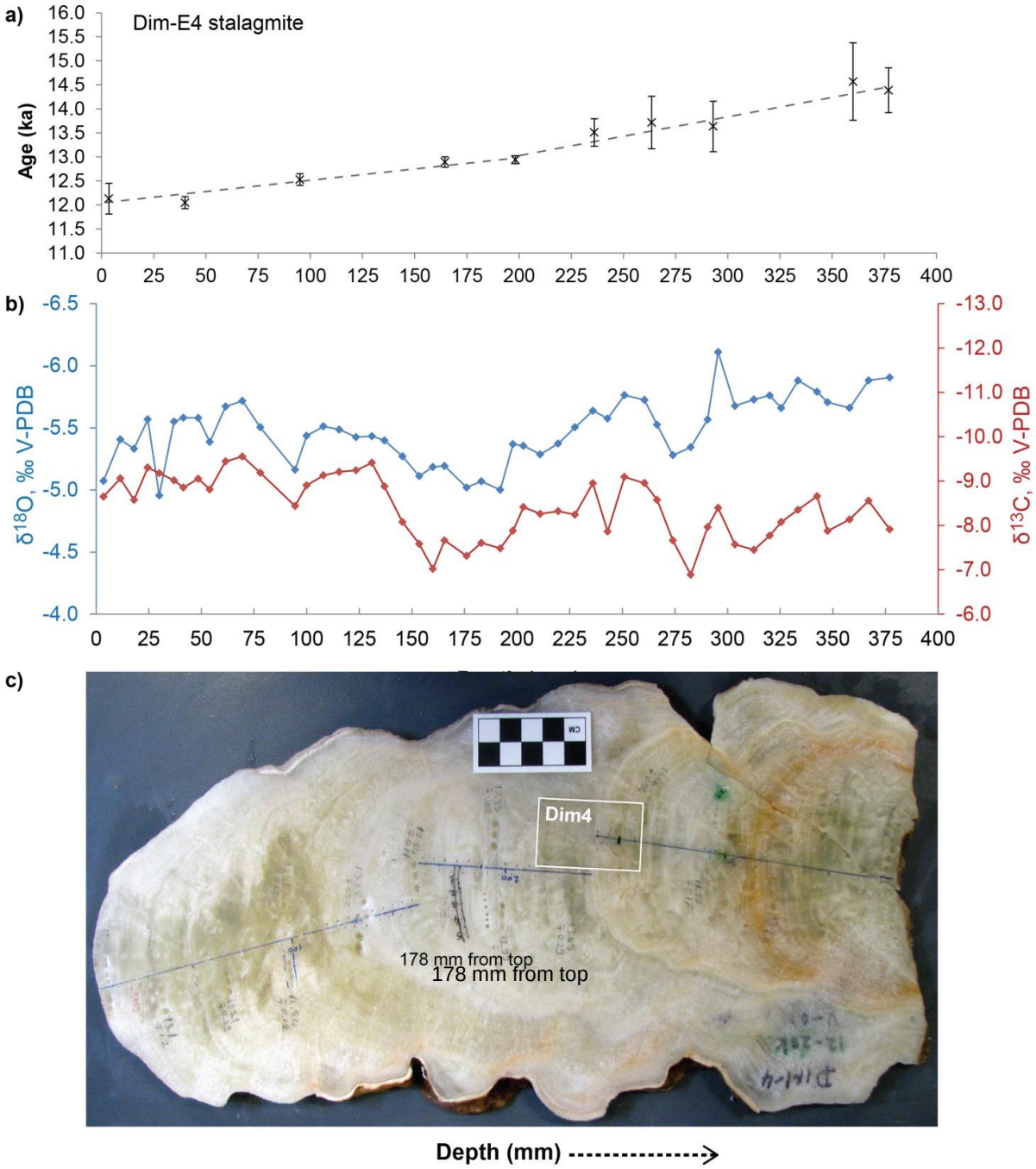

Figure S4 (a) Growth periods observed in stalagmite Dim-E4 and **(b)** δ18O and δ13C isotopic values measured along the axis (mm) of Dim-E4. **(c)** Photo of Dim-E4 showing Hendy test location at 178mm from the tip. White rectangular area in (**c**) shows the location for the thin section Dim4. Microstratigraphic study shows three distinct growth periods with milky/transparent, open, columnar and diagenetic mosaic and colloform/dendritic fabrics, indicative of seasonal changes in drip rate. Rapidly-grown Dim-E4 shows two lateral displacements at around 160 and 275 mm from the tip corresponding to the ages of 12.8 and 13.6 kyr, which may indicate a minor break in growth.

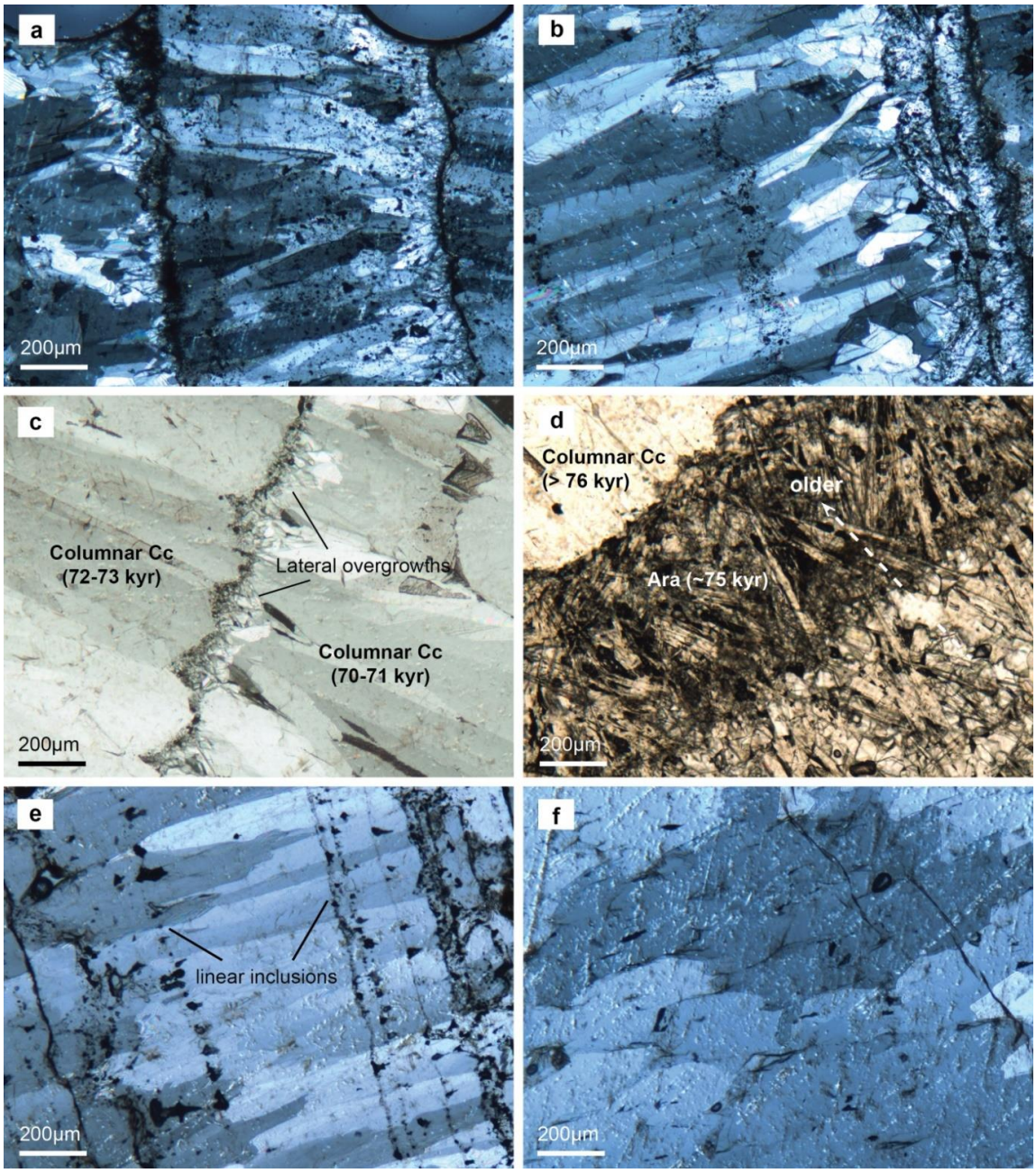

Figure S5 Representative microstructure and calcite fabrics of Dim-E3 (**a, b, c,** and **d**), Dim-E2 (**e**), and Dim-E4 (**f**) under transmitted light. **(a)** Columnar (open) calcite with clear parallel banding and sharp terminations in growth, XPL, from thin section Dim3-1 (marked with rectangular area in Fig. S2c). **(b)** Columnar (open) calcite showing intercrystalline boundaries (dark coloured linear inclusions and micritic formations) when growth (or drip rate) is interrupted, XPL, Dim3-2 section in Fig. S2c. **(c)** Younger calcite generations and lateral overgrowths in Dim3-3 section, Fig. S2c, XPL. **(d)** Acicular/radiating aragonite (Ara) layers at ~75 kyr with replacement textures towards younger columnar calcite (Cc) layers, section Dim3-3 in Fig.S2c, PPL. **(e)** Open/compact columnar calcite indicating relatively constant drip rate, section Dim2 in Fig.S3c, XPL. **(f)** Diagenetic mosaic calcite (crystals >30µm) (Frisia 2015) with irregular boundaries (and inclusions), section Dim4 (at ~13 kyr) in Fig. S4c, XPL.

Table S1 MC-ICP-MS Uranium (U)-series age data for speleothems Dim-E2, Dim-E3, and Dim-E4 from Dim Cave (Alanya, SW Turkey)

Sample	Depth (mm)	U (ppm)	±2σ	232Th (ppb)	±2σ	(230Th/ 232Th)	±2σ	(230Th/ 238U)	±2σ	(234U/ 238U)	±2σ	Uncorr. Age (kyr)	±2σ	*Corr. Age (kyr)	±2σ	Corr. Initial (234U/ 238U)	±2σ
Dim-E3-0050	5	0.2389	0.0001	6.16	0.007	17.56	0.12	0.1494	0.001	1.2435	0.0016	13.90	0.10	13.28	0.31	1.2546	0.0019
Dim-E3-0115	11.5	0.1756	0.0001	6.56	0.007	12.95	0.07	0.1595	0.0008	1.2106	0.0016	15.35	0.09	14.44	0.45	1.2216	0.002
Dim-E3-0165	16.5	0.1608	0.0001	13.56	0.014	6.9	0.07	0.1919	0.0018	1.2325	0.0023	18.36	0.20	16.3	1.0	1.2491	0.0038
Dim-E3-0225	23	0.075	0.0000	0.98	0.003	63.03	0.78	0.2716	0.0032	1.7733	0.0058	17.92	0.24	17.70	0.26	1.8158	0.0061
Dim-E3-0270	27	0.0767	0.0000	1.98	0.003	34.96	0.45	0.2968	0.0038	1.4943	0.0027	23.85	0.34	23.35	0.41	1.5317	0.0034
Dim-E3-0340	34	0.0997	0.0001	1.69	0.003	68.81	0.42	0.3852	0.0023	1.4198	0.002	34.00	0.24	33.66	0.28	1.4638	0.0024
Dim-E3-0360	36	0.1143	0.0001	0.95	0.002	137.22	0.86	0.3759	0.0023	1.3253	0.0027	35.86	0.27	35.68	0.28	1.3606	0.0029
Dim-E3-0400	40	0.1365	0.0001	2.07	0.002	82.58	0.37	0.4133	0.0018	1.322	0.0018	40.22	0.22	39.89	0.27	1.3619	0.0021
Dim-E3-0510	51	0.1711	0.0001	6.68	0.008	32.14	0.15	0.4137	0.0019	1.2227	0.0015	44.43	0.26	43.50	0.49	1.2545	0.0021
Dim-E3-0630	63	0.2166	0.0001	1.68	0.005	158.54	1.28	0.4043	0.003	1.2092	0.0017	43.88	0.40	43.70	0.41	1.2372	0.0019
Dim-E3-0760	76	0.1901	0.0002	6.88	0.009	37.57	0.13	0.448	0.0014	1.2573	0.0013	47.25	0.20	46.42	0.41	1.2962	0.002
Dim-E3-0920	92	0.1759	0.0002	1.55	0.002	159.61	0.65	0.4629	0.0019	1.2671	0.0016	48.71	0.26	48.51	0.28	1.3071	0.0019
Dim-E3-0995	99.5	0.2043	0.0001	3.55	0.004	77.87	0.32	0.4457	0.0018	1.1869	0.001	50.63	0.26	50.21	0.32	1.2164	0.0013
Dim-E3-1040	104	0.2035	0.0001	0.61	0.001	450.07	2.36	0.4475	0.0022	1.2031	0.0014	49.99	0.32	49.92	0.32	1.234	0.0016
Dim-E3-1220	122	0.2097	0.0002	0.58	0.001	560.68	2.33	0.5103	0.002	1.3405	0.002	51.09	0.27	51.03	0.27	1.3935	0.0022
Dim-E3-1250	125	0.2827	0.0002	0.82	0.001	611.94	1.4	0.5828	0.0011	1.4749	0.0015	53.22	0.14	53.16	0.14	1.5522	0.0016
Dim-E3-1300	130	0.1447	0.0001	0.87	0.002	366.64	2.25	0.7226	0.0042	1.7196	0.0021	56.99	0.43	56.90	0.43	1.8463	0.0025
Dim-E3-1330	133	0.0543	0.0000	1.2	0.002	98.69	0.83	0.7215	0.006	1.6516	0.0021	60.02	0.65	59.64	0.66	1.7757	0.0034
Dim-E3-1370	137	0.1401	0.0001	0.39	0.002	779.07	5.53	0.7125	0.0036	1.5742	0.0018	63.11	0.43	63.06	0.43	1.6867	0.0022
Dim-E3-1700	170	0.1798	0.0001	0.42	0.001	954.21	3.76	0.7277	0.0025	1.5336	0.0011	67.28	0.31	67.24	0.31	1.6457	0.0014
Dim-E3-1950	195	0.1578	0.0001	0.71	0.001	538.62	1.94	0.8008	0.0026	1.6546	0.002	68.69	0.32	68.61	0.32	1.7957	0.0023
Dim-E3-2200	220	0.1744	0.0001	0.13	0.001	3202.78	16.55	0.7673	0.0025	1.5768	0.0018	69.44	0.33	69.43	0.33	1.702	0.0021
Dim-E3-2430	243	0.3062	0.0002	0.77	0.003	926.05	4.85	0.7649	0.003	1.5324	0.0023	72.02	0.42	71.98	0.42	1.6529	0.0027
Dim-E3-2500	250	0.5386	0.0003	0.1	0.001	13369	147	0.7941	0.0023	1.5644	0.001	73.47	0.30	73.47	0.30	1.6944	0.0013
Dim-E3-2560	256	33.6032	0.0245	1.865	0.050	42397	1147	0.7787	0.0021	1.4832	0.0009	77.42	0.30	77.42	0.30	1.6012	0.0011

Dim-E3-2580	258	3.3317	0.0027	0.42	0.005	19598	262	0.8048	0.0024	1.5019	0.001	79.48	0.34	79.48	0.34	1.6281	0.0013
Dim-E3-2840	284	0.1732	0.0001	1.93	0.005	257.96	1.46	0.9471	0.0049	1.6711	0.0025	85.29	0.66	85.11	0.66	1.8562	0.0033
Dim-E3-3200	320	0.284	0.0002	0.84	0.001	925.59	3.09	0.9011	0.0026	1.5432	0.0014	89.77	0.41	89.71	0.41	1.7005	0.0018
Dim-E2-0400	40	0.2707	0.0002	0.39	0.01	258.3	6.99	0.1218	0.0013	1.3845	0.0015	10.02	0.11	9.99	0.11	1.3957	0.0015
Dim-E2-1150	115	0.2636	0.0001	0.6	0.003	173.69	1.66	0.1309	0.0011	1.4026	0.0018	10.65	0.09	10.61	0.10	1.4151	0.0019
Dim-E2-1730	173	0.3733	0.0002	0.27	0.002	557.13	6.28	0.1307	0.0011	1.3555	0.0018	11.03	0.10	11.01	0.10	1.3668	0.0019
Dim-E2-1940	194	0.2927	0.0002	0.3	0.002	389.77	4.48	0.1334	0.0013	1.3589	0.0017	11.24	0.12	11.21	0.12	1.3706	0.0018
Dim-E2-2200	220	0.2695	0.0002	0.34	0.002	336.98	3.45	0.1409	0.0012	1.4061	0.0021	11.47	0.10	11.44	0.11	1.4196	0.0021
Dim-E2-2880	288	0.1262	0.0001	1.21	0.004	51.22	0.79	0.1612	0.0024	1.3992	0.0019	13.30	0.21	13.09	0.23	1.4154	0.0020
Dim-E4-0035	3.5	0.262	0.0002	7.81	0.015	15.36	0.09	0.1509	0.0008	1.3656	0.0011	12.72	0.08	12.08	0.32	1.3813	0.0019
Dim-E4-0400	40	0.2705	0.0001	0.34	0.003	346.19	4.29	0.145	0.0014	1.3768	0.0018	12.09	0.12	12.07	0.12	1.39	0.0019
Dim-E4-0950	95	0.2262	0.0001	1.99	0.004	51.32	0.3	0.1487	0.0008	1.3448	0.0015	12.74	0.08	12.55	0.12	1.3581	0.0016
Dim-E4-1645	164.5	0.2151	0.0001	1.2	0.002	83.63	0.55	0.1544	0.001	1.3728	0.002	12.96	0.09	12.84	0.11	1.3872	0.0020
Dim-E4-1980	198	0.1969	0.0001	0.91	0.001	102.23	0.52	0.1561	0.0008	1.3749	0.0014	13.09	0.07	13.00	0.08	1.3894	0.0014
Dim-E4-2360	236	0.1867	0.0001	4.93	0.005	18.9	0.1	0.1645	0.0009	1.358	0.0015	14.02	0.08	13.45	0.29	1.3746	0.0021
Dim-E4-2635	263.5	0.1886	0.0001	9.55	0.021	10.24	0.07	0.1709	0.0011	1.3439	0.002	14.77	0.10	13.66	0.54	1.3625	0.0033
Dim-E4-2930	293	0.1402	0.0001	6.95	0.018	11	0.14	0.1796	0.0022	1.4193	0.0019	14.68	0.20	13.65	0.53	1.4417	0.0036
Dim-E4-3600	360	0.1322	0.0001	10.19	0.023	7.57	0.08	0.1924	0.0021	1.3841	0.0021	16.24	0.19	14.59	0.81	1.4088	0.0049

Table S2 (a) Monthly precipitation $\delta^{18}O$ and δD means of the GNIP Antalya station (36°52'48" N 30°42' 00" E; 49 m a.s.l.) during 1963–2009 (IAEA/WMO, 2015)., and **(b)** average $\delta^{18}O$, δD, and precipitation (mm) values for 2009 (most recent data from the station)

a)

Months	$\delta^{18}O$‰ (VSMOW)	δD‰ (VSMOW)	Precipitation (mm)	Air Temperature (°C)	d-excess value
January	-6.23	-32.80	205.4	9.7	18
February	-5.91	-30.60	159.1	10.3	16.5
March	-4.89	-25.30	106.9	12.6	14.1
April	-4.14	-22.40	56.7	16	11.6
May	-3.17	-18.20	29.5	20.4	7.3
June	-3.36	-20.60	7.0	25.4	7.5
July	-4.44	-25.40	3.1	28.4	11.4
August	-3.70	-18.80	2.2	28.1	10.8
September	-2.55	-10.90	12.6	24.6	9.5
October	-4.66	-23.00	84.1	19.9	15.1
November	-4.92	-22.10	150.3	14.7	17
December	-6.21	-30.50	260.2	11.2	19.4
Lon-term Weighted Annual Means	-5.47	-27.58	-	-	-
Long-term annual means	-4.52	-23.38	89.76	18.44	13.18

b)

Year	Avg. $\delta^{18}O$‰ (VSMOW)	Avg. δD‰ (VSMOW)	Avg. Precipitation (mm)
2009	-5.59	-29.48	1513.7

Table S3 $\delta^{18}O$ and $\delta^{13}C$ isotope rations of the speleothem sub-samples from Dim Cave (Alanya, SW Turkey) (values are in per mil)

Sample name	Depth (mm)	$\delta^{13}C$ (VPDB)	$\delta^{18}O$ (VPDB)	$\delta^{18}O$ (VSMOW)
Dim-E3-0010	1	-8.371	-5.157	25.59
Dim-E3-0015	1.5	-8.477	-5.063	25.69
Dim-E3-0020	2	-8.001	-4.726	26.04
Dim-E3-0025	2.5	-5.883	-4.583	26.19
Dim-E3-0030	3	-8.265	-5.398	25.35
Dim-E3-0035	3.5	-6.798	-4.595	26.17
Dim-E3-0040	4	-5.818	-4.845	25.92
Dim-E3-0045	4.5	-5.748	-4.709	26.06
Dim-E3-0050	5	-5.165	-4.342	26.43
Dim-E3-0060	6	-6.845	-4.912	25.85
Dim-E3-0065	6.5	-6.534	-4.928	25.83
Dim-E3-0070	7	-5.912	-4.832	25.93
Dim-E3-0075	7.5	-7.325	-4.861	25.90
Dim-E3-0080	8	-6.611	-4.802	25.96
Dim-E3-0085	8.5	-7.196	-4.951	25.81
Dim-E3-0095	9	-6.366	-5.113	25.64
Dim-E3-0100	10	-7.199	-5.091	25.66
Dim-E3-0105	10.5	-7.254	-5.343	25.40
Dim-E3-0110	11	-7.108	-5.240	25.51
Dim-E3-0115	11.5	-7.533	-6.220	24.50
Dim-E3-0125	12.5	-7.537	-5.756	24.98
Dim-E3-0130	13	-6.283	-5.057	25.70
Dim-E3-0135	13.5	-7.418	-5.192	25.56
Dim-E3-0140	14	-5.977	-4.950	25.81
Dim-E3-0145	14.5	-5.683	-4.996	25.76
Dim-E3-0150	15	-5.435	-5.024	25.73
Dim-E3-0155	15.5	-6.010	-5.143	25.61
Dim-E3-0165	16.5	-5.611	-4.853	25.91
Dim-E3-0170	17	-4.669	-5.134	25.62
Dim-E3-0175	17.5	-4.420	-4.646	26.12
Dim-E3-0180	18	-4.900	-4.710	26.06
Dim-E3-0185	18.5	-4.795	-5.284	25.46
Dim-E3-0195	19.5	-4.915	-4.485	26.29
Dim-E3-0200	20	-3.990	-4.411	26.36
Dim-E3-0205	20.5	-4.034	-4.870	25.89
Dim-E3-0210	21	-4.044	-4.498	26.27
Dim-E3-0225	22.5	-4.016	-4.525	26.25
Dim-E3-0240	24	-4.719	-4.487	26.28
Dim-E3-0250	25	-6.491	-4.481	26.29
Dim-E3-0260	26	-6.988	-4.340	26.44
Dim-E3-0265	26.5	-5.705	-4.188	26.59
Dim-E3-0270	27	-5.638	-4.093	26.69

Dim-E3-0275	27.5	-4.892	-4.249	26.53
Dim-E3-0280	28	-6.432	-4.306	26.47
Dim-E3-0290	29	-6.405	-4.519	26.25
Dim-E3-0300	30	-5.635	-4.690	26.08
Dim-E3-0305	30.5	-5.697	-4.450	26.32
Dim-E3-0310	31	-5.711	-4.277	26.50
Dim-E3-0315	31.5	-6.670	-4.483	26.29
Dim-E3-0320	32	-6.584	-4.446	26.33
Dim-E3-0325	32.5	-4.529	-4.803	25.96
Dim-E3-0330	33	-4.219	-4.654	26.11
Dim-E3-0335	33.5	-4.336	-4.577	26.19
Dim-E3-0340	34	-4.864	-5.291	25.46
Dim-E3-0345	34.5	-4.099	-4.244	26.53
Dim-E3-0350	35	-5.406	-4.119	26.66
Dim-E3-0355	35.5	-5.129	-4.010	26.78
Dim-E3-0365	36.5	-5.869	-5.117	25.64
Dim-E3-0375	37.5	-4.677	-4.453	26.32
Dim-E3-0380	38	-4.839	-4.838	25.92
Dim-E3-0385	38.5	-4.201	-4.399	26.38
Dim-E3-0390	39	-6.109	-4.646	26.12
Dim-E3-0395	39.5	-5.886	-4.714	26.05
Dim-E3-0400	40	-5.077	-4.414	26.36
Dim-E3-0405	40.5	-6.625	-4.865	25.89
Dim-E3-0410	41	-5.094	-4.818	25.94
Dim-E3-0415	41.5	-5.277	-5.183	25.57
Dim-E3-0425	42.5	-6.611	-4.731	26.03
Dim-E3-0430	43	-5.982	-4.380	26.40
Dim-E3-0435	43.5	-6.031	-4.637	26.13
Dim-E3-0440	44	-7.015	-4.996	25.76
Dim-E3-0445	44.5	-7.215	-4.799	25.96
Dim-E3-0455	45.5	-6.191	-4.583	26.19
Dim-E3-0460	46	-6.369	-4.502	26.27
Dim-E3-0465	46.5	-5.957	-4.564	26.21
Dim-E3-0470	47	-7.493	-4.766	26.00
Dim-E3-0475	47.5	-7.376	-4.584	26.18
Dim-E3-0480	48	-7.318	-4.880	25.88
Dim-E3-0485	48.5	-7.021	-4.738	26.03
Dim-E3-0490	49	-7.938	-4.960	25.80
Dim-E3-0500	50	-7.886	-5.036	25.72
Dim-E3-0505	50.5	-6.846	-4.889	25.87
Dim-E3-0510	51	-7.832	-4.994	25.76
Dim-E3-0515	51.5	-8.072	-4.946	25.81
Dim-E3-0520	52	-7.424	-4.886	25.87
Dim-E3-0525	52.5	-8.058	-4.996	25.76
Dim-E3-0530	53	-8.486	-5.371	25.37
Dim-E3-0535	53.5	-8.057	-4.938	25.82

Dim-E3-0540	54	-7.541	-5.530	25.21
Dim-E3-0545	54.5	-7.748	-5.564	25.17
Dim-E3-0550	55	-7.673	-5.746	24.99
Dim-E3-0555	55.5	-7.715	-5.613	25.12
Dim-E3-0560	56	-7.647	-5.389	25.35
Dim-E3-0565	56.5	-8.015	-5.542	25.20
Dim-E3-0570	57	-7.573	-5.461	25.28
Dim-E3-0575	57.5	-8.034	-5.360	25.39
Dim-E3-0580	58	-8.403	-5.366	25.38
Dim-E3-0585	58.5	-8.419	-5.332	25.41
Dim-E3-0590	59	-8.838	-5.552	25.19
Dim-E3-0595	59.5	-8.482	-5.334	25.41
Dim-E3-0600	60	-8.780	-5.219	25.53
Dim-E3-0610	61	-9.125	-5.655	25.08
Dim-E3-0615	61.5	-8.876	-5.423	25.32
Dim-E3-0620	62	-8.797	-5.318	25.43
Dim-E3-0625	62.5	-9.221	-5.951	24.78
Dim-E3-0630	63	-8.347	-5.446	25.30
Dim-E3-0640	64	-8.489	-5.535	25.20
Dim-E3-0650	65	-8.809	-5.790	24.94
Dim-E3-0660	66	-8.612	-5.830	24.90
Dim-E3-0670	67	-8.634	-5.481	25.26
Dim-E3-0680	68	-8.901	-5.562	25.18
Dim-E3-0690	69	-8.845	-5.548	25.19
Dim-E3-0700	70	-8.814	-5.108	25.64
Dim-E3-0710	71	-8.945	-5.695	25.04
Dim-E3-0720	72	-8.612	-5.476	25.27
Dim-E3-0730	73	-8.690	-5.620	25.12
Dim-E3-0740	74	-8.666	-5.714	25.02
Dim-E3-0750	75	-7.716	-5.536	25.20
Dim-E3-0760	76	-7.502	-5.272	25.48
Dim-E3-0770	77	-8.529	-5.456	25.29
Dim-E3-0780	78	-8.728	-5.465	25.28
Dim-E3-0790	79	-7.528	-5.225	25.52
Dim-E3-0800	80	-7.617	-5.085	25.67
Dim-E3-0805	80.5	-7.489	-4.945	25.81
Dim-E3-0810	81	-8.186	-5.196	25.55
Dim-E3-0820	82	-7.767	-4.822	25.94
Dim-E3-0830	83	-7.716	-4.903	25.86
Dim-E3-0840	84	-7.988	-4.967	25.79
Dim-E3-0850	85	-7.668	-5.130	25.62
Dim-E3-0860	86	-6.968	-4.704	26.06
Dim-E3-0870	87	-7.281	-4.677	26.09
Dim-E3-0880	88	-8.229	-4.745	26.02
Dim-E3-0890	89	-7.480	-4.580	26.19
Dim-E3-0900	90	-6.258	-4.406	26.37

Dim-E3-0910	91	-5.697	-4.287	26.49
Dim-E3-0915	91.5	-5.745	-4.112	26.67
Dim-E3-0920	92	-5.057	-4.155	26.63
Dim-E3-0925	92.5	-4.650	-4.713	26.05
Dim-E3-0930	93	-5.385	-4.431	26.34
Dim-E3-0935	93.5	-6.501	-5.211	25.54
Dim-E3-0940	94	-6.404	-4.308	26.47
Dim-E3-0945	94.5	-7.186	-4.528	26.24
Dim-E3-0950	95	-8.680	-4.973	25.78
Dim-E3-0955	95.5	-10.28	-5.818	24.91
Dim-E3-0960	96	-9.427	-5.037	25.72
Dim-E3-0965	96.5	-10.61	-6.057	24.67
Dim-E3-0970	97	-10.34	-5.767	24.97
Dim-E3-0975	97.5	-10.59	-5.723	25.01
Dim-E3-0980	98	-10.42	-6.047	24.68
Dim-E3-0985	98.5	-9.857	-5.578	25.16
Dim-E3-0995	99.5	-9.789	-5.622	25.11
Dim-E3-1000	100	-6.586	-4.804	25.96
Dim-E3-1005	100.5	-6.675	-4.627	26.14
Dim-E3-1010	101	-6.855	-4.679	26.09
Dim-E3-1015	101.5	-7.864	-4.855	25.91
Dim-E3-1020	102	-8.613	-5.136	25.62
Dim-E3-1025	102.5	-8.264	-5.080	25.67
Dim-E3-1030	103	-7.970	-5.059	25.70
Dim-E3-1035	103.5	-5.969	-4.461	26.31
Dim-E3-1040	104	-6.717	-4.963	25.79
Dim-E3-1050	105	-7.606	-5.110	25.64
Dim-E3-1055	105.5	-6.925	-4.908	25.85
Dim-E3-1060	106	-6.724	-4.832	25.93
Dim-E3-1065	106.5	-6.333	-4.863	25.90
Dim-E3-1070	107	-7.166	-4.958	25.80
Dim-E3-1075	107.5	-6.816	-5.159	25.59
Dim-E3-1080	108	-6.775	-4.916	25.84
Dim-E3-1085	108.5	-6.752	-4.830	25.93
Dim-E3-1095	109	-6.182	-4.607	26.16
Dim-E3-1100	110	-6.185	-4.561	26.21
Dim-E3-1105	110.5	-6.116	-4.774	25.99
Dim-E3-1110	111	-6.450	-4.828	25.93
Dim-E3-1115	111.5	-6.968	-4.917	25.84
Dim-E3-1120	112	-6.911	-4.932	25.83
Dim-E3-1125	112.5	-7.332	-4.824	25.94
Dim-E3-1130	113	-7.763	-4.969	25.79
Dim-E3-1135	113.5	-7.636	-4.768	25.99
Dim-E3-1140	114	-7.535	-4.598	26.17
Dim-E3-1145	114.5	-7.624	-4.627	26.14
Dim-E3-1150	115	-7.428	-4.767	26.00

Dim-E3-1155	115.5	-7.822	-4.964	25.79
Dim-E3-1160	116	-7.563	-4.806	25.96
Dim-E3-1165	116.5	-7.429	-4.910	25.85
Dim-E3-1170	117	-7.848	-5.251	25.50
Dim-E3-1175	117.5	-7.721	-5.230	25.52
Dim-E3-1180	118	-8.510	-5.484	25.26
Dim-E3-1185	118.5	-8.510	-5.539	25.20
Dim-E3-1190	119	-8.549	-5.453	25.29
Dim-E3-1200	120	-8.095	-5.322	25.42
Dim-E3-1205	120.5	-8.183	-5.131	25.62
Dim-E3-1210	121	-9.236	-5.720	25.01
Dim-E3-1215	121.5	-8.470	-5.552	25.19
Dim-E3-1220	122	-8.428	-5.543	25.20
Dim-E3-1225	122.5	-8.391	-5.780	24.95
Dim-E3-1230	123	-6.470	-4.996	25.76
Dim-E3-1235	123.5	-7.238	-5.259	25.49
Dim-E3-1240	124	-4.557	-4.576	26.19
Dim-E3-1245	124.5	-4.085	-4.538	26.23
Dim-E3-1250	125	-4.319	-4.358	26.42
Dim-E3-1255	125.5	-3.706	-4.241	26.54
Dim-E3-1260	126	-4.548	-4.334	26.44
Dim-E3-1265	126.5	-4.767	-4.466	26.31
Dim-E3-1270	127	-3.666	-4.272	26.51
Dim-E3-1275	127.5	-3.723	-4.266	26.51
Dim-E3-1280	128	-4.673	-4.755	26.01
Dim-E3-1285	128.5	-5.272	-5.224	25.53
Dim-E3-1290	129	-4.763	-5.088	25.67
Dim-E3-1295	129.5	-6.584	-5.804	24.93
Dim-E3-1300	130	-6.207	-5.536	25.20
Dim-E3-1305	130.5	-5.655	-5.473	25.27
Dim-E3-1310	131	-4.917	-5.211	25.54
Dim-E3-1315	131.5	-4.143	-4.753	26.01
Dim-E3-1320	132	-1.798	-5.360	25.38
Dim-E3-1325	132.5	-1.295	-4.090	26.69
Dim-E3-1330	133	-0.311	-3.658	27.14
Dim-E3-1335	133.5	-0.218	-3.708	27.09
Dim-E3-1340	134	-2.928	-3.967	26.82
Dim-E3-1345	134.5	-3.313	-4.021	26.76
Dim-E3-1350	135	-2.783	-4.030	26.76
Dim-E3-1355	135.5	-3.781	-4.443	26.33
Dim-E3-1360	136	-5.329	-5.054	25.70
Dim-E3-1365	136.5	-3.465	-3.960	26.83
Dim-E3-1370	137	-4.074	-4.417	26.36
Dim-E3-1375	137.5	-5.168	-4.327	26.45
Dim-E3-1380	138	-5.432	-4.392	26.38
Dim-E3-1390	139	-5.166	-4.177	26.60

Dim-E3-1400	140	-5.302	-4.472	26.30
Dim-E3-1410	141	-4.829	-4.303	26.47
Dim-E3-1420	142	-4.967	-4.356	26.42
Dim-E3-1430	143	-4.582	-4.340	26.44
Dim-E3-1440	144	-5.114	-4.089	26.69
Dim-E3-1450	145	-6.346	-4.342	26.43
Dim-E3-1460	146	-6.482	-4.319	26.46
Dim-E3-1470	147	-5.323	-4.097	26.69
Dim-E3-1480	148	-5.279	-4.213	26.57
Dim-E3-1490	149	-5.619	-4.135	26.65
Dim-E3-1500	150	-5.643	-4.086	26.70
Dim-E3-1510	151	-3.847	-4.199	26.58
Dim-E3-1520	152	-5.394	-4.131	26.65
Dim-E3-1530	153	-4.719	-3.939	26.85
Dim-E3-1540	154	-5.963	-4.283	26.50
Dim-E3-1550	155	-6.781	-4.665	26.10
Dim-E3-1560	156	-7.505	-4.708	26.06
Dim-E3-1570	157	-8.402	-5.053	25.70
Dim-E3-1580	158	-8.891	-5.160	25.59
Dim-E3-1590	159	-8.598	-4.777	25.99
Dim-E3-1600	160	-7.774	-4.529	26.24
Dim-E3-1610	161	-8.084	-4.731	26.03
Dim-E3-1620	162	-8.147	-4.696	26.07
Dim-E3-1630	163	-7.888	-4.680	26.09
Dim-E3-1640	164	-8.258	-4.470	26.30
Dim-E3-1650	165	-8.235	-4.597	26.17
Dim-E3-1660	166	-8.096	-4.673	26.09
Dim-E3-1670	167	-8.123	-4.742	26.02
Dim-E3-1680	168	-8.070	-4.711	26.05
Dim-E3-1690	169	-8.291	-5.002	25.75
Dim-E3-1700	170	-8.895	-4.649	26.12
Dim-E3-1710	171	-8.661	-4.758	26.01
Dim-E3-1720	172	-8.198	-4.705	26.06
Dim-E3-1730	173	-8.417	-5.069	25.69
Dim-E3-1740	174	-8.434	-4.832	25.93
Dim-E3-1750	175	-8.709	-4.977	25.78
Dim-E3-1760	176	-8.584	-4.768	26.00
Dim-E3-1770	177	-8.546	-4.960	25.80
Dim-E3-1780	178	-8.046	-4.760	26.00
Dim-E3-1790	179	-8.808	-5.070	25.68
Dim-E3-1800	180	-8.916	-5.000	25.76
Dim-E3-1810	181	-9.124	-4.923	25.84
Dim-E3-1820	182	-8.962	-4.828	25.93
Dim-E3-1830	183	-9.039	-4.890	25.87
Dim-E3-1840	184	-8.837	-4.769	25.99
Dim-E3-1850	185	-8.714	-4.734	26.03

Dim-E3-1860	186	-8.735	-4.514	26.26
Dim-E3-1870	187	-8.913	-4.440	26.33
Dim-E3-1880	188	-9.048	-4.626	26.14
Dim-E3-1890	189	-8.954	-4.514	26.26
Dim-E3-1900	190	-9.011	-4.401	26.37
Dim-E3-1910	191	-9.104	-4.633	26.13
Dim-E3-1920	192	-8.975	-4.512	26.26
Dim-E3-1930	193	-8.934	-4.514	26.26
Dim-E3-1940	194	-8.846	-4.641	26.13
Dim-E3-1950	195	-8.071	-4.367	26.41
Dim-E3-1960	196	-8.698	-4.346	26.43
Dim-E3-1970	197	-7.817	-4.457	26.32
Dim-E3-1980	198	-7.758	-4.429	26.34
Dim-E3-1990	199	-7.250	-4.270	26.51
Dim-E3-2000	200	-7.986	-4.197	26.58
Dim-E3-2010	201	-8.348	-4.250	26.53
Dim-E3-2020	202	-8.389	-4.755	26.01
Dim-E3-2030	203	-8.602	-4.794	25.97
Dim-E3-2040	204	-9.497	-5.522	25.22
Dim-E3-2050	205	-9.357	-4.750	26.01
Dim-E3-2060	206	-9.013	-4.910	25.85
Dim-E3-2070	207	-9.100	-4.894	25.86
Dim-E3-2080	208	-8.749	-4.650	26.12
Dim-E3-2090	209	-8.405	-4.743	26.02
Dim-E3-2100	210	-7.962	-4.670	26.10
Dim-E3-2110	211	-8.250	-4.613	26.15
Dim-E3-2120	212	-8.426	-4.483	26.29
Dim-E3-2130	213	-7.780	-4.172	26.61
Dim-E3-2140	214	-7.788	-4.184	26.60
Dim-E3-2150	215	-9.086	-4.723	26.04
Dim-E3-2160	216	-9.800	-4.865	25.90
Dim-E3-2170	217	-9.853	-4.854	25.91
Dim-E3-2180	218	-9.077	-4.679	26.09
Dim-E3-2190	219	-7.581	-4.244	26.54
Dim-E3-2200	220	-7.346	-4.080	26.70
Dim-E3-2210	221	-7.836	-4.246	26.53
Dim-E3-2220	222	-9.145	-4.842	25.92
Dim-E3-2230	223	-8.975	-4.654	26.11
Dim-E3-2240	224	-8.540	-4.478	26.29
Dim-E3-2250	225	-8.255	-4.435	26.34
Dim-E3-2260	226	-8.999	-4.926	25.83
Dim-E3-2270	227	-9.308	-4.961	25.80
Dim-E3-2280	228	-9.672	-4.986	25.77
Dim-E3-2290	229	-9.673	-5.114	25.64
Dim-E3-2300	230	-9.685	-5.203	25.55
Dim-E3-2310	231	-6.978	-4.119	26.66

Dim-E3-2320	232	-6.191	-4.068	26.72
Dim-E3-2330	233	-6.205	-3.908	26.88
Dim-E3-2340	234	-7.764	-5.282	25.47
Dim-E3-2350	235	-8.267	-4.429	26.34
Dim-E3-2360	236	-8.535	-4.308	26.47
Dim-E3-2370	237	-8.436	-4.386	26.39
Dim-E3-2380	238	-7.520	-4.048	26.74
Dim-E3-2390	239	-8.094	-4.340	26.44
Dim-E3-2400	240	-8.497	-4.427	26.35
Dim-E3-2410	241	-9.647	-4.909	25.85
Dim-E3-2420	242	-9.871	-4.650	26.12
Dim-E3-2430	243	-9.003	-5.129	25.62
Dim-E3-2440	244	-6.281	-3.901	26.89
Dim-E3-2445	244.5	-7.001	-4.194	26.59
Dim-E3-2450	245	-7.884	-4.363	26.41
Dim-E3-2455	245.5	-7.022	-4.350	26.43
Dim-E3-2460	246	-7.052	-4.116	26.67
Dim-E3-2465	246.5	-7.406	-4.207	26.57
Dim-E3-2470	247	-6.936	-4.032	26.75
Dim-E3-2475	247.5	-7.757	-4.069	26.72
Dim-E3-2480	248	-7.823	-4.114	26.67
Dim-E3-2485	248.5	-8.156	-4.701	26.06
Dim-E3-2490	249	-8.304	-4.889	25.87
Dim-E3-2495	249.5	-8.718	-4.809	25.95
Dim-E3-2500	250	-8.911	-5.098	25.65
Dim-E3-2505	250.5	-8.622	-5.156	25.60
Dim-E3-2510	251	-8.295	-4.716	26.05
Dim-E3-2515	251.5	-8.216	-4.360	26.42
Dim-E3-2520	252	-8.835	-4.263	26.52
Dim-E3-2525	252.5	-8.122	-3.934	26.85
Dim-E3-2530	253	-6.733	-3.874	26.92
Dim-E3-2535	253.5	-5.096	-3.652	27.15
Dim-E3-2540	254	-6.382	-3.552	27.25
Dim-E3-2550	255	-5.942	-3.455	27.35
Dim-E3-2555	255.5	-5.238	-3.531	27.27
Dim-E3-2560	256	-4.706	-3.653	27.14
Dim-E3-2565	256.5	-6.061	-3.954	26.83
Dim-E3-2570	257	-6.189	-3.885	26.91
Dim-E3-2575	257.5	-8.241	-4.869	25.89
Dim-E3-2580	258	-9.066	-5.038	25.72
Dim-E3-2585	258.5	-7.119	-4.755	26.01
Dim-E3-2590	259	-7.392	-4.842	25.92
Dim-E3-2595	259.5	-7.235	-4.898	25.86
Dim-E3-2600	260	-6.864	-5.535	25.20
Dim-E3-2605	260.5	-7.701	-6.048	24.68
Dim-E3-2610	261	-7.735	-5.491	25.25

Dim-E3-2615	261.5	-7.414	-5.672	25.06
Dim-E3-2620	262	-7.123	-5.504	25.24
Dim-E3-2625	262.5	-7.358	-5.522	25.22
Dim-E3-2630	263	-7.444	-5.428	25.31
Dim-E3-2635	263.5	-7.324	-5.388	25.36
Dim-E3-2640	264	-7.183	-5.209	25.54
Dim-E3-2645	264.5	-7.283	-5.200	25.55
Dim-E3-2650	265	-8.658	-5.620	25.12
Dim-E3-2655	265.5	-9.038	-5.670	25.07
Dim-E3-2660	266	-8.758	-5.832	24.90
Dim-E3-2665	266.5	-8.818	-5.774	24.96
Dim-E3-2670	267	-8.952	-5.785	24.95
Dim-E3-2675	267.5	-9.066	-5.846	24.88
Dim-E3-2680	268	-8.842	-5.961	24.77
Dim-E3-2690	269	-8.937	-6.022	24.70
Dim-E3-2695	269.5	-7.367	-5.221	25.53
Dim-E3-2700	270	-7.332	-5.266	25.48
Dim-E3-2705	270.5	-7.896	-5.632	25.10
Dim-E3-2710	271	-7.875	-5.584	25.15
Dim-E3-2715	271.5	-8.263	-5.617	25.12
Dim-E3-2720	272	-8.465	-5.443	25.30
Dim-E3-2725	272.5	-8.425	-5.566	25.17
Dim-E3-2730	273	-8.416	-5.453	25.29
Dim-E3-2735	273.5	-8.551	-5.587	25.15
Dim-E3-2740	274	-8.674	-5.987	24.74
Dim-E3-2745	274.5	-8.834	-6.060	24.66
Dim-E3-2750	275	-8.719	-5.881	24.85
Dim-E3-2755	275.5	-8.776	-5.608	25.13
Dim-E3-2760	276	-8.758	-5.485	25.26
Dim-E3-2765	276.5	-8.777	-5.500	25.24
Dim-E3-2770	277	-8.723	-5.716	25.02
Dim-E3-2775	277.5	-9.091	-5.928	24.80
Dim-E3-2780	278	-8.813	-5.617	25.12
Dim-E3-2785	278.5	-8.806	-5.820	24.91
Dim-E3-2790	279	-8.821	-5.734	25.00
Dim-E3-2800	280	-8.984	-5.997	24.73
Dim-E3-2805	280.5	-9.116	-5.996	24.73
Dim-E3-2810	281	-9.214	-6.097	24.63
Dim-E3-2815	281.5	-8.893	-6.159	24.56
Dim-E3-2820	282	-9.230	-6.085	24.64
Dim-E3-2830	283	-8.669	-5.641	25.10
Dim-E3-2840	284	-8.954	-6.083	24.64
Dim-E3-2850	285	-8.724	-5.796	24.94
Dim-E3-2860	286	-8.679	-5.894	24.83
Dim-E3-2870	287	-8.609	-5.468	25.27
Dim-E3-2880	288	-8.132	-5.757	24.98

Dim-E3-2890	289	-8.123	-5.704	25.03
Dim-E3-2900	290	-7.179	-5.280	25.47
Dim-E3-2910	291	-7.449	-5.296	25.45
Dim-E3-2920	292	-8.055	-5.338	25.41
Dim-E3-2930	293	-8.096	-5.385	25.36
Dim-E3-2940	294	-7.584	-5.231	25.52
Dim-E3-2950	295	-7.531	-5.187	25.56
Dim-E3-2960	296	-8.092	-5.501	25.24
Dim-E3-2970	297	-7.650	-5.207	25.54
Dim-E3-2980	298	-7.887	-5.263	25.48
Dim-E3-2990	299	-7.927	-5.271	25.48
Dim-E3-3000	300	-7.237	-5.045	25.71
Dim-E3-3010	301	-7.618	-5.119	25.63
Dim-E3-3020	302	-7.477	-4.925	25.83
Dim-E3-3030	303	-6.993	-4.809	25.95
Dim-E3-3040	304	-7.777	-5.089	25.66
Dim-E3-3050	305	-7.765	-5.048	25.71
Dim-E3-3060	306	-7.528	-4.805	25.96
Dim-E3-3070	307	-7.942	-5.147	25.60
Dim-E3-3080	308	-9.042	-5.348	25.40
Dim-E3-3090	309	-9.198	-5.494	25.25
Dim-E3-3100	310	-9.221	-5.349	25.40
Dim-E3-3110	311	-8.646	-5.439	25.30
Dim-E3-3120	312	-8.667	-5.371	25.37
Dim-E3-3130	313	-8.722	-5.284	25.46
Dim-E3-3140	314	-8.611	-5.286	25.46
Dim-E3-3150	315	-9.299	-5.717	25.02
Dim-E3-3160	316	-9.633	-5.695	25.04
Dim-E3-3170	317	-9.702	-6.036	24.69
Dim-E3-3180	318	-9.812	-6.017	24.71
Dim-E3-3190	319	-9.480	-5.635	25.10
Dim-E3-3200	320	-8.779	-5.499	25.24
Dim-E2-0100	10	-9.709	-6.095	24.63
Dim-E2-0130	13	-11.51	-6.233	24.48
Dim-E2-0160	16	-11.14	-6.764	23.94
Dim-E2-0190	19	-11.19	-6.472	24.24
Dim-E2-022	22	-11.63	-6.804	23.90
Dim-E2-025	25	-10.63	-6.403	24.31
Dim-E2-028	28	-11.74	-6.814	23.89
Dim-E2-031	31	-11.29	-6.528	24.18
Dim-E2-034	34	-11.05	-6.391	24.32
Dim-E2-037	37	-11.35	-6.260	24.46
Dim-E2-040	40	-11.14	-6.617	24.09
Dim-E2-043	43	-11.63	-6.580	24.13
Dim-E2-046	46	-11.31	-6.536	24.17
Dim-E2-049	49	-11.58	-6.216	24.50

Dim-E2-052	52	-11.83	-6.665	24.04
Dim-E2-055	55	-11.65	-6.454	24.26
Dim-E2-058	58	-11.56	-5.960	24.77
Dim-E2-061	61	-11.67	-6.546	24.16
Dim-E2-065	64	-11.58	-6.077	24.65
Dim-E2-067	67	-11.24	-6.175	24.54
Dim-E2-070	70	-12.11	-6.531	24.18
Dim-E2-073	73	-11.81	-5.985	24.74
Dim-E2-076	76	-11.68	-6.147	24.57
Dim-E2-079	79	-11.52	-6.209	24.51
Dim-E2-082	82	-11.72	-6.151	24.57
Dim-E2-085	85	-11.76	-5.747	24.99
Dim-E2-088	88	-11.30	-5.825	24.91
Dim-E2-091	91	-11.04	-6.166	24.55
Dim-E2-094	94	-10.92	-5.921	24.81
Dim-E2-097	97	-11.51	-5.971	24.76
Dim-E2-100	100	-12.07	-6.431	24.28
Dim-E2-103	103	-11.64	-6.038	24.69
Dim-E2-106	106	-12.10	-6.387	24.33
Dim-E2-109	109	-11.47	-6.210	24.51
Dim-E2-112	112	-11.46	-5.954	24.77
Dim-E2-115	115	-11.19	-6.129	24.59
Dim-E2-118	118	-11.16	-5.616	25.12
Dim-E2-121	121	-11.11	-5.988	24.74
Dim-E2-124	124	-11.08	-5.810	24.92
Dim-E2-127	127	-10.98	-5.856	24.87
Dim-E2-130	130	-11.38	-5.670	25.07
Dim-E2-133	133	-11.14	-5.963	24.76
Dim-E2-136	136	-11.12	-5.710	25.02
Dim-E2-139	139	-10.39	-5.877	24.85
Dim-E2-142	142	-10.83	-5.881	24.85
Dim-E2-145	145	-11.46	-5.893	24.83
Dim-E2-148	148	-11.60	-5.918	24.81
Dim-E2-151	151	-12.11	-5.912	24.82
Dim-E2-154	154	-12.55	-5.842	24.89
Dim-E2-157	157	-12.54	-6.099	24.62
Dim-E2-160	160	-12.08	-5.760	24.97
Dim-E2-163	163	-12.03	-6.189	24.53
Dim-E2-166	166	-11.46	-5.776	24.96
Dim-E2-169	169	-11.24	-5.553	25.19
Dim-E2-175	175	-11.70	-5.733	25.00
Dim-E2-178	178	-11.50	-5.755	24.98
Dim-E2-181	181	-11.39	-6.024	24.70
Dim-E2-184	184	-11.40	-5.923	24.80
Dim-E2-187	187	-10.62	-5.900	24.83
Dim-E2-190	190	-10.89	-5.827	24.90

Dim-E2-193	193	-11.26	-6.149	24.57
Dim-E2-196	196	-10.78	-5.840	24.89
Dim-E2-199	199	-11.44	-6.053	24.67
Dim-E2-202	202	-11.48	-5.995	24.73
Dim-E2-205	205	-10.66	-5.835	24.89
Dim-E2-208	208	-11.06	-5.989	24.74
Dim-E2-211	211	-10.71	-5.911	24.82
Dim-E2-214	214	-10.10	-5.739	24.99
Dim-E2-217	217	-9.943	-5.846	24.88
Dim-E2-220	220	-9.495	-5.365	25.38
Dim-E2-223	223	-8.948	-4.893	25.87
Dim-E2-226	226	-8.687	-5.040	25.71
Dim-E2-229	229	-8.901	-5.116	25.64
Dim-E2-232	232	-9.156	-5.308	25.44
Dim-E2-235	235	-9.776	-5.613	25.12
Dim-E2-238	238	-9.172	-5.400	25.34
Dim-E2-241	241	-8.645	-5.115	25.64
Dim-E2-244	244	-8.223	-5.358	25.39
Dim-E2-247	247	-7.972	-5.239	25.51
Dim-E2-250	250	-8.774	-5.338	25.41
Dim-E2-253	253	-8.814	-5.555	25.18
Dim-E2-256	256	-9.074	-5.619	25.12
Dim-E2-259	259	-8.583	-5.203	25.55
Dim-E2-264	264	-7.652	-5.189	25.56
Dim-E2-270	270	-8.63	-5.593	25.14
Dim-E2-276	276	-7.771	-5.243	25.51
Dim-E2-282	282	-8.951	-5.783	24.95
Dim-E2-288	288	-8.055	-5.577	25.16
Dim-E4-0035	3.5	-8.649	-5.073	25.68
Dim-E4-0115	11.5	-9.06	-5.406	25.34
Dim-E4-0180	18	-8.576	-5.332	25.41
Dim-E4-0245	24.5	-9.305	-5.569	25.17
Dim-E4-0300	30	-9.18	-4.956	25.80
Dim-E4-0370	37	-9.018	-5.551	25.19
Dim-E4-0415	41.5	-8.855	-5.582	25.16
Dim-E4-0485	48.5	-9.053	-5.580	25.16
Dim-E4-0540	54	-8.812	-5.386	25.36
Dim-E4-0615	61.5	-9.445	-5.671	25.06
Dim-E4-0695	69.5	-9.554	-5.717	25.02
Dim-E4-0780	78	-9.188	-5.505	25.24
Dim-E4-0945	94.5	-8.439	-5.163	25.59
Dim-E4-1000	100	-8.905	-5.437	25.31
Dim-E4-1080	108	-9.129	-5.512	25.23
Dim-E4-1155	115.5	-9.21	-5.487	25.25
Dim-E4-1235	123.5	-9.242	-5.426	25.32
Dim-E4-1310	131	-9.414	-5.433	25.31

Dim-E4-1370	137	-8.88	-5.399	25.34
Dim-E4-1455	145.5	-8.08	-5.271	25.48
Dim-E4-1535	153.5	-7.586	-5.112	25.64
Dim-E4-1600	160	-7.019	-5.186	25.56
Dim-E4-1655	165.5	-7.665	-5.193	25.56
Dim-E4-1760	176	-7.315	-5.020	25.74
Dim-E4-1830	183	-7.607	-5.069	25.68
Dim-E4-1920	192	-7.486	-5.001	25.75
Dim-E4-1985	198.5	-7.88	-5.369	25.38
Dim-E4-2030	203	-8.413	-5.356	25.39
Dim-E4-2110	211	-8.262	-5.287	25.46
Dim-E4-2195	219.5	-8.321	-5.373	25.37
Dim-E4-2275	227.5	-8.245	-5.505	25.24
Dim-E4-2360	236	-8.953	-5.638	25.10
Dim-E4-2430	243	-7.862	-5.575	25.16
Dim-E4-2510	251	-9.094	-5.763	24.97
Dim-E4-2605	260.5	-8.954	-5.725	25.01
Dim-E4-2665	266.5	-8.578	-5.525	25.22
Dim-E4-2740	274	-7.664	-5.279	25.47
Dim-E4-2905	290.5	-6.89	-5.344	25.40
Dim-E4-2955	295.5	-7.964	-5.567	25.17
Dim-E4-3035	303.5	-8.398	-6.110	24.61
Dim-E4-3125	312.5	-7.572	-5.677	25.06
Dim-E4-3200	320	-7.449	-5.728	25.01
Dim-E4-3255	325.5	-7.771	-5.761	24.97
Dim-E4-3335	333.5	-8.079	-5.659	25.08
Dim-E4-3425	342.5	-8.353	-5.881	24.85
Dim-E4-3475	347.5	-8.66	-5.791	24.94
Dim-E4-3525	352.5	-7.877	-5.706	25.03
Dim-E4-3580	358	-8.135	-5.660	25.08
Dim-E4-3670	367	-8.558	-5.883	24.85
Dim-E4-3770	377	-7.913	-5.905	24.82
Dim-HR*	-	5.439	-0.714	30.17

*Dim-HR denotes for the dolomitic limestone host-rock for the Dim Cave.

Table S4 Hendy test $\delta^{18}O$ and $\delta^{13}C$ isotope values of the speleothems from the Dim Cave (Alanya, SW Turkey) (values are in per mil)

Growth period	Sample ID	Depth (mm)	Distance to axes (mm)	$\delta^{13}C$ (VPDB)	$\delta^{18}O$ (VPDB)	$\delta^{18}O$ VSMOW
1st growth phase (~80–90 ka)	H-Dim-E3-261-1	261.0	4.0	-7.062	-5.376	25.37
	H-Dim-E3-261-2	261.0	18.0	-7.745	-6.443	24.27
	H-Dim-E3-261-3	261.0	23.0	-6.834	-5.356	25.39
	H-Dim-E3-261-4	261.0	29.0	-6.442	-5.039	25.72
	H-Dim-E3-261-5	261.0	34.0	-8.078	-5.259	25.49
2nd growth phase (~62–72 ka)	H-Dim-E3-194-1	194.0	9.0	-9.115	-4.589	26.18
	H-Dim-E3-194-2	194.0	17.0	-8.914	-4.591	26.18
	H-Dim-E3-194-3	194.0	23.0	-9.138	-5.102	25.65
	H-Dim-E3-194-4	194.0	30.0	-8.875	-4.543	26.23
	H-Dim-E3-194-5	194.0	36.0	-8.614	-4.392	26.38
3rd growth phase (~40–52 ka)	H-Dim-E3-085-1	8.5	4.0	-7.084	-4.663	26.10
	H-Dim-E3-085-2	8.5	11.0	-7.174	-4.614	26.15
	H-Dim-E3-085-3	8.5	18.0	-6.434	-4.515	26.25
	H-Dim-E3-085-4	8.5	27.0	-7.468	-4.607	26.16
	H-Dim-E3-085-5	8.5	34.0	-7.266	-4.561	26.21
4th growth phase (~13–40 ka)	H-Dim-E3-040-1	4.0	6.0	-5.721	-4.719	26.05
	H-Dim-E3-040-2	4.0	14.0	-5.257	-4.842	25.92
	H-Dim-E3-040-3	4.0	21.0	-5.186	-4.818	25.94
	H-Dim-E3-040-4	4.0	28.0	-5.081	-4.695	26.07
	H-Dim-E3-040-5	4.0	34.0	-5.079	-4.471	26.30
Growth period (10.6–11.9ka)	H-Dim-E2-130-1	130.0	5.0	-11.096	-5.633	25.10
	H-Dim-E2-130-2	130.0	13.0	-11.299	-5.589	25.15
	H-Dim-E2-130-3	130.0	20.0	-11.036	-5.704	25.03
	H-Dim-E2-130-4	130.0	27.0	-10.704	-5.449	25.29
	H-Dim-E2-130-5	130.0	34.0	-10.498	-5.310	25.44
Growth period (12.8–12.9 ka)	H-Dim-E4-178-1	178.0	5.5	-7.393	-5.637	25.10
	H-Dim-E4-178-2	178.0	11.0	-7.346	-4.995	25.76
	H-Dim-E4-178-3	178.0	16.0	-7.367	-4.996	25.76
	H-Dim-E4-178-4	178.0	23.0	-7.531	-4.967	25.79
	H-Dim-E4-178-5	178.0	29.0	-7.651	-5.125	25.63

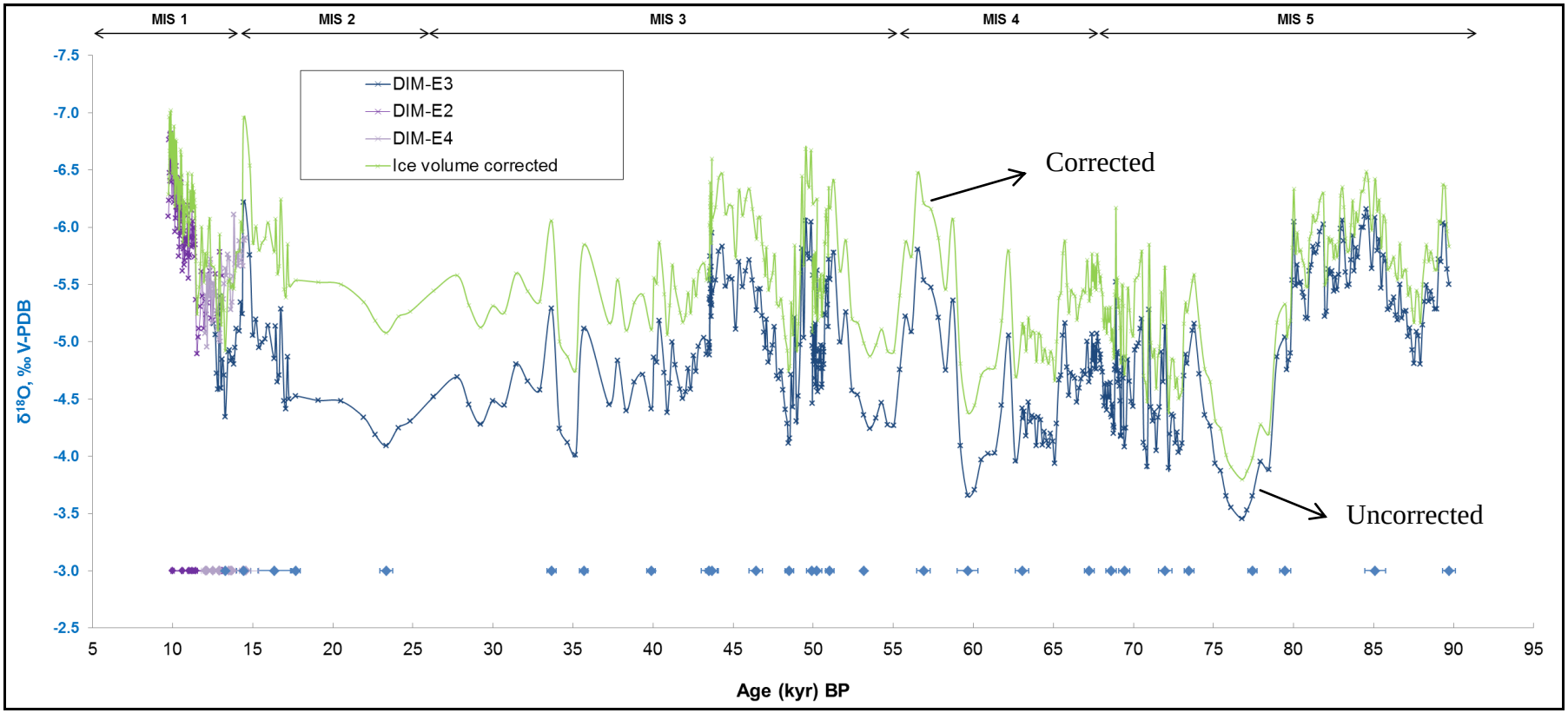

Figure S6 The ice volume-corrected stalagmite $\delta^{18}O$ record of Dim cave. The light green curve shows the composite stalagmite $\delta^{18}O$ record after correction for ice volume-related $\delta^{18}O$ contributions to seawater (Bintanja and van de Wal 2008). The blue, purple and light purple curves denote for the stalagmites Dim-E3, Dim-E2, and Dim-E4 respectively. Corresponding-coloured diamonds show U-series ages of the stalagmites. Age models are constructed by linear interpolation. Abbreviations: MIS = Marine Isotope Stage.

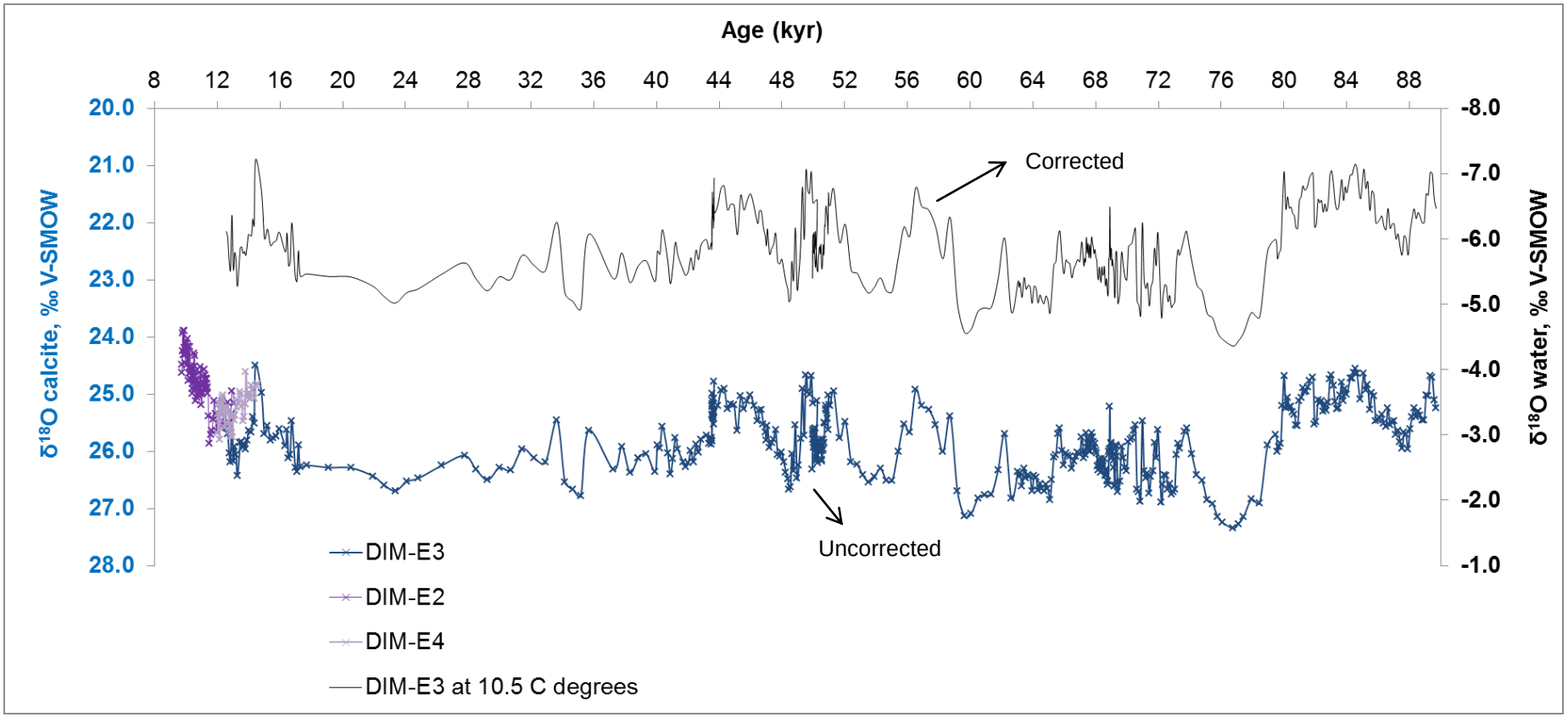

Figure S7 Calcite-water fractionation-corrected stalagmite $\delta^{18}O$ record of Dim Cave. Light black curve shows composite $\delta^{18}O_{water}$ record after applying calcite-water fractionation equation(Kim & O'Neil 1997) on $\delta^{18}O_{calcite}$, assuming 10.5 °C (8 degrees lower than today(Hughes et al. 2013; Gündalı et al. 1989; Sarıkaya et al. 2014)) within the cave during glacial times. Blue, purple and light purple curves represent uncorrected $\delta^{18}O$ records of stalagmites Dim-E3, Dim-E2, and Dim-E4 respectively. Note that correction is applied only to the stalagmite Dim-E3, which formed between ~90 and 13 kyr during the last glaciation.

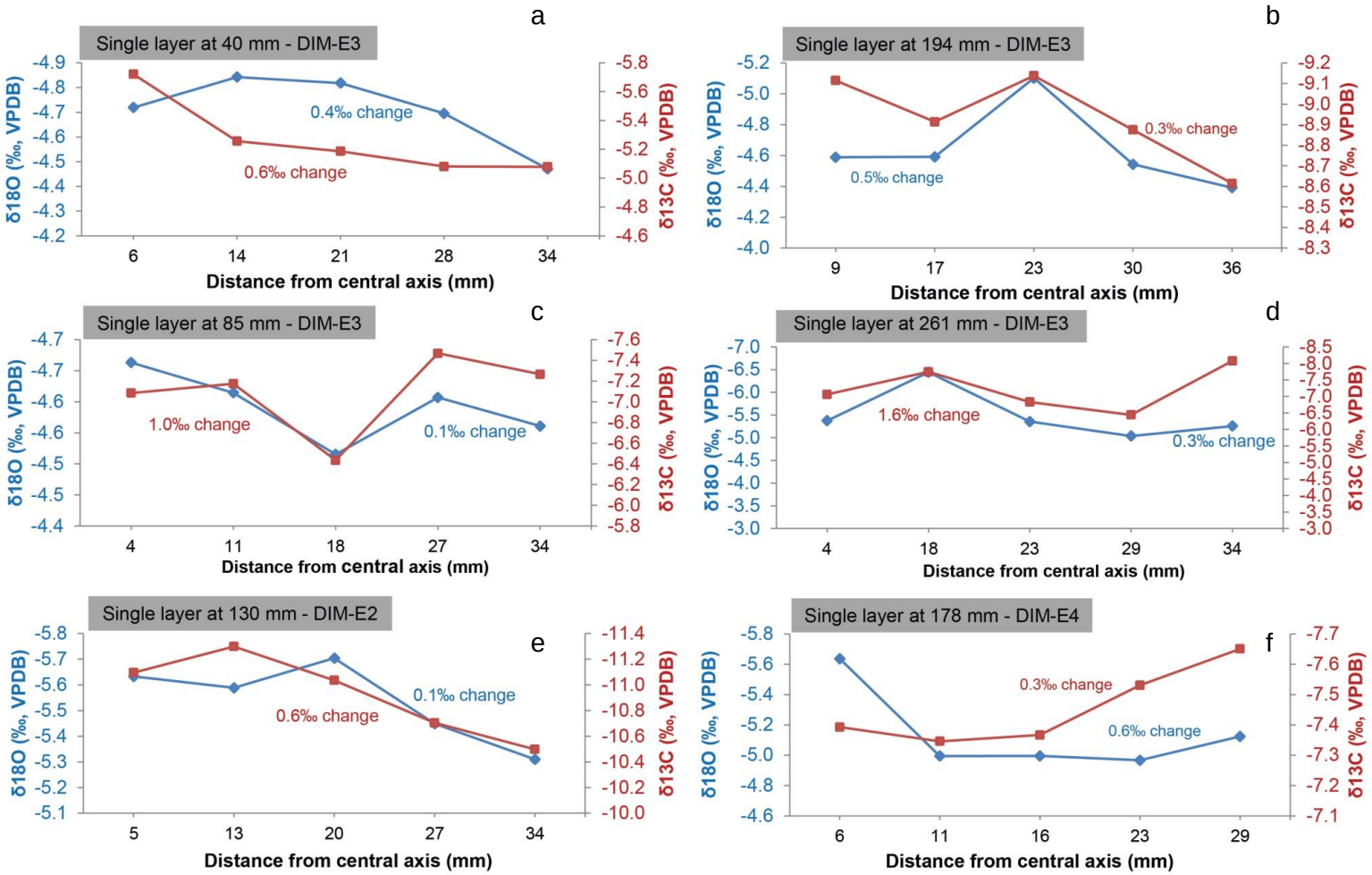

Figure S8 $\delta^{18}O$ and $\delta^{13}C$ plots for Hendy tests (Hendy 1971) along individual layers of stalagmites Dim-E3 (**a, b, c**, and **d**), Dim-E2 (**e**) and Dim-E4 (**f**). Isotopic values are plotted as distances away from the central growth axis. Note that the $\delta^{18}O$ values have not varied by more than 0.5‰ along the majority of tested growth layers (except for Dim-E4; **f**) and do not correlate with $\delta^{13}C$ values (R^2= 0.2), suggesting that the stalagmites were deposited at or close to quasi-isotopic equilibrium.

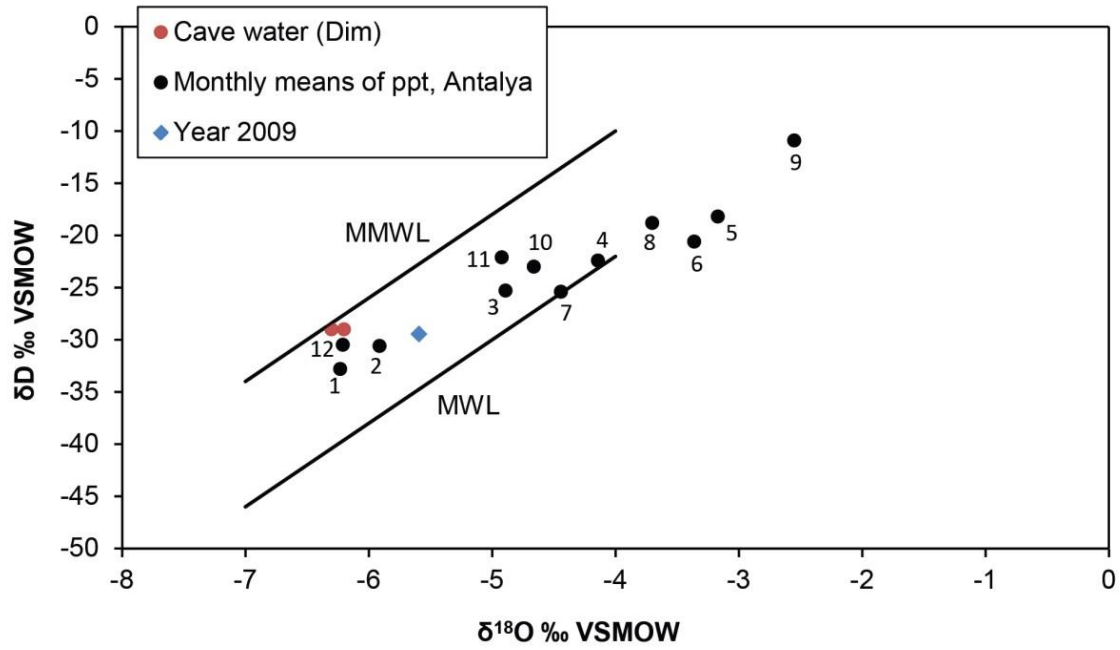

Figure S9 $\delta^{18}O$ and δD relationships of rainfall for the GNIP Antalya station for the period 1963–2009(IAEA/WMO 2015); numbers signify the respective month in Northern Hemisphere. Note that the modern cave water values are very close to winter rainfall and most recent 2009 rainfall values. The Mediterranean Meteoric Water Line (MMWL) (Gat & Carmi 1987) and Meteoric Water Line (MWL) (Craig 1961) are shown as references. Note that the winter rainfall data plot close to MMWL, while summer/spring rainfall show global MML signals.

Alternative Hypotheses for the interpretation of Dim isotope record

1. Temperature-based interpretation

The temperature dependence of speleothem $\delta^{18}O$ is variable and closely linked to the site conditions (McDermott 2004). In principle the regional mean annual temperature over the cave is assumed to control the $\delta^{18}O$ of calcite deposited from drip waters. Thus, $\delta^{18}O$ of calcite will reflect more depleted values during glacial periods and vice versa for the interglacials (e.g. Holocene), which is opposite to what is observed in the Dim Cave. The Dim record shows isotopically lighter values (from -4.5 to -7‰ VPDB; Fig. 2) in the Holocene than in the glacial periods (Hughes et al. 2013; Essallami et al. 2007). Temperature dependence of isotopic signatures of speleothems are well-exemplified from the Sofular record from Black Sea region(Fleitmann et al. 2009) where $\delta^{18}O$ values of calcite becomes less negative towards Holocene (~-13 to -8‰ VPDB; Fig. 2).In contrast, the Dim record cannot reflect temperature changes. This situation is quite common in the literature for relatively close sites. For example some records from New Zealand follow temperature (Williams et al. 2005) while others sites have a reverse isotopic signal from the $\delta^{18}O$ (Hellstrom et al. 1998).

2. Volume of rainfall (amount effect)

The amount effect is widely interpreted as a control on the isotopic composition of speleothems. In the case of the last glaciation from DIM, this interpretation is difficult to sustain. We have independent evidence from two

sources that show that conditions during glacial periods are drier or at least no wetter than in the Holocene. The PMIP reconstruction for the LGM (Braconnot et al. 2007) suggests rainfall values that are virtually identical to modern. More tellingly, our speleothem growth rates from Dim-E3 (Fig. S2-a) reveal that growth rates are positive during glacial times but are much slower than the early Holocene (which is known to be wet in the EM (Jones et al. 2007; Lisker et al. 2010)). The fact that the moisture balance is positive in glacial times does not imply higher rainfall. In fact, reduced evaporative flux due to depressed temperatures, reduced forest cover and increased snow-cover all divert the limited moisture flow to groundwater pathways. It is highly likely that all of the glacial period has less rainfall than the Holocene.

3. Seasonality of rainfall

SW Turkey is located in the heart of the westerly flow zone. At the present day almost no precipitation occurs in summer and if the shoulder months are taken into account winter rainfall dominates completely (IAEA/WMO 2015). This is evident from all the modern climatological data (Jex et al. 2011; Sarıkaya et al. 2008; Türkeş & Erlat 2009). For the last glacial cycle, the coldest period is the LGM and the PMIP models clearly demonstrate that there is no switch from winter to summer dominated rainfall in this part of the EM (Braconnot et al. 2007). It is virtually impossible for monsoonal rain to penetrate this far north under modern conditions and the likelihood under glacial conditions is significantly reduced.

4. Evaporation effects

Evaporation effects on the speleothem isotopic signal are important. This is actually embedded in our interpretation because the air mass changes involve a complex mix of changed temperature and evaporation due to source area, cloud cover and other variables.

5. Sea air temperature

The changes in ocean source moisture will relate to a series of independent variables. These include; 1) regional changes in air temperature, which is also caused by the air masses passing over the region; 2) changes in the thermohaline circulation in the eastern Mediterranean (Bar-Matthews et al. 1999). In theory this is hard to incorporate, but the thermohaline circulation reflects primarily wind stress across the basin and the through flow to/from the Atlantic. Both of these are directly related to the westerly circulation and what is happening in the North Atlantic source area, and so are closely linked with the westerly air masses. We also note that the smaller scale changes in deep/intermediate water formation relate to decadal scale changes in the Mediterranean Basin (Pinardi & Masetti 2000) and these are likely to be integrated out of a millennial scale record.

REFERENCES (PAPER 3)

Abrantes, F. et al., 2012. Paleoclimate Variability in the Mediterranean Region. In *The Climate of the Mediterranean Region* (ed. Lionello, P.). Elsevier, pp. 1–86.

Akman, Y. & Ketenoğlu, O. 1986. The climate and vegetation of Turkey. *Proceedings of the Royal Society of Edinburgh* 89B, pp. 123–134.

Ayalon, A. et al., 2002. Climatic conditions during marine oxygen isotope stage 6 in the eastern Mediterranean region from the isotopic composition of speleothems of Soreq Cave, Israel. *Geology*, 30, pp.303–306.

Badertscher, S. et al., 2014. Speleothems as sensitive recorders of volcanic eruptions – the Bronze Age Minoan eruption recorded in a stalagmite from Turkey. *Earth and Planetary Science Letters*, 392, pp.58–66.

Baker, A. et al., 1997. Elevated and variable values of 13C in speleothems in a British cave system. *Chemical Geology*, 136(3-4), pp.263–270.

Bar-Matthews, M. et al., 1996. Carbon and oxygen isotope study of the active water-carbonate system in a karstic Mediterranean cave: Implications for paleoclimate research in semiarid regions. *Geochimica et Cosmochimica Acta*, 60(2), pp.337–347.

Bar-Matthews, M. et al., 1999. The Eastern Mediterranean paleoclimate as a reflection of regional events: Soreq cave, Israel. *Earth and Planetary Science Letters*, 166(1-2), pp.85–95.

Bar-Matthews, M. et al., 2003. Sea–land oxygen isotopic relationships from planktonic foraminifera and speleothems in the Eastern Mediterranean region and their implication for paleorainfall during interglacial intervals. *Geochimica et Cosmochimica Acta*, 67(17), pp.3181–3199.

Bar-Matthews, M., Ayalon, A. & Kaufman, A., 1997. Late Quaternary Paleoclimate in the Eastern Mediterranean Region from Stable Isotope Analysis of Speleothems at Soreq Cave, Israel. *Quaternary Research*, 47(47), pp.155–168.

Berger, A. & Loutre, M.F., 1991. Insolation values for the climate of the last 10 million years. *Quaternary Science Reviews*, 10(1988), pp.297–317.

Bintanja, R. & van de Wal, R.S.W., 2008. North American ice-sheet dynamics and the onset of 100,000-year glacial cycles. *Nature*, 454(7206), pp.869–72.

Braconnot, P. et al., 2007. Results of PMIP2 coupled simulations of the Mid-Holocene and Last Glacial Maximum – Part 1: experiments and large-scale features. *Climate of the Past*, 3(2), pp.261–277.

Cerling, T.E. et al., 1991. On the isotopic composition of carbon in soil carbon dioxide. *Geochimica et Cosmochimica Acta*, 55, pp.3403–3405.

Craig, H., 1961. Isotopic Variations in Meteoric Waters. *Science*, 133, pp.1702–1703.

Dietzel, M. et al., 2009. Oxygen isotopic fractionation during inorganic calcite precipitation — Effects of temperature, precipitation rate and pH. *Chemical Geology*, 268(1-2), pp.107–115.

Essallami, L. et al., 2007. Hydrological changes in the Mediterranean Sea over the last 30,000 years. *Geochemistry, Geophysics, Geosystems*, 8(7), pp.1–11.

Fleitmann, D. et al., 2009. Timing and climatic impact of Greenland interstadials recorded in stalagmites from northern Turkey. *Geophysical Research Letters*, 36(19), pp.1–5.

Frisia, S.A., 2015. Microstratigraphic logging of calcite fabrics in speleothems as tool for palaeoclimate studies. *International Journal of Speleology*, 44(January), pp.1–16.

Frumkin, A., Bar-Yosef, O. & Schwarcz, H.P. 2011. Possible paleohydrologic and paleoclimatic effects on hominin migration and occupation of the Levantine Middle Paleolithic. *Journal of human evolution*, 60(4), pp.437–51.

Frumkin, A. Ford, D.C., Schwarcz, H.P. 1999. Continental Oxygen Isotopic Record of the Last 170,000 Years in Jerusalem. *Quaternary Research*, 51, pp. 317–327.

Gat, J.R. & Carmi, I., 1987. Effect of climate changes on the precipitation patterns and isotopic composition of water in a climate transition zone: Case of the Eastern Mediterranean Sea area. In *The Influence of Climate Chnage and Climatic Variability on the Hydrolic Regime and Water Resources*. Vancouver: IAHS Publ. no. 168, pp. 513–524.

Gat, J.R. & Rindsberger, M., 1985. The isotopic signature of precipitation originating in the Mediterranean Sea area: A possible monitor of climate modification? *Israel Journal of Earth Sciences*, 34, pp.80–85.

Göktürk, O.M.M. et al., 2011. Climate on the southern Black Sea coast during the Holocene: implications from the Sofular Cave record. *Quaternary Science Reviews*, 30(19-20), pp.2433–2445.

Grootes, P.M. & Stuiver, M., 1997. Oxygen 18/16 variability in Greenland snow and ice with 10 -3- to 105-year time resolution. *Journal of Geophysical Research*, 102(C12), pp.26,455–26,470.

Gündalı, N. et al., 1989. Dim Mağarası (Alanya) Araştırma Raporu, Mimari ve Elektrikasyon Uygulama Projeleri (in Turkish, unpublished report 369), Ankara.

Hellstrom, J., Mcculloch, M. & Stone, J., 1998. A Detailed 31 , 000-Year Record of Climate and Vegetation Change , from the Isotope Geochemistry of Two New Zealand Speleothems. *Quaternary Research*, 178, pp.167–178.

Hendy, C.H., 1971. The isotopic geochemistry of speleothems-I. The calculation of the effects of different modes of formation on the isotopic composition of speleothems and their applicability as paleoclimatic indicators. *Geochimica et Cosmochimica Acta*, 35(8), p.80l–824.

Horowitz, A. & Gat, J.R. 1984. Floral and Isotopic Indications for Possible Summer Rains in Israel during Wetter Climates. *Pollen et Spores*, 26, pp. 61–68.

Hughes, P.D., Gibbard, P.L. & Ehlers, J., 2013. Timing of glaciation during the last glacial cycle: evaluating the concept of a global “Last Glacial Maximum” (LGM). *Earth-Science Reviews*, 125, pp.171–198.

IAEA/WMO, 2015. Global Network of Isotopes in Precipitation-The GNIP Database. Available at: http://www.iaea.org/water. (Last accessed Feb 2015).

Jex, C.N. et al., 2011. A 500yr speleothem-derived reconstruction of late autumn–winter precipitation, northeast Turkey. *Quaternary Research*, 75(3), pp.399–405.

Jones, M.D., Roberts, C.N. & Leng, M.J., 2007. Quantifying climatic change through the last glacial–interglacial transition based on lake isotope palaeohydrology from central Turkey. *Quaternary Research*, 67(3), pp.463–473.

Kim, S.-T. & O’Neil, J.R., 1997. Equilibrium and nonequilibrium oxygen isotope effects in synthetic carbonates. *Geochimica et Cosmochimica Acta*, 61(16), pp.3461–3475.

Kleman, J. et al., 2013. Pre-LGM Northern Hemisphere ice sheet topography. *Climate of the Past*, 9(5), pp.2365–2378.

Kutzbach, J.E. et al., 2014. Potential role of winter rainfall in explaining increased moisture in the Mediterranean and Middle East during periods of maximum orbitally-forced insolation seasonality. *Climate Dynamics*, 42(3-4), pp.1079–1095.

Kwiecien, O. et al., 2009. North Atlantic control on precipitation pattern in the eastern Mediterranean/Black Sea region during the last glacial. *Quaternary Research*, 71(3), pp.375–384.

Lisker, S. et al., 2010. Late Pleistocene palaeoclimatic and palaeoenvironmental reconstruction of the Dead Sea area (Israel), based on speleothems and cave stromatolites. *Quaternary Science Reviews*, 29(9-10), pp.1201–1211.

McDermott, F., 2004. Palaeo-climate reconstruction from stable isotope variations in speleothems: a review. *Quaternary Science Reviews*, 23(7-8), pp.901–918.

Minissale, A. et al., 2002. Geochemistry of Quaternary travertines in the region north of Rome (Italy): structural, hydrologic and paleoclimatic implications. *Earth and Planetary Science Letter*s, 203(2), pp.709–728.

Pearson, P.N. & Palmer, M.R., 2000. Atmospheric carbon dioxide concentrations over the past 60 million years. *Nature*, 406, pp.695–699.

Petit, J.R. et al., 1999. Climate and atmospheric history of the past 420, 000 years from the Vostok ice core, Antarctica. *Nature*, 399, pp.429–436.

Pinardi, N. & Masetti, E., 2000. Variability of the large scale general circulation of the Mediterranean Sea from observations and modelling: a review. *Palaeogeography, Palaeoclimatology, Palaeoecology*, 158(3-4), pp.153–173.

Prentice, I.C., Guiot, J. & Harrison, S.P., 1992. Mediterranean vegetation, lake levels and paleoclimate at the Last glacial Maximum. *Nature*, 360, pp.658–660.

Rindsberger, B.M. et al., 1990. Patterns of the isotopic composition of precipitation in time and space : data from the Israeli storm water collection program. *Tellus*, 42B, pp.263–271.

Rindsberger, M. et al., 1983. The relationship between air mass trajectories and the water isotope composition of rain in the Mediterranean Sea area. *Geophysical Research Letters*, 10(1), pp.43–46.

Rollinson, H.R., 1993. Using Geochemical Data Evalution, Presentation, Interpretation, Taylor & Francis.

Sarıkaya, M.A. et al., 2008. Cold and wet Last Glacial Maximum on Mount Sandıras, SW Turkey, inferred from cosmogenic dating and glacier modeling. *Quaternary Science Reviews*, 27(7-8), pp.769–780.

Sarıkaya, M.A. et al., 2014. An early advance of glaciers on Mount Akdağ, SW Turkey, before the global Last Glacial Maximum; insights from cosmogenic nuclides and glacier modeling. *Quaternary Science Reviews*, 88, pp.96–109.

Still, C.J. et al., 2003. Global distribution of C3 and C4 vegetation: Carbon cycle implications. *Global Biogeochemical Cycles*, 17(1), pp.6–1–6–14.

Svensson, A. et al., 2008. A 60,000 year Greenland stratigraphic ice core chronology. *Climate of the Past*, 4, pp.47–57.

Türkeş, M. & Erlat, E., 2009. Winter mean temperature variability in Turkey associated with the North Atlantic Oscillation. *Meteorology and Atmospheric Physics*, 105(3-4), pp.211–225.

Tzedakis, P.C., 2007. Seven ambiguities in the Mediterranean palaeoenvironmental narrative. *Quaternary Science Reviews*, 26(17-18), pp.2042–2066.

Vaks, A. et al., 2003. Paleoclimate reconstruction based on the timing of speleothem growth and oxygen and carbon isotope composition in a cave located in the rain shadow in Israel. *Quaternary Research*, 59(2), pp.182–193.

Wang, Y. et al., 2008. Millennial- and orbital-scale changes in the East Asian monsoon over the past 224,000 years. *Nature*, 451(7182), pp.1090–1093.

Wang, Y.J. et al., 2001. A high-resolution absolute-dated late Pleistocene Monsoon record from Hulu Cave, China. *Science*, 294(5550), pp.2345–2348.

Wickens, L. et al., 2011. The Last Interglacial and Holocene in SW Turkey: Evidence from Calcite-Aragonite Speleothems. In American Geophysical Union, Fall Meeting. San Francisco, California, USA: AGU.

Wigley, T.M.L. & Farmer, G. 1982. Climate of the Eastern Mediterranean and the Near East in Paleoclimates, Paleoenvironments and Human Communities in the Eastern Mediterranean Region in Later Prehistory (eds Bintliff, J.L. et al.), Part ii, 3–37 (B.A.R. Oxford).

Williams, P.W. et al., 2005. Late Pleistocene to Holocene composite speleothem 18O and 13C chronologies from South Island, New Zealand—did a global Younger Dryas really exist? *Earth and Planetary Science Letters*, 230(3-4), pp.301–317.

Zhou, H. et al., 2011. Speleothem-derived Asian summer monsoon variations in Central China, 54-46 ka. *Journal of Quaternary Science*, 26(8), pp.781–790.

PAPER 4

The following study presents and synthesis high-resolution trace element/Ca ratios with stable and radiogenic isotope (O, C, and Sr) profiles from Dim Cave (SW Turkey). These multi-proxy data help to constrain the climatic conditions in Dim Cave over the last glacial cycle.

High-resolution trace element and stable/radiogenic isotope profiles of late Pleistocene to Holocene speleothems from Dim Cave, SW Turkey

Abstract

Multiple climate-sensitive trace element/Ca and stable isotope (O and C) profiles derived from Dim Cave speleothems (S-SW Turkey) provide evidence of climatic changes and define a series of paleohydrological conditions for the period ~9–90 kyr. Dim Cave speleothem Mg/Ca, Sr/Ca, U/Ca, Ba/Ca, and Y/Ca ratios demonstrate similar patterns over glacial-interglacial scales, in agreement with $\delta^{18}O$ and $\delta^{13}C$ records. Three episodes of increased precipitation or specifically more positive moisture balance (71–63 kyr, 51–40 kyr, and 18–10 kyr) were observed based on Y/Ca (Zr/Ca) ratios, calcite micromorphology, and growth rates. Increasing concentrations of Y, Zr (and U) are attributed to enhanced levels of terrestrial input during these periods. Correlations between $\delta^{13}C$, $\delta^{18}O$ and Mg/Ca during 40–18 kyr (corresponding with the lowest observed growth rate of ~0.8 mm/kyr), 63–51, and 80–71 kyr (growth rates of 1.3 and 2.0 mm/kyr respectively), as well as co-varying and enhanced Mg/Ca, Sr/Ca, and to a lesser extent Ba/Ca, ratios point to the prior calcite precipitation, wall rock interaction, and preferential dolomite dissolution over calcite in the host dolomitic limestone during these periods. This relationship suggests that water-rock interactions are maximised during episodes of slower drip rates of water through the karst under drier conditions. Chondrite-normalized rare earth element and yttrium (REY) patterns of the stalagmites reveal seawater signatures closely linked to the dolomitic limestone. Excluding the aragonite formation during ~80–75 kyr period, which is an autogenic effect, trace element/Ca ratios appear to respond to millennial scale global cooling periods such as Heinrich events.

Keywords: speleothems, elemental geochemistry, stable isotopes, radiogenic Sr-isotopes, Dim Cave, SW Turkey, Eastern Mediterranean

1. Introduction

Geochemical records derived from speleothems are becoming significantly more important in constraining past climatic conditions. Together with stable/radiogenic isotope data, trace element/Ca (TE/Ca) ratios (e.g. Mg/Ca, Sr/Ca, and U/Ca) can be used to define and refine climate-driven paleohydrological variability, including the extent of soil-fluid-rock interactions and exotic terrestrial inputs into cave systems (e.g. riverine input or aeolian dust). High-resolution, continuous records with precise chronological control give the opportunity to investigate the interplay between various environmental and climate-sensitive proxies that have been preserved by terrestrial cave deposits (Fairchild & Treble 2009; Wang et al. 2001; Zhao et al. 2001). Changes in climate and particularly precipitation over annual to centennial timescales have always been important for the ancient civilizations of the Eastern Mediterranean (EM) (e.g. Bar-Matthews &Ayalon 2011; Robinson et al. 2006; Roberts et al. 2011; Frumkin et al. 2011). Research suggests that decreases in rainfall-driven water availability during the Holocene (after ~7000 cal BP) in this region (Vaks et al. 2003; Tzedakis 2007; Jalut et al. 2009), was one of the main reasons for the decline and/or collapse of some former civilizations (e.g. decline of Ottoman Empire in the preindustrial era, the collapse of Uruk society in Mesopotamia, and transition from chalcolithic to the early Bronze Age; societal collapse of the Late Bronze Age; Dean et al. 2015; Kaniewski et al. 2012; Staubwasser & Weiss 2006; Roberts et al. 2011). Therefore, climatic archives revealing past variability of rainfall regimes is of great importance for society.

Trace element variations within speleothems have been investigated in many experimental and cave monitoring studies (e.g. Bar-Matthews et al. 1999; Fairchild et al. 2000; Fairchild & Treble 2009; Murray 1954), underlining their potential as an independent qualitative paleoenvironmental proxy. The transmission of the trace elements into the karst host-rock is based on the geochemical behaviour of the trace elements (i.e. partitioning coefficients (D) of individual elements between host-rock, seepage water and speleothems; Morse & Bender 1990) in the overlying soil and unsaturated epikarst zones, and hydrological processes affecting the infiltration of surface and soil waters (Roberts et al. 1998; Fairchild et al. 2001; Fairchild & Treble 2009). Moreover, the differential dissolution of host rock calcite and dolomite controlled by rainfall and pathway-driven residence times can cause considerable variation in trace element chemistry of the waters (Fairchild et al. 1994; Fairchild et al. 2000). The Mg/Ca ratio, in particular, has been used to determine temperature-related partitioning at the water-calcite interface (Gascoyne 1983) and also effective precipitation (i.e. precipitation minus evapotranspiration) that controls the dripping rate and hence the residence time of the seepage water (Fairchild & Treble 2009; Roberts et al. 1998; Gascoyne

1983; Hellstrom & Mcculloch 2000). For example, drier conditions limit the seepage rates, maximizing the water-soil-rock interactions, leading to incongruent dolomite dissolution relative to calcite in solution, and hence yield higher Mg/Ca in cave waters and speleothems (Roberts et al. 1998; Fairchild et al. 2000).

In addition to Mg/Ca, Sr/Ca and Ba/Ca ratios are also used as proxies for paleo-aridity, although increasing Sr/Ca may also reflect input from additional sources such as terrestrial aeolian dust and sea salt in near-coastal sites (Goede et al. 1998). Drier conditions also promote CO_2 degassing during the infiltration of seepage waters and result in "upflow" or prior calcite precipitation (PCP) along the flow path (e.g. in the epikarst or on the cave roof) removing Ca^{+2} and ^{12}C from the solution, and leading to elevated Mg/Ca, Sr, Ba/Ca, and $\delta^{13}C$ in speleothems (Huang et al. 2001; Fairchild & Treble 2009; Fairchild and McMillan 2007; Johnson et al. 2006; Regattieri et al. 2014). Zr/Ca, U/Ca, and Y/Ca can also be used as indicators of both relative aridity and the degree of exotic terrestrial input (e.g. from leached felsic or other types of silicate rocks), though this is best achieved in conjunction with cave monitoring data and other proxies (e.g. stable isotope data) showing similar trends. Overall, the host and basement rock compositions play a vital role in sourcing the trace element inventory of the drip waters and speleothems (Fairchild & Treble 2009; Belli et al. 2013).

As with most of the global speleothem-based studies, regional studies in the EM focus primarily on stable isotope ($\delta^{18}O$ and $\delta^{13}C$) variations (e.g. Bar-Matthews et al. 2003; Fleitmann et al. 2009; Bar-Matthews et al. 1999) to reconstruct the paleo-rainfall, paleo-temperature, and paleo-vegetation styles. In this region, the climate system is complex as it is located at the boundary location between the northern hemisphere westerlies and the sub-tropical high pressure belt (Türkeş 1996; Jex et al. 2011). This also necessitates the use of multiple proxies in paleoclimatic interpretations, most commonly attempting to reconstruct the temperature and meteoric precipitation characteristics of a specific site.

The current study presents a number of TE/Ca ratios and bulk concentrations from several stalagmites (Dim-E2, Dim-E3, and Dim-E4) in Dim Cave, SW Turkey (Fig. 1) for the time period spanning from ~10 to 90 kyr. Geochronological (U-series ages) and isotopic ($\delta^{18}O$ and $\delta^{13}C$) data of these stalagmites have already been discussed in Paper 3 (Ünal-İmer et al. 2015) (App. 3). Here, we combine new trace element and Sr-isotope data with the existing stable isotope record to provide a better understanding of the paleoenvironmental conditions of the southern coastal Turkey, and to characterize the past climate in the EM region for the last glaciation and the start of the Holocene.

2. Site description

Dim Cave (also known as Gavurini Cave; Gündalı et al. 1987; Gündalı et al. 1989) (36°32'N, 32°06'E, 232 m a.s.l.) is located in the Cebel Reis Mountains of SW Turkey and occurs in faulted recrystallized Permian limestones of the Alanya Nappes (Fig.1; Bozkaya & Yalçin 2004; Gündalı et al. 1989; Okay & Özgul 1984) capping Permian metamorphic basement, which is dominantly composed of mica-schist, quartzite, and dolomite (Fig. 1; Gündalı et al. 1989). The cave is originally related to drainage associated with Dim River (Fig. 1) but due to tectonic uplift the river is now incised to a base level several hundred metres below the cave which is now entirely in the vadose zone. It has been reported that the cave hydrological system is largely inactive, or more precisely rarely active, and only forms aragonite-type speleothems at present (Gündalı et al. 1989; Wickens et al. 2011) due to low seepage rates. There are, however, small pool formations (Fig. S1; App. 3) towards the lower and deeper parts of the cave (~150 m deep w.r.t. speleothem collection locations) where the water reaches a level of impermeable rocks including micaschist.

The modern climate above the cave is characterized by a Mediterranean climate with warm, dry summers and mild, wet winters. Based on the GNIP data, the mean annual precipitation averages around 1075 mm (Antalya Station: 36°52' N, 30°42' E, 49 m a.s.l.), dominantly occurring in winter (58%; 625 mm yr^{-1}) and a very dry summer characterised by only 1% (12 mm yr^{-1}) of total rainfall (IAEA/WMO 2015). Precipitation is primarily sourced from the EM air masses (Türkeş & Erlat 2009). Water samples collected from the pools in the cave display similar stable isotope ($\delta^{18}O$ and δD; -6.2 ±0.1‰ and -29.0 ±2.0‰ VSMOW; Fig. S1b; App. 3) characteristics when compared with average isotopic data of modern winter (Dec-Feb) rainfall received in Antalya ($\delta^{18}O$: -6.1 and δD:-31.3‰; Table S2; App. 3). These values correlate well with the Mediterranean Meteoric Water Line (MMWL; Fig. S9; App.3; Gat & Carmi 1987).

3. Sample and methods

Three stalagmite samples (Dim-E2, Dim-E3, and Dim-E4; Fig. S2–S4 in App.3; Paper 3) collected from Dim Cave (Fig. 1) were latitudinally halved using a diamond blade rock saw to reveal their internal stratigraphy and texture. The stalagmites show changes in growth axes marked by sudden lateral shifts in color and/or texture with three distinct sections, 30, 40, and 35 cm in length, respectively. While Dim-E2 (29 cm-long) displays no changes in growth axes; Dim-E3 (32 cm-long) and Dim-E4 (38 cm-long) samples demonstrate two and three shifts in growth direction, respectively (Paper 3; App. 3). For microscopic stratigraphy studies, three thin sections from three main growth periods of Dim-E3 and one thin section from each Dim-E2 and –E4 were prepared at

the Rock Laboratory of the School of Earth Sciences (UQ). These representative thin section studies and related observations are first reported in Paper 3 (App. 3).

One half of each stalagmite was chosen for microdrilling with 0.5–1.5mm diamond-tipped burrs attached to a dental drill (5000 rpm) for geochemical analyses. Microdrilling was first performed at the top and bottom of stalagmites, and at the points where growth direction and/or color and/or texture changed, to sample for U-series analyses. Stalagmites were later microdrilled along their growth axes at 0.5 to 1 mm increments, for stable isotope and TE/Ca ratio analyses. ~100 mg samples of stalagmite powder were used for U-series dating using a Nu Plasma multi-collector plasma mass spectrometer (MC-ICP-MS), housed at the Radiogenic Isotope Facility (RIF), the University of Queensland, while ~3–6 mg of powder were used for TE/Ca ratio analyses using a Thermo X-series II ICP-MS equipped with an ESI FC4 autosampler. 3–4 mg of sample powders were used for stable isotope analyses, which were conducted at the Stable Isotope Geochemistry Laboratory (SIGL) of UQ using an Isoprime Dual Inlet Mass Spectrometer with a Multiprep (DI-IRMS) attachment. Detailed methodology for U-series dating and stable isotope analyses is given in Papers 1 and 3 and in Appendices 1 and 2. For TE/Ca ratio analyses, ~2 mg of pure carbonate per sample was dissolved in 10 ml of 2% double-distilled nitric acid mixed with a multi-element internal standard solution consisting of Sc, V, Bi, and U, to achieve a dilution factor of ~1:50,000. Final solutions were analysed using the protocol given in Nguyen et al. (2012) with minor modifications. Measured elemental signals of sub-samples were first subtracted for the background (blank) signal and then corrected for internal drift before calculating the signal ratios of TE/Ca. Elemental signal ratios were later corrected for external drift based on the correction factors calculated from the elemental signal ratios of the monitor solution, which was measured repeatedly between groups of samples (3–5 samples). Final corrected signal ratios of Mg/Ca, Sr/Ca, Y/Ca, Ba/Ca, and U/Ca were calibrated against the known values of TE/Ca ratios of a synthetic carbonate standard (made of Japanese coral standard JCP-1doped with several single element standard solutions of known concentrations), while the signals of Zr/Ca was calibrated against the USGS W-2 diabase rock standard. Ratios are reported in µmol/mol or mmol/mol together with long-term precisions (%) for each ratio (Table S1, App. 4).

In addition to TE/Ca ratio analyses of the sub-samples, a total of 14 speleothem and host-rock samples were analysed for their trace element concentrations using the same ICP-MS, following a procedure modified after Eggins et al. (1997) and Kamber et al. (2003). Around 50 mg of samples were digested in 2 ml of 15.8 N double-distilled HNO_3. A small aliquot of each sample was transferred into a tube and spiked with the internal standards (^{7}Li, ^{103}Rh, ^{115}In, ^{187}Re, ^{209}Bi, and

^{235}U). The solution was further diluted with 2% HNO_3 to achieve a dilution factor of ~4,000 in the final solution. The raw signals obtained were subtracted for the background/blank signals, and further corrected for the internal and external drift, and for oxide and double charge interference. Element concentrations (reported in ppb) were calibrated against the preferred elemental concentrations in USGS W-2 diabase rock standard (Table S2; App. 4).

4. Results

4.1. U-series dating and stable isotope data

U-series age data (a total of 46 samples) of the stalagmites are presented in Table S1 and the sample locations for the U-series ages are shown in Figures S2–S4 (Paper 3=Ünal-İmer et al. 2015; App. 3). Stalagmite Dim-E3, which is the main focus of this study, reveals growth with at least seven different growth phases. Its continuous growth from 89.7 ± 0.41 kyr to 13.3 ± 0.31 kyr fluctuates in rate from a maximum of 11.9 mm/kyr to a minimum of 0.8 mm/kyr at 72–63 kyr and 40–18 kyr, respectively. Two other stalagmites, Dim-E2 and Dim-E4, show relatively faster growth rates with one or two main growth episodes collectively spanning the period between 14.4 ± 0.47 and 10.0 ± 0.1 kyr.

Results of stable isotope (C and O) analyses of stalagmites are given in Table S2 (App. 3) and are summarized briefly and illustrated in Paper 3 (Fig. 2 in pages 70, 71, and 76). Without adjustments for the effect of ice-volume-related changes, the $\delta^{18}O$ record of the Dim stalagmites span between -3.3 and -6.6‰ VPDB, while the overall $\delta^{13}C$ record varies from -12.5 to -0.2‰ VPDB. Stable isotope variations of the stalagmites are plotted in Figs. 2 and 3 along with their high-resolution TE/Ca profiles and calculated summer insolation curve for 30°N, for comparison purposes (Berger & Loutre 1991). In addition, Hendy tests (Hendy 1971) showed that the Dim stalagmites were deposited in quasi-isotopic equilibrium (Table S4 and Fig. S4; App. 3).

4.2. Trace element data

TE/Ca ratios (Mg/Ca, Sr/Ca, Y/Ca, Ba/Ca, Zr/Ca, and U/Ca) of a total of 575 sub-samples from all stalagmites (Dim-E2, Dim-E3, and Dim-E4) are reported in Table S1 (App. 4) and illustrated in Fig. 2, covering the period between ~90 and 10 kyr. TE/Ca profiles of Dim-E2 and Dim-E4 are shown in Fig. 3 to show detailed trace element variations for the period from ~15 to 9 kyr. Mg/Ca ranges from 52.6 to 4.1 mmol/mol (mean = 29.9), Sr/Ca varies between 0.85 and 0.03 mmol/mol (mean = 0.06), U/Ca ranges from 8.4 to 0.03 µmol/mol (mean = 0.18), Ba/Ca ranges from 46.3 to 2.1 µmol/mol (mean = 4.5), Zr/Ca ranges from 8.2 to 0.01 µmol/mol (mean = 0.48), and Y/Ca varies

widely between 6.7 and 0.002 µmol/mol (mean = 0.7). It should be noted that the aragonite layer observed in Dim-E3 corresponding to a time interval of ~80–75 kyr has significantly different trace element ratios to all the calcite values, and is not included in the general analyses of the trace elements.

The dataset is sub-divided into different periods based on the calculated growth rates, and changes in Y/Ca ratios (i.e. 18–10; 40–18, 51–40, 63–51, 71–63, 80–71, and 89–80 kyr). In general, Mg/Ca, Sr/Ca, and Ba/Ca ratios exhibit similar trends, except in the aragonite layer (~80–75 kyr) and at the termination of the Last Glacial Maximum (LGM) at ~19–18 kyr (Fig. 2). Similarly, Y/Ca, Zr/Ca, and U/Ca show covarying trends, specifically during the periods between ~51–40, 71–63, and 89–80 kyr. Their higher values also correspond to periods of high growth rates of Dim-E3 (i.e. 7.4, 11.9, and 6.1 mm/kyr, respectively; Fig. 2). Dim-E3 has its lowest growth rate between ~40 and 18 kyr (0.8 mm/kyr; Fig. 2) and therefore microsampling yielded the lowest resolution during this interval. In Figure 3, Dim-E2 displays elevated $\delta^{13}C$ or $\delta^{18}O$, but lower Mg/Ca, Sr/Ca, U/Ca, Zr/Ca, and Ba/Ca ratios during the Younger Dryas (YD). Conversely, Dim-E4 shows generally higher ratios in both isotope ($\delta^{13}C$, $\delta^{18}O$) and TE/Ca ratios during the YD. Note that Y/Ca ratios in both Dim-E2 and Dim-E4 were elevated during the YD. Ba/Ca ratios positively correlate with Sr/Ca ratios in all sub-samples of stalagmites (Fig. 4a). Mg/Ca ratios and $\delta^{13}C$ values show almost no correlation during 18–10 kyr in Dim-E3 and Dim-E2, while they display a moderately strong correlation in Dim-E4 ($R^2 = 0.43$; Fig. 4b). Strong positive relationships between Mg/Ca and $\delta^{13}C$ ($R^2 = 0.44$, 0.47, and 0.70; Figs. 4c, d, e) and between Mg/Ca and $\delta^{18}O$ ($R^2 = 0.59$; Fig. 4f) were present in Dim-E3 for the periods of 40–18, 63–51, and 89–80 kyr respectively.

Chondrite-normalized (Sun & McDonough 1989) rare earth element and yttrium (REY) plot of the selected 14 speleothem sub-samples and the host-limestone is shown in Figure 5. Corresponding REY data are provided in Table S2 (App. 4). In addition, geochemical data obtained from the host dolomitic limestone are given in Table S3 (App. 4). Distinct negative Ce and positive Y anomalies observed in all sub-samples indicate a seawater signal derived from the host limestone, which is also supported by the elevated Y/Ho ratios averaging around 68 (Table S2) (Bau 1996). REY pattern of the host-rock sample exhibits relatively weak Ce and distinct positive Y anomalies and relative enrichments in the heavy rare earth elements (HREE) compared to those of speleothem samples. Some of the speleothem sub-samples also show similar Ce and Y anomalies (Dim-E3-135, 61 kyr; Dim-E2-173, 11 kyr; Dim-E4-293, 13.6; Dim-E4-360, 14.6 kyr; Fig. 5 and Table S2). The host limestone has a low Y/Ho value of 35, which is higher than the chondritic value of 28 (Bau 1996) (Table S2, App.4).

4.3. Radiogenic Sr-isotope data

Strontium isotope ratios ($^{87}Sr/^{86}Sr$) were measured for 13 calcite speleothem sub-samples from Dim Cave, and the analytical results are presented in Fig. 6a and Table S2 (with % analytical errors). $^{87}Sr/^{86}Sr$ ratios of Dim speleothems show a large range changing from 0.708098± 0.000007 (Dim-E4-040) to 0.708407 ± 0.000007 (Dim-E3-240). This range is significantly higher than the $^{87}Sr/^{86}Sr$ ratio of the seawater during Permian times (averaging around ~0.7075; McArthur et al. 2012) and lower than the modern seawater value of 0.7092 although it plots within the range of Cenozoic seawater between 0.7080 and 0.7090 roughly (Capo et al. 1998; Veizer 1989).

Dim-E3 indicate an overall increase in Sr-isotope compositions from 0.70819 (62nd mm; 44 kyr) to 0.70837 (280th mm; 84 kyr), with sudden drop between 72 kyr and 84 kyr (Fig. 6b). Youngest speleothem Dim-E2 (~9–13 kyr) reveal an increase in Sr-isotope compositions from 0.70817 (40 mm; 9.9 kyr) to 0.70822 (173rd mm; 11 kyr) from the tip, but shows drops from 0.708217 at194th mm (11.2 kyr) towards the end at 0.70816 (290th mm; 13.1 kyr; Fig.6c). Dim-E4 shows decrease between two measured sub-samples from 0.70826 to 0.70809, and from 12 to 14 kyr.

5. Discussion

5.1. Processes controlling the TE/Ca ratios

The primary sources of the trace elements in speleothems are the host rock and the overlying soil and epikarstic zones, through which meteoric water passes before entering into the cave. The TE composition of the meteoric waters is the other significant source. Dolomitic limestone can affect TE/Ca ratios (and specifically Mg/Ca) since the concentration of Mg in dripwaters draining from an aquifer which consist of dolomitized limestone is higher than that in dripwaters draining through pure limestone (Fairchild et al. 2000). Given that the host rock of the Dim Cave is a recrystallised dolomitic limestone (Gündalı et al. 1989), the source of Mg and Sr (and Ba) of the cave waters is mainly supplied from dissolution of this host rock. The impact of the host rock on the speleothem is affected by the hydrological routing of cave waters and their residence time before precipitation and hence reflects both climatic and host rock characteristics (Fairchild & Treble 2009). The variations in Mg/Ca ratios of the Dim speleothems are interpreted to have been affected by changing degrees of dissolution rates of Mg-rich (i.e. dolomite) and Ca-rich (i.e. calcite) minerals in the host rock, with Ca:Mg = 2:1(Table S3, App. 4). It is argued that the partially dolomitic nature of the host carbonate rock is a result of interactions with Mg-rich fluids associated with metamorphic rocks in the basement (Gündalı et al. 1989; Okay & Özgul 1984). Prolonged wall-rock interaction results in

the dissolution of dolomite during drier conditions in response to the increased residence time of seepage waters, resulting in higher Mg/Ca ratios in drip waters and subsequently, in speleothems (e.g. Johnson et al. 2006 and references therein). Under ideal circumstances, the changes in Mg/Ca ratios can be interpreted as changes in temperature signal (e.g. Gascoyne 1983). However, this is dependent on the assumption that the drip water Mg/Ca remains constant, which cannot be true for Dim Cave (Fig. 2). In these circumstances, we consider that Mg/Ca ratios in Dim speleothem can be best interpreted as an indicator of moisture balance (Regattieri et al. 2014; Johnson et al. 2006; Fairchild et al. 2000; Hellstrom & Mcculloch 2000; Huang et al. 2001), which is consistent with the $\delta^{13}C$ ratios and other variables.

Another important factor that might have influenced the trace element abundances is prior calcite precipitation (PCP) as regulated by the partial pressure of CO_2 gas (Fairchild & Treble 2009; Fairchild and McMillan 2007; Fohlmeister et al. 2011). If water seepage rate through the cave is low, which is favourable in dry conditions, deposition of calcite occurs upstream of the drip point because of the degassing into the empty voids/pores/fractures and some of the trace elements will be taken out of the water carrying the dissolved cations. This is supported by the covariance of Mg/Ca, Sr/Ca, and Ba/Ca ratios at broad multi-millennial scales throughout the entire record (Fig. 2), although the covariance between specifically Mg and Sr could also be facilitated by increasing interactions with the host limestone (Sinclair et al. 2012). This covariation appears to be more significant during 40–18 kyr period when the growth rate of Dim-E3 is the lowest (0.8 mm/kyr), suggesting drier conditions (or low flux rates) for this period. It is also noted that the $\delta^{18}O$ and $\delta^{13}C$ record is more negative when Mg/Ca and Sr/Ca ratios are higher and vice versa. In addition, there are strong positive correlations (R^2 = 0.44, 0.47, and 0.70; Figs. 4c–e) between $\delta^{13}C$ and Mg/Ca during 40–18, 63–51, 89–80 kyr respectively, supporting the preferential increase of lighter isotope ^{12}C into the degassed CO_2 under relatively drier conditions (Fairchild and McMillan 2007; Johnson et al. 2006). Also, the lowest radiogenic $^{87}Sr/^{86}Sr$ ratio (0.7082) at 43.7 kyr and relatively lower $^{87}Sr/^{86}Sr$ ratios (0.7083 and 0.7084) at 61.3 and 84.2 kyr in Dim-E3 (Fig. 6a) are inferred to reflect contributions from dolomitic limestone under low groundwater levels (or low flux rates). This is comparable with $^{87}Sr/^{86}Sr$ range of 0.7082–0.7086 (Fig. 6a), which is interpreted as Sahara-originated dust deposition and Terra Rossa soil development in Jerusalem speleothem (Frumkin and Stein 2004). Similarly, positive correlations between $\delta^{18}O$ and Mg/Ca ratios during 89–80 kyr period (late MIS 5) may be linked to relatively drier conditions during warmer parts of the last interglacial. Prior calcite precipitation along the pathway would have led to further release of lighter isotope ^{16}O within degassed CO_2 (Weidner et al. 2008). All these time periods also correspond to

times of lower growth rates in Dim-E3 (Fig. 2). Therefore, prior calcite precipitation in addition to wall rock interaction processes are thought to be the dominant mechanisms leading to increased values and covariance of Mg/Ca, Sr/Ca, and Ba/Ca during times of lower flux rates. On the other hand, although Sr/Ca and Mg/Ca ratios are generally in phase throughout the record, these ratios display discordant behaviour over some millennial-scale intervals (Fig. 2). Such a relationship may be due to short-term aragonite formation associated with dry periods (Fig. S5 cf. Ünal-İmer et al. 2015) and lower water availability (McDermott 2004), since Sr/Ca and Mg/Ca behave oppositely within the aragonite layer at 80–75 kyr (Fig. 2). This is supported by the fact that Sr is preferentially hosted by the aragonite lattice, whereas Mg is preferentially incorporated in the calcite lattice. Likewise, decreasing trends (towards lower values) in Y/Ca, Zr/Ca, and U/Ca ratios during 40–18, 63–51, and 80–71 kyr can be regarded as a response to lower rainfall regimes in SW Turkey.

Depending specifically on the Zr/Ca and Y/Ca ratios and growth rates of Dim-E3 (Fig. 2), it appears that at least three main wet periods are present in the record; the first occurred between 71–63 kyr, the second spanned the period from 51–40kyr, and the third prevailed from ~18 to 9 kyr in Dim Cave. During these periods, U/Ca, Zr/Ca, and Y/Ca ratios exhibit covarying increased trends (Fig. 2) and Dim-E3 has an elevated $^{87}Sr/^{86}Sr$ ratio = 0.7084 at 48 and 72 kyr (Fig. 6b), which suggest an increased supply of exotic terrestrial input such as aeolian dust or leached material from silica-rich basement rocks. Increased dust flux from central Europe (Újvári et al. 2010) and North Africa (e.g. sedimentary basins at north-eastern Sahara; Frumkin & Stein 2004; Vaks et al. 2013 and Saudi Arabia and Israel; Ganor et al. 2001) could be possible source areas for these signals (Fig. 6a). In this case, it occurs through the wet deposition of transported aeolian dust (i.e. washing out of atmospheric aerosols scavenged by rainfall) to the soils above the Dim speleothems. Based on the $\delta^{18}O$ changes (Ünal-İmer et al. 2015), it can be argued that the isotopically less depleted northern track of westerlies might have transported central Europe-based dust at early in the glacial period, while southern (more depleted) westerly track could have transported Saharan dust to the Dim site later in the glacial period (~after 50 kyr). This is consistent with the stable isotope record of the Dim Cave (Ünal-İmer et al. 2015). Alternatively, it is known that the host dolomitic limestone is not pure and is intercalated with quartzofeldspathic (or silica-rich) rocks (Gündalı et al. 1989; Bozkaya & Yalçin 2004). This suggests the possibility of enhanced erosion of these inliers during periods of higher flux and the consequent increased transport of Zr, U, and Y to the cave. We cannot distinguish between the two models of detrital input from the data available to us, but both imply higher seepage rates in the limestones and thereby ‘wetter’ conditions. High to moderate constant drip rates (inferring availability of water to deposit) are supported by micromorphological

characteristics of the speleothem calcite; for example Dim-E3 shows dominantly open/elongated columnar calcite at ~15, 63, and, 72 kyr (Fig. 7a–c). In general, columnar fabric in calcite infer competitive growth with occasional breaks at crystal boundaries (or interfaces) and slow but constant drip rates, while open and elongated types of columnar fabric indicate faster flow (Frisia 2015). Consequently, we infer that the Marine Isotope Stage (MIS) 4 may have been cold but wet in S-SW Turkey; given that the 71–63 kyr period with higher TE/Ca ratios covers most of MIS 4 (Hughes et al. 2013). It is important to note that increased water flux does not automatically mean higher rainfall as the seepage rates will be a consequence of both rainfall and evapotranspiration. Under lower ambient temperatures and/or weaker vegetation cover flux rates are likely to increase even if rainfall remains relatively constant.

Overall we believe that, for most of the record covering the entire last glacial period (~74 to 13 kyr), in phase variations between Mg/Ca, Sr/Ca, and (to a minor extent) Ba/Ca can be interpreted as a reflection of variations in moisture balance, with relatively higher values indicative of drier conditions through a combination of PCP process and enhanced dissolution of Mg-rich minerals of the host dolomitic limestone. In contrast, higher values of U/Ca, Zr/Ca, and Y/Ca, $^{87}Sr/^{86}Sr$ ratios, and columnar calcite generations observable in three speleothems (Fig. S2 cf. Ünal-İmer et al. 2015 and Fig.7) suggest a predominance of faster flux rates and contributions from aeolian dust and/or leached silica-rich impurities within the host rock during relatively wet periods.

5.2. Trace elements and abrupt climate events in Dim records

The Dim TE/Ca time series exhibit in-phase behaviour with global rapid climate changes notably Heinrich (H) events and the Younger Dryas (Fig. 2). As noted with the isotopic data ($\delta^{13}C$ and $\delta^{18}O$) presented in Paper 3, Heinrich events, especially H4, H5, and H6, are associated with distinct TE anomalies, whereas TE anomalies during H1, H2 and H3 are less obvious. This is likely an effect of changing winter westerly tracks with different moisture source characteristics between earlier and later H events (Ünal-İmer et al. 2015). Mg/Ca, Sr/Ca, and Ba/Ca ratios show elevated values, whereas U/Ca, Zr/Ca, and Y/Ca ratios appear to display decreasing trends towards lower values during the earlier three Heinrich events. Because all TE/Ca ratio changes are interpreted as a function of infiltrating meteoric water flux, paleohydrological conditions are argued to reflect relatively drier conditions during these Heinrich events in the Dim Cave, and potentially in S-SW Turkey. However, previous work on $\delta^{13}C$ and $\delta^{18}O$ records of Dim speleothems (Ünal-İmer et al. 2015) showed that the main controlling factor of the rainfall characteristics is changing moisture source tracks (westerlies) rather than the amount effect (Gat & Gonfiantini 1981). Isotopically

heavier (lighter) moisture tracks from north (south) sources regulates the less depleted (more depleted) $\delta^{18}O$ values from early part of the glaciation to the later part of the glaciation (after ~50 kyr) of the Dim record (Ünal-İmer et al. 2015). In contrast, speleothem works from other sites in the Eastern Mediterranean (e.g. Soreq and Peqiin caves; Israel) mainly argue for the amount effect influencing the long-term (10^{4-6} years) $\delta^{18}O$ values (e.g. Bar-Matthew et al. 1999; Frumkin et al. 1999; Bar-Matthew et al. 2003). Variation in rainfall is invoked to explain $\delta^{13}C$ variations in the Dim record, primarily indicating changes in the soil activity (e.g. thickness and organic matter concentration). Minimal biological activity is suggested during the periods of drier climate, which, together with increased residence times of drip water, leads to increased interactions with the host rock. In addition the positive correlations of $\delta^{13}C$ with the Mg/Ca ratios (Fig. 5) are thought to result from decreased water fluxes in Dim Cave. At a regional scale, the highest isotopic enrichment in $\delta^{13}C$ and apparent increases in Mg/Ca and Sr/Ca (also associated with a sudden drop in U/Ca, Zr/Ca, and Y/Ca; Fig. 2) occurs at around 60 kyr (H6 event) and coincides with the termination of speleothem growth in a French cave (Villars Cave; Genty et al. 2003). Accordingly, we argue that both Dim and Villars caves experienced dry conditions during H6, and that the linkage is through the winter westerly circulation that affects both France and Turkey.

Although the resolution was lower than other segments of the record, the LGM (~23 to 19 kyr) section of the Dim record shows relative decreases in $\delta^{18}O$, $\delta^{13}C$, Mg/Ca, Sr/Ca and increases in U/Ca, Zr/Ca, and Y/Ca ratios. It is generally considered that the LGM in Turkey is cold (8–9 °C colder than present; Hughes et al. 2013). In contrast, there is little consensus on the availability of moisture (see Papers 1 and Paper 3= Ünal-İmer et al. 2015). Studies from the Soreq Cave in Israel in the same climate zone as SW Turkey, infer colder and drier LGM conditions (Bar-Matthews et al. 1997; Bar-Matthews et al. 1999). Conversely, recent studies considering high lake levels (Dead Sea basin) and deposition of speleothems are considered as indication of wet and cool glacial periods including the LGM in the Levant region, Israel (Frumkin et al. 2011; Lisker et al. 2010). Studies on the LGM advances of Turkish glaciers (Sarıkaya et al. 2008; Sarıkaya et al. 2014) and dense vegetation cover (Şenkul & Doğan 2013) support a cold and wet LGM. Stable isotope work in this thesis suggests a more positive water balance at the LGM than at present, though likely due to reduced evapotranspiration rather than increased precipitation, which perhaps reconciles the interpretations.

In terms of the global Younger Dryas event, the responses of the Dim-E2, E3 and E4 speleothems appear contradictory (Fig. 3). Dim-E2 and -E4 suggest relatively wetter conditions during this time interval, as deduced from compact/open columnar calcite indicating relatively constant high drip

rates (Fig. S5; cf. Ünal-İmer et al. 2015), while Dim-E3 supports drier conditions on the basis of TE/Ca ratios (Fig. 2). This suggests that the speleothems of the same site can respond differently and thus some caution is needed as there are both geological and climatic considerations. The Dim-E3 speleothem growth terminated at the end of the YD whereas both Dim-E2 and -E4 grew rapidly from 15 to 9 kyr. The latter support a continuously positive water balance in Dim Cave. The termination of the -E3 speleothem must be associated with the diversion or blocking of the seepage path to this particular speleothem rather than a cave wide effect and as the drip rate slowed, PCP or differential dolomite dissolution effects are likely to have increased Mg/Ca ratios. Consequently interpretations during YD times are based on E2 and E4.

It is known that Dim cave witnessed a change to mainly aragonite-rich speleothem deposition from 7 kyr to present (Wickens et al. 2011), which is also inferred during ~76–74 kyr with aragonite deposition at the Dim Cave (see Fig. S5d; App. 3 and Fig. 7d). The metastable form of calcium carbonate, aragonite, is known to dominate calcite formation in the presence of excess Mg^{+2} ion under the conditions of high degassing rates (e.g. Frisia et al. 2002; Murray 1954; McDermott 2004), and is favoured by more arid conditions (facilitating dissolution of dolomite in high-Mg host rock and enhanced CO_2 degassing; Fairchild & McMillan 2007). Late Holocene arid conditions in the Eastern Mediterranean are also supported by the termination speleothem growth in Israeli caves, highlighting the negative moisture balance (reduced water availability) (Tzedakis 2007; Vaks et al. 2003; Vaks et al. 2006; Lisker et al. 2010; Frumkin et al. 2011).

6. Conclusions

This paper reports multi-proxy climate-sensitive records derived from the Dim speleothems and include stable isotope ($\delta^{18}O$ and $\delta^{13}C$) and trace element/Ca data, as well as full trace element concentrations of the speleothem and the host rock. Relatively immobile REY element signatures characterized by negative Ce and positive Y anomalies in the stalagmites reflect a seawater origin for the host limestone, confirming a close genetic link between the stalagmites and the host dolomitic limestone. Chemical variations in seepage water and resultant changes in speleothem geochemical compositions (Dim-E2, Dim-E3, and Dim-E4) are examined using high-resolution Mg/Ca, Sr/Ca, U/Ca, Ba/Ca, Y/Ca, and Zr/Ca ratio time profiles over an 80 kyr period, which covers almost the entire last glaciation. The trends of TE/Ca ratios reveal covariance between Mg/Ca, Sr/Ca, and Ba/Ca, and between U/Ca, Y/Ca, and Zr/Ca. The record can be subdivided into specific growth episodes (i.e. 18–10; 40–18, 51–40, 63–51, 71–63, 80–71, and 89–80 kyr), based primarily on the growth rate of Dim-E3 speleothem for the ~90–13 kyr period as calculated from U-

series ages. These growth episodes are characterized by distinct Y/Ca (and Zr/Ca) ratio anomalies. The host rock of the Dim Cave is a dolomitic limestone and appears to be the main source of the trace elements. Together with less depleted $\delta^{13}C$ ratios, higher values in Mg/Ca, Sr/Ca, and Ba/Ca ratios during 40–18, 63–51, and 80–71 kyr (corresponding lower growth rates of Dim-E3) are interpreted to be mainly controlled by enhanced interactions between the host dolomitic limestone and seepage waters, under longer residence times and pathways for seepage flows. Prior calcite precipitation, wall rock interaction, and differential dissolution of the dolomite over calcite in the host rock are thought to be main processes yielding high TE/Ca ratios during these periods. Conversely, high Zr/Ca, U/Ca, and Y/Ca values (during 51–40, 71–63, and 89–80 kyr) are associated with periods of more positive water balance in SW Turkey. Increased terrestrial input from either aeolian dust deposition (i.e. wet deposition of loess or desert dust) and/or leached detrital materials of quartzofeldspathic rocks within the host limestone may provide the increased availability of Y, Zr, and U observed during these periods. In addition to these overall patterns, the Dim record responds to global Heinrich events but the response is not stationary in time. It appears to reflect changes in winter air mass flow over the site with earlier Heinrich events in the last glacial cycle (H5 and H6) reflecting more northerly air mass tracks while later H events (H1 and H2) are consistent with a southerly track.

7. Acknowledgements

This research was funded by the Queensland Geothermal Energy Centre of Excellence (QGECE), with some support by the School of Geography, Planning, and Environmental Management through E. Ü.İ.'s PhD project fund. We thank Ai Duc Nguyen, Wei Zhou, Kim Baublys and Sue Golding for their help during trace element and stable isotope analyses.

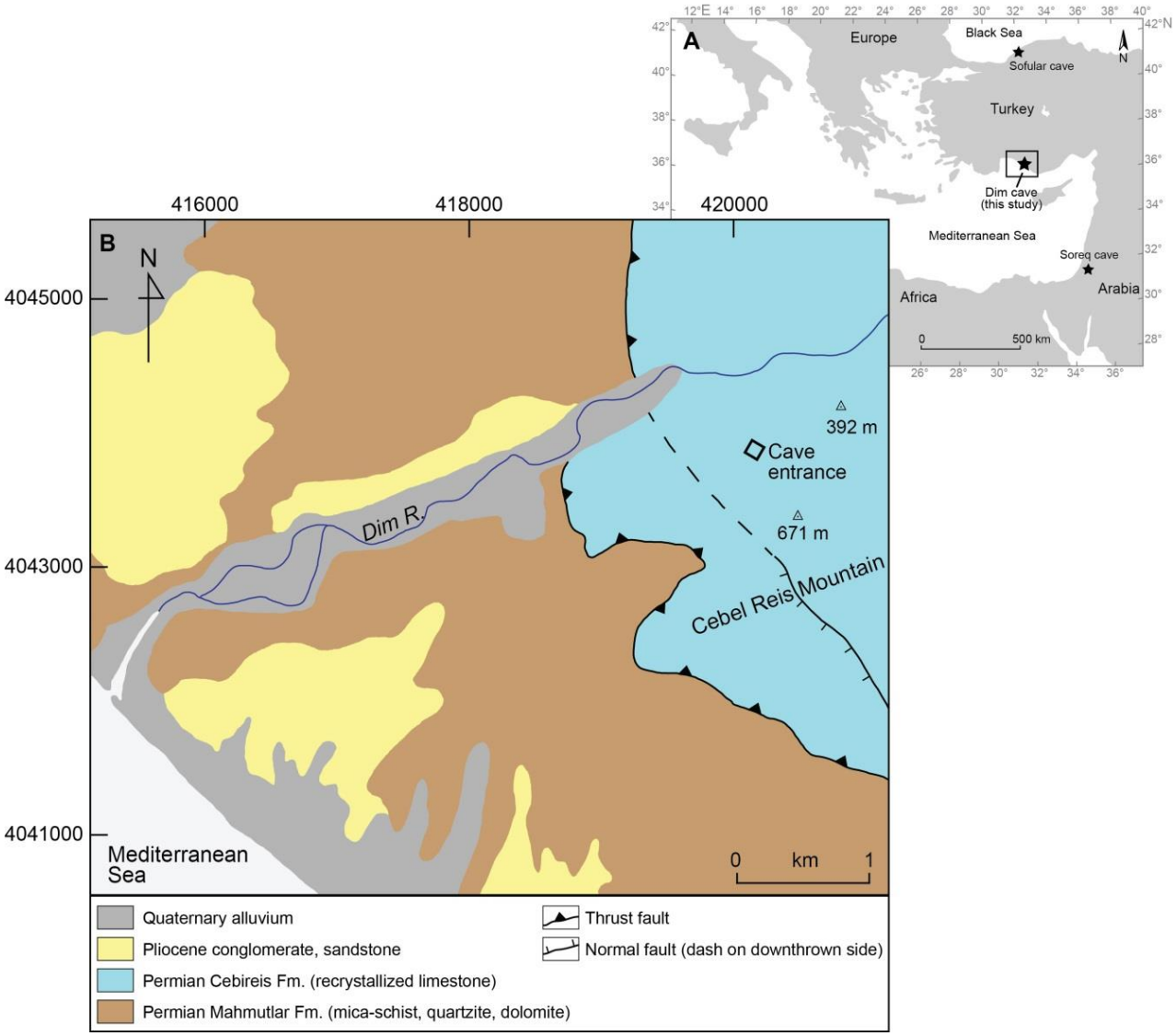

Figure 1 Location (A) and (B) geological map of the Dim Cave (232 m a.s.l.) and the surrounding area (modified from Gündalı et al. 1989). Permian dolomitic limestone (Cebireis Fm) hosts Dim Cave, see Table S3 (App. 4) for trace element concentration of the host dolomitic limestone.

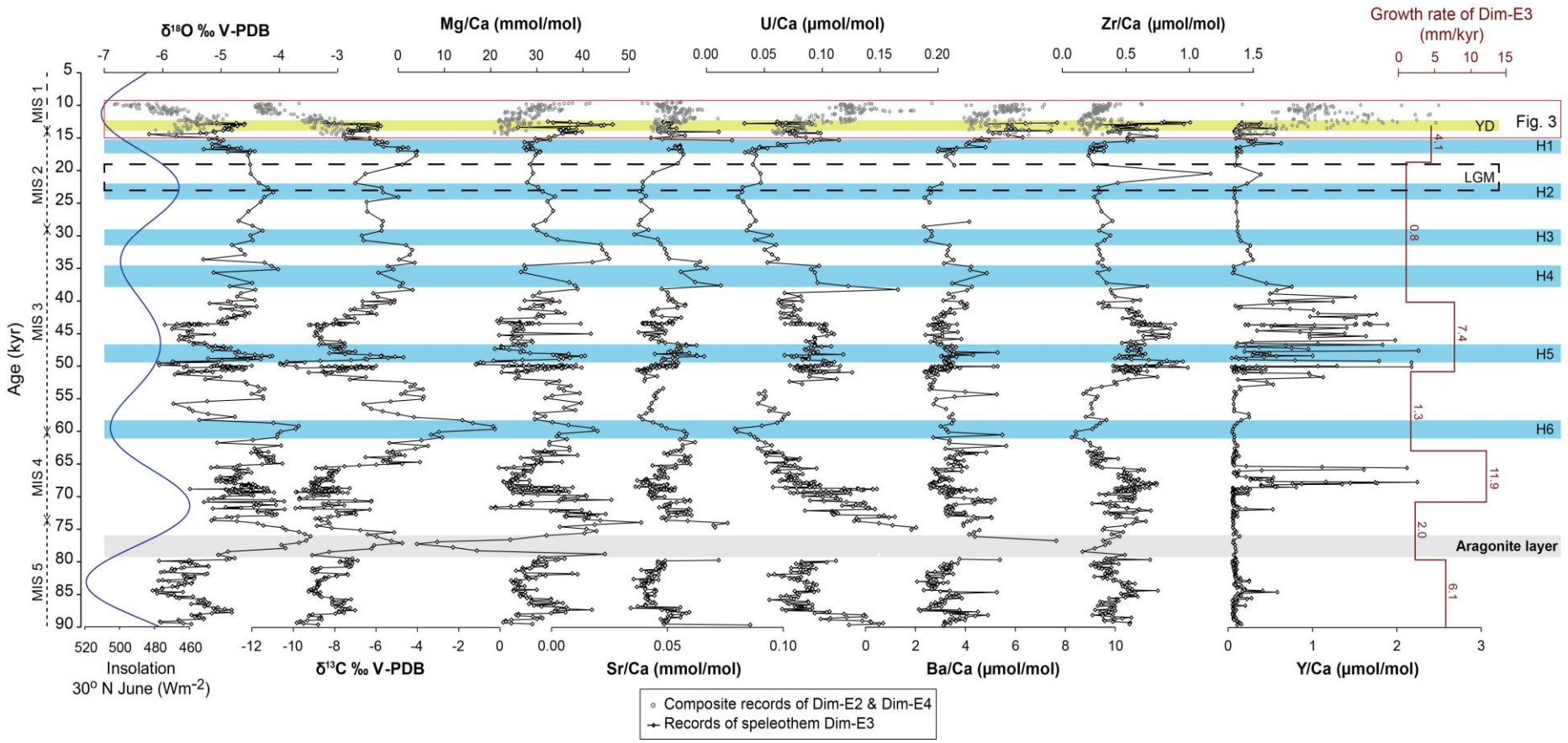

Figure 2 Stable isotope ($\delta^{18}O$ and $\delta^{13}C$) and trace element/Ca (Mg/Ca, Sr/Ca, U/Ca, Ba/Ca, Zr/Ca, and Y/Ca) profiles of Dim-E2, Dim-E3, and Dim-E4 speleothems between 90–5 kyr. Summer insolation (30°N June, Berger and Loutre 1991) and growth rate for the Dim-E3 speleothem are represented by blue and red curves respectively. The durations of the Younger Dryas (YD), LGM, and Heinrich (H) events are highlighted with light yellow, hashed, and light blue areas, respectively. The light grey area corresponds with the aragonite layer observed in Dim-E3 at ~80–75 kyr. Fig.3 inset (red rectangular area) shows the composite records for Dim-E2 and Dim-E4. The durations of Marine Isotope Stages (e.g. MIS 1) are indicated by dashed line and arrows.

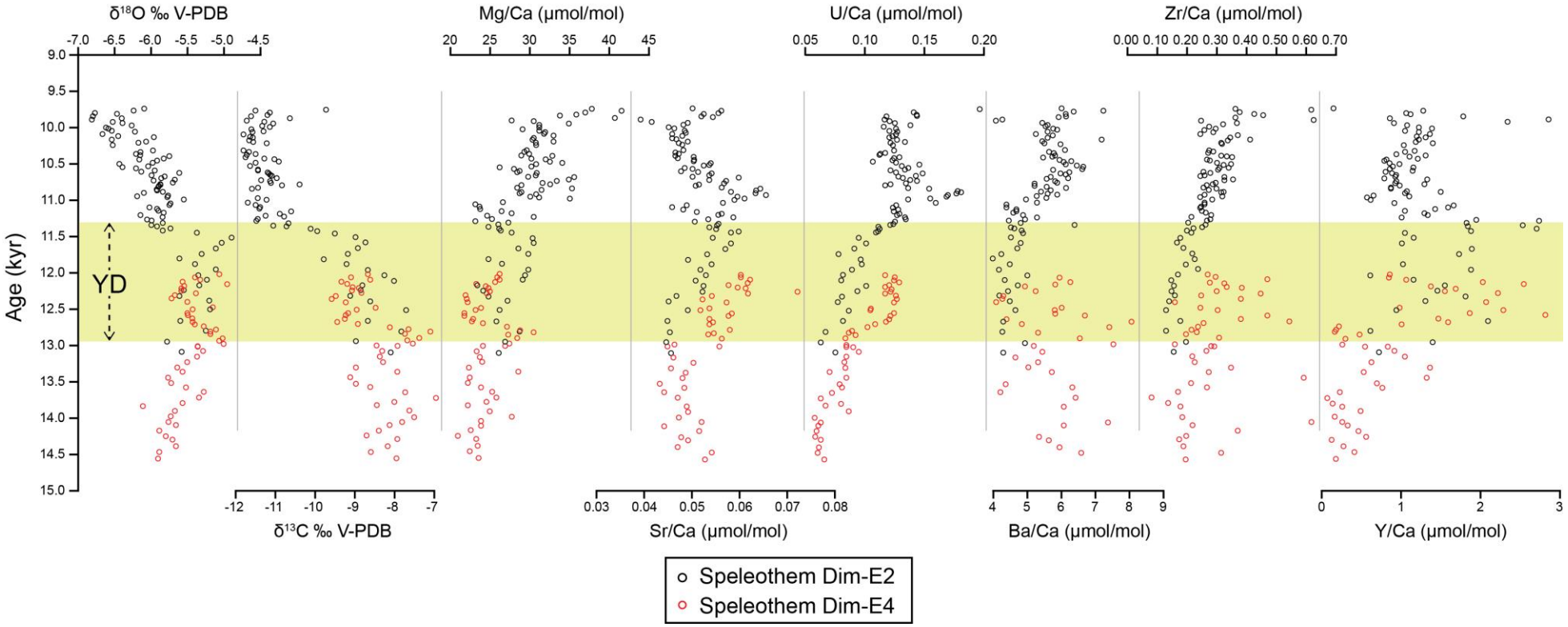

Figure 3 Stable isotope ($\delta^{18}O$ and $\delta^{13}C$) and trace element/Ca (Mg/Ca, Sr/Ca, U/Ca, Ba/ Ca, Zr/Ca, and Y/Ca) profiles of Dim-E2 and Dim-E4 speleothems showing the Younger Dryas (YD) time window (yellow shaded area).

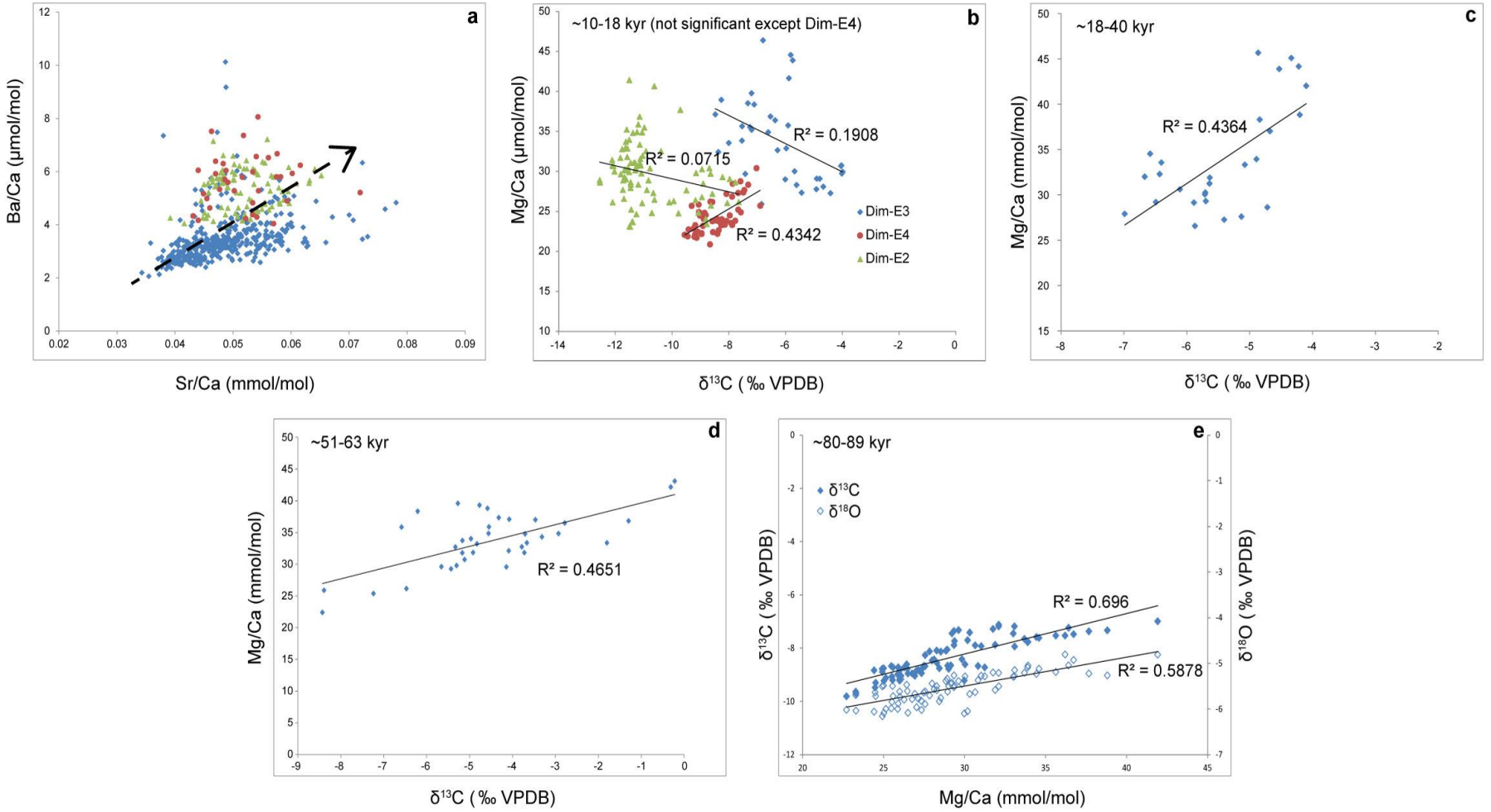

Figure 4 X-Y relationships of selected speleothem sub-samples including TE/Ca and stable isotope (O, C) ratios. a) Sr/Ca versus Ba/Ca for all sub-samples, b) $\delta^{13}C$ and Mg/Ca of Dim-E2, Dim-E3, and Dim-E4 sub-samples for 18–10 kyr period, c) and d) $\delta^{13}C$ and Mg/Ca of Dim-E3 for the periods of 40–18 aand 63–51 kyr respectively, and e) Mg/Ca versus $\delta^{13}C$ and $\delta^{18}O$ of Dim-E3 for the period 89–80 kyr.

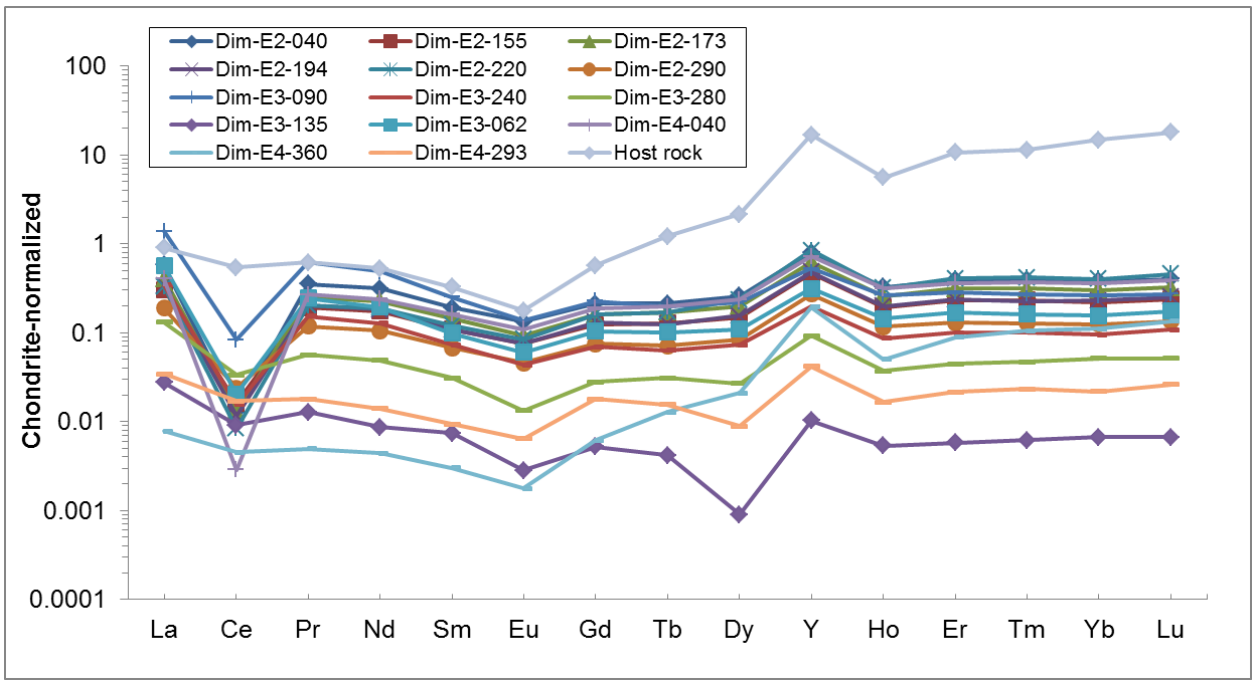

Figure 5 Chondrite-normalised (Sun & McDonough 1989) REY diagrams of 14 samples from the Dim speleothems and the host rock (dolomitic limestone; Gündalı et al. 1989). REY data are reported in Table S2, App. 4.

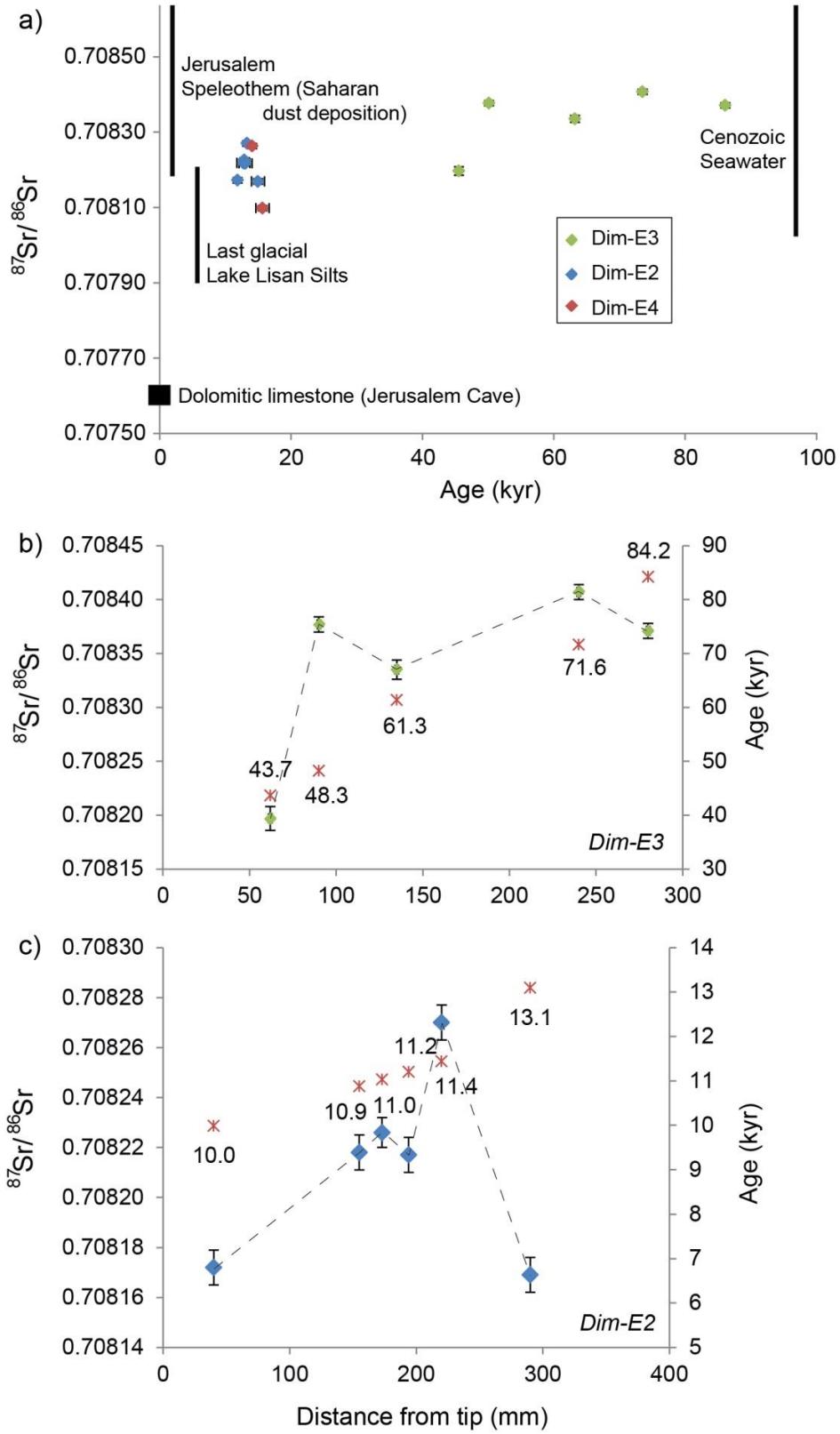

Figure 6 (a) Dim Cave Sr-isotope data; **(b)** Dim-E3 Sr-isotope composition and U-series age variation along the growth (mm); and **(c)** Dim-E2 Sr-isotope composition and U-series age variation along the growth (mm). Sr-isotope ratio ranges for the Jerusalem speleothem, host limestone and Last Glacial Lake Lisan silts are gathered from Frumkin and Stein 2004. Cenozoic water S-isotope ratio is from Capo et al. 1998.

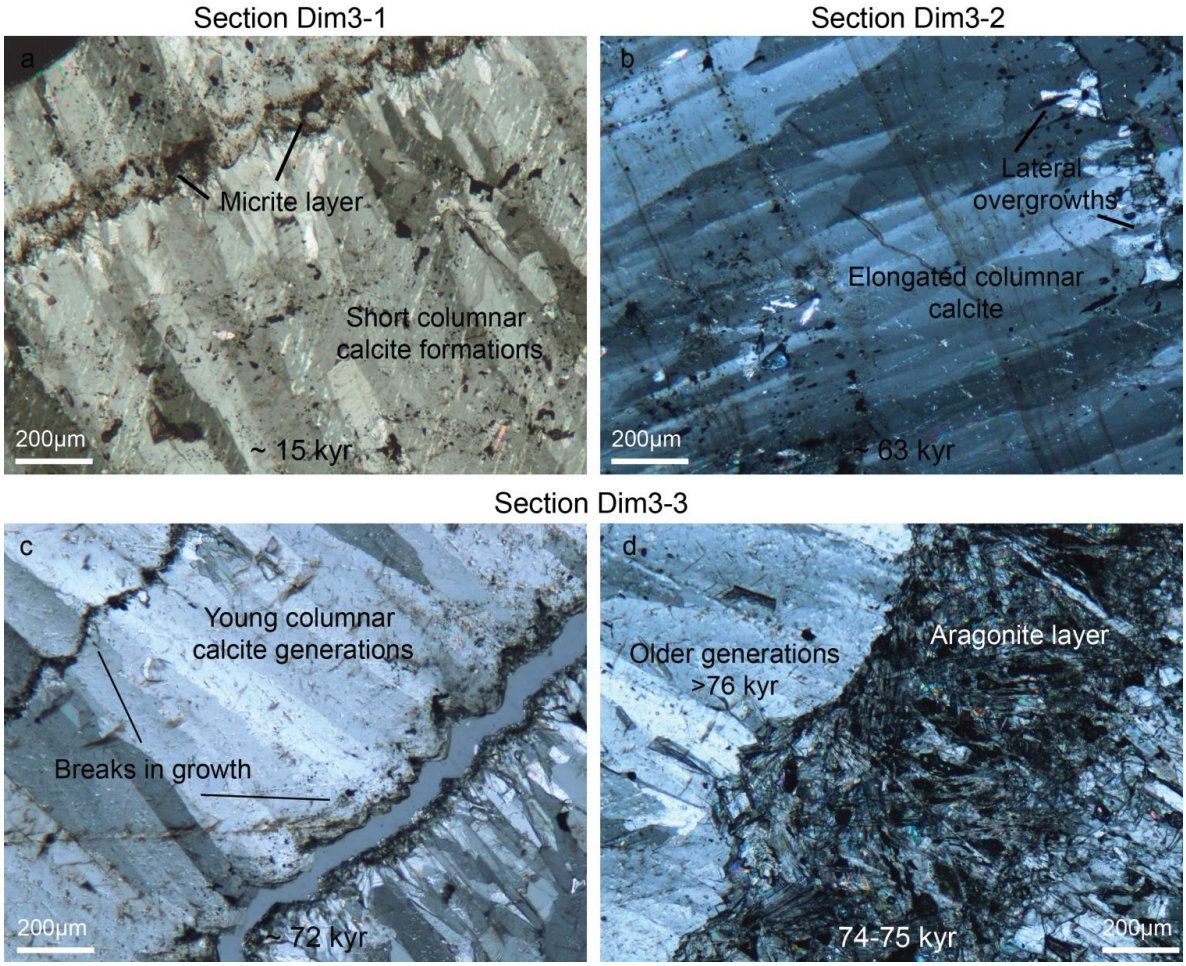

Figure 7 Dim-E3 speleothem with microstructural change from young to old (15 to 76 kyr) in deposition (from **a** to **d**).

APPENDIX 4: Supplementary Data for Paper 4

Table S1 Trace element/Ca data* of Dim Cave speleothems (Dim-E2, Dim-E3, and Dim-E4), SW Turkey.

Sample name	$^{25}Mg/^{43}Ca$	$^{88}Sr/^{43}Ca$	$^{89}Y/^{43}Ca$	$^{137}Ba/^{43}Ca$	$^{139}L/^{43}Ca$	$^{140}Ce/^{43}Ca$	$^{238}U/^{43}Ca$	$^{90}Zr/^{43}Ca$
Dim-E3-0010	32.4230	0.0563	0.1429	7.7302	0.0393	0.0602	0.0613	0.8023
Dim-E3-0015	37.1402	0.0531	0.4054	6.4419	0.1095	0.1366	0.0888	1.0054
Dim-E3-0020	33.5644	0.0545	0.1315	4.8397	0.0304	0.0356	0.0689	0.7800
Dim-E3-0025	41.6579	0.0482	0.2202	28.6542	0.0801	0.1036	0.0330	0.5192
Dim-E3-0035	38.9447	0.0486	0.3784	10.8823	0.1570	0.2490	0.0913	0.9554
Dim-E3-0035	46.3921	0.0520	0.0966	5.7411	0.0407	0.0486	0.0611	0.2955
Dim-E3-0040	44.5582	0.0515	0.2138	5.8992	0.0737	0.0698	0.0651	0.6050
Dim-E3-0045	43.8979	0.0507	0.1771	5.7767	0.0926	0.1068	0.0658	0.3998
Dim-E3-0060	25.9124	0.0898	0.6090	5.8661	0.1045	0.1224	0.0810	0.5788
Dim-E3-0065	36.8710	0.0507	0.0597	6.0343	0.0231	0.0524	0.0832	0.4260
Dim-E3-0070	35.7389	0.0473	0.0577	5.6669	0.0277	0.0436	0.0791	0.4434
Dim-E3-0075	38.5185	0.0498	0.0597	6.5932	0.0390	0.0738	0.0774	0.6646
Dim-E3-0080	34.9034	0.0540	0.1149	7.4793	0.0626	0.0929	0.0700	0.7442
Dim-E3-0085	35.2142	0.0460	0.0355	4.9513	0.0185	0.0285	0.0785	0.4531
Dim-E3-0095	36.3911	0.0480	0.0426	12.6495	0.0446	0.0721	0.0744	0.3916
Dim-E3-0100	39.7805	0.0482	0.0480	5.4220	0.0239	0.1687	0.0667	0.3606
Dim-E3-0105	35.5356	0.0462	0.1102	5.1347	0.0715	0.0913	0.0962	0.4542
Dim-E3-0110	38.3780	0.0723	0.5775	19.2806	0.2644	0.6358	0.0987	4.1650
Dim-E3-0115	35.6423	0.0474	0.1375	5.7444	0.0650	0.1033	0.0721	0.5275
Dim-E3-0125	33.8490	0.0507	0.0965	6.3336	0.0543	0.0837	0.0775	0.7387
Dim-E3-0130	32.6389	0.0577	0.0580	4.6764	0.0324	0.0383	0.0859	0.5111
Dim-E3-0135	29.6933	0.0517	0.3291	4.3958	0.0536	0.0361	0.0988	0.5143
Dim-E3-0140	32.8828	0.0430	0.2269	4.9682	0.0616	0.0796	0.1145	0.5580
Dim-E3-0145	30.0137	0.0479	0.2658	4.1917	0.0505	0.0358	0.0927	0.5129
Dim-E3-0150	27.3421	0.0781	0.6813	4.1009	0.0930	0.0226	0.0883	0.3317
Dim-E3-0155	29.0104	0.1177	0.3041	4.0441	0.0355	0.0160	0.0617	0.2479
Dim-E3-0165	28.3079	0.1188	0.1190	4.8301	0.0242	0.0343	0.0685	0.3459
Dim-E3-0170	28.0870	0.0556	0.0654	3.6725	0.0099	0.0194	0.0464	0.2222
Dim-E3-0175	27.2720	0.0535	0.0729	2.9452	0.0070	0.0117	0.0454	0.3285
Dim-E3-0180	29.0985	0.0556	0.0822	3.6399	0.0156	0.0210	0.0527	0.2365
Dim-E3-0185	29.0823	0.0553	0.1207	3.5045	0.0140	0.0153	0.0399	0.2649
Dim-E3-0195	27.7772	0.0536	0.1034	2.8993	0.0086	0.0087	0.0425	0.2137
Dim-E3-0200	29.9576	0.0507	0.1350	3.2963	0.0246	0.0813	0.0410	0.3261
Dim-E3-0205	30.7435	0.0564	0.0717	3.5087	0.0171	0.0509	0.0364	0.2527
Dim-E3-0210	30.6653	0.0562	0.0743	3.5341	0.0201	0.0453	0.0334	0.2193
Dim-E3-0225	29.7330	0.0555	0.0770	3.2212	0.0277	0.0516	0.0432	0.2047
Dim-E3-0240	28.6277	0.0571	0.0488	3.5714	0.0152	0.0323	0.0401	0.2427
Dim-E3-0250	29.1930	0.0547	0.4036	11.0642	0.1270	0.2320	0.0467	1.1660
Dim-E3-0260	27.8934	0.0440	0.2148	3.0632	0.0304	0.0728	0.0470	0.4352
Dim-E3-0265	30.2612	0.0394	0.0408	2.5848	0.0087	0.0220	0.0314	0.2845
Dim-E3-0270	31.2484	0.0396	0.0444	2.6208	0.0123	0.0323	0.0310	0.2960
Dim-E3-0275	33.9368	0.0380	0.0352	2.3644	0.0137	0.0251	0.0269	0.2494
Dim-E3-0280	32.2956	0.0409	0.0726	2.5748	0.0204	0.1453	0.0319	0.2785
Dim-E3-0290	33.5619	0.0385	0.0641	7.3518	0.0223	0.0492	0.0375	0.3079
Dim-E3-0300	31.8985	0.0434	0.0855	4.1783	0.0474	0.0684	0.0427	0.3945
Dim-E3-0305	29.3058	0.0386	0.0812	2.3356	0.0101	0.0123	0.0375	0.3197
Dim-E3-0310	30.0506	0.0377	0.0809	2.6512	0.0143	0.0281	0.0349	0.2902
Dim-E3-0315	32.0043	0.0419	0.0999	2.6624	0.0168	0.0193	0.0564	0.3800
Dim-E3-0320	34.5343	0.0358	0.1262	2.4060	0.0168	0.0450	0.0419	0.3322
Dim-E3-0325	43.8837	0.0459	0.2598	3.3754	0.0643	0.0154	0.0602	0.2725
Dim-E3-0330	44.1540	0.0472	0.2173	3.3115	0.0561	0.0326	0.0502	0.2890
Dim-E3-0335	45.0985	0.0490	0.2619	3.2576	0.0774	0.0369	0.0567	0.2969
Dim-E3-0340	45.6780	0.0497	0.2956	3.5483	0.0710	0.0480	0.0619	0.3192

Dim-E3-0345	42.0191	0.0508	0.1742	3.1500	0.0477	0.0235	0.0528	0.2782
Dim-E3-0350	27.2640	0.0643	0.0267	4.2578	0.0094	0.0177	0.0973	0.3197
Dim-E3-0355	27.5918	0.0624	0.0426	4.2092	0.0091	0.0275	0.0904	0.3699
Dim-E3-0365	26.5721	0.0671	0.0170	4.8836	0.0078	0.0200	0.0937	0.2766
Dim-E3-0375	37.0353	0.0559	0.4794	3.4854	0.1105	0.0937	0.0960	0.3488
Dim-E3-0380	38.3047	0.0621	0.8276	4.2862	0.1517	0.0827	0.1225	0.6685
Dim-E3-0385	38.8331	0.0732	0.6246	4.0839	0.1110	0.0821	0.1655	0.3794
Dim-E3-0390	30.6147	0.0476	0.5281	3.3292	0.0968	0.0317	0.0675	0.3903
Dim-E3-0395	29.1372	0.0502	1.6962	3.5525	0.2858	0.0150	0.0815	0.4165
Dim-E3-0400	33.3206	0.0504	0.5191	3.1205	0.0831	0.0651	0.0627	0.6136
Dim-E3-0405	27.3646	0.0523	1.3959	3.8767	0.2730	0.1237	0.0828	0.5559
Dim-E3-0410	34.8908	0.0505	0.7668	3.8163	0.1377	0.0543	0.0648	0.3238
Dim-E3-0415	32.9814	0.0525	0.5659	4.0832	0.0965	0.0159	0.0620	0.2848
Dim-E3-0425	29.4150	0.0537	0.0511	3.9631	0.0116	0.0150	0.0749	0.3665
Dim-E3-0430	31.2951	0.0579	0.1249	4.0768	0.0274	0.0230	0.0650	0.3661
Dim-E3-0435	31.3166	0.0577	0.0986	3.9967	0.0184	0.0186	0.0672	0.3191
Dim-E3-0440	28.4988	0.0545	0.8044	3.4106	0.1916	0.0285	0.0764	0.5444
Dim-E3-0445	26.3611	0.0544	1.1267	3.4001	0.3016	0.0196	0.0811	0.5079
Dim-E3-0455	34.1630	0.0460	4.0340	3.1205	0.9929	0.0722	0.0757	0.6028
Dim-E3-0460	34.7131	0.0440	1.1872	3.5770	0.2439	0.0328	0.0640	0.5254
Dim-E3-0465	36.0273	0.0433	1.9915	3.0124	0.5142	0.0460	0.0669	0.5747
Dim-E3-0470	30.3447	0.0436	1.8870	3.1881	0.4845	0.0353	0.0736	0.5862
Dim-E3-0475	31.0799	0.0445	1.0788	3.1430	0.2227	0.0426	0.0784	0.6241
Dim-E3-0480	31.3902	0.0438	1.7071	2.8687	0.4670	0.0434	0.0711	0.5614
Dim-E3-0485	29.8579	0.0478	1.5528	2.7364	0.3766	0.0160	0.0644	0.4755
Dim-E3-0490	22.3227	0.0561	5.2850	2.9099	2.1777	0.0304	0.0811	0.5456
Dim-E3-0500	21.4308	0.0539	4.9938	3.0841	1.9403	0.0366	0.0803	0.6471
Dim-E3-0505	26.3244	0.0511	1.8656	3.0741	0.5115	0.0272	0.0739	0.5850
Dim-E3-0510	21.8195	0.0523	5.1399	2.9257	2.0421	0.0208	0.0813	0.6150
Dim-E3-0515	24.1017	0.0501	2.9033	3.2100	0.5929	0.0481	0.0806	0.7736
Dim-E3-0520	24.7174	0.0526	1.7152	3.6821	0.5980	0.0305	0.0831	0.5697
Dim-E3-0525	26.0152	0.0447	3.8870	3.0319	0.8537	0.0269	0.0770	0.6878
Dim-E3-0530	26.2713	0.0405	1.8240	2.9124	0.3276	0.0203	0.0810	0.6419
Dim-E3-0535	26.3614	0.0432	4.3979	3.1222	0.9930	0.0172	0.0778	0.7186
Dim-E3-0540	28.5099	0.0415	1.8946	2.8559	0.4028	0.0285	0.0679	0.5457
Dim-E3-0545	28.3442	0.0417	3.2410	2.8125	0.9402	0.0290	0.0785	0.5726
Dim-E3-0550	29.0711	0.0394	1.9175	2.9835	0.4010	0.0163	0.0727	0.5611
Dim-E3-0555	30.4659	0.0396	2.1420	2.6710	0.5835	0.0373	0.0783	0.6024
Dim-E3-0560	29.1515	0.0409	4.7256	2.8911	1.5689	0.0369	0.0753	0.8882
Dim-E3-0565	27.8925	0.0395	3.5170	2.7521	0.8534	0.0417	0.0811	0.6569
Dim-E3-0570	29.0590	0.0398	5.1219	2.7843	1.6506	0.0701	0.0808	0.6433
Dim-E3-0575	39.4789	0.0427	1.6900	2.7303	0.4981	0.0913	0.1021	0.6438
Dim-E3-0580	28.2535	0.0499	0.1906	2.9979	0.0520	0.0808	0.0858	8.1517
Dim-E3-0585	30.5148	0.0436	0.2347	2.7798	0.0693	0.1848	0.0941	0.6457
Dim-E3-0590	27.8265	0.0415	0.1886	2.6573	0.0462	0.0578	0.0896	0.6402
Dim-E3-0600	27.6500	0.0444	0.2286	2.8837	0.0601	0.0794	0.0891	0.7330
Dim-E3-0610	25.5736	0.0404	0.4484	2.6723	0.0760	0.0270	0.0901	0.7566
Dim-E3-0615	24.5971	0.0406	0.5994	2.5181	0.1305	0.0372	0.0916	0.7560
Dim-E3-0620	25.5705	0.0422	0.4118	2.7654	0.1039	0.0610	0.0917	0.7753
Dim-E3-0625	26.2320	0.0523	1.1395	3.3738	0.2523	0.0705	0.0974	0.6842
Dim-E3-0630	26.0206	0.0474	0.8880	2.8503	0.1933	0.0138	0.1039	0.6342
Dim-E3-0640	26.6455	0.0478	0.5504	2.8898	0.0988	0.0249	0.1016	0.6039
Dim-E3-0650	26.8165	0.0452	1.5806	3.3287	0.3309	0.0672	0.1016	0.8088
Dim-E3-0660	25.0878	0.0438	1.0939	2.7437	0.1948	0.0272	0.0976	0.8486
Dim-E3-0670	27.0853	0.0479	0.3492	3.0756	0.0661	0.0599	0.1038	0.7025
Dim-E3-0680	25.6437	0.0453	0.9404	3.7125	0.1759	0.0223	0.1003	0.5984
Dim-E3-0690	24.7430	0.0495	1.5547	3.0902	0.2953	0.0243	0.1080	0.7092
Dim-E3-0700	41.7003	0.0377	1.0689	2.4026	0.3082	0.0729	0.1103	0.8388
Dim-E3-0710	21.8432	0.0489	1.8478	3.0813	0.3533	0.0161	0.1041	0.6376
Dim-E3-0720	26.6609	0.0403	1.0758	2.7882	0.2114	0.0362	0.0930	0.8356
Dim-E3-0730	24.8656	0.0464	3.0669	3.8504	0.6881	0.0442	0.0938	0.7361
Dim-E3-0740	24.5220	0.0436	2.2491	2.7952	0.4717	0.0315	0.0938	0.6370

Dim-E3-0750	28.8716	0.0429	0.2804	2.6112	0.0680	0.0115	0.0860	0.5392
Dim-E3-0760	29.0817	0.0478	0.0831	3.0424	0.0167	0.0060	0.0895	0.4682
Dim-E3-0770	25.9403	0.0464	1.1842	2.8896	0.2992	0.0082	0.0936	0.5782
Dim-E3-0780	24.9273	0.0492	2.0749	3.0170	0.5851	0.0073	0.0934	0.6483
Dim-E3-0790	27.2646	0.0545	0.7467	3.4572	0.1884	0.0074	0.0939	0.5575
Dim-E3-0800	27.6091	0.0582	0.1951	3.4998	0.0375	0.0041	0.0934	0.5291
Dim-E3-0805	26.3085	0.0627	0.0623	3.6404	0.0152	0.0213	0.1078	0.5179
Dim-E3-0810	22.3288	0.0584	0.3806	3.2981	0.0469	0.0075	0.0995	0.5643
Dim-E3-0820	22.4327	0.0547	0.8266	3.1713	0.1317	0.0039	0.0903	0.5896
Dim-E3-0830	22.7675	0.0557	1.0583	3.2318	0.1700	0.0078	0.0881	0.6160
Dim-E3-0840	20.9263	0.0556	3.2374	3.2489	0.6552	0.0061	0.0850	0.6167
Dim-E3-0850	23.9999	0.0549	2.5685	3.4715	0.4992	0.0276	0.0860	0.5083
Dim-E3-0860	26.8381	0.0540	0.1777	3.5606	0.0147	0.0057	0.0928	0.5229
Dim-E3-0870	27.1913	0.0561	0.3137	5.3203	0.0788	0.1136	0.0962	0.6009
Dim-E3-0880	26.4499	0.0516	0.5226	3.3818	0.0486	0.0497	0.0925	0.6053
Dim-E3-0890	28.5172	0.0505	0.4058	3.5250	0.0413	0.0196	0.0894	0.6532
Dim-E3-0900	36.8785	0.0595	0.2894	4.3240	0.0940	0.0381	0.1182	0.5925
Dim-E3-0910	33.5492	0.0447	1.1151	3.0795	0.3074	0.0397	0.0675	0.4484
Dim-E3-0915	34.3153	0.0531	0.6163	3.0384	0.1145	0.0425	0.0777	0.6302
Dim-E3-0920	40.4219	0.0627	0.4463	3.6603	0.0817	0.1371	0.0737	0.5084
Dim-E3-0925	39.6098	0.0629	0.0652	3.2904	0.0257	0.0640	0.0755	0.5413
Dim-E3-0930	35.2582	0.0660	0.0038	3.3403	0.0244	0.0236	0.0887	0.4586
Dim-E3-0935	37.1553	0.0545	0.0948	3.2163	0.0238	0.0473	0.0833	0.4162
Dim-E3-0940	35.7672	0.0524	0.2003	3.3331	0.0447	0.0834	0.0882	0.5443
Dim-E3-0945	34.8191	0.0482	0.8738	3.1650	0.1970	0.0225	0.0831	0.6793
Dim-E3-0950	26.8924	0.0491	2.0263	3.3622	0.4483	0.0210	0.1010	0.8220
Dim-E3-0955	20.6450	0.0485	4.9379	3.1677	1.3244	0.0227	0.1031	0.9495
Dim-E3-0960	25.1012	0.0476	2.4715	3.5191	0.5787	0.0365	0.1106	0.8996
Dim-E3-0965	17.7609	0.0539	5.8002	3.2285	1.6290	0.0204	0.1004	0.7824
Dim-E3-0970	18.4576	0.0524	6.6728	3.4188	2.0454	0.0138	0.1019	0.7609
Dim-E3-0975	17.0862	0.0548	5.4450	3.4243	1.4914	0.0245	0.1078	0.7627
Dim-E3-0980	16.7774	0.0531	6.2653	3.4320	1.8048	0.0116	0.1023	0.6600
Dim-E3-0985	26.9185	0.0450	5.4950	3.1994	2.0850	0.0241	0.0978	0.8524
Dim-E3-0995	22.7123	0.0470	5.8045	3.7968	2.2222	0.0467	0.0914	0.9871
Dim-E3-1000	31.1215	0.0523	0.2471	3.1667	0.0532	0.0247	0.0893	0.5855
Dim-E3-1005	29.7624	0.0535	0.3917	3.3104	0.0614	0.0859	0.0840	0.5497
Dim-E3-1010	30.4767	0.0540	0.4604	3.2337	0.0753	0.0298	0.0870	0.5551
Dim-E3-1015	27.1775	0.0458	2.4727	2.6400	0.6022	0.0700	0.0892	0.7365
Dim-E3-1020	23.9722	0.0435	3.6479	3.0296	1.0271	0.0146	0.0958	0.6635
Dim-E3-1025	25.6972	0.0430	4.1931	5.1540	1.2592	0.1316	0.1155	0.4066
Dim-E3-1030	28.2764	0.0460	3.5071	5.3211	1.0382	0.1244	0.0936	0.7469
Dim-E3-1035	38.4830	0.0482	1.4475	3.1643	0.4237	0.0517	0.0723	0.4945
Dim-E3-1040	35.1875	0.0508	1.1859	6.7722	0.3224	0.0586	0.0786	0.8780
Dim-E3-1050	35.6331	0.0538	0.3423	3.3067	0.0962	0.0182	0.0902	0.4008
Dim-E3-1055	31.4303	0.0530	0.0538	2.9230	0.0132	0.0080	0.1058	0.5077
Dim-E3-1060	34.7805	0.0471	0.1729	2.7757	0.0434	0.0089	0.0844	0.6264
Dim-E3-1065	36.4985	0.0464	0.1443	2.9565	0.0337	0.0169	0.0795	0.6059
Dim-E3-1070	30.2182	0.0462	0.0015	2.8140	0.0140	0.0488	0.0941	0.4297
Dim-E3-1075	37.4498	0.0502	0.0431	3.1885	0.0175	0.0241	0.0779	0.4968
Dim-E3-1080	32.5114	0.0512	0.0576	3.2905	0.0209	0.0329	0.0858	0.5142
Dim-E3-1085	33.6386	0.0451	0.0335	2.6838	0.0095	0.0099	0.0848	0.5248
Dim-E3-1095	35.6064	0.0443	0.3265	2.6897	0.0738	0.0168	0.0773	0.6000
Dim-E3-1100	31.7661	0.0466	0.0233	2.9069	0.0065	0.0087	0.0904	0.5066
DIM-E3-1105	36.2318	0.0467	0.2234	3.0589	0.0530	0.0151	0.0786	0.5272
Dim-E3-1110	39.6875	0.0497	0.0702	3.4023	0.0204	0.0219	0.0809	2.5483
Dim-E3-1115	37.7966	0.0499	0.0390	2.9858	0.0154	0.0361	0.0814	0.4493
Dim-E3-1120	35.6406	0.0437	0.0698	2.6802	0.0269	0.0216	0.0759	0.4331
Dim-E3-1125	33.6582	0.0427	0.0685	2.5827	0.0202	0.0203	0.0838	0.4380
Dim-E3-1130	35.3227	0.0455	0.1011	3.3726	0.0261	0.0270	0.0833	0.5158
Dim-E3-1140	32.0708	0.0415	0.4699	2.8296	0.1090	0.0304	0.0856	0.6134
Dim-E3-1145	32.7205	0.0401	0.3989	2.6221	0.0926	0.0151	0.0816	0.5813
Dim-E3-1150	31.7080	0.0424	0.0711	2.7652	0.0213	0.0123	0.0797	0.4995
Dim-E3-1155	31.7379	0.0403	0.0680	2.5853	0.0167	0.0113	0.0792	0.5306

Dim-E3-1160	30.1598	0.2741	0.0617	2.8667	0.0289	0.0307	0.1142	0.4273
Dim-E3-1165	28.6918	0.0401	0.0312	3.3099	0.0100	0.0127	0.0867	0.5386
Dim-E3-1170	28.7161	0.0377	0.0244	2.4252	0.0113	0.0119	0.0825	2.2201
Dim-E3-1175	29.2178	0.0370	0.0430	2.3709	0.0153	0.0249	0.0806	0.4755
Dim-E3-1180	27.3483	0.0410	0.0277	2.4991	0.0079	0.0179	0.0835	0.4021
Dim-E3-1185	27.8071	0.0426	0.0388	2.5647	0.0223	0.0368	0.0895	0.6666
Dim-E3-1190	25.6147	0.0389	0.0346	2.4131	0.0094	0.0122	0.0981	0.5516
Dim-E3-1200	28.0989	0.0403	0.0735	2.7341	0.0252	0.0169	0.0953	0.5960
Dim-E3-1205	25.9884	0.0411	0.4163	2.5501	0.0889	0.0083	0.1032	0.5663
Dim-E3-1210	27.9467	0.0403	0.1943	2.5436	0.0300	0.0091	0.0900	0.4946
Dim-E3-1215	27.5978	0.1910	0.1550	2.9046	0.0496	0.0375	0.1259	0.4826
Dim-E3-1220	22.3906	0.0388	1.0650	2.4667	0.2380	0.0067	0.1012	0.5995
Dim-E3-1225	25.8809	0.0399	1.0759	2.7830	0.2248	0.0043	0.0895	0.5783
Dim-E3-1230	26.1522	0.0403	1.2593	2.7326	0.2759	0.0147	0.0888	0.7477
Dim-E3-1235	25.3685	0.0457	0.0865	2.5788	0.0209	0.0083	0.1125	0.5183
Dim-E3-1240	34.8532	0.0405	0.4844	2.6847	0.1395	0.0139	0.0718	0.4070
Dim-E3-1245	32.1147	0.0402	0.5721	2.5695	0.1576	0.0065	0.0827	0.4292
Dim-E3-1250	37.3354	0.0859	0.1080	4.0097	0.0297	0.0205	0.2400	0.3105
Dim-E3-1255	34.7823	0.1240	0.1251	5.2914	0.0436	0.0372	0.3738	0.2261
Dim-E3-1260	35.8894	0.0483	0.0368	3.5887	0.0141	0.0242	0.0506	0.1913
Dim-E3-1265	39.3086	0.0464	0.0666	2.8395	0.0176	0.0261	0.0453	0.1656
Dim-E3-1270	33.3641	0.0451	0.0426	2.8726	0.0129	0.0193	0.0512	0.2789
Dim-E3-1275	31.8290	0.0443	0.0271	2.7324	0.0078	0.0190	0.0498	0.2634
Dim-E3-1280	40.8516	0.0470	0.0533	3.2823	0.0154	0.0174	0.0449	0.2259
Dim-E3-1285	39.5952	0.0453	0.0280	3.2404	0.0096	0.0125	0.0444	0.2318
Dim-E3-1290	40.2680	0.8465	1.4837	13.9233	0.7060	0.3798	0.1356	2.9749
Dim-E3-1295	35.8503	0.0433	0.0384	3.5001	0.0168	0.0218	0.0589	0.2403
Dim-E3-1300	38.3572	0.0422	0.0327	3.3534	0.0137	0.0189	0.0541	0.1835
Dim-E3-1305	29.6072	0.0435	0.2357	3.5413	0.0359	0.0216	0.0709	0.3477
Dim-E3-1310	31.8393	0.0408	0.2440	3.4687	0.0336	0.0172	0.0668	0.2977
Dim-E3-1315	29.5637	0.0380	0.1342	3.0223	0.0220	0.0148	0.0652	0.2658
Dim-E3-1320	33.3606	0.0394	0.0785	3.2403	0.0146	0.0115	0.0611	0.2380
Dim-E3-1325	36.8146	0.0439	0.0374	3.3325	0.0166	0.0328	0.0478	0.1041
Dim-E3-1330	42.1746	0.0475	0.0179	5.5118	0.1973	0.4380	0.0246	0.1098
Dim-E3-1335	43.1078	0.0498	0.0063	2.7189	0.0515	0.0467	0.0265	0.0745
Dim-E3-1340	34.8328	0.0573	0.0332	3.3820	0.0088	0.1772	0.0378	0.1736
Dim-E3-1345	34.3057	0.0585	0.0379	3.3613	0.0145	0.0557	0.0416	0.2190
Dim-E3-1350	36.4911	0.0580	0.0329	5.6731	0.0185	0.0873	0.0446	0.2237
Dim-E3-1355	32.7346	0.0556	0.0493	3.2070	0.0171	0.0756	0.0509	0.2966
Dim-E3-1360	32.7005	0.0621	0.0873	3.9013	0.0310	0.1203	0.0565	0.2593
Dim-E3-1365	37.0214	0.0567	0.0408	3.7072	0.0134	0.1055	0.0444	0.2067
Dim-E3-1370	37.0933	0.0568	0.0638	4.8674	0.0230	0.0907	0.0479	0.1965
Dim-E3-1375	31.7770	0.0540	0.0703	3.8051	0.0667	0.2239	0.0560	0.3175
Dim-E3-1380	29.2623	0.0558	0.0474	4.4600	0.0154	0.1360	0.0621	0.2914
Dim-E3-1390	33.7295	0.0527	0.0353	3.8369	0.0125	0.4232	0.0526	0.2396
Dim-E3-1400	29.7838	0.0514	0.0665	3.5953	0.0110	0.0413	0.0656	0.3102
Dim-E3-1410	33.2207	0.0487	0.0347	3.3853	0.0098	0.0720	0.0511	0.2254
Dim-E3-1420	34.0154	0.0505	0.0334	3.4456	0.0136	0.3281	0.0516	0.2650
Dim-E3-1430	38.8026	0.0502	0.1040	3.2158	0.0215	0.0680	0.0519	0.4387
Dim-E3-1440	30.7314	0.0575	0.0146	3.5928	0.0059	0.2905	0.0671	0.2382
Dim-E3-1460	26.5747	0.0600	0.0522	3.9467	0.0172	0.0856	0.0809	0.3395
Dim-E3-1470	29.2056	0.0578	0.0183	3.6163	0.0075	0.0724	0.0691	0.3011
Dim-E3-1480	31.0433	0.0581	0.0353	3.6138	0.0080	0.0334	0.0796	0.2295
Dim-E3-1490	29.9952	0.0590	0.0192	3.7225	0.0136	0.0684	0.0692	0.2424
Dim-E3-1500	30.3125	0.0553	0.0280	3.3303	0.0074	0.0577	0.0687	0.2783
Dim-E3-1510	35.4432	0.0568	0.0162	3.5524	0.0052	0.0328	0.0517	0.2299
Dim-E3-1520	30.0113	0.0593	0.0313	3.8377	0.0098	0.0570	0.0664	0.2721
Dim-E3-1530	30.9358	0.0585	0.0229	3.8262	0.0077	0.0505	0.0658	0.2668
Dim-E3-1540	27.3399	0.0600	0.0403	4.0756	0.0083	0.0932	0.0762	0.2978
Dim-E3-1550	29.5486	0.0537	0.2029	3.4944	0.0483	0.1066	0.0726	0.3165
Dim-E3-1560	29.3708	0.0437	1.2430	2.7040	0.2483	0.0182	0.0623	0.4828
Dim-E3-1570	25.0542	0.0473	2.4095	2.8514	0.3938	0.0493	0.0791	0.6224
Dim-E3-1580	21.7785	0.0540	3.3300	3.2360	0.6237	0.0590	0.0951	0.6446

Dim-E3-1590	23.4382	0.0533	1.8176	3.8646	0.3235	0.0498	0.0812	0.5953
Dim-E3-1600	29.0943	0.0492	0.4151	2.8241	0.0195	0.2497	0.0593	0.4905
Dim-E3-1610	27.1725	0.0473	0.1037	2.8160	0.0117	0.0395	0.0620	0.5095
Dim-E3-1620	27.1996	0.0464	0.0532	2.8088	0.0089	0.0385	0.0625	0.4884
Dim-E3-1630	28.7852	0.0472	0.0260	2.9307	0.0116	0.0819	0.0570	0.4404
Dim-E3-1640	27.1085	0.0468	0.0464	2.9774	0.0079	0.0574	0.0720	0.5387
Dim-E3-1650	24.7066	0.0488	0.0843	12.7119	0.0116	0.2728	0.0832	0.4862
Dim-E3-1660	25.5022	0.0477	0.0863	3.1271	0.0133	0.2052	0.0786	0.5002
Dim-E3-1670	27.2542	0.0489	0.0697	3.3419	0.0187	0.0664	0.0694	0.4440
Dim-E3-1680	27.4147	0.0447	0.1987	2.9947	0.0260	0.0742	0.0730	0.5200
Dim-E3-1690	26.1088	0.0450	0.5743	3.0324	0.0613	0.0533	0.0735	0.5419
Dim-E3-1700	25.3280	0.0487	0.2648	3.1304	0.0250	0.0584	0.0783	0.6013
Dim-E3-1710	25.4416	0.0503	0.3291	3.4985	0.0288	0.0672	0.0762	0.5962
Dim-E3-1720	25.7817	0.0459	0.2590	3.0769	0.0185	0.0593	0.0710	0.4991
Dim-E3-1730	25.6219	0.0465	0.3912	3.3623	0.0421	0.0315	0.0736	0.5659
Dim-E3-1740	25.1483	0.0410	0.2596	2.9664	0.0220	0.0212	0.0650	0.4840
Dim-E3-1750	24.5897	0.0413	0.5494	2.9462	0.0381	0.0120	0.0734	0.5107
Dim-E3-1760	24.8941	0.0410	0.5583	2.9831	0.0355	0.0204	0.0706	0.5574
Dim-E3-1770	24.8498	0.0403	0.4916	2.7565	0.0356	0.0169	0.0706	0.5244
Dim-E3-1780	28.3702	0.0371	0.5191	2.7186	0.0591	0.0769	0.0636	0.5778
Dim-E3-1790	25.8840	0.0399	1.2963	2.7716	0.2787	0.0273	0.0808	0.6347
Dim-E3-1800	24.1623	0.0417	2.5523	2.8241	0.6017	0.0202	0.0937	0.6851
Dim-E3-1810	22.7546	0.0400	1.9738	2.7345	0.4925	0.0113	0.0918	0.7302
Dim-E3-1820	24.0830	0.0395	1.6310	2.6351	0.3708	0.0294	0.0867	0.7440
Dim-E3-1830	22.9884	0.0407	2.0018	2.6541	0.4376	0.0091	0.0906	0.6906
Dim-E3-1840	24.3590	0.0416	0.8380	2.7021	0.2002	0.0119	0.0792	0.6208
Dim-E3-1850	24.5361	0.0391	0.9652	2.5663	0.2422	0.0183	0.0761	0.6764
Dim-E3-1860	23.5338	0.0398	1.5189	2.6625	0.3183	0.0196	0.0817	0.7388
Dim-E3-1870	24.4524	0.0427	0.5618	2.6234	0.1018	0.0096	0.0813	0.5544
Dim-E3-1880	24.0417	0.0442	0.4045	2.7241	0.0808	0.0138	0.0927	0.5715
Dim-E3-1890	24.6003	0.0502	0.4048	3.1768	0.0851	0.0271	0.0977	0.5260
Dim-E3-1900	28.4492	0.0497	0.4184	3.2256	0.0875	0.0257	0.0984	0.5771
Dim-E3-1910	24.8141	0.0485	0.4259	3.3897	0.0434	0.0104	0.0888	0.4675
Dim-E3-1920	23.5850	0.0426	0.6256	2.8831	0.0719	0.0493	0.0894	0.6002
Dim-E3-1930	24.1945	0.0435	0.5988	3.0549	0.0472	0.0150	0.0908	0.5819
Dim-E3-1940	25.2054	0.0438	0.8884	3.1495	0.0562	0.0077	0.0935	0.6113
Dim-E3-1950	33.8345	0.0363	0.1434	11.0444	0.0104	0.0182	0.0575	0.6504
Dim-E3-1960	28.9861	0.0379	0.2164	2.6182	0.0313	0.0210	0.0893	0.6848
Dim-E3-1970	34.7184	0.0445	0.0143	3.8669	0.0070	0.0248	0.0680	0.4539
Dim-E3-1980	34.5492	0.0425	0.0214	2.9684	0.0090	0.0290	0.0777	0.4327
Dim-E3-1990	37.7573	0.0452	0.0237	3.2233	0.0095	0.0259	0.0702	0.4158
Dim-E3-2000	30.5177	0.0535	0.0244	3.9911	0.0087	0.0273	0.1191	0.4710
Dim-E3-2010	28.1738	0.0491	0.0196	3.5620	0.0046	0.0071	0.1305	0.5906
Dim-E3-2020	27.5668	0.0487	0.1342	3.5007	0.0273	0.0143	0.1314	0.5418
Dim-E3-2030	26.6952	0.0518	0.2567	4.4496	0.0507	0.0249	0.1472	0.5267
Dim-E3-2040	24.0986	0.0468	0.0842	3.4409	0.0171	0.0177	0.1436	1.5517
Dim-E3-2050	24.3629	0.0473	0.0350	3.3219	0.0102	0.0328	0.1439	0.6108
Dim-E3-2060	27.0097	0.0481	0.0377	3.3586	0.0111	0.0155	0.1361	0.4977
Dim-E3-2070	25.9867	0.0493	0.0244	3.6809	0.0063	0.0185	0.1351	0.4704
Dim-E3-2080	26.0339	0.0497	0.0375	4.2195	0.0077	0.0106	0.1336	0.4266
Dim-E3-2090	28.8378	0.0486	0.0389	3.4891	0.0079	0.0141	0.1243	0.4820
Dim-E3-2100	31.0731	0.0524	0.0369	3.8175	0.0073	0.0397	0.1201	0.4819
Dim-E3-2110	31.9540	0.0532	0.0673	3.8695	0.0216	0.0515	0.1167	0.5103
Dim-E3-2120	30.9887	0.0508	0.0262	3.4298	0.0084	0.0456	0.1233	0.5171
Dim-E3-2130	35.7864	0.0514	0.0157	3.5926	0.0053	0.0374	0.1033	0.4226
Dim-E3-2140	36.2486	0.0513	0.0173	3.6442	0.0068	0.0223	0.0990	0.4158
Dim-E3-2150	33.8105	0.0446	0.0160	3.4397	0.0057	0.0179	0.0842	0.4604
Dim-E3-2160	26.3702	0.0426	0.0640	2.9802	0.0142	0.0440	0.1082	0.5618
Dim-E3-2170	24.8384	0.0428	0.1791	3.1275	0.0156	0.0143	0.1200	0.5732
Dim-E3-2180	29.4547	0.0427	0.2244	3.1556	0.0210	0.0224	0.0933	0.5690
Dim-E3-2190	34.7454	0.0456	0.0171	3.4131	0.0056	0.0223	0.0788	0.3643
Dim-E3-2200	36.9577	0.0455	0.0110	3.4807	0.0047	0.0196	0.0724	0.2904
Dim-E3-2210	34.6776	0.0436	0.0171	3.4531	0.0047	0.0150	0.0754	0.3411

Dim-E3-2220	24.8713	0.0432	0.2257	3.2899	0.0318	0.0239	0.1245	0.5701
Dim-E3-2230	27.0503	0.0424	0.0375	3.3119	0.0068	0.0169	0.1075	0.5490
Dim-E3-2240	30.2258	0.0420	0.0228	3.2507	0.0070	0.0271	0.0957	0.4796
Dim-E3-2250	40.5585	0.0428	0.0301	3.9626	0.0095	0.0283	0.0838	0.4479
Dim-E3-2260	40.8099	0.0447	0.0252	4.5315	0.0087	0.0283	0.1003	0.5714
Dim-E3-2270	38.8726	0.0489	0.0146	5.2085	0.0053	0.1035	0.1124	0.4855
Dim-E3-2280	36.0743	0.0446	0.0267	4.7127	0.0095	0.0820	0.1118	0.5448
Dim-E3-2290	35.6988	0.0434	0.0135	4.3146	0.0054	0.0156	0.1133	0.5313
Dim-E3-2300	35.2485	0.0436	0.0083	4.7742	0.0036	0.0349	0.1159	0.5513
Dim-E3-2310	46.1143	0.0572	0.0260	5.0521	0.0093	0.0381	0.0896	0.3795
Dim-E3-2320	38.2564	0.0598	0.0140	4.3935	0.0043	0.0155	0.1015	0.3167
Dim-E3-2330	34.7898	0.0600	0.0374	4.3896	0.0136	0.0230	0.1210	0.2350
Dim-E3-2340	28.7668	0.0578	0.0173	3.6509	0.0128	0.0238	0.1357	0.3458
Dim-E3-2350	26.9043	0.0541	0.0186	3.5400	0.0055	0.0119	0.1375	0.4162
Dim-E3-2360	26.4646	0.0516	0.0363	3.3231	0.0130	0.0178	0.1332	0.4271
Dim-E3-2370	26.2930	0.0508	0.0352	3.3981	0.0105	0.0194	0.1291	0.4401
Dim-E3-2380	28.8895	0.0498	0.0260	3.3142	0.0067	0.0232	0.1172	0.3734
Dim-E3-2390	26.2854	0.0489	0.0791	3.2292	0.0159	0.0281	0.1267	0.5128
Dim-E3-2400	24.4243	0.0510	0.0713	3.5171	0.0133	0.0149	0.1376	0.5061
Dim-E3-2410	21.0653	0.0509	0.1067	3.4962	0.0164	0.0204	0.1406	0.6058
Dim-E3-2420	20.0998	0.0466	0.1965	3.2206	0.0348	0.0164	0.1396	0.6960
Dim-E3-2430	21.0933	0.0498	0.5680	3.3011	0.0952	0.0102	0.1456	0.5860
Dim-E3-2440	39.6980	0.0594	0.0191	3.9926	0.0061	0.0126	0.0852	0.3612
Dim-E3-2445	34.2138	0.0602	0.0364	3.9284	0.0117	0.0196	0.1087	0.3331
Dim-E3-2450	33.1026	0.0500	0.0290	3.2410	0.0080	0.0228	0.1123	0.5592
Dim-E3-2455	36.6120	0.0583	0.0764	3.5305	0.0260	0.0351	0.1086	0.3823
Dim-E3-2460	41.4088	0.0548	0.0172	4.0520	0.0055	0.0143	0.1136	0.4242
Dim-E3-2465	36.7162	0.0504	0.0231	3.3222	0.0054	0.0244	0.1090	0.4424
Dim-E3-2470	44.8858	0.0574	0.0378	4.3556	0.0127	0.0345	0.1102	0.4392
Dim-E3-2475	40.5623	0.0589	0.0199	5.0609	0.0094	0.0301	0.1533	0.4586
Dim-E3-2480	43.0290	0.0605	0.0825	5.0831	0.0301	0.0413	0.1490	0.4221
Dim-E3-2485	36.0708	0.0542	0.0325	4.5073	0.0411	0.0718	0.1629	0.5852
Dim-E3-2490	36.3760	0.0510	0.0119	4.2381	0.0062	0.0114	0.1575	0.5772
Dim-E3-2495	41.2231	0.0486	0.0227	4.0889	0.0111	0.0229	0.1297	0.6582
Dim-E3-2500	40.2850	0.0476	0.0238	3.9278	0.0126	0.0278	0.1316	0.5540
Dim-E3-2505	43.7304	0.0496	0.0184	3.9446	0.0066	0.0309	0.1276	0.4946
Dim-E3-2510	52.5923	0.0589	0.0295	13.3283	0.0468	0.0463	0.1490	0.3322
Dim-E3-2515	42.5405	0.0762	0.0193	4.5899	0.0108	0.0299	0.1608	0.3178
Dim-E3-2520	34.9873	0.0700	0.0186	4.3689	0.0091	0.0215	0.1812	0.4788
Dim-E3-2525	40.7284	0.0707	0.0417	4.1696	0.0172	0.0425	0.1771	0.3869
Dim-E3-2530	42.9155	0.1033	0.0711	4.4104	0.0224	0.0420	0.5257	0.4520
Dim-E3-2535	40.3173	0.2487	0.0252	7.6933	0.0161	0.0190	2.1509	0.3218
Dim-E3-2540	32.0995	0.2365	0.1142	9.1749	0.0387	0.1447	2.8139	0.3731
Dim-E3-2550	24.2624	0.3256	0.0286	11.1511	0.0230	0.1737	4.0346	0.3371
Dim-E3-2555	8.4683	0.5185	0.0194	13.5706	0.0079	0.0599	5.1434	0.2557
Dim-E3-2560	4.0560	0.5696	0.0484	16.0917	0.0124	0.0433	6.6560	0.1598
Dim-E3-2565	11.8811	0.5701	0.0541	19.1820	0.0411	0.1636	8.4056	0.4932
Dim-E3-2570	17.0309	0.4972	0.0612	16.4187	0.0359	0.0710	6.1417	0.3471
Dim-E3-2575	44.7315	0.0494	0.0298	3.7859	0.0113	0.3204	0.1489	0.4239
Dim-E3-2580	30.5391	0.0979	0.0579	5.4149	0.0117	0.0389	1.2183	0.6906
Dim-E3-2585	31.5885	0.2981	0.0538	11.1989	0.0196	0.1379	4.2748	0.3308
Dim-E3-2590	36.0172	0.2321	0.0554	9.4487	0.0238	0.1638	3.4871	0.3860
Dim-E3-2595	34.6914	0.2339	0.0573	10.1235	0.0300	0.0997	3.9408	0.3985
Dim-E3-2600	34.0707	0.0723	0.0118	3.4584	0.0047	0.0550	0.1119	0.2503
Dim-E3-2605	30.1911	0.0491	0.0263	3.7071	0.0089	0.0329	0.0822	0.2908
Dim-E3-2610	29.3826	0.0459	0.0803	3.1528	0.0286	0.0597	0.1039	0.4437
Dim-E3-2615	30.3235	0.0465	0.0259	3.2766	0.0136	0.0978	0.0834	0.3056
Dim-E3-2620	32.1141	0.0482	0.0095	3.4257	0.0052	0.0468	0.0773	0.2245
Dim-E3-2625	29.3437	0.0489	0.0284	3.4639	0.0085	0.0851	0.0846	0.2677
Dim-E3-2630	29.2244	0.0459	0.0533	2.9948	0.0152	0.1090	0.0914	0.2592
Dim-E3-2635	29.6310	0.0487	0.0639	3.2394	0.0216	0.0772	0.0900	0.3865
Dim-E3-2640	32.1100	0.0491	0.0478	3.4463	0.0210	0.0830	0.0818	0.2874
Dim-E3-2645	31.7598	0.0479	0.0237	3.0677	0.0100	0.1284	0.0803	0.3122

Dim-E3-2650	28.9599	0.0481	0.0522	3.3743	0.0207	0.1064	0.0734	0.3688
Dim-E3-2655	26.9354	0.0458	0.0300	3.1177	0.0099	0.0684	0.0946	0.3810
Dim-E3-2660	28.4498	0.0486	0.0716	3.3713	0.0259	0.0899	0.0861	0.3519
Dim-E3-2665	27.1495	0.0451	0.0560	2.7903	0.0147	0.0892	0.0838	0.4113
Dim-E3-2670	26.7709	0.0388	0.0365	2.4847	0.0092	0.0739	0.0889	0.4300
Dim-E3-2675	25.5215	0.0465	0.0375	3.5261	0.0103	0.0590	0.0731	0.3367
Dim-E3-2680	27.0404	0.0465	0.0549	3.1570	0.0165	0.2321	0.0803	0.3855
Dim-E3-2690	27.3487	0.0411	0.0499	2.4737	0.0204	0.1247	0.0884	0.3876
Dim-E3-2695	37.6761	0.0433	0.0608	2.5044	0.0222	0.0894	0.0588	0.3547
Dim-E3-2700	38.8164	0.0436	0.0444	2.4719	0.0159	0.0981	0.0537	0.2518
Dim-E3-2705	30.6597	0.0463	0.0633	3.1009	0.0328	0.3217	0.0667	0.3279
Dim-E3-2710	31.8906	0.0430	0.0468	2.5399	0.0156	0.1421	0.0651	0.3190
Dim-E3-2715	27.5735	0.0445	0.0542	2.6188	0.0185	0.1108	0.0818	0.3552
Dim-E3-2720	27.9951	0.0418	0.1213	5.9911	0.0206	0.1323	0.0795	0.4089
Dim-E3-2725	28.1273	0.0436	0.0810	2.8365	0.0440	0.1702	0.0722	0.4213
Dim-E3-2730	29.8409	0.0423	0.0643	2.6210	0.0192	0.0616	0.0756	0.4009
Dim-E3-2735	28.2990	0.0355	0.1285	2.0620	0.0382	0.0650	0.0801	0.4553
Dim-E3-2740	25.4854	0.0463	0.2444	3.3075	0.0446	0.0934	0.0788	0.5188
Dim-E3-2745	24.4219	0.0422	0.2428	3.1197	0.0340	0.0307	0.0869	0.5294
Dim-E3-2750	25.9104	0.0389	0.1185	2.5011	0.0214	0.0227	0.0875	0.5716
Dim-E3-2755	26.4786	0.0438	0.0536	2.8958	0.0167	0.0164	0.0848	0.4700
Dim-E3-2760	25.0036	0.0400	0.0583	2.5288	0.0127	0.0121	0.0921	0.5070
Dim-E3-2765	24.9171	0.0419	0.0337	2.7776	0.0086	0.0139	0.0928	0.4768
Dim-E3-2770	25.5938	0.0401	0.0507	2.6441	0.0117	0.0139	0.0952	0.4965
Dim-E3-2780	26.0006	0.0389	0.1430	2.7941	0.0291	0.0120	0.0921	0.5312
Dim-E3-2785	27.3345	0.0401	0.0831	2.6610	0.0178	0.0293	0.0863	0.5506
Dim-E3-2790	26.0138	0.0369	0.0745	2.3322	0.0119	0.0097	0.0890	0.5158
Dim-E3-2800	25.8799	0.0405	0.1850	3.3832	0.0242	0.0308	0.0916	0.7512
Dim-E3-2805	25.1475	0.0405	0.1773	3.0091	0.0185	0.0136	0.0874	0.5269
Dim-E3-2810	29.9885	0.0446	0.4264	5.2920	0.0736	0.0739	0.0967	0.5725
Dim-E3-2815	24.9292	0.0452	0.1473	3.6509	0.0233	0.0345	0.0763	0.4614
Dim-E3-2820	25.0264	0.0452	0.6279	3.3636	0.0892	0.0271	0.0930	0.5756
Dim-E3-2830	27.4854	0.0444	0.0858	3.7586	0.0201	0.0294	0.0785	0.4814
Dim-E3-2840	26.5099	0.0404	0.1242	3.2676	0.0175	0.0199	0.0800	0.5931
Dim-E3-2850	26.2788	0.0414	0.1337	3.4129	0.0137	0.0088	0.0692	0.4961
Dim-E3-2860	27.5706	0.0446	0.0479	3.8742	0.0079	0.0080	0.0641	0.3690
Dim-E3-2870	26.4332	0.0415	0.0838	3.0251	0.0138	0.0075	0.0791	0.4294
Dim-E3-2880	28.5393	0.0415	0.2744	3.1631	0.0611	0.0212	0.0731	0.4338
Dim-E3-2890	27.8472	0.0406	0.2129	3.1970	0.0325	0.0112	0.0755	0.4439
Dim-E3-2900	33.0830	0.0417	0.0223	3.0839	0.0072	0.0088	0.0544	0.2985
Dim-E3-2910	33.0138	0.0414	0.0103	2.8001	0.0029	0.0085	0.0671	0.3190
Dim-E3-2920	28.9351	0.0423	0.0811	3.1777	0.0111	0.0100	0.0877	0.4167
Dim-E3-2930	28.8503	0.0427	0.0734	2.6348	0.0164	0.0172	0.0882	0.3880
Dim-E3-2940	34.4411	0.0443	0.0462	2.8448	0.0109	0.0147	0.0699	0.3078
Dim-E3-2950	35.6352	0.0437	0.0303	2.8297	0.0109	0.0206	0.0716	0.2792
Dim-E3-2960	28.2843	0.0450	0.0136	3.0484	0.0037	0.0067	0.0915	0.4133
Dim-E3-2970	33.6994	0.0406	0.1895	2.5810	0.0568	0.0202	0.0762	0.3782
Dim-E3-2980	29.3533	0.0407	0.0240	2.5153	0.0065	0.0117	0.0851	0.4078
Dim-E3-2990	31.0349	0.0373	0.0234	2.1336	0.0057	0.0117	0.0772	0.3709
Dim-E3-3000	36.4245	0.0557	0.0215	3.7780	0.0056	0.0364	0.0916	0.2585
Dim-E3-3010	34.5964	0.0343	0.0207	2.1930	0.0062	0.0081	0.0654	0.4166
Dim-E3-3020	36.7377	0.0532	0.0655	4.5256	0.0186	0.0154	0.0894	0.3651
Dim-E3-3030	41.9213	0.0477	0.0313	3.1941	0.0102	0.0101	0.0688	0.2976
Dim-E3-3040	33.8956	0.0547	0.0495	4.0673	0.0157	0.0179	0.1064	0.3395
Dim-E3-3050	33.9232	0.0502	0.0232	3.4474	0.0078	0.0084	0.1041	0.3978
Dim-E3-3060	36.2085	0.0596	0.0118	4.9310	0.0046	0.0087	0.0936	0.2380
Dim-E3-3070	33.0936	0.0583	0.0309	4.4213	0.0131	0.0134	0.1188	0.3195
Dim-E3-3080	26.0846	0.0565	0.0147	4.0578	0.0037	0.0065	0.1363	0.3904
Dim-E3-3090	25.5596	0.0519	0.0381	3.7953	0.0087	0.0112	0.1356	0.5436
Dim-E3-3100	25.9984	0.0515	0.0413	3.5422	0.0070	0.0130	0.1379	0.4726
Dim-E3-3110	29.1564	0.0503	0.0241	3.3888	0.0066	0.0066	0.1212	0.4152
Dim-E3-3120	30.8386	0.0557	0.0617	3.9965	0.0192	0.0149	0.1071	0.3271

Dim-E3-3130	31.2492	0.0509	0.0258	3.6456	0.0086	0.0100	0.0987	0.3357
Dim-E3-3140	30.0366	0.0472	0.0311	3.1765	0.0076	0.0069	0.1059	0.3981
Dim-E3-3150	24.5176	0.0496	0.0652	3.1969	0.0097	0.0071	0.1347	0.5342
Dim-E3-3160	23.2857	0.0504	0.0868	3.4085	0.0128	0.0092	0.1415	0.5285
Dim-E3-3170	23.3021	0.0496	0.1095	3.1836	0.0157	0.0077	0.1425	0.5289
Dim-E3-3180	22.7147	0.0483	0.1169	3.1262	0.0129	0.0073	0.1527	0.4711
Dim-E3-3190	24.4854	0.0488	0.1379	3.5985	0.0191	0.0179	0.1490	0.5099
Dim-E3-3200	29.0246	0.0487	0.0763	3.4048	0.0095	0.0078	0.1232	0.3489
Dim-E4-0035	26.2116	0.0601	0.8578	37.0195	0.0569	0.1859	0.1159	0.2716
Dim-E4-0115	25.8481	0.0602	0.8433	5.9338	0.0845	0.2642	0.1240	0.2951
Dim-E4-0180	26.1855	0.0620	1.0603	17.5316	0.1307	1.2572	0.1234	0.4696
Dim-E4-0245	25.6815	0.0616	2.0186	6.2379	0.1559	0.3615	0.1284	0.2758
Dim-E4-0300	23.2750	0.0575	2.5412	5.8036	0.1856	0.4662	0.1194	0.3273
Dim-E4-0370	24.4808	0.0593	1.3740	4.8969	0.1133	0.9573	0.1160	0.3323
Dim-E4-0415	24.8155	0.0611	1.6876	8.9010	0.2008	1.2681	0.1215	0.3854
Dim-E4-0485	24.9160	0.0719	1.5443	5.2114	0.2566	1.0700	0.1202	0.3012
Dim-E4-0540	24.5438	0.0616	2.2116	10.2582	0.1801	0.6848	0.1162	0.4465
Dim-E4-0615	21.8872	0.0541	4.1756	4.2879	0.2607	0.3508	0.1252	0.2463
Dim-E4-0695	22.0691	0.0522	4.6913	4.2288	0.3265	0.2789	0.1264	0.3813
Dim-E4-0780	22.1142	0.0570	2.0584	4.0439	0.1270	0.1397	0.1233	0.1586
Dim-E4-0945	23.8529	0.0534	0.9682	5.9902	0.1236	0.3084	0.1045	0.2433
Dim-E4-1000	23.1869	0.0516	2.2757	5.7908	0.1641	0.5989	0.1038	0.3046
Dim-E4-1080	21.7013	0.0582	1.8552	5.8045	0.1446	0.6907	0.1238	2.4566
Dim-E4-1155	21.8108	0.0576	2.8058	6.6713	0.1548	0.5626	0.1204	0.4693
Dim-E4-1235	22.8560	0.0534	1.4650	4.3841	0.0729	0.4338	0.1200	0.3822
Dim-E4-1310	22.7362	0.0543	1.5925	8.0586	0.0829	1.1833	0.1167	0.5461
Dim-E4-1370	24.0445	0.0534	1.0068	4.8272	0.0408	0.3893	0.1078	0.2553
Dim-E4-1455	27.1924	0.0895	0.2197	7.3943	0.0333	0.2295	0.1009	0.2378
Dim-E4-1535	28.7565	0.0577	0.1713	16.5421	0.1069	0.4657	0.0884	0.2136
Dim-E4-1600	30.4004	0.0544	0.1627	5.2813	0.0261	0.8914	0.0856	0.2325
Dim-E4-1655	27.3010	0.0533	0.4750	13.2478	0.0341	0.7543	0.0916	0.1957
Dim-E4-1760	28.3386	0.0561	0.3002	6.5239	0.0559	0.3388	0.0828	0.3066
Dim-E4-1830	36.2560	0.0870	2.7688	46.3235	3.4381	3.5047	1.2497	4.4362
Dim-E4-1920	27.3630	0.0463	0.2518	7.5164	0.0305	0.2184	0.0840	0.1597
Dim-E4-1985	26.8420	0.0556	0.5407	9.0266	0.0997	0.5953	0.0891	0.2940
Dim-E4-2030	24.0748	0.0449	0.8314	5.1717	0.0494	0.2641	0.0838	0.2830
Dim-E4-2110	23.2498	0.1206	0.9017	5.4043	0.0642	0.2820	0.0939	0.2671
Dim-E4-2195	23.6901	0.0460	1.0469	4.6347	0.0507	0.5692	0.0841	0.2179
Dim-E4-2275	24.0106	0.0502	0.6221	5.2769	0.0557	0.8985	0.0816	0.2252
Dim-E4-2360	22.2748	0.0455	1.3607	4.9869	0.0840	2.9321	0.0833	0.3474
Dim-E4-2430	28.4712	0.0486	0.5234	5.7017	0.0755	1.1360	0.0697	0.2733
Dim-E4-2510	22.4541	0.0478	1.3086	13.9700	0.1078	1.2109	0.0840	0.5928
Dim-E4-2605	22.1757	0.0431	0.6876	4.3327	0.0802	0.7187	0.0782	0.2146
Dim-E4-2665	23.7861	0.0483	0.7533	6.3015	0.0767	0.8249	0.0798	0.2647
Dim-E4-2740	25.2146	0.0440	0.2210	4.1660	0.0199	0.3392	0.0715	0.1711
Dim-E4-2905	25.7027	0.0470	0.0640	6.3928	0.0277	0.5539	0.0623	0.0801
Dim-E4-2955	24.4989	0.0881	0.1267	12.9113	0.0332	0.3876	0.0791	0.1378
Dim-E4-3035	22.1936	0.0488	0.2504	6.0410	0.0570	0.4849	0.0666	0.1775
Dim-E4-3125	24.8844	0.0491	0.4857	8.4646	0.1248	1.0900	0.0856	1.3014
Dim-E4-3200	27.6576	0.0471	0.1658	8.7920	0.0745	1.1517	0.0571	0.1859
Dim-E4-3255	23.8203	0.0518	0.2545	7.3605	0.0772	1.3578	0.0629	0.6196
Dim-E4-3335	23.8024	0.0440	0.3255	6.0496	0.0304	0.8278	0.0608	0.2170
Dim-E4-3425	22.6284	0.0514	0.4585	9.1468	0.4058	1.6062	0.0594	0.3688
Dim-E4-3475	20.8683	0.0477	0.5484	5.3322	0.0745	0.4570	0.0585	0.1972
Dim-E4-3525	23.3012	0.0491	0.1201	5.5971	0.0329	0.3930	0.0626	0.1742
Dim-E4-3580	23.3431	0.0470	0.2657	5.9201	0.0393	0.7704	0.0610	0.1892
Dim-E4-3670	22.4012	0.0540	0.4005	6.5675	0.0597	1.4167	0.0600	0.3149
Dim-E4-3770	23.5536	0.0526	0.1792	17.9492	0.0788	0.8250	0.0653	0.1943
Dim-E2-010	37.7028	0.0499	0.1484	5.9986	0.0122	0.0320	0.1947	0.3637
Dim-E2-013	41.4213	0.0559	1.2775	7.2138	0.0923	0.0423	0.2630	0.6188
Dim-E2-016	36.8495	0.0555	1.0599	6.3268	0.0818	0.0273	0.1401	0.3793
Dim-E2-019	35.8722	0.0524	1.1106	6.1054	0.0832	0.0128	0.1424	0.4255

Dim-E2-022	33.7136	0.0519	1.7725	6.1072	0.1384	0.0216	0.1428	0.4554
Dim-E2-025	40.6524	0.0543	0.8493	5.8909	0.0693	0.0255	0.1174	0.3642
Dim-E2-028	27.6997	0.0392	2.8452	4.2570	0.2357	0.0245	0.1159	0.6247
Dim-E2-031	30.4365	0.0416	2.3331	4.0454	0.2008	0.0056	0.1195	0.2492
Dim-E2-034	34.8733	0.0491	0.9012	5.4157	0.0702	0.0295	0.1240	0.3672
Dim-E2-037	31.0594	0.0481	1.0646	5.5630	0.0777	0.0189	0.1370	0.3237
Dim-E2-040	31.0642	0.0450	1.2175	5.5170	0.0926	0.0283	0.1153	0.2734
Dim-E2-043	29.0413	0.0463	1.3850	5.7268	0.1012	0.0280	0.1252	0.2951
Dim-E2-046	31.0934	0.0484	1.0483	5.8728	0.0823	0.0262	0.1193	0.2571
Dim-E2-049	31.8051	0.0485	1.2199	5.5765	0.1019	0.0395	0.1259	0.2899
Dim-E2-052	31.7017	0.0458	1.3538	5.2167	0.0967	0.0024	0.1250	0.2438
Dim-E2-055	32.9476	0.0479	1.1965	5.7185	0.0928	0.0215	0.1227	0.3714
Dim-E2-058	30.4821	0.0457	1.2996	5.5630	0.0977	0.0317	0.1197	0.3441
Dim-E2-061	30.2456	0.0466	1.2209	7.1423	0.0990	0.0354	0.1262	0.4120
Dim-E2-065	32.8730	0.0490	1.1756	5.3994	0.0910	0.0494	0.1322	0.3361
Dim-E2-067	30.6983	0.0471	1.4013	5.4928	0.1032	0.1455	0.1205	0.3156
Dim-E2-070	30.7527	0.0479	1.0337	5.9616	0.0746	0.1137	0.1224	0.3170
Dim-E2-073	29.6623	0.0482	1.1704	6.0675	0.0911	0.0787	0.1234	0.2752
Dim-E2-076	29.2796	0.0465	1.0418	5.6119	0.0721	0.0605	0.1163	0.2875
Dim-E2-079	29.9234	0.0472	0.9340	5.7483	0.0629	0.0749	0.1119	0.2691
Dim-E2-082	28.8945	0.0464	1.2983	5.7845	0.0869	0.1270	0.1115	0.3155
Dim-E2-085	32.7796	0.0502	1.0966	5.6904	0.0739	0.0915	0.1276	0.3320
Dim-E2-088	30.1222	0.0469	1.2058	5.4360	0.0794	0.1580	0.1231	0.3532
Dim-E2-091	31.9644	0.0503	0.8071	5.9080	0.0574	0.1240	0.1227	0.2661
Dim-E2-094	32.5403	0.0502	0.7842	6.2758	0.0577	-0.2300	0.1063	0.2771
Dim-E2-097	33.9533	0.0538	0.8546	6.0499	0.0648	0.0692	0.1254	0.2998
Dim-E2-100	30.7150	0.0534	0.9686	6.1007	0.0723	0.0684	0.1449	0.3484
Dim-E2-103	30.1236	0.0523	0.8991	6.4162	0.0707	0.1224	0.1295	0.3215
Dim-E2-106	26.1362	0.0483	1.1487	6.6112	0.0838	0.0642	0.1358	0.3420
Dim-E2-109	27.9466	0.0500	0.8572	6.5888	0.0590	0.0699	0.1324	0.3070
Dim-E2-112	28.6382	0.0476	1.1347	5.7365	0.0844	0.1046	0.1204	0.3035
Dim-E2-115	28.3697	0.0511	0.8003	6.2066	0.0562	0.1158	0.1256	0.2564
Dim-E2-118	30.7885	0.0539	0.8790	5.9502	0.0566	0.0771	0.1470	0.2786
Dim-E2-121	30.7485	0.0535	0.9212	6.0993	0.0642	0.2129	0.1414	0.2596
Dim-E2-124	29.7497	0.0500	0.9165	5.6816	0.0643	0.2119	0.1267	0.2427
Dim-E2-127	35.4781	0.0596	0.7865	6.1611	0.0605	0.1802	0.1310	0.3261
Dim-E2-130	34.8092	0.0536	1.3109	5.5259	0.0896	0.1792	0.1368	0.3556
Dim-E2-133	33.3521	0.0570	0.9334	5.7966	0.0672	0.1040	0.1427	0.3259
Dim-E2-136	31.5676	0.0566	0.9166	5.8504	0.0701	0.0837	0.1338	0.2967
Dim-E2-139	32.5307	0.0513	1.2843	5.1984	0.0858	0.1123	0.1204	0.2858
Dim-E2-142	28.8942	0.0506	0.9789	5.2079	0.0957	0.1426	0.1163	0.2646
Dim-E2-145	28.3630	0.0560	0.8655	5.5541	0.0629	0.3105	0.1353	0.2544
Dim-E2-148	35.2395	0.0641	0.8676	6.0967	0.0602	0.1040	0.1525	0.2986
Dim-E2-151	31.4435	0.0632	1.0642	5.6652	0.0797	0.1581	0.1770	0.2754
Dim-E2-154	28.9102	0.0579	1.4859	5.3928	0.1096	0.1026	0.1791	0.3214
Dim-E2-157	28.6165	0.0631	1.0368	5.5646	0.0751	0.0930	0.1761	0.3148
Dim-E2-160	30.6735	0.0652	0.6423	5.8549	0.0471	0.1425	0.1684	0.2581
Dim-E2-163	29.9930	0.0595	1.0942	5.2510	0.0808	0.1472	0.1671	0.3167
Dim-E2-166	31.0823	0.0609	0.5626	5.5463	0.0409	0.2078	0.1541	0.2441
Dim-E2-169	34.9228	0.0587	0.6092	4.9322	0.0474	0.0939	0.1352	0.2845
Dim-E2-175	26.5678	0.0564	0.9107	5.2690	0.0694	0.1309	0.1582	0.2593
Dim-E2-178	23.1471	0.0487	1.6510	4.3813	0.1175	0.1193	0.1254	0.2590
Dim-E2-181	23.6399	0.0457	1.5844	4.3625	0.1180	0.1739	0.1222	0.2460
Dim-E2-184	23.7249	0.0480	1.4201	4.6530	0.1000	0.0906	0.1267	0.2436
Dim-E2-187	26.4498	0.0509	1.0497	4.6388	0.0810	0.2425	0.1232	0.2482
Dim-E2-190	27.6861	0.0562	1.2921	4.5616	0.0902	0.2977	0.1281	0.2629
Dim-E2-193	24.6641	0.0554	1.3326	4.8300	0.0920	0.0867	0.1263	0.2816
Dim-E2-196	30.3761	0.0585	1.0027	5.2487	0.0725	0.1153	0.1326	0.2143
Dim-E2-199	25.2294	0.0532	1.9336	4.9076	0.1380	0.1567	0.1334	0.2769
Dim-E2-202	23.1001	0.0504	2.7289	4.4211	0.1851	0.1671	0.1245	0.2673
Dim-E2-205	27.3030	0.0555	1.8162	4.7779	0.1245	0.1454	0.1232	0.2034
Dim-E2-208	26.0325	0.0551	2.5214	6.3690	0.1755	0.1148	0.1209	0.2613
Dim-E2-211	24.8024	0.0534	1.8363	4.5106	0.1066	0.1321	0.1107	0.2517

Dim-E2-214	26.1279	0.0550	2.7025	4.5947	0.1479	0.0725	0.1112	0.2217
Dim-E2-217	26.2990	0.0597	1.8750	4.8032	0.1109	0.1066	0.1107	0.1981
Dim-E2-220	27.6533	0.0580	1.0465	4.8561	0.0565	0.1689	0.1089	0.2151
Dim-E2-223	30.2787	0.0543	1.1460	4.5000	0.0612	0.0757	0.0942	0.1784
Dim-E2-226	30.3993	0.0581	0.9981	4.7873	0.0704	0.2431	0.1004	0.1665
Dim-E2-229	28.4778	0.0567	1.8826	4.6844	0.1333	0.1106	0.0907	0.1883
Dim-E2-232	29.7949	0.0530	1.7291	4.2105	0.1087	0.1408	0.0778	0.2164
Dim-E2-235	24.7613	0.0490	3.0828	3.9613	0.1875	0.0796	0.0958	0.2245
Dim-E2-238	26.4103	0.0539	1.0091	4.4765	0.0594	0.2259	0.0964	0.1941
Dim-E2-241	29.7169	0.0516	1.8771	4.1529	0.1278	0.1517	0.0889	0.2364
Dim-E2-244	29.3018	0.0528	0.6097	4.9681	0.0484	0.3014	0.0810	0.1703
Dim-E2-247	29.0458	0.0508	1.1480	4.3103	0.0826	0.0904	0.0793	0.1483
Dim-E2-250	23.4295	0.0524	1.5402	4.6819	0.0996	0.2746	0.1001	0.1554
Dim-E2-253	24.0695	0.0520	1.4469	4.3966	0.0900	0.1102	0.0929	0.1481
Dim-E2-256	24.8358	0.0466	1.8024	4.1336	0.1220	0.1471	0.0806	0.1599
Dim-E2-259	27.1896	0.0451	1.3019	4.4514	0.0812	0.1111	0.0763	0.1417
Dim-E2-264	26.1743	0.0491	0.9295	4.6310	0.0578	0.0564	0.0861	0.1284
Dim-E2-270	25.7440	0.0448	2.0828	4.2582	0.1390	0.1386	0.0808	0.1756
Dim-E2-276	28.6370	0.0453	0.6099	4.2429	0.0407	0.0869	0.0668	0.1283
Dim-E2-282	26.7848	0.0445	1.3972	4.9032	0.0909	0.0906	0.0628	0.1961
Dim-E2-288	26.0549	0.0454	0.7114	4.2580	0.0538	0.1635	0.0744	0.1535
Long-term precision	0.43%	0.29%	6.39%	0.93%	10.23%	9.60%	2.02%	1.40%

*Ratios are reported in mmol/mol for Mg/Ca and Sr/Ca, and in µmol/mol for rest of the ratios.

Note: Sr/Ca values >0.08 mmol/mol, U/Ca values >0.4µmol/mol, Ba/Ca values > 9 µmol/mol, Y/Ca values >2.5 µmol/mol, and Zr/Ca values >1.2 µmol/mol are removed from plots in Figs. 2 and 3 to simplify the presentation of the data.

Table S2 Summary of Rare Earth Element (including Yttrium: REY) and Sr-isotope data of the representative sub-samples, Dim Cave speleothems (Dim-E2, Dim-E3, and Dim-E4), SW Turkey. Concentrations are in ppb.

Sample	Depth (mm)	Age* (kyr)	La	Ce	Pr	Nd	Sm	Eu	Gd	Tb	Dy	Y	Ho	Er	Tm	Yb	Lu	Y/ Ho	$^{87}Sr/^{86}Sr$	Err. %
Dim-E2-040	40	9.99	137.58	7.86	33.38	146.56	29.44	7.67	43.85	8.00	65.64	1261.97	18.55	64.45	9.96	64.84	10.20	68.0	0.708172	0.000007
Dim-E2-155	155	10.88	72.94	9.88	18.09	81.28	16.70	4.35	25.17	4.79	37.49	726.49	10.97	38.25	5.92	37.73	6.09	66.3	0.708218	0.000007
Dim-E2-173	173	11.03	96.51	7.98	23.95	105.59	21.90	5.34	32.95	6.36	50.82	980.60	14.70	51.76	7.97	51.51	8.22	66.7	0.708226	0.000006
Dim-E2-194	194	11.20	80.43	7.17	19.40	85.04	16.52	4.38	26.87	4.63	39.35	759.44	11.22	38.82	5.73	39.00	6.41	67.7	0.708217	0.000007
Dim-E2-220	220	11.44	78.04	5.08	19.04	88.22	18.70	4.89	32.64	6.36	60.19	1326.42	17.99	67.19	10.61	68.22	11.64	73.7	0.708270	0.000007
Dim-E2-290	290	13.09	44.53	14.70	11.26	49.25	10.38	2.66	15.48	2.68	21.45	425.84	6.62	21.41	3.28	21.33	3.41	64.4	0.708169	0.000007
Dim-E3-062	62	43.67	134.43	12.49	23.15	90.95	15.13	3.47	21.46	3.81	27.92	492.58	8.19	27.78	4.15	26.47	4.45	60.1	0.708197	0.000011
Dim-E3-090	90	48.25	329.18	50.65	58.83	228.90	38.58	8.05	46.74	7.42	55.93	830.73	15.07	47.72	6.96	44.71	6.90	55.1	0.708377	0.000007
Dim-E3-135	135	61.35	6.50	5.59	1.22	4.02	1.14	0.16	1.07	0.16	0.23	16.20	0.30	0.96	0.16	1.14	0.17	53.2	0.708335	0.000009
Dim-E3-240	240	71.64	81.03	9.53	14.63	59.82	11.22	2.54	14.27	2.36	18.50	308.35	4.93	16.58	2.57	16.20	2.75	62.5	0.708407	0.000007
Dim-E3-280	280	84.23	31.08	20.60	5.38	22.93	4.74	0.78	5.72	1.16	6.86	144.23	2.10	7.40	1.20	8.72	1.31	68.6	0.708371	0.000007
Dim-E4-040	40	12.05	95.28	1.76	25.40	111.38	24.61	6.34	38.88	7.39	59.75	1139.04	17.66	59.69	9.40	61.50	9.87	64.5	0.708263	0.000007
Dim-E4-293	293	13.63	8.15	10.42	1.71	6.52	1.43	0.37	3.69	0.58	2.26	65.74	0.94	3.54	0.59	3.72	0.67	70.3	0.708098	0.000007
Dim-E4-360	360	14.57	1.86	2.75	0.47	2.05	0.47	0.10	1.27	0.48	5.33	303.26	2.83	14.66	2.68	18.85	3.41	107.1		
Host limestone	-	Permian	329.34	660.24	70.96	267.63	52.33	11.00	50.88	8.10	42.71	311.89	8.95	24.16	3.71	21.02	3.21	34.8		
Chondrite**	-	-	237	612	95	467	153	58	205.5	37.4	254	1570	56.6	165.5	25.5	170	25.4	27.7		

*U-series ages are calculated by linear regression based on actual age results given in Paper 3 (Unal-Imer et al.2015; App. 3).

** Chondrite REY values are gathered from (Sun & McDonough 1989).

Table S3 Elemental data of the host dolomitic limestone of the Dim Cave, SW Turkey. REY data is given in Table S2.

	7Li	9Be	25Mg	31P	43Ca	45Sc	49Ti	51V	53Cr	57Fe	59Co	60Ni	65Cu	66Zn	71Ga	84Sr	85Rb	86Sr	89Y	90Zr	93Nb
ppb	0.75	0.03	125541.37	641.36	230289.17	0.22	13.73	7.02	6.26	632.2	0.31	4.54	0.79	16.29	0.06	57.8	0.27	56.64	0.31	0.68	0.08
%	0.00	0.00	35.14	0.18	64.46	0.00	0.00	0.00	0.00	0.18	0.00	0.00	0.00	0.00	0.00	0.02	0.00	0.02	0.00	0.00	0.00

	98Mo	111Cd	184W	187Re	205Tl	206Pb	207Pb	208Pb	232Th	238U
ppb	0.16	0.04	0.02	0	0.06	0.81	0.45	0.52	0.06	2.99
%	0.00	0.00	0.00	0.00	0.00	0.00	0.00	0.00	0.00	0.00

REFERENCES (PAPER 4)

Bar-Matthews, M. & Ayalon, A., 2011. Climatic, vegetation and cultural change in the eastern Mediterranean during the mid-Holocene environmental transition. *The Holocene*, 21, pp. 147–162.

Bar-Matthew, M. et al., 2003. Sea – land oxygen isotopic relationships from planktonic foraminifera and speleothems in the Eastern Mediterranean region and their implication for paleorainfall during interglacial intervals. *Geochimica et Cosmochimica Acta*, 67(17), pp.3181–3199.

Bar-Matthews, M., Ayalon, A., Kaufman, A. & Wasserburg, G.J., 1999. The Eastern Mediterranean paleoclimate as a reflection of regional events: Soreq cave, Israel. *Earth and Planetary Science Letters*, 166(1-2), pp.85–95. Available at: http://linkinghub.elsevier.com/retrieve/pii/S0012821X98002751.

Bar-Matthews, M., Ayalon, A., Kaufman, A. & Wasserburg, G.J., 1999. The Eastern Mediterranean paleoclimate as a reflection of regional, Soreq cave. *Earth and Planetary Science Letters*, 166(1-2), pp.85–95. Available at: http://linkinghub.elsevier.com/retrieve/pii/S0012821X98002751.

Bar-Matthews, M., Ayalon, A. & Kaufman, A., 1997. Late Quaternary Paleoclimate in the Eastern Mediterranean Region from Stable Isotope Analysis of Speleothems at Soreq Cave, Israel. *Quaternary Research*, 47(47), pp.155–168.

Bau, M., 1996. Controls on the fractionation of isovalent trace elements in magmatic and aqueous systems: evidence from Y/Ho, Zr/Hf, and lanthanide tetrad effect. *Contributions to Mineralogy and Petrology*, 123(3), pp.323–333. Available at: http://www.springerlink.com/openurl.asp?genre=article&id=doi:10.1007/s004100050159.

Belli, R. et al., 2013.Regional climate variability and ecosystem responses to the last deglaciation in the northern hemisphere from stable isotope data and calcite fabrics in two northern Adriatic stalagmites. *Quaternary Science Reviews* 72, pp. 146–158

Berger, A. & Loutre, M.F., 1991. Insolation values for the climate of the last 10 million years. *Quaternary Science Reviews*, 10(1988), pp.297–317.

Bozkaya, Ö. & Yalçin, H., 2004. New Mineralogic Data and Implications for the Tectonometamorphic Evolution of the Alanya Nappes, Central Tauride Belt, Turkey. *International Geology Review*, 46(4), pp.347–365. Available at: http://www.tandfonline.com/doi/abs/10.2747/0020-6814.46.4.347 [Accessed December 2, 2014].

Capo, R. C., Stewart, B.W., Chadwick, O.A., 1998. Strontium isotopes as tracers of ecosystem processes: theory and methods. *Geoderma*, 82, pp. 197–225.

Dean J.R. et al., 2015. Eastern Mediterranean hydroclimate over the late glacial and Holocene, reconstructed from the sediments of Nar lake, central Turkey, using stable isotopes and carbonate mineralogy. *Quaternary Science Reviews* 124, pp.162–174.

Eggins, S.M. et al., 1997. A simplemethod for the precise determination of N40 trace elements in geological samples by ICPMS using enriched isotope internal standardisation. *Chemical Geology*, 134, pp.311–326.

Fairchild, I. J. et al., 2001. Annual to sub-annual resolution of multiple trace-element trends in speleothems. *Journal of Geologial Society, London*, 158, pp.831–841.

Fairchild, I.J. et al., 2000. Controls on trace element (Sr – Mg) compositions of carbonate cave waters: implications for speleothem climatic records. *Chemical Geology*, 166, pp.255–269.

Fairchild, I.J. et al., 1994. Hydrochemistry of carbonate terrains in alpine glacial settings. *Earth Surface Processes and Landforms*, 19(1), pp.33–54. Available at: http://doi.wiley.com/10.1002/esp.3290190104.

Fairchild, I.J. & Treble, P.C., 2009. Trace elements in speleothems as recorders of environmental change. *Quaternary Science Reviews*, 28(5-6), pp.449–468. Available at: http://linkinghub.elsevier.com/retrieve/pii/S0277379108003326 [Accessed October 30, 2012].

Fairchild, I.J. & McMillan, E.A., 2007. Speleothems as indicators of wet and dry periods. *International Journal of Speleology*, 36 (2), pp. 69–74.

Fleitmann, D. et al., 2009. Timing and climatic impact of Greenland interstadials recorded in stalagmites from northern Turkey. *Geophysical Research Letters*, 36(19), pp.1–5. Available at: http://www.agu.org/pubs/crossref/2009/2009GL040050.shtml [Accessed August 10, 2012].

Fohlmeister, J. et al. 2011. Modelling carbon isotopes of carbonates in cave drip water. *Geochimica et Cosmochimica Acta*, 75, pp.5219–5228.

Frisia, S. 2015. Microstratigraphic logging of calcite fabrics in speleothems as tool for palaeoclimate studies. *International Journal of Speleology*, 44(1), pp. 1–16.

Frisia, S. et al., 2002. Aragonite – Calcite Relationships in Speleothems (Grotte De Clamouse, France): Environment, Fabrics, and Carbonate Geochemistry. *Journal of Sedimentary Research*, 72, pp.687–699.

Frumkin, A., Bar-Yosef, O. & Schwarcz, H.P., 2011. Possible paleohydrologic and paleoclimatic effects on hominin migration and occupation of the Levantine Middle Paleolithic. *Journal of Human Evolution*, 60, pp. 437–451.

Frumkin, A. & Stein, M., 2004. The Sahara–East Mediterranean dust and climate connection revealed by strontium and uranium isotopes in a Jerusalem speleothem. *Earth and Planetary Science Letters*, 217(3-4), pp.451–464. Available at: http://linkinghub.elsevier.com/retrieve/pii/S0012821X03005892 [Accessed November 7, 2012].

Frumkin, A., Ford, D.C. & Schwarcz, H.P., 1999. Continental Oxygen Isotopic Record of the Last 170,000 Years in Jerusalem. *Quaternary Research*, 51, pp.317–327.

Ganor, E. & Foner, H.A., 2001. Mineral dust concentrations, deposition fluxes and deposition velocities in dust episodes over Israel. *Journal of Geophysical Research,*106(D16), pp. 18,431–18,43.

Gascoyne, M., 1983. Trace-element partition coefficients in the calcite-water system and their paleoclimatic significance in cave studies. *Journal of Hydrology*, 61(1-3), pp.213–222. Available at: http://linkinghub.elsevier.com/retrieve/pii/0022169483902494.

Gat, J.R. & Carmi, I., 1987. Effect of climate changes on the precipitation patterns and isotopic composition of water in a climate transition zone : Case of the Eastern Mediterranean Sea area. In *The Influence of Climate Chnage and Climatic Variability on the Hydrolic Regime and Water Resources*. Vancouver: IAHS Publ. no. 168, pp. 513–524.

Gat, J.R. & Gonfiantini, R., 1981. *Stable Isotope Hydrology. Deuterium and oxygen-18 in water cycle.* J. R. Gat & R. Gonfiantini, eds., Vienna: International Atomic Energy Agency Technical Report Series No.210.

Genty, D. et al., 2003. Precise dating of Dansgaard-Oeschger climate oscillations in western Europe from stalagmite data. *Nature*, 421(6925), pp.833–7. Available at: http://www.ncbi.nlm.nih.gov/pubmed/12594510.

Goede, A. et al., 1998. Aeolian contribution to strontium and strontium isotope variations in a Tasmanian speleothem. *Chemical Geology*, 149, pp.37–50.

Gündalı, N. et al., 1989. *Dim Mağarası (Alanya) Araştırma Raporu, Mimari ve Elektrikasyon Uygulama Projeleri, Report no. 369 (unpublished, in Turkish)*, General Directorate of Mineral Research and Exploration, Ankara, Turkey.

Gündalı, N. et al., 1987. *Alanya-Gazipaşa ve Manavgat Çevresinin Mağaraları, (unpublished, in Turkish)*, General Directorate of Mineral Research and Exploration, Ankara, Turkey.

Hellstrom, J.C. & Mcculloch, M.T., 2000. Multi-proxy constraints on the climatic significance of trace element records from a New Zealand speleothem. *Earth and Planetary Science Letters*, 179, pp.287–297.

Hendy, C., 1971. The isotopic geochemistry of speleothems-I. The calculation of the effects of different modes of formation on the isotopic composition of speleothems and their applicability as paleoclimatic indicators. *Geochimica et Cosmochimica Acta*, 35(8), p.80l–824.

Huang, Y. et al., 2001. Seasonal variations in Sr , Mg and P in modern speleothems (Grotta di Ernesto, Italy). *Chemical Geology*, 175, pp.429–448.

Hughes, P.D., Gibbard, P.L. & Ehlers, J., 2013. Timing of glaciation during the last glacial cycle: evaluating the concept of a global “Last Glacial Maximum” (LGM). *Earth-Science Reviews*, 125, pp.171–198. Available at: http://linkinghub.elsevier.com/retrieve/pii/S0012825213001190 [Accessed July 18, 2014].

IAEA/WMO, 2015. Global Network of Isotopes in Precipitation—The GNIP Database. Available at: http://www.iaea.org/water.

Jalut, G. et al., 2009. Holocene circum-Mediterranean vegetation changes: Climate forcing and human impact. *Quaternary International*, 200(1-2), pp.4–18. Available at: http://linkinghub.elsevier.com/retrieve/pii/S1040618208000736 [Accessed January 30, 2013].

Jex, C.N. et al., 2011. A 500yr speleothem-derived reconstruction of late autumn–winter precipitation, northeast Turkey. *Quaternary Research*, 75(3), pp.399–405. Available at: http://linkinghub.elsevier.com/retrieve/pii/S0033589411000160 [Accessed August 21, 2012].

Johnson, K. et al., 2006. Seasonal trace-element and stable-isotope variations in a Chinese speleothem: The potential for high-resolution paleomonsoon reconstruction. *Earth and Planetary Science Letters*, 244(1-2), pp.394–407. Available at: http://linkinghub.elsevier.com/retrieve/pii/S0012821X06001191 [Accessed December 5, 2014].

Kamber, B.S. et al., 2003. A refined solution to Earth's hidden niobium: implications for evolution of continental crust and mode of core formation. *Precambrian Research*, 126(3-4), pp.289–308. Available at: http://linkinghub.elsevier.com/retrieve/pii/S0301926803001001 [Accessed March 5, 2014].

Kaniewski, D., Campo, E. Van & Weiss, H., 2012. Drought is a recurring challenge in the Middle East. *Proceedings of the National Academy of Sciences*, 109(10), pp.3862–3867.

Lisker,S. et al., 2010. Late Pleistocene palaeoclimatic and palaeoenvironmental reconstruction of the Dead Sea area (Israel), based on speleothems and cave stromatolites. *Quaternary Science Reviews*, 29, pp. 1201–1211.

McArthur, J.M., Howarth R.J. & Shields, G.A., 2012. Strontium Isotope Stratigraphy. In F. M. Gradstein, J. G. Ogg, M. Schmitz and G. Ogg, eds. *The Geologic Time Scale 2012*, Ch. 7. Elsevier B.V.

McDermott, F., 2004. Palaeo-climate reconstruction from stable isotope variations in speleothems: a review. *Quaternary Science Reviews*, 23(7-8), pp.901–918. Available at: http://linkinghub.elsevier.com/retrieve/pii/S0277379104000198 [Accessed July 9, 2014].

Morse, J.W. & Bender, M.L., 1990. Partition coefficients in calcite: Examination of factors influencing the validity of experimental results and their application to natural systems. *Chemical Geology*, 82, pp.265–277. Available at: http://linkinghub.elsevier.com/retrieve/pii/000925419090085L.

Murray, J.W., 1954. The Deposition of Calcite and Aragonite in Caves. *The Journal of Geology*, 62(5), pp.481–492.

Nguyen, a. D. et al., 2012. Impact of recent coastal development and human activities on Nha Trang Bay, Vietnam: evidence from a Porites lutea geochemical record. *Coral Reefs*, 32(1), pp.181–193. Available at: http://link.springer.com/10.1007/s00338-012-0962-4 [Accessed November 17, 2014].

Okay, A.I. & Özgul, N., 1984. HP/LT metamorphism and the structure of the Alanya Massif, Southern Turkey: an allochthonous composite tectonic sheet. *Geological Society, London, Special Publications*, 17(1), pp.429–439. Available at: http://sp.lyellcollection.org/cgi/doi/10.1144/GSL.SP.1984.017.01.30 [Accessed August 5, 2014].

Regattieri, E. et al., 2014. Lateglacial to Holocene trace element record (Ba, Mg, Sr) from Corchia Cave (Apuan Alps, central Italy): paleoenvironmental implications. *Journal of Quaternary Science*, 29(4), pp.381–392. Available at: http://doi.wiley.com/10.1002/jqs.2712 [Accessed October 22, 2014].

Roberts, N. et al., 2011. Climatic, vegetation and cultural change in the eastern Mediterranean during the mid-Holocene environmental transition. *The Holocene*, 21(1), pp. 147–162.

Roberts, M.S., Smart, P.L. & Baker, A., 1998. Annual trace element variations in a Holocene speleothem. *Earth and Planetary Science Letters*, 154(1-4), pp.237–246. Available at: http://linkinghub.elsevier.com/retrieve/pii/S0012821X97001167.

Robinson, S. a. et al., 2006. A review of palaeoclimates and palaeoenvironments in the Levant and Eastern Mediterranean from 25,000 to 5000 years BP: setting the environmental background for the evolution of human civilisation. *Quaternary Science Reviews*, 25(13-14), pp.1517–1541. Available at: http://linkinghub.elsevier.com/retrieve/pii/S0277379106000825 [Accessed November 12, 2012].

Sarıkaya, M.A. et al., 2014. An early advance of glaciers on Mount Akdağ, SW Turkey, before the global Last Glacial Maximum; insights from cosmogenic nuclides and glacier modeling. *Quaternary Science Reviews*, 88, pp.96–109. Available at: http://linkinghub.elsevier.com/retrieve/pii/S0277379114000298 [Accessed March 18, 2014].

Sarıkaya, M.A. et al., 2008. Cold and wet Last Glacial Maximum on Mount Sandıras, SW Turkey, inferred from cosmogenic dating and glacier modeling. *Quaternary Science Reviews*, 27(7-8), pp.769–780. Available at: http://linkinghub.elsevier.com/retrieve/pii/S027737910800005X [Accessed December 3, 2012].

Şenkul, Ç. & Doğan, U., 2013. Vegetation and climate of Anatolia and adjacent regions during the Last Glacial period. *Quaternary International*, 302, pp.110–122. Available at: http://linkinghub.elsevier.com/retrieve/pii/S1040618212002649 [Accessed October 2, 2014].

Sinclair, D. J. Banner, J. L., Taylor, F. W., Partin, J., Jenson, J., Mylroi, J., Goddard, E., Quinn, T., Jocson, J., Miklavič, B., 2012. Magnesium and strontium systematics in tropical speleothems from the Western Pacific. *Chemical Geology* 294–295, pp. 1–17.

Staubwasser, M. & Weiss, H., 2006. Holocene climate and cultural evolution in late prehistoric–early historic West Asia. *Quaternary Research*, 66(3), pp.372–387. Available at: http://linkinghub.elsevier.com/retrieve/pii/S0033589406001116 [Accessed January 7, 2015].

Sun, S.S. & McDonough, W.F., 1989. Chemical and isotopic systematics of oceanic basalts: implications for mantlencomposition and processes. In A. D. Saunders & M. J. Norry, eds. *Magmatism in the Ocean Basins*. pp. 313–345.

Türkeş, M., 1996. Spatial and Temporal Analysis of Annual Rainfall Variations in Turkey. *International Journal of Climatology*, 16, pp.1057–1076.

Tzedakis, P.C., 2007. Seven ambiguities in the Mediterranean palaeoenvironmental narrative. *Quaternary Science Reviews*, 26(17-18), pp.2042–2066. Available at: http://linkinghub.elsevier.com/retrieve/pii/S0277379107001308 [Accessed September 14, 2014].

Újvári, G. et al., 2010. Dust flux estimates for the Last Glacial Period in East Central Europe based on terrestrial records of loess deposits: a review. *Quaternary Science Reviews*, 29(23-24), pp.3157–3166. Available at: http://linkinghub.elsevier.com/retrieve/pii/S0277379110002568 [Accessed January 12, 2015].

Ünal-İmer. E. et al., 2015. An 80 kyr-long continuous speleothem record from Dim Cave, SW Turkey with paleoclimatic implications for the Eastern Mediterranean. *Nature Scientific Reports*, 5, 13560, doi: 10.1038/srep13560.

Vaks, A. et al., 2003. Paleoclimate reconstruction based on the timing of speleothem growth and oxygen and carbon isotope composition in a cave located in the rain shadow in Israel. *Quaternary Research*, 59(2), pp.182–193.

Vaks, A. et al., 2003. Paleoclimate reconstruction based on the timing of speleothem growth and oxygen and carbon isotope composition in a cave located in the rain shadow in Israel. *Quaternary Research*, 59(2), pp.182–193. Available at: http://linkinghub.elsevier.com/retrieve/pii/S0033589403000139 [Accessed November 12, 2012].

Veizer, J. 1989. Strontium Isotopes In Seawater Through Time. *Annual Review of Earth and Planetary Sciences*, 17, pp. 141-167.

Wang, Y.J. et al., 2001. A high-resolution absolute-dated late Pleistocene Monsoon record from Hulu Cave, China. *Science (New York, N.Y.)*, 294(5550), pp.2345–2348. Available at: http://www.ncbi.nlm.nih.gov/pubmed/11743199 [Accessed October 30, 2012].

Wickens, L. et al., 2011. The Last Interglacial and Holocene in SW Turkey : Evidence from Calcite-Aragonite Speleothems. In *American Geophysical Union, Fall Meeting 2011*.

Wiedner E. et al., 2008. Investigation of the stable isotope fractionation in speleothems with laboratory experiments. *Quaternary International*, 187, pp. 15–24.

Zhao, J., Xia, Q. & Collerson, K.D., 2001. Timing and duration of the Last Interglacial inferred from high resolution U-series chronology of stalagmite growth in Southern Hemisphere. *Earth and Planetary Science Letters*, 184, pp.635–644.

CONCLUSION

1. Summary

The main aim of this research was to determine the timing of CO_2 degassing events and late Quaternary major climate changes in order to understand varying roles of tectonic and climate processes in SW Turkey. To facilitate this, I investigated i) *multi-generation carbonate veins and carbonate-cemented breccia* within active fault zones in Marmaris (SW Turkey) that represent CO_2 degassing and associated seismic events and ii) *speleothem samples* from the Dim Cave in S-SW Turkey to determine regional climatic conditions. The intention was to compare the climatic data obtained from the speleothems to the results from the calcite vein samples to determine whether, and if appropriate how, climate interacted with CO_2 degassing processes. Laboratory analyses consisted of intensive petrographical, geochronological (U-series dating), and geochemical (O-C-Sr isotope and trace element analyses) studies from both calcite veins and speleothem samples. A substantial new data set has been produced and interpreted.

This thesis has provided a general overview of the complex interplay between active tectonism and climate variability affecting both the geological and environmental controls on CO_2 degassing events as reflected through calcite formation. The processes that are facilitating and/or limiting the accumulation, migration and degassing of CO_2 volatiles within crustal levels in both relatively protected (cave) and open (fault-related vein systems) environments have been comprehensively investigated. The first two papers describe and interpret two calcite vein systems (Kumlubük and Amos, SW Turkey) in terms of their temporal and geochemical relation to regional tectonic trends and climatic conditions (first two objectives of the thesis), while the latter two papers present ~80-kyr continuous stable isotope and trace element/Ca time profiles derived from speleothems in Dim Cave, S-SW Turkey. They constrain regional paleoclimatic conditions, and add significant knowledge to the terrestrial climate history of the Eastern Mediterranean (third objective of the thesis). Furthermore, the general climate history outlined in the speleothem records helps to define the background conditions that affected vein calcite production, thus helping to constrain the tectonic processes. The main findings of the papers can be summarised as the followings;

- In Paper 1, a number of vein/breccia carbonate formations in tectonically active zones of SW Turkey have been investigated through a large U-series age dataset. The paper presents an exceptional 150 kyr-long age record of the vein/breccia formations from two vein systems (Kumlubük and Amos, SW Turkey). The timing of vein formation coincides preferentially with low and intermediate insolation phases during the last glacial period, suggesting positive moisture balance for the aquifer systems, which is critical for calcite

vein formation in terms of transporting CO_2-rich fluids to the surface. It is argued that the surface water circulation reaching deeper levels of the fault zone leads to upward passive convection of CO_2-rich with subsequent degassing at the surface, while relatively less amounts of water circulation within the fault zone facilitates the carbonate-sourced CO_2 build up in sealed reservoirs and degassing at or near the surface occur largely during rupture events. This paper highlights the possible links between climate-driven hydrological conditions controlling CO_2 enrichment and dissipation within a faulted system. It is demonstrated that fault-related calcite veins are not only valuable proxies of seismic activity but also potentially useful climate archives, providing a new tool to examine long-term climate change in semi-arid regions.

- Paper 2 provides a comprehensive data set of U-series, $\delta^{13}C$, $\delta^{18}O$ and Sr isotope, and REY concentrations to determine the timing of secondary vein deposits and constrain the origin of fluids from which the calcite was deposited. The veins formed in an area undergoing significant extensional tectonic activity in southwest Turkey (i.e. Kumlubük and Amos calcite vein systems). U-series age data reveal that the vein formation occurred between 272.6 and 20.5 kyr. Petrographical observations demonstrate that the vein formation is mainly controlled by a crack-seal mechanism, initiated by intense multi-stage fracturing of the host limestone (brecciation), which is interpreted be associated with faulting in this area. Main stress distributions of the extension veins, which are demonstrated by bi-directional rose diagrams, appear to be controlled by regional active normal faulting, trending in NNW-SSE and E-W in Kumlubük and Amos respectively. Stable isotope records (O, C) of the veins reveal the cyclic nature of CO_2-degassing events and meteoric water infiltration through normal faults affecting multiple growth-cycles of the veins, which is ultimately controlled by regional seismic activity.

  Accumulation of volatile CO_2 within the brittle upper crust can result in significant fluid overpressures, which in turn is interpreted to have led to initial fracturing (or crack opening) and multi-episodic brecciation. It is argued that the fluid source is dominantly the meteoric water, while the CO_2 is sourced mainly from the dissolved host limestone. Trace element and Sr isotope geochemistry of the calcite veins and breccia indicate interactions between circulating meteoric water and the host limestone. While this is valid for the growth of the majority of veins, elevated Sr-isotope and noticeable positive Eu anomalies in some veinlets imply that deeply circulated meteoric water also interacted with basement metamorphic rocks at higher temperatures. Overall, it is interpreted that isotopic and chemical variations are due to episodic emissions of CO_2 as a result of seismicity. This study highlights the

potential capacity and/or usage of co-seismic calcite precipitations to determine structural controls in an active faulting setting.

- Paper 3 presents highly-resolved speleothem-based stable isotope (C, O) profiles from the Dim Cave (36ºN, 232 m a.s.l.) in S-SW Turkey supported by an intensive, high precision U-series chronology. The record covers the whole of the last glaciation at good to excellent resolution and gives detailed insights into changes in northern hemisphere atmospheric circulation during the period ~9–90 kyr. Three stalagmites from Dim Cave are examined, but the main focus of the paper is stalagmite Dim-E3, which contained a continuous record for the period ~13 to 90 kyr. The findings reveal how stalagmite oxygen ($\delta^{18}O$) and carbon ($\delta^{13}C$) records track changes in the trajectory of winter westerlies during the course of the last ice age. It is interpreted that these changes can be related to the growth of the northern Ice Sheets, especially the Fennoscandian, through the glacial period with trajectories gradually depressed southward as the ice sheets grew. It was concluded that abrupt cold events in the North Atlantic (i.e. Heinrich events) resulted in accelerated westerly flow in the Eastern Mediterranean. It is also noted that Dim cave has had a positive moisture water balance throughout the last glaciation, based primarily on continuous speleothem calcite growth. This contrasts with late Holocene conditions when speleothems are either aragonitic or absent. This also demonstrates stronger meteoric water flux during glacial times than at the present day but with strong variability within the glacial period. Glacial-interglacial changes in carbon isotope profiles ($\delta^{13}C$) reflect changes in thicknesses in the vegetation cover and interactions with the host dolomitic limestone. While $\delta^{13}C$ depletion during interglacials reflects elevated mixing with the soil organic carbon (with more depleted values ~25‰), glacial times are reflected by less negative $\delta^{13}C$ values pointing to increased interactions with the host limestone ($\delta^{13}C$ ~5.4 ‰) due to higher residence time of drip waters. It is also noted that the Dim Cave record shows synchronous responses to global climatic variations (e.g. Heinrich events) driven by the evolution of the northern hemisphere ice sheets and higher frequency climate events.

- Paper 4 presents trace element/Ca ratio records derived from the Dim speleothems and relates these records to the stable/radiogenic isotope ($\delta^{18}O$, $\delta^{13}C$, $^{87}Sr/^{86}Sr$) data, as well as full trace element concentrations of the speleothem sub-samples. This paper complements the ideas/interpretations discussed in Paper 3 (Ünal-İmer et al. 2015) and highlights the geochemical/climatic processes responsible for the speleothem deposition during the last glaciation from 90 to 10 kyr. Physicochemical changes in the cave drip water and resultant speleothem chemistry are explained using high-resolution Mg/Ca, Sr/Ca, U/Ca, Ba/Ca,

Y/Ca, and Zr/Ca time profiles of the speleothems. The results show similar trends between Mg/Ca, Sr/Ca, and Ba/Ca, while U/Ca, Y/Ca, and Zr/Ca display inverse but covarying trends. The main source of speleothem trace elements is the host limestone with significant interactions between soil, unsaturated epikarst, groundwater (and surface runoff), and basement rocks (composed predominantly of mica-schist, quartzite, and dolomite). Higher values in Zr/Ca, U/Ca, and Y/Ca during times of higher growth rates (at 51–40, 71–63, and 89–80 kyr) reflect inputs of quartzofeldspathic elements (Zr, U and Y) and are most likely associated with wet periods over SW Turkey. We cannot be certain of the source but the two strong candidates are the wet deposition of aeolian dust (supported by elevated Sr-isotope ratios in speleothems) and/or dissolution of quartzofeldspathic rock inliers within the host rock. Similarly, the variations in Mg/Ca, Sr/Ca, and Ba/Ca are interpreted to be mainly controlled by enhanced interactions between the host limestone and seepage waters during relatively drier conditions (or during times of lower growth rates of Dim-E3; 40–18, 63–51, and 80–71 kyr). Covariance and increase of these ratios under drier conditions can also be explained by the prior calcite precipitation process, which modifies the drip waters before deposition and yields increased values of $\delta^{13}C$, Mg/Ca, Sr/Ca, and Ba/Ca. In addition, relatively immobile REE (and Yttrium) element data indicates a seawater origin with negative Ce and positive Y anomalies for the stalagmites, confirming their close link with the host dolomitic limestone.

Excluding the aragonite layer during 80–75 kyr, the Dim record responds synchronously to the global Heinrich events and displays distinct TE/Ca anomalies during specifically H6, H5, and to a lesser extent during H4. This indicates the changes in westerlies over the site corresponding to a northerly air mass tracks during the earlier Heinrich events (H4, H5, and H6) in the last glacial cycle, while later H events (H1 and H2) reflect the effect of a more southerly track. Depending on both stable isotope (O, C) and TE/Ca ratio anomalies, the LGM is interpreted as cold and wet, probably due to reduced evapotranspiration. Although Dim-E3 stopped growing during the YD, other two speleothems (Dim-E2 and -E4) show continuous growth signifying positive moisture balance at Dim Cave during the YD. In addition, the Mid to Late Holocene is characterized by arid conditions in the Dim Cave.

2. Recommendations for future research

The first two studies of this thesis concerning fault-related calcite vein/breccia deposits from SW Turkey use a large set of U-series, $\delta^{13}C$-$\delta^{18}O$, Sr-isotope, and REY concentration data to investigate the temporal relationships of vein formation, regional faulting, and climatic variability, as well as

tracing the sources of the fluids and geological/hydrological processes during calcite precipitation. Future research of the calcite veins in association with the active tectonism could investigate the genetic models (i.e. CO_2-rich fluid over-pressuring, rupture, and crack-and-seal depositional mechanisms) of the vein emplacement in greater depth. The proposed mechanisms in the papers can be further supported by studying additional samples from other shallow sources (e.g. groundwater and soil) through isotopic (O, C, Sr) and trace element analyses, helping to eliminate possible interactions of these sources with calcite depositing systems. In addition, the analyses of carbonate deposition from other types of fault systems (e.g. strike-slip or low angle detachment fault systems), as well as from other continental extensional systems could allow us investigate the distribution of calcite vein/breccia formations (through their U-series ages) in association with different style of faulting environments. This would help us to identify the effect of changing fault mechanisms on vein formation, and accordingly on the effect of meteoric water infiltration and migration. Further, additional microstructural and geochemical analyses of fault-related calcite veins would be helpful to distinguish among different formation mechanisms related with different fault behaviours and varying geochemical conditions under which calcite precipitated.

The last two papers contain information gathered from Late Pleistocene to Holocene stalagmites from Dim Cave (SW Turkey), which record climatic conditions (e.g. near-surface moisture availability) that affected the calcite vein formation in the same region. The Dim Cave has already yielded a complete glacial cycle, with >80 kyr-long continuous record from fairly opportunistic collection of speleothems. A more intensive investigation of this cave and other cave systems in this region is warranted as they likely will yield further exceptional records. Recommendations for the development of cave research are highlighted below.

- Many modern speleothem studies have a strong focus on understanding hydrological processes within cave systems (e.g. Cuthbert et al. 2014; Bar-Matthews et al. 1997; Fairchild et al. 2000; Jex et al. 2011). A detailed investigation of drip water chemistry over a cycle of several years would be very useful from different cave sites, especially if water samples could be taken in close proximity to speleothems. Continuous or regular (seasonally) monitoring of the chemical characteristics of the drip water can allow us to identify the seasonal hydrological conditions regulating how rainfall infiltrates through the karst system, reacts with the host rock, and causes isotopic and chemical changes. This would help assess the representativeness of the key variables (e.g. seasonal change in the rainfall amount or mean annual temperature) being used to understand the conditions in the past. Further geochemical analyses should be performed on additional host limestone, soil, and cave pool and rain waters to improve our understanding of the range of isotopic

compositions in rock, regolith and cave waters. This will help provide more robust insights into chemical factors controlling the deposition of speleothems.

- Additional (and at higher resolution) petrographical work should be performed on Dim Cave speleothems in order to better understand the changes in drip rate of the seepage waters responsible for the speleothem deposition during different periods in the Last Glacial (from 90 to 10 kyr).

- Research could be expanded at the Dim Cave and other cave systems in Turkey to locate/collect older stalagmites and produce longer and more high-resolution records.

- In addition to stable isotope and trace element variations, many studies (Bar-Matthews et al. 1999; Verheyden et al. 2000; Goede et al. 1998; Frumkin & Stein 2004; Ayalon et al. 1999) have shown that Sr isotopes have potential to constrain detailed paleohydrological conditions (e.g. siliciclastic aeolian dust, loess or any other detrital input), in association with interactions between atmosphere-water-soil-host rock. Although some Sr-isotope ratio analyses were already performed on Dim Cave speleothems and helped resolve the possible sources of Sr in Dim Cave (see Paper 4), higher resolution (at each laminae of the stalagmites) Sr isotope measurements can strengthen the arguments in this study.

3. Final remark

As a final point, it is worth emphasizing that this thesis has presented two world class records; one for the calcite-filled veins and one for Dim Cave speleothems from SW Turkey. It presents new insights into tectonic processes in SW Turkey and highlights the possibility of using vein calcites as both a paleotectonic and paloeclimatic tool. The role of CO_2-rich fluids within fault-related terrains such as travertine deposits have been well recognized and studied in the context of paleoclimate and paleohydrological cycles (Kampman et al. 2012; Priewisch et al. 2014; Szabo 1990; Minissale et al. 2002; Uysal et al. 2011). This thesis illustrates the usage of fault-related calcite vein/breccia deposits and argues that the climate-driven hydrological conditions may control CO_2 enrichment or dissipation in relation to the stress release episodes. It is concluded that during cold periods, regardless of whether precipitation increased or decreases, net moisture balance was positive as reflected in the formation of vein calcites and the continuous formation of speleothems in the Dim Cave. It has been demonstrated that there is a strong climate forcing (in terms of changes in westerly tracks) as the main control on speleothem geochemistry and growth and an indirect climatic control on calcite vein formation.

REFERENCES (CONCLUSION)

Ayalon, A., Bar-matthews, M., Kaufman, A., Survey, G., St, M.I., 1999. Petrography, strontium, barium and uranium concentrations, and strontium and uranium isotope ratios in speleothems as palaeoclimatic proxies : Soreq Cave, Israel. The Holocene 6, 715–722.

Bar-Matthews, M., Ayalon, A., Kaufman, A., 1997. Late Quaternary Paleoclimate in the Eastern Mediterranean Region from Stable Isotope Analysis of Speleothems at Soreq Cave, Israel. Quat. Res. 47, 155–168.

Bar-Matthews, M., Ayalon, A., Kaufman, A., Wasserburg, G.J., 1999. The Eastern Mediterranean paleoclimate as a reflection of regional events: Soreq cave, Israel. Earth Planet. Sci. Lett. 166, 85–95.

Cuthbert, M.O., Rau, G.C., Andersen, M.S., Roshan, H., Rutlidge, H., Marjo, C.E., Markowska, M., Jex, C.N., Graham, P.W., Mariethoz, G., Acworth, R.I., Baker, a, 2014. Evaporative cooling of speleothem drip water. Sci. Rep. 4, 5162.

Fairchild, I.J., Borsato, A., Tooth, A.F., Frisia, S., Hawkesworth, C.J., Huang, Y., Mcdermott, F., 2000. Controls on trace element (Sr – Mg) compositions of carbonate cave waters: implications for speleothem climatic records. Chem. Geol. 166, 255–269.

Frumkin, A., Stein, M., 2004. The Sahara–East Mediterranean dust and climate connection revealed by strontium and uranium isotopes in a Jerusalem speleothem. Earth Planet. Sci. Lett. 217, 451–464.

Goede, A., Mcculloch, M., McDermott, F., Hawkesworth, C., 1998. Aeolian contribution to strontium and strontium isotope variations in a Tasmanian speleothem. Chem. Geol. 149, 37–50.

Jex, C.N., Baker, A., Eden, J.M., Eastwood, W.J., Fairchild, I.J., Leng, M.J., Thomas, L., Sloane, H.J., 2011. A 500yr speleothem-derived reconstruction of late autumn–winter precipitation, northeast Turkey. Quat. Res. 75, 399–405.

Kampman, N., Ellam, R.M., Bickle, M.J., Burnside, N.M., Shipton, Z.K., Chapman, H.J., Nicholl, J.A., 2012. Pulses of carbon dioxide emissions from intracrustal faults following climatic warming. Nat. Geosci. 5, 352–358.

Minissale, A., Kerrick, D.M.D.M., Magro, G., Murrell, M.T.T., Paladini, S., RIHS, S., Sturchio, N.C.C., Tassi, F., Vaselli, O., Paladini, M., 2002. Geochemistry of Quaternary travertines in the region north of Rome (Italy): structural, hydrologic and paleoclimatic implications. Earth Planet. Sci. Lett. 203, 709–728.

Ünal-İmer E. et al., 2015. An 80 kyr-long continuous speleothem record from Dim Cave, SW Turkey with paleoclimatic implications for the Eastern Mediterranean. *Nature Scientific Reports*, 5, 13560, doi: 10.1038/srep13560.

Priewisch, A., Crossey, L.J., Karlstrom, K.E., Polyak, V.J., Asmerom, Y., Nereson, A., Ricketts, J.W., 2014. U-series geochronology of large-volume Quaternary travertine deposits of the southeastern Colorado Plateau: Evaluating episodicity and tectonic and paleohydrologic controls. Geosphere 10, 401–423.